Technische Universität München
TUM School of Natural Sciences

Interfacing Microwaves, Mechanical Vibrations, and Sound Waves through Superconducting Quantum Circuits

Thomas Luschmann

Vollständiger Abdruck der von der TUM School of Natural Sciences der Technischen Universität München zur Erlangung des akademischen Grades eines

Doktors der Naturwissenschaften (Dr. rer. nat.)

genehmigten Dissertation

Vorsitz: Prof. Dr. Johannes Knolle

Prüfende der Dissertation:

1. Priv.-Doz. Dr. Hans-Gregor Hübl
2. Prof. Dr. Eva Weig

Die Dissertation wurde am 28.05.2024 bei der Technischen Universität München eingereicht und durch die TUM School of Natural Sciences am 17.07.2024 angenommen.

Thomas Luschmann
Interfacing Microwaves, Mechanical Vibrations, and Sound Waves through Superconducting Quantum Circuits
Dissertation, 2024

Technische Universität München
TUM School of Natural Sciences
Lehrstuhl E23 für Technische Physik
Walther-Meissner-Institut für Tieftemperaturforschung
der Bayerischen Akademie der Wissenschaften

Abstract

Nano-electromechanical devices implement the versatile optomechanical interaction by combining nanoscale mechanical elements with superconducting circuits. Recently, first realizations of a novel approach have been achieved where a mechanical displacement modulates the magnetic flux in a Superconducting QUantum Interference Device (SQUID), coupling the inductance of the circuit to the motion of the mechanical element. Inductively coupled devices provide exciting opportunities to significantly increase the single-photon coupling rate beyond what could previously be achieved by solid state based systems. Previous studies on this class of devices have been constrained by limitations in external magnetic field strengths and high microwave loss rates. This thesis addresses these challenges by introducing improved fabrication techniques to reduce intrinsic losses and advanced experimental protocols to enable operation in higher magnetic fields. In our experiments, we determine the achievable single-photon single-phonon coupling rates g_0 and explore the scaling behavior with increasing magnetic fields, demonstrating a coupling rate of $g_0/2\pi = (53.72 \pm 2.91)$ kHz, exceeding any previously reported value. We also delve into the phenomena of Electromechanically Induced Transparency (EMIT) and optomechanical sideband cooling, demonstrating the adaptability of the inductively coupled architecture. Due to the unprecedented interaction strength, we demonstrate sideband cooling of the mechanical motion of a nanostring to a mode occupation of less than 10 phonons, using ultra-low drive powers equivalent to less than a single photon. Additionally, we demonstrate the effective control of the resonance frequency of the nanostring through electromechanical backaction. In this context, we quantitatively describe a Lorentz force induced shift of the mechanical resonance frequency and further identify an additional field-dependent mechanical frequency shift attributed to the interplay between the superconductivity of the nanostring with the external magnetic field, mediated by the elasticity of the flux-line-lattice. The broad range of our findings underscores the potential of inductively coupled electromechanics and demonstrates progress towards reaching the single-photon single-phonon strong coupling regime. Finally, we present a complementary research direction on quantum acoustic hybrid systems combining superconducting circuits and surface acoustic wave (SAW) devices. We fabricate SAW resonators on thin-film lithium niobate (LNO) substrates and perform the first comprehensive study of their performance in the quantum regime. Based on our results, SAW resonators on thin film LNO achieve performance comparable to devices on bulk LNO and show potential to be used in quantum acoustic applications.

Contents

Introduction

1

1.1 Background and motivation

Quantum physics, since its inception, has profoundly altered our understanding of the universe, revealing a rich and unpredictable world, full of mind-bending concepts that often clash with our human desire for causality and logic. It has brought to light phenomena such as entanglement [1], superposition [2, 3] and tunneling [4], far removed from our everyday notions of reality. A growing understanding of the underlying rules and frameworks governing this quantum world has not only enabled the emergence of groundbreaking technologies, like magnetic resonance imaging [5, 6] and GPS [7], but also promises even more wide-reaching disruptions in the near future. One such disruption could be quantum computing [8, 9], which taps into the inherent properties of quantum mechanics to solve certain complex problems exponentially faster than classical computers [10].

One of the most intriguing unsolved questions in quantum physics is the *measurement problem* [11], the question of how and why the act of observing a quantum system causes it to transition from a state of superposition to a single, definitive state. This problem touches the very heart of quantum theory and the nature of reality itself, provoking various interpretations and philosophical debates [2, 12–14]. It is also intertwined with our naive understanding that there is a classical regime, where our human intuition applies, and a quantum regime, where it does not [15]. Various theories have been developed to explain the absence of quantum superposition in our *macroscopic* lives [16], each of them predicting some kind of additional decay of superposition that scales with an object's mass or the number of particles involved [17–19].

Therefore, researchers are vying to observe quantum phenomena in ever heavier macroscopic objects to test these theories and locate the boundary between the classical and the quantum regime [20, 21]. An invaluable tool in this pursuit is cavity optomechanics [22], where the light field in a optical cavity is coupled to the motion of a mechanical oscillator, allowing extremely precise displacement detection and, potentially, quantum control of the oscillator [23, 24]. The versatile scheme can be implemented in platforms spanning several orders of magnitude in mass, from clouds of atoms with masses of 10^{-20} g [25, 26] to massive mirrors weighing several kg [27], where it recently rose to fame by achieving the first detection of gravitational waves [28].

Nano-electromechanics has evolved from these roots, enabled by advances in nano-fabrication technology. These advances have made it possible to explore interactions between light and mechanical motion in on-chip systems integrating mechanical elements with superconducting resonant circuits [29–31]. In circuit based systems, researchers have achieved radiation pressure ground state cooling [32], entanglement of mechanical oscillators [33, 34], and detection of mechanical displacement beyond the standard quantum limit [31]. All of these feats were achieved in the limit of devices with low single-photon coupling strengths, making use of a feature of the linearized optomechanical interaction, where the effective coupling can be enhanced by increasing the applied microwave power. However, in this linear regime, all of the underlying states of the system remain inevitably Gaussian, classical states [22].

Therefore, to leave the realm of classical states and push the boundaries of quantum state preparation for mechanical modes, a different approach is needed:
Inductively coupled or *flux-mediated* electromechanics, which is the focus of this thesis, is a novel implementation of the optomechanical interaction in the context of superconducting circuits. With this approach, the displacement of a mechanical oscillator modulates the magnetic flux in a Superconducting QUantum Interference Device (SQUID), coupling the inductance of the circuit to the motion of the mechanical element. The inductively coupled architecture provides exciting opportunities to significantly increase the single-photon coupling rate g_0 beyond the above-mentioned boundaries [35–39] and ultimately reach the single-photon strong coupling regime [40]. In this regime, g_0 exceeds all of the individual loss rates present in the system and the linear approximation of the optomechanical Hamiltonian breaks down, opening up possibilities for creating non-classical mechanical states [25, 41, 42] with negative Wigner densities [43] and exploring phenomena such as photon granularity [25] and photon blockade [44].

In parallel, quantum acoustics [45, 46] has emerged as an equally intriguing field to study the quantum nature of macroscopic objects. Instead of designing artificial mechanical oscillators like strings, cantilevers or pendulums, quantum acoustics focuses on the intrinsic motional degrees of freedom of solid-state systems: the quantized elastic excitations carried by their crystal lattices. Recently, by interfacing a superconducting qubit with the bulk acoustic waves of a sapphire crystal, researchers accomplished the generation of a Schrödinger cat state consisting of 10^{17} atoms, one of the heaviest to date [47]. Similar hybrid systems of superconducting circuits and surface acoustic waves (SAWs) are discussed in the context of information storage [48–51] and to explore the novel interaction of the giant atom limit [52–55], where the wavelength of the interacting wave becomes comparable to the dimensions of the (artificial) atom. The key element enabling this symbiotic relationship between electrical circuits and acoustic waves is the piezoelectric effect, which mediates the transduction between the electromagnetic and elastic fields. However, a main challenge, which will be the focus of the latter part of this thesis, arises from the diametrically opposed requirements that SAW devices and superconducting circuits pose on the used substrate: High piezoelectric coupling rates are desired for efficient SAW generation, while the same piezoelectric coupling constitutes a highly unwanted loss channel for the electric fields in superconducting qubits.

1.2 Scope and objectives of the study

Only recently, intensive efforts by a small number of research groups have cumulated in the first successful proofs of concept for the realization of flux-mediated inductive coupling in electromechanical devices [56–59]. In these pioneering experiments, the feasibility of the interaction scheme was demonstrated and the expected scaling and in-situ tuneability of g_0 verified. Furthermore, single-photon coupling rates of $g_0/2\pi > 1.5\,\mathrm{kHz}$ were reported, constituting already a significant improvement over existing, capacitively coupled electromechanical devices. However, for various reasons, the studies remained limited to moderate external magnetic fields below 10 mT, stopping short of realizing the full scaling potential of the field-dependent nature of g_0. Additionally, the complex fabrication processes required to combine flux-tuneable microwave circuitry and nanomechanical elements required certain compromises that caused the microwave loss rate κ in the prototype devices to remain relatively large. Therefore, as of today, the threshold of single-photon strong coupling, defined by $g_0 > \kappa$, remains out of reach.

In this thesis, we aim to advance the state-of-the-art towards reaching the single-photon single-phonon strong coupling regime by tackling both of the aforementioned aspects limiting the previous experiments. On the one hand, we introduce alterations and improvements to the experimental setup and measurement protocol that make the operation of the electromechanical device in external fields up to 50 mT possible, promising substantial improvements to the achievable g_0. In parallel, we develop an entirely new fabrication procedure and adapt the device design with the goal to significantly reduce the loss rate κ in the microwave circuit. In concert, both of these undertakings aim to bring g_0 and κ closer together and eventually reach the declared objective $g_0 \approx \kappa$.

Experimentally, we determine the maximally achievable single-photon single-phonon coupling rate and investigate whether the expected scaling behavior remains valid towards larger fields. We also use the enhanced interaction strength enabled by the larger fields to investigate several interesting physical phenomena present in optomechanical systems, such as Electromechanically Induced Transparency (EMIT), Optomechanical sideband cooling, and a dynamic backaction effect that can be used to control the eigenfrequency of the mechanical subsystem.

With respect to quantum acoustics, we aim to examine the potential of two thin-film material systems, Lithium Niobate on Insulator (LNOI) and Lithium Niobate on Silicon (LNO-on-silicon) for SAW-based quantum acoustic applications. Our focus is on assessing the performance of GHz-frequency SAW resonators under typical operating conditions for quantum acoustic experiments, including millikelvin temperatures and low signal powers corresponding to individual phonons. By comparing these thin-film materials with traditional bulk LNO using a standard resonator design, we aim to determine their suitability for scalable quantum acoustics applications.

1.3 Thesis outline

The thesis is structured in the following fashion:

Chapter 2 forms the theoretical backbone of the thesis, providing a comprehensive overview of the foundational principles in superconducting circuits and nanomechanics. It delves into the specifics of nanostring oscillators, SQUIDs, and Frequency Tunable Resonators (FTRs), and presents a detailed treatment of the flux-mediated coupling mechanism.

Chapter 3 is focused on design and optimization. It details the circuit designs for flux-tuneable resonators with mechanically compliant SQUIDs and surface acoustic wave (SAW) devices for quantum acoustics. The chapter also outlines the nanofabrication techniques used to manufacture the samples studied in the thesis.

Chapter 4 covers the experimental setups and measurement techniques. It introduces the cryogenic setup for millikelvin temperature experiments, microwave components for signal processing, and describes specialized measurement and analysis protocols.

Chapter 5 is dedicated to the experimental investigation of inductively coupled electromechanical devices. It includes a comprehensive pre-characterization of the device, a study of the optomechanical coupling strength, and its application in the sideband cooling protocol. Additionally, a study of a novel technique for mechanical frequency control is presented.

Chapter 6 presents a low-temperature study of SAW resonators on thin-film piezoelectric substrates, assessing their performance for quantum acoustics applications.

Finally, **Chapter 7** briefly summarizes the most important results and learnings acquired over the course of this work and provides an outlook towards future research directions as well as a preview of preliminary findings.

Theoretical Background

2

To investigate the complex electromechanical interactions at the heart of this work, a general understanding of the underlying principles and theoretical concepts that govern these systems is paramount. This chapter lays the theoretical groundwork for the experimental study presented in subsequent sections, beginning with an overview of the foundations of superconducting circuits and nanomechanics. We introduce the basic building blocks, such as harmonic oscillators and Josephson Junctions, followed by a detailed examination of more specialized components of electromechanical circuits such as nanostring oscillators, Superconducting Quantum Interference Devices (SQUIDs), and Frequency Tunable Resonators (FTRs). The principles of optomechanics with superconducting circuits are explored, with a detailed description of the flux-mediated coupling mechanism implemented in this work. In order to establish a mathematical framework to describe the experimental system, a linearization of an electromechanical Hamiltonian including a Kerr non-linearity is performed. Moreover, this chapter provides a brief excursion into the field of quantum acoustics with surface acoustic waves, introducing the most relevant concepts and components. Finally, a section is dedicated to the description of the most impactful loss mechanism inherent in superconducting circuits, the coupling to a bath of Two-Level-Systems (TLS).

2.1 The Harmonic oscillator

The following section is dedicated to the harmonic oscillator, an ubiquitous model in both classical and quantum physics. We discuss its application in mechanical and electrical LC oscillators, using both classical and quantum mechanical frameworks to derive its properties and behavior.

2.1.1 Mechanical oscillator

Classical picture In the realm of classical physics any mechanical oscillator can be described using a toy model of an object of mass m that is attached to a spring. The mass is located at position x, has the momentum p and is subject to a restoring force $F = -kx$ due to the spring, where k is called the spring constant. The total energy of the system can then be described by a classical Hamiltonian as the sum of the system's potential and kinetic energy contributions

$$H = \frac{p^2}{2m} + \frac{1}{2} m \Omega_{\mathrm{m}}^2 x^2 \,, \tag{2.1}$$

where we define $\Omega_{\mathrm{m}} = \sqrt{k/m}$ as the (mechanical) resonance frequency of the oscillator. Using the corresponding Hamilton equations

$$\dot{x} = \frac{\partial H}{\partial p} = \frac{p}{m} \tag{2.2}$$

$$\dot{p} = -\frac{\partial H}{\partial x} = -m\Omega_{\mathrm{m}}^2 x \tag{2.3}$$

we arrive at the equation of motion of the harmonic oscillator

$$\ddot{x} + \Omega_{\mathrm{m}}^2 x = 0 \,. \tag{2.4}$$

Now, Eq. (2.4) only describes the motion of the harmonic oscillator in an isolated, ideal scenario absent of energy dissipation and external forces. To incorporate both effects into the model we introduce a damping term $-\Gamma_{\mathrm{m}}\dot{x}$ quantified by the mechanical decay rate Γ_{m} and an external, sinusoidal driving force $F_{\mathrm{ext}} = F_0 e^{-i\Omega t}$ at frequency Ω. This leads to the equation of motion of a damped, driven harmonic oscillator

$$\ddot{x} + \Gamma_{\mathrm{m}}\dot{x} + \Omega_{\mathrm{m}}^2\, x = \frac{F_{\mathrm{ext}}}{m} \,. \tag{2.5}$$

Borrowing from linear response theory, we employ Fourier transformation to rewrite Eq. (2.5) to frequency space, where the expression takes a simpler form without derivatives

$$(\Omega_{\mathrm{m}}^2 - \Omega^2 - i\Gamma_{\mathrm{m}}\Omega)x(\Omega) = \frac{F_{\mathrm{ext}}}{m} \,. \tag{2.6}$$

In the context of mechanical oscillators, we call this linear response function *mechanical susceptibility* χ_{m} and define it by $x(\Omega) = \chi_{\mathrm{m}}(\Omega) F_{\mathrm{ext}}$, i.e. as the reaction of the system to an external stimulus. From the definition and Eq. (2.6) we can see directly that

$$\chi_{\mathrm{m}}(\Omega) = \frac{1}{m} \frac{1}{\Omega_{\mathrm{m}}^2 - \Omega^2 - i\Gamma_{\mathrm{m}}\Omega} \,. \tag{2.7}$$

Expressing the behavior of the harmonic oscillator in terms of its mechanical susceptibility is convenient for experimentalists, since there is often a direct relationship between χ_m and the observables in experiments, as we will discuss in later stages of this work.

Quantum mechanical description In the next step we want to describe the system introduced above using a quantum mechanics picture. To this end we closely follow the canonical quantization method first introduced by Dirac [60]. First, we replace the canonical variables x, p of the Hamilton equations with the position and momentum operators

$$\hat{x} = x \tag{2.8}$$

$$\hat{p} = p \tag{2.9}$$

which adhere to the commutation relation $[\hat{x}, \hat{p}] = i\hbar$. The corresponding Hamiltonian in the quantum description reads

$$\hat{H} = \frac{\hat{p}^2}{2m} + \frac{1}{2} m \Omega_\mathrm{m}^2 \hat{x}^2. \tag{2.10}$$

Following the canonical quantization, we move away from the position and momentum operators which are hermetian and therefore represent real physical variables, to a more general description using the annihilation and creation operators $\hat{b}$ and $\hat{b}^\dagger$, which are defined as

$$\hat{b} = \sqrt{\frac{m\Omega_\mathrm{m}}{2\hbar}} \left(\hat{x} + \frac{i}{m\Omega_\mathrm{m}} \hat{p} \right) \tag{2.11}$$

$$\hat{b}^\dagger = \sqrt{\frac{m\Omega_\mathrm{m}}{2\hbar}} \left(\hat{x} - \frac{i}{m\Omega_\mathrm{m}} \hat{p} \right) . \tag{2.12}$$

Inserting these definitions into Eq. (2.10) results in the commonly used Hamiltonian for a quantum harmonic oscillator

$$\hat{H} = \hbar \Omega_\mathrm{m} \left(\hat{b}^\dagger \hat{b} + \frac{1}{2} \right) . \tag{2.13}$$

In the next step, this Hamiltonian can be used to formulate the time independent Schrödinger equation

$$\hat{H} |\Psi\rangle = E |\Psi\rangle \, . \tag{2.14}$$

By solving the Schrödinger equation for the eigenvalues of the number operator $\hat{n} = \hat{b}^\dagger \hat{b}$, we can calculate the expectation value for the energy states of the quantum harmonic oscillator given by

$$E = \hbar\Omega_\mathrm{m}\left(n + \frac{1}{2}\right), \tag{2.15}$$

where n corresponds to the number of excitations. Equation (2.15) aptly illustrates two characteristics of the harmonic oscillator that become apparent only by using the quantum mechanical description:

First, the quantum number n corresponds to a well-defined number of excitations, it is a natural number and describes a specific energy eigenstate Ψ of the system. These eigenstates and the corresponding energy levels are quantized. This quantization manifests as discrete energy states, separated by a constant energy difference of $\hbar\Omega_\mathrm{m}$. Such quantum states that can be described by the quantum number n are also called *Fock* states.
Secondly, even for $n = 0$, when the system is found in a so-called *vacuum state*, the energy of the oscillator never reaches absolute zero, but instead remains at the *zero-point energy* $\hbar\Omega_\mathrm{m}/2$. Due to the remaining energy, the system is never truly at rest and subject to motional fluctuations which can be expressed by the zero-point motion

$$x_\mathrm{zpf} = \sqrt{\hbar/2\Omega_\mathrm{m} m}\,. \tag{2.16}$$

The quantum fluctuations can be understood as a manifestation of the uncertainty principle: Since a zero energy state would correspond to the particle being perfectly localized in space and momentum, such a state is not possible.

Quality factor The quality factor, or Q-factor, commonly denoted by Q, is a dimensionless parameter that characterizes a harmonic oscillator's energy loss per oscillation cycle compared to the stored energy. The quality factor can be defined as: [61, 62]

$$Q = \frac{2\pi \times \text{Energy stored}}{\text{Energy lost per cycle}} = \frac{\Omega_\mathrm{m}}{\Gamma}\,. \tag{2.17}$$

In the context of the toy model described above, the quality factor would describe how many oscillations the mass on the spring can perform before its energy falls to approximately $1/e = 37\%$ of its initial value. A high Q value signifies low damping, and the system will keep the contained energy for many cycles before significant energy is lost. Since in the expression above, one compares the oscillators resonance frequency to its loss rate, the Q-factor also provides a useful tool to compare the performance of various oscillator implementations across widely different operating frequencies.

2.1.2 Electrical LC resonators

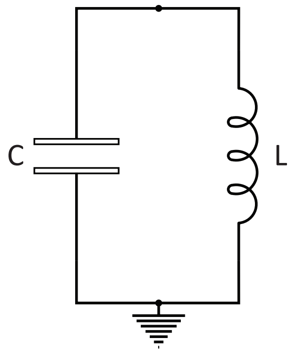

Fig. 2.1.: **LC oscillator circuit diagram.** The most basic circuit implementation of an electrical harmonic oscillator, consisting of a lumped element capacitance C and inductance L, connected in parallel.

Classcial picture Having established the principles governing mechanical harmonic oscillators, we can find a parallel in electrical systems. Here, the *LC resonator* serves as an analogous structure, which is depicted in the form of a circuit diagram in Fig. 2.1. The oscillatory behavior in the circuit arises from the interplay between the inductive and capacitive circuit elements. Therefore, the LC resonator is characterized by the respective inductance L and capacitance C. The energy stored in the resonator is given by the sum of charging and inductive energy, which is expressed in the Hamiltonian

$$H = \frac{Q_{\mathrm{el}}^2}{2C} + \frac{\Phi^2}{2L} \,. \tag{2.18}$$

Here, we have introduced the electric charge of the capacitor Q_{el}, which is related to the current I via $Q_{\mathrm{el}}(t) = \int_{t_0}^{t} dt' I(t')$. Similarly, Faraday's law of induction defines the flux Φ threading the inductor using the voltage V as $\Phi = \int_{t_0}^{t} dt' V(t')$ [63].

By defining the angular resonance frequency of the circuit as $\omega_{\mathrm{r}} = 1/\sqrt{LC}$, we can rewrite H to

$$H = \frac{Q_{\mathrm{el}}^2}{2C} + \frac{1}{2} C \omega_{\mathrm{r}}^2 \Phi^2 \,. \tag{2.19}$$

Comparing the above expression to Eq. (2.1), we find a clear analogy to the mechanical oscillator with the canonical variables Φ and Q_{el} taking the place of position and momentum and C acting as effective mass.

Quantum mechanical description Based on this analogy, the path towards a quantum mechanical treatment using canonical quantization is clear: The canonical variables Q_{el} and Φ are replaced with quantum operators $\hat{Q}$ and $\hat{\Phi}$, obeying the commutation relation $[\hat{Q}, \hat{\Phi}] = i\hbar$. To generalize the description, we define suitable annihilation and creation operators [64]

$$\hat{a} = \sqrt{\frac{\omega_{\mathrm{r}} C}{2\hbar}} \left(\hat{\Phi} + i \frac{\hat{Q}}{\omega_{\mathrm{r}} C} \right) \tag{2.20}$$

$$\hat{a}^\dagger = \sqrt{\frac{\omega_{\mathrm{r}} C}{2\hbar}} \left(\hat{\Phi} - i \frac{\hat{Q}}{\omega_{\mathrm{r}} C} \right) \tag{2.21}$$

with the commutation relation $[\hat{a}, \hat{a}^\dagger] = 1$.

In analogy to the zero-point motion x_{zpf} defined for the mechanical oscillator above we can define expressions for the magnitude of zero-point fluctuations in flux and charge as $\Phi_{\mathrm{zpf}} = \sqrt{\hbar / 2\omega_{\mathrm{r}} C}$ and $Q_{\mathrm{zpf}} = \sqrt{\hbar \omega_{\mathrm{r}} C / 2}$, respectively, and find a convenient expression for the operators

$$\hat{\Phi} = \Phi_{\mathrm{zpf}} \left(\hat{a}^\dagger + \hat{a} \right) \tag{2.22}$$

$$\hat{Q} = i Q_{\mathrm{zpf}} \left(\hat{a}^\dagger - \hat{a} \right). \tag{2.23}$$

Using the above definitions the quantum mechanical Hamiltonian for the LC oscillator takes the familiar form

$$\hat{H} = \hbar \omega_{\mathrm{r}} \left(\hat{a}^\dagger \hat{a} + \frac{1}{2} \right). \tag{2.24}$$

Again, the corresponding energy eigenstates are quantized and equally spaced and can be characterized by the number of quasi-particles, in this case the photon number n with $\hat{a}^\dagger \hat{a} |n\rangle = n |n\rangle$ for $n = 0, 1, 2 \ldots$.

2.2 Electromechanical circuit elements

In the following section, we briefly introduce the concepts, working principles and realizations behind the fundamental components for the electromechanical circuits investigated in this work. This includes nanomechanical string resonators, the building blocks of microwave resonators and the non-linear Josephson elements essential for superconducting quantum circuits.

2.2.1 Nanomechanical string oscillators

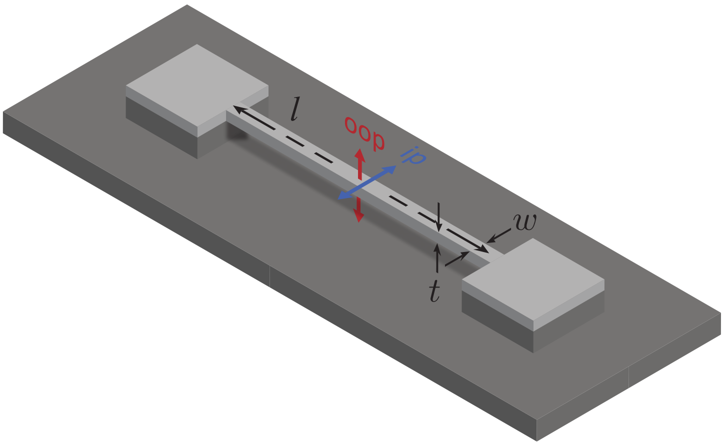

Fig. 2.2.: Nanomechanical string oscillator. Schematic illustration of a nanomechanical string oscillator (light grey), or nanostring, of length l, width w and thickness t. The center part of the string is released from the substrate (dark grey) and free to perform both in-plane (ip) and out-of-plane (oop) oscillations, where the displacement directions are illustrated by arrows. It is possible to model each motion as a one-dimensional harmonic oscillator with a suitable effective mass m_{eff}.

The elements incorporating the mechanical degree of freedom in our electromechanical circuits are nanomechanical string oscillators, often referred to as *nanostrings*. A nanostring, as depicted in Fig. 2.2, is essentially a freely suspended beam with large aspect ratio ($l \gg w, t$) anchored to a substrate at both ends under tensile stress. While their form is inherently macroscopic and three-dimensional, Euler-Bernoulli beam theory [65, 66] reveals that their motion can be effectively modeled as a one-dimensional, point-like mass acting as a harmonic oscillator, as introduced in Sec. 2.1.

By adopting parameters analog to the harmonic oscillator, such as an effective mass m_{eff}, spring constant k, and damping rate Γ_{m}, we can distill the system dynamics down to a single degree of freedom for each mode. It's important to highlight that nanostrings exhibit a variety of oscillatory modes, including transversal and torsional motion. However, given that these modes operate independently of one another, they can be assumed to be isolated and treated independently. In this work, our focus is primarily on the in-plane and out-of-plane vibrational modes, which play an essential role in the flux-mediated electromechanical coupling scheme described in Sec. 2.5.2.

Response of a driven string Formally, the motion of each mode's center of mass can be described by an equivalent one-dimensional damped and driven harmonic oscillator, described by the equation of motion Eq. (2.5) and solved by a linear response $x(t) = x_0 e^{-i\Omega t}$ with $x_0 = \chi_\mathrm{m} F_0$, using the susceptibility χ_m defined in Eq. (2.7). Since experimental signatures are often proportional to the squared magnitude of the displacement $x(t)$, we derive the expression

$$|x_0|^2 = \frac{F_0^2/m_\mathrm{eff}^2}{(\Omega_\mathrm{m}^2 - \Omega^2)^2 + \Gamma_\mathrm{m}^2\Omega^2} \approx \left(\frac{F_0/m_\mathrm{eff}}{2\Omega_\mathrm{m}}\right)^2 \frac{1}{(\Omega_\mathrm{m} - \Omega)^2 + \Gamma_\mathrm{m}^2/4}\,, \tag{2.25}$$

where $\Omega_\mathrm{m} = \sqrt{k/m_\mathrm{eff}}$ is the string's mechanical resonance frequency. The last approximation assumes high quality factors or $\Omega_\mathrm{m} \gg \Gamma_\mathrm{m}$, which is generally fulfilled for the nanostrings studied in this work.

The effective mass, m_eff, in the above equations is a conceptual tool arising from the simplified description as a point-like mass. The real three-dimensional structure and varied cross-sectional geometry of the nanostring mean that different sections of the string contribute differently to its vibrational modes. The effective mass abstracts these discrepancies. Instead of analyzing the specific movement of each infinitesimally small section of the string, using the concept of effective mass allows the entire string's motion to be described as a textbook one-dimensional mechanical oscillator with a discrete effective mass m_eff and a spring constant k. The exact calculation of m_eff involves factors such as the string's geometry, boundary conditions, and the displacement profiles of the vibrational modes [67]. However, we generally study nanostrings in the highly tensile-stressed (HTS) limit, where m_eff approximates to half the physical mass of the string [68]

$$m_\mathrm{eff} = 0.5m\,, \tag{2.26}$$

where $m = \rho l w t$ with the material density ρ and the string dimensions l, w, t, as introduced in Fig. 2.2.
Furthermore, the angular resonance frequency for a nanostring's nth vibrational mode in the HTS limit can be approximated to [69]

$$\Omega_{\mathrm{m},n}^\mathrm{HTS} = \frac{n\pi}{l}\sqrt{\frac{\sigma_0}{\rho}}\,. \tag{2.27}$$

The accuracy of this approximation can be enhanced by a first-order correction accounting for string bending effects [68]

$$\Omega_{\mathrm{m},n}^{\mathrm{TS}} = \Omega_{\mathrm{m},n}^{\mathrm{HTS}} \left(\frac{l\sqrt{\sigma_0 wt}}{l\sqrt{\sigma_0 wt} - 2\sqrt{EI}} \right) , \tag{2.28}$$

using the Young's modulus E of the material and the moment of inertia I, which depends on the string geometry and the investigated mode. Notably, only the more accurate model lifts the degeneracy between in-plane (ip) and out-of-plane (oop) mode of the string, since $I_{\mathrm{ip}} = w^3t/12$ and $I_{\mathrm{oop}} = wt^3/12$ [70].

Thermal motion The force acting on the nanostring F_{ext} is not strictly required to be an externally applied drive. Even in an undriven experiment, the string will exhibit *Brownian* or thermal motion, caused by the coupling of the mechanical mode to the thermal energy of the environment. The fluctuation-dissipation theorem [71] can be used in conjunction with the equipartition theorem [72] to find an expression for the driving force exerted by a thermal bath of temperature T [73, 74]

$$S_{\mathrm{FF}}^{\mathrm{th}}(\Omega) = 2m_{\mathrm{eff}}\Gamma_{\mathrm{m}}k_{\mathrm{B}}T \,, \tag{2.29}$$

with the Boltzmann constant k_{B}. Note that $S_{\mathrm{FF}}^{\mathrm{th}}(\Omega)$ is a spectral force density given in units of N^2/Hz, even though the thermal force is assumed to be frequency independent. Through the susceptibility of the nanostring oscillator (cf. Eq. (2.7)), the thermal driving force translates to a double-sided displacement spectral density [73, 75]

$$S_{\mathrm{xx}}^{\mathrm{th}}(\Omega) = |\chi_{\mathrm{m}}(\Omega)|^2 \, S_{\mathrm{FF}}^{\mathrm{th}}(\Omega) \approx \frac{k_{\mathrm{B}}T}{m_{\mathrm{eff}}} \frac{2\Gamma_{\mathrm{m}}}{(\Omega^2 - \Omega_{\mathrm{m}}^2)^2 + \Gamma_{\mathrm{m}}^2\Omega^2} \,, \tag{2.30}$$

given in units of m^2/Hz and using an approximation of large mechanical occupation numbers, i.e. $\bar{n}_{\mathrm{ph}} \approx k_{\mathrm{B}}T/\hbar\Omega_{\mathrm{m}} \gg 1$. In the high-$Q$ limit, which we already assumed in Eq. (2.25), the spectrum can be further approximated with a Lorentzian lineshape

$$S_{\mathrm{xx}}^{\mathrm{th}}(\Omega) \approx \frac{k_{\mathrm{B}}T}{2\Omega_{\mathrm{m}}^2 m_{\mathrm{eff}}} \frac{\Gamma_{\mathrm{m}}}{(\Omega - \Omega_{\mathrm{m}})^2 + (\Gamma_{\mathrm{m}}/2)^2} \,. \tag{2.31}$$

Knowledge of the thermal amplitude spectrum presents a useful baseline to calibrate any measurement signal proportional to the displacement of the nanostring and we will make extensive use of this technique in Chap. 5.

2.2.2 CPW resonators

In the realm of circuit Quantum Electrodynamics (cQED), LC oscillators commonly appear in the form of microwave resonators, which play a fundamental role in the routing, control and readout of quantum signals [64]. While any electric resonator shares many characteristics with the basic LC resonator circuit introduced in Sec. 2.1.2, a multitude of microwave resonator implementations exist, each with its own caveats and benefits. Two-dimensional coplanar waveguide (CPW) resonators have become one of the most commonly employed architectures, being used as filters [76], sensitive readout devices [77] and quantum memories [78]. Their wide ranging appeal is largely owed to the compact geometry, low dissipation and compatibility with CMOS fabrication processes. This section elaborates on the working principles and the underlying theory of CPW resonators.

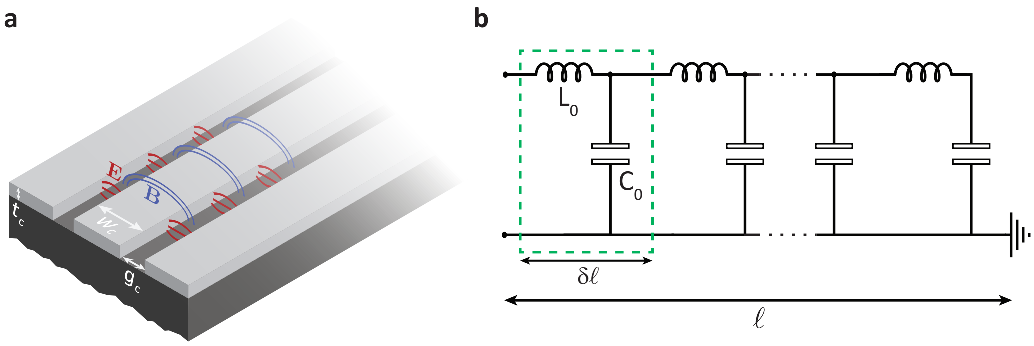

Fig. 2.3.: Coplanar Waveguide (CPW) geometry and equivalent circuit. **a** Schematic of a coplanar waveguide with center conductor width w_c, gap separation g_c, and metallized layer thickness t_c. The non-metallized substrate is shown in dark grey. The blue and red lines are schematic illustrations of the magnetic and electric field distributions, respectively. **b** Equivalent circuit representation of a CPW resonator of total length ℓ, which is modeled as a series of infinitesimally small lumped element circuits (green box) with inductance L_0 and capacitance C_0.

Working principle A CPW is composed of a center conductor with width w_c and thickness t_c, flanked by two gaps of distance g_c from a ground plane of equivalent thickness. Both conductors are generally deposited on a dielectric substrate characterized by permittivity ϵ, where the substrate's thickness is significantly larger than the dimensions w_c, g_c, t_c [79]. Figure 2.3**a** illustrates this arrangement. Materials such as aluminum, niobium, and niobium titanium nitride (NbTiN) are used as conductors in combination with low-loss-tangent dielectrics like sapphire and high-resistivity silicon to minimize losses [80].
The CPW functions akin to a conventional coaxial cable, but transmitting sig-

nals through a planar structure. Its design constrains the electromagnetic field within a small volume between the center conductor and the ground, as shown in Fig. 2.3**a**. The electromagnetic field partially resides in the dielectric substrate and partly in the vacuum or another dielectric above the substrate, being subject to an effective dielectric constant ϵ_{eff}. The largest concentration of the field is found in the gaps between the center conductor and the ground planes.

A resonator is typically created from a coplanar waveguide by enforcing boundary conditions of either zero current (open boundary) or zero voltage (shorted boundary) at the endpoints. The chosen type of boundary conditions at the endpoints along with the distance ℓ between them determines the fundamental frequency and harmonics of the resonator. A resonator with one open and one shorted-to-ground boundary is known as quarter-wavelength or $\lambda/4$ resonator, as its fundamental resonance wavelength is $\lambda = 4\ell$, corresponding to a fundamental resonance frequency

$$\frac{\omega_0}{2\pi} = \frac{c}{\sqrt{\epsilon_{\text{eff}}}}\frac{1}{4\ell} = \frac{v_0}{4\ell}, \tag{2.32}$$

defining the effective speed of light within the waveguide v_0. Conversely, designing both of the boundaries to be open, a half-wavelength or $\lambda/2$ resonator is created with $\omega_0/2\pi = v_0/2\ell$.

Generally, both types of resonators support an infinite number of higher harmonic modes. Each of these modes, identified by a mode number n, can be considered an independent harmonic oscillator with its resonance frequency given by $\omega_n = n\omega_0$ or $\omega_n = (2n-1)\omega_0$ for $\lambda/2$ and $\lambda/4$ resonators, respectively.

Similar to the LC oscillator, the electromagnetic characteristics of a CPW resonator, in particular, the effective speed of light v_0, and, therefore, its resonance frequency, is defined by its inductance and capacitance. However, since the wavelength of the confined microwaves is on the same order as the lateral dimensions of the waveguide structure, we cannot consider the circuit to consist of isolated, lumped-elements L and C. Instead, inductance and capacitance are distributed across the entire length ℓ of the resonator and interact with the propagating microwaves [79]. Fortunately, the circuit can still be modeled as a series of small lumped-element circuits with infinitesimal length $\delta\ell$ and characteristic inductance L_0 and capacitance to ground C_0, each per unit length of the line. An equivalent circuit for this distributed element model is shown in Fig. 2.3**b**, with the green rectangle highlighting one of the infinitesimally small unit cells. Based on this picture, the characteristic impedance

$$Z_0 = \sqrt{L_0 C_0} \tag{2.33}$$

and phase velocity

$$v_0 = 1/\sqrt{L_0 C_0} \tag{2.34}$$

can be calculated [81]. The characteristic impedance is an important figure of merit for the microwave resonator. In order to avoid impedance mismatches and the associated reflections, it should generally be designed to match the 50 Ω impedance of commercial microwave equipment. However, since the CPW geometry offers large freedom in the choice of the parameters w_c and g_c, this can generally be achieved for a large range of different parameter combinations. Lastly, it is worth noting that the calculation of L_0 and C_0 is non-trivial. While, when neglecting kinetic inductance and substrate permeability, L_0 is purely defined by the CPW geometry, C_0 depends on the geometry as well as the effective dielectric constant ϵ_eff of the substrate-metal-air multi-layer. Analytical models for ϵ_eff based on conformal mapping techniques exist [82], but the accuracy of these models can decrease significantly for certain ratios of substrate thickness to metal thickness [83]. In these cases, researchers have to rely on finite element electromagnetic simulations to generate accurate predictions of ϵ_eff [84].

Lumped element approximation To facilitate a more intuitive understanding of CPW resonators and ensure compatibility with numerous theoretical models that are grounded in the lumped element picture, it is often practical to approximate the CPW resonator as a lumped element model. Around resonance ($\omega \approx \omega_n$), the nth mode of a $\lambda/4$ CPW resonator can be approximated as an equivalent LC circuit with effective characteristic parameters [79]

$$L_n = \frac{8 L_0 \ell}{n^2 \pi^2} \tag{2.35}$$

$$C = \frac{C_0 \ell}{2}\,. \tag{2.36}$$

In the case of $\lambda/2$ boundary conditions, the expression for the inductance modifies to $L_{n,\lambda/2} = 2L_0\ell/(n^2\pi^2)$. Using the transformed values, the expression for ω_n simplifies back to $\omega_n = 1/\sqrt{L_n C}$, in analogy to the simple LC resonator.

As all CPW resonators fabricated and investigated over the course of this work are designed in $\lambda/4$ geometry, we will generally omit specification of the resonator type from now on.

Losses and quality factors In analogy to the generic harmonic oscillator, the quality factor of the fundamental mode in a CPW resonator is defined as $Q = \omega_0/\kappa$, where κ represents the mode's total loss rate. The relaxation process in these resonators is influenced by a combination of internal and external sources of loss. Internal losses, which account for relaxation into uncontrolled channels, encompass a variety of mechanisms such as dielectric and conductor losses, the presence of quasiparticles, vortices, and two-level fluctuators (TLS), extensively discussed in Refs. [80, 84, 85] and Sec. 2.7. On the other hand, external losses stem from the resonator's coupling to input and output ports. Based on this relationship, the external loss rate κ_{ext} can be finely tuned through the design of the coupling geometry to the input-output transmission lines, as detailed in Sec. 3.1 and Ref. [84]. The internal and external loss channels collectively determine the total dissipation rate $\kappa = \kappa_{\mathrm{ext}} + \kappa_{\mathrm{int}}$. Consequently, the overall (or loaded) quality factor of the resonator is given by $Q_{\mathrm{l}} = \left(Q_{\mathrm{ext}}^{-1} + Q_{\mathrm{int}}^{-1}\right)^{-1}$.

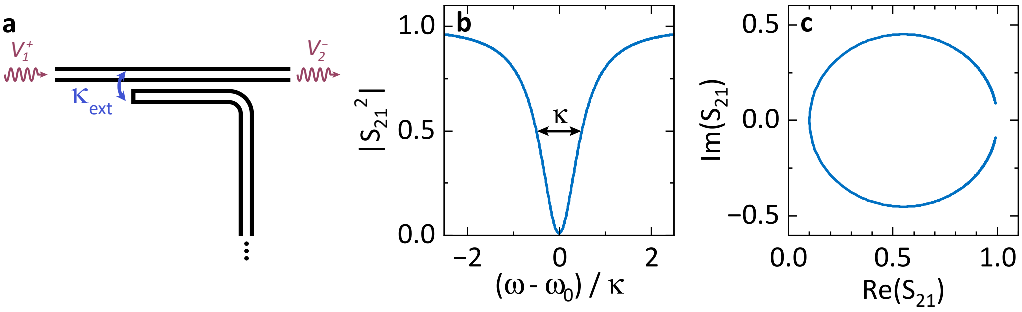

Fig. 2.4.: Transmission response of a side-coupled CPW resonator. **a** Schematic of a CPW resonator (bottom) side-coupled to a input-output transmission line (top). Metallized surfaces are shown in white, non-metallized substrate in dark grey. The coupling is dominantly capacitive and leads to an external loss rate κ_{ext}. **b,c** Ideal S_{21} response of the side-coupled CPW resonator, calculated from Eq. (2.37) and represented as squared amplitude of the complex transmission parameter S_{21} (**b**) and in the complex plane (**c**). The total loss rate κ is discernible from the full width at half maximum (FWHM) of the Lorentzian amplitude response. For the calculation a coupling efficiency of $\eta = \kappa_{\mathrm{ext}}/\kappa = 0.9$ is used.

Scattering parameter of a side-coupled CPW resonator Experimentally, the properties of a microwave resonator are often probed by measuring the response of the device to an external microwave drive signal. Different options exist for coupling the drive signal to the resonator. In our experiments, we predominantly use *side-coupling*, which is illustrated in Fig. 2.4**a**. A small section of the CPW resonator is placed parallel to the input-output transmission line, which is connected to the signal generation and detection electronics. This allows for a (primarily) capacitive coupling of the microwave signals travelling in the transmission line to the CPW resonator, represented by an external loss rate κ_{ext}. The transmitted signal interacting with the resonator can then be described in the framework of scattering parameters. The S-parameter $S_{21} = V_2^-/V_1^+$ describes the voltage arriving at the output port 2, normalized to the voltage generated at the input port 1 [79]. Expressed in terms of S_{21}, the ideal response of a side-coupled CPW resonator with resonance frequency ω_0 to a coherent drive of frequency ω is given by [86, 87]

$$S_{21}(\omega) = 1 - \frac{\kappa_{\mathrm{ext}}/2}{\kappa/2 - i(\omega - \omega_0)} = 1 - \frac{\eta}{1 - 2i(\omega - \omega_0)/\kappa}, \tag{2.37}$$

where we define the coupling efficiency $\eta = \kappa_{\mathrm{ext}}/\kappa$. This expression corresponds to a Lorentzian lineshape in the amplitude response and describes a circle in the complex plane, as illustrated in Fig. 2.4**b** and **c**, respectively, for $\eta = 0.9$. Notably, the total loss rate κ of the device is directly discernible from the full-width-half-maximum of the Lorentzian amplitude response.

2.2.3 Josephson Junctions

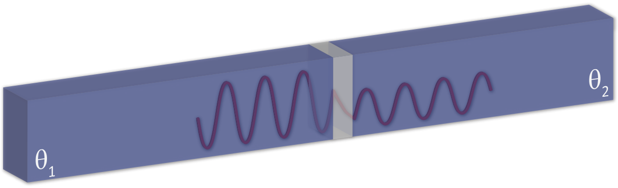

Fig. 2.5.: **Schematic illustration of a Superconductor-Insulator-Superconductor (SIS) Josephson Junction.** For a sufficiently thin insulating barrier (grey), tunneling of Cooper pairs between the two superconductors (blue) is possible. In this case, the macroscopic wave functions overlap and can be described by a common current-phase-relation based on the phase difference across the junction $\varphi = \theta_2 - \theta_1$. The Josephson equations governing this behavior are described in the main text.

Josephson junctions represent a key element in the field of superconducting quantum circuits, acting as essential non-linear circuit elements. At the heart of the Josephson junction (JJ) lies the Josephson effect, which can be understood as the coherent tunneling of Cooper pairs through an insulating barrier. This effect was predicted by Brian D. Josephson [88] and later observed in 1963 [89], earning the Nobel Prize in Physics in 1973.

The working principle of a Josephson junction relies on two superconducting electrodes separated by a thin insulating barrier, as illustrated in Fig. 2.5. If the tunnel barrier is thin enough, the macroscopic wave functions of the two superconducting electrodes overlap, resulting in a finite tunneling probability for the Cooper pairs. This tunneling effect manifests as a finite supercurrent I_s flowing across the insulating barrier. This overlap can be mathematically described by the sinusoidal current-phase relation [90]

$$I_\mathrm{s}(\varphi) = I_\mathrm{c0}\sin(\varphi), \tag{2.38}$$

where I_c0 is the maximum or critical current the junction can carry, and $\varphi = \theta_2 - \theta_1$ is the phase difference between the two superconductor wave functions. Equation (2.38) is called the first Josephson equation and fundamentally governs the junction's physics together with the second Josephson equation [91]

$$\frac{\partial\varphi}{\partial t} = \frac{2\pi}{\Phi_0}V\,, \tag{2.39}$$

where V denotes the voltage drop across the junction.
Additionally, the characteristic properties of any one junction are crucially dependent on its geometry: The critical current is defined via $I_\mathrm{c0} = j_\mathrm{c}A_\mathrm{J}$ by the area of the junction, i.e. the overlap region A_J, and by the critical current density j_c, which itself depends exponentially on the insulating barrier's height and thickness [92].

The non-linear current-phase relationship, as described by Eq. (2.38), gives rise to a distinctive attribute of the Josephson junction: the non-linear Josephson inductance, denoted as L_J. To deduce L_J, we apply the standard definition of inductance, $V = L\cdot\partial I/\partial t$, in conjunction with the two fundamental Josephson equations. This process leads to the following derivation [92]:

$$L_\mathrm{J} = \frac{\partial I_\mathrm{s}}{\partial t}\frac{1}{V} \overset{(2.38)}{=} I_\mathrm{c0}\cos(\varphi)\frac{\partial\varphi}{\partial t}\frac{1}{V} \overset{(2.39)}{=} \frac{\Phi_0}{2\pi}I_\mathrm{c0}\cos(\varphi) = L_\mathrm{J0}\frac{1}{\cos(\varphi)}\,, \tag{2.40}$$

where $L_\mathrm{J0} = \Phi_0/(2\pi I_\mathrm{c0})$ is defined as the maximum Josephson inductance of the junction. The presence of the cosine term in the denominator effectively transforms the Josephson junction into an adjustable inductor, which presents a valuable and versatile asset in designing electromechanical circuits.

Josephson junctions in external magnetic fields As some of the experiments shown in this work require circuits containing Josephson junctions to be operated in the presence of external magnetic fields, we want to briefly discuss the implications of such scenarios.

We consider a magnetic field B being applied parallel to the plane of the junction, as represented in Fig. 2.6. In this case, B causes a spatial inhomogeneity in the phase difference between the wave functions and therefore induces a dependence of the effective tunneling current on B. This dependency is expressed in terms of the critical current as [92]

$$I_\mathrm{s}(\Phi) = I_\mathrm{c0}\left|\frac{\sin\left(\frac{\pi\Phi}{\Phi_0}\right)}{\frac{\pi\Phi}{\Phi_0}}\right|. \tag{2.41}$$

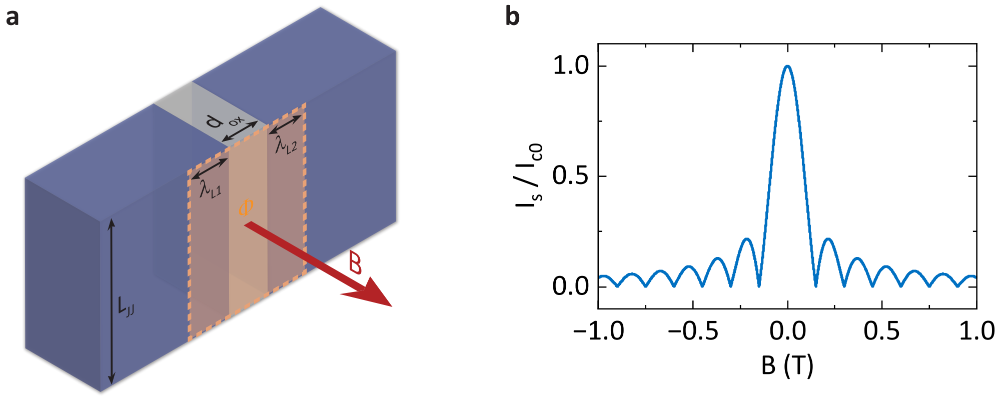

Fig. 2.6.: Josephson junction in external magnetic field. a Illustration of a Josephson junction in an external magnetic field. The external field B is applied perpendicular to the flow of the tunnel current. The oxide thickness d_ox, junction length L_JJ and London penetration depths λ_L1 and λ_L2 are highlighted. **b** Magnetic field dependence of the maximum tunneling current I_s normalized to the junction critical current I_c0, calculated according to Eq. (2.41), using Eq. (2.42) with realistic junction parameters $t_\mathrm{b} = 92\,\mathrm{nm}$ and $L_\mathrm{JJ} = 150\,\mathrm{nm}$.

Here, I_c0 is the junction's critical current in a zero magnetic field environment, as before, and Φ is the magnetic flux arising from B. The flux can be expressed by

$$\Phi = B L_\mathrm{JJ} t_\mathrm{b}\,, \tag{2.42}$$

incorporating the length of the junction L_JJ, and a defined magnetic thickness t_b, expressed as $t_\mathrm{b} = d_\mathrm{ox} + \lambda_\mathrm{L1} + \lambda_\mathrm{L2}$. The magnetic thickness considers not only the thickness d_ox of the insulating barrier but also the London penetration depths, λ_L1 and λ_L2, of each of the junction electrodes.

In Fig. 2.6**b**, we calculate the field dependence of an exemplary junction based on realistic geometric parameters (see caption) according to Eq. (2.41). It becomes apparent that the magnetic flux dependence of the critical current essentially forms a Fraunhofer diffraction pattern equivalent to a slit of width L_JJ. However, it should be noted that this solution describes an ideal case. Effects like flux focusing due to, e.g., the Meissner-Effect or Oersted fields generated by the currents flowing through the contacts are not considered and can lead to a deviating result.

2.2.4 SQUIDs

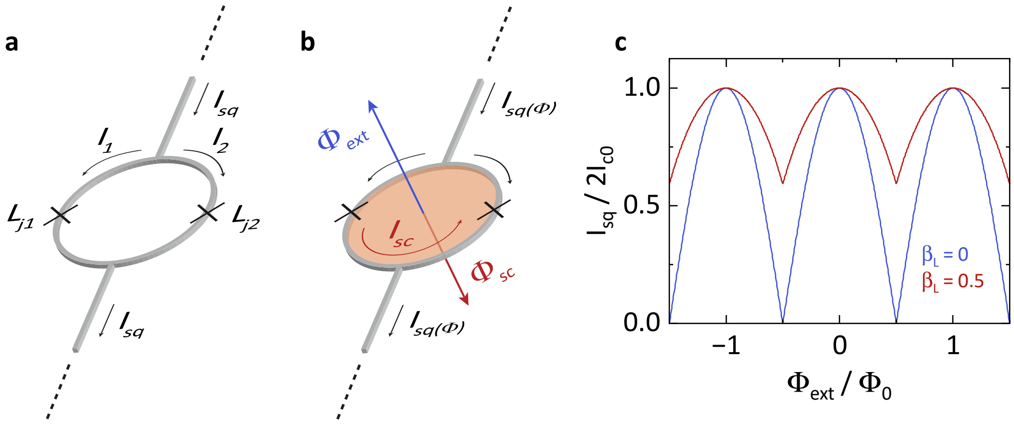

Fig. 2.7.: SQUID geometry and response to an external magnetic field B_{oop}. Schematic illustration of a simplified SQUID loop in zero-field (**a**) and in the presence of an external magnetic field (**b**). In **a**, the total transport current I_{sq} is equally split between the two arms of the SQUID. In **b**, the external flux Φ_{ext} breaks the symmetry and the SQUID generates a screening current I_{sc} in order to fulfill the fluxoid quantization (see main text). This leads to a flux-dependent reduction of the SQUIDs critical current $I_{\mathrm{c0}}(\Phi)$. When considering a finite inductance of the loop itself, I_{sc} leads to an associated flux Φ_{sc}, which counteracts the external flux Φ_{ext}. This effect is often neglected in simplified models and discussed in the main text. **c** Flux-dependent critical current I_{sq} of the SQUID in the case of negligible loop inductance ($\beta_{\mathrm{L}} = 0$) and finite loop inductance ($\beta_{\mathrm{L}} = 0.5$), numerically calculated using Eq. (2.45) and Eq. (2.51). For simplicity, multi-valued solutions that arise from the hysteretic behavior of the SQUID for $\beta_{\mathrm{L}} = 0.5$ are omitted.

The Superconducting QUantum Interference Device (SQUID) is one of the most popular devices in superconducting electronics, offering the most sensitive detection of magnetic flux currently achievable in solid state devices [93, 94]. This sensitivity is put to use for versatile applications ranging from detection of individual electron spins [95] to neurological brain scans [96].

Fundamentally, a SQUID consists of a superconducting loop containing two Josephson junctions in parallel[1], as illustrated in Fig. 2.7**a**. In the absence of a magnetic field, the current distribution in a SQUID operating in a zero-voltage

---

[1] More precisely, a SQUID using the parallel arrangement of two junctions is called a *dc-SQUID* to differentiate from the *rf-SQUID* that uses a single junction [97]. In the context of this work, we exclusively use dc-SQUIDs and use simply the term SQUID.

state is straightforward. Assuming both Josephson junctions have a sinusoidal current-phase relation and equal critical currents I_{c0}, the total supercurrent passing through the SQUID is given by [97]

$$I_{sq} = I_1 + I_2 = I_{c0}\left[\sin(\varphi_1) + \sin(\varphi_2)\right], \tag{2.43}$$

where I_1 and I_2 are the supercurrents flowing in each arm and φ_1 and φ_2 denote the phase difference across the respective junction.

Aside from the previously introduced Josephson effect, the second key principle in the operation of a SQUID is fluxoid quantization, which imposes the condition that the total phase change around the superconducting loop must be a multiple of 2π. This leads to a relation between the phase differences of the two Josephson junctions and the total magnetic flux Φ threading the loop of the SQUID [92]

$$\varphi_2 - \varphi_1 = \frac{2\pi\Phi}{\Phi_0}. \tag{2.44}$$

When an external magnetic field B_{oop} is applied perpendicularly to the SQUID loop, it creates a magnetic flux Φ_{ext}, leading to the generation of a screening current I_{sc}, as shown in Fig. 2.7**b**. This current attempts to compensate for the external flux by adjusting the phase difference $\varphi_2 - \varphi_1$ as required by flux quantization. Consequently, the SQUID will break the symmetry between the currents of the two arms, thus modulating the total supercurrent across the device.

For a negligible self inductance, the total flux is given by $\Phi = \Phi_{ext}$, and the critical current of the SQUID can be written as [97]

$$I_{sq}(\Phi) = 2I_{c0}\left|\cos\left(\pi\frac{\Phi}{\Phi_0}\right)\right|. \tag{2.45}$$

This expression shows an effective reduction of the SQUID's critical current, oscillating between a maximum of $2I_{c0}$ and zero depending on the magnetic flux, as illustrated in Fig. 2.7**c** (blue curve). Accordingly, the inductance of a SQUID can be expressed as

$$L_{sq}(\Phi) = \frac{L_{J0}}{2}\frac{1}{\left|\cos\left(\pi\frac{\Phi}{\Phi_0}\right)\right|}, \tag{2.46}$$

with the Josephson inductance of a single junction L_{J0}.

Equation (2.46) exemplifies the ability of the SQUID to act as a flux-tunable inductive element. Based on this property, the integration of SQUIDs into superconducting LC oscillator circuits allows for the engineering of resonant circuits with a natural frequency dependent on the flux-tuneable inductance, $\omega_0 =$

$1/\sqrt{L(\Phi)C}$. The resulting flux-tuneable resonators are discussed in a subsequent section.

Considering non-negligible loop inductance In the previous discussion, we have approached the behavior of the SQUID with the simplified assumption of negligible self inductance, focusing exclusively on the influence of an externally applied magnetic field. However, in many real-world applications, especially in the realm of electromechanical circuits involving nano- or micro-mechanical oscillators, the SQUID loop inductance can become a significant factor. As the SQUID loop area is increased, for example to incorporate larger mechanical oscillators, the loop inductance L_loop also grows, which subsequently influences the dynamics and performance of SQUID cavities.

When considering a non-negligible L_loop, the magnetic flux generated by the screening current $\Phi_\mathrm{sc} = L_\mathrm{loop} \cdot I_\mathrm{sc}$ must be incorporated into the previously discussed model and contributes alongside the external flux Φ_ext. The total flux threading the SQUID is then given by

$$\Phi = \Phi_\mathrm{ext} + L_\mathrm{loop} I_\mathrm{sc}. \tag{2.47}$$

A useful figure of merit to distinguish the different regimes of this interplay is the screening parameter [91]

$$\beta_\mathrm{L} = \frac{2 L_\mathrm{loop} I_\mathrm{c0}}{\Phi_0}. \tag{2.48}$$

We have previously discussed scenarios where $\beta_\mathrm{L} \ll 1$ and the loop inductance's effect is minor. In those cases, the total flux is $\Phi = \Phi_\mathrm{ext}$ and the SQUID's critical current is well described by Eq. (2.45).

However, as β_L increases, the situation changes: The screening current becomes relevant in determining the net flux experienced by the SQUID, as it acts to counterbalance the externally applied magnetic field (see Fig. 2.7**b**). The more substantial the loop inductance, the more pronounced is this compensatory effect. Taking the compensation into account via Eq. (2.47), re-deriving the equations governing the SQUID leads to more intricate expressions for the total flux and the transport current I_{sq} [92]

$$\frac{\Phi}{\Phi_0} = \frac{\Phi_{\mathrm{ext}}}{\Phi_0} - \frac{\beta_{\mathrm{L}}}{2} \sin\left(\pi\frac{\Phi}{\Phi_0}\right) \cos\left(\varphi_1 + \pi\frac{\Phi}{\Phi_0}\right) \tag{2.49}$$

$$I_{\mathrm{sq}} = 2I_{\mathrm{c0}} \cos\left(\pi\frac{\Phi}{\Phi_0}\right) \sin\left(\varphi_1 + \pi\frac{\Phi}{\Phi_0}\right) . \tag{2.50}$$

We can see that for non-negligible β_{L} the total flux threading the loop is described by a transcendental equation. The solution for the SQUID's critical current can be numerically determined by optimizing the transport current I_{sq} concerning the phase difference of a single junction φ_1 [97]. In an intuitive picture, the loop inductance shields the SQUID against the effects of the external magnetic flux, which would otherwise reduce the critical current towards zero for $\Phi_{\mathrm{ext}} = 0.5\Phi_0$. In this way, the accessible range of amplitude modulation of the SQUID's critical current is reduced. To provide perspective, we plot the numerically calculated flux-dependent critical current of a SQUID with $\beta_{\mathrm{L}} = 0.5$ in Fig. 2.7**c** next to the ideal case of $\beta_{\mathrm{L}} = 0$. Clearly, the available range of critical currents is significantly reduced compared to the case of negligible loop inductance.

Finally, for the modeling and analysis of the SQUID based devices investigated in this thesis, we employ a simplified version of Eq. (2.49)

$$\frac{\Phi}{\Phi_0} = \frac{\Phi_{\mathrm{ext}}}{\Phi_0} - \frac{\beta_{\mathrm{L}}}{2} \sin\left(\pi\frac{\Phi}{\Phi_0}\right) , \tag{2.51}$$

which is valid for our experiments in the quantum regime, where no dedicated bias currents are applied and the SQUIDs are subject to very low powers.

2.3 Flux-Tuneable Resonators (FTRs)

In the preceding sections, we've repeatedly highlighted the impact of external magnetic fields on devices relying on the Josephson effect, such as Josephson junctions and SQUIDs. Central to these components is their characteristic non-linear, flux-dependent inductance, which presents a versatile tool for the design of multi-purpose superconducting circuits. Introducing a SQUID into an LC resonator allows for the in-situ modulation of the circuit's total inductance. Consequently, this manipulation affects its resonance frequency, rendering it flux-tuneable. We call this class of devices *flux-tuneable resonators* (FTRs). The frequency tuning capability not only enhances the precision of magnetic field sensing as seen in Refs. [98, 99], but also grants the circuit a dynamic character that forms the basis for a flux-mediated electromechanical interaction that lies at the heart of this work and will be explored theoretically in Sec. 2.5.2 and experimentally in Sec. 5. Furthermore, the inclusion of Josephson junctions into the LC oscillator circuit introduces an inherent Kerr-type non-linearity. This results in an anharmonic distribution of the resonator's energy levels, diverging from the equidistant nature observed in traditional harmonic oscillators. This induced non-linearity has practical implications, paving the way for applications such as single photon detection and parametric amplification [100].

In the following section, we will explicitly derive the effective Hamiltonian of a flux-tuneable microwave resonator (FTR) and explore its frequency tuning capabilities, comparing an approximate and an exact theoretical model in the process. Based on these calculations, we we will be able to examine the influence of the Josephson non-linearity on the characteristic parameters ω_0 and $\mathcal{K}$ of the flux-tuneable circuit. Finally, we use input-output-theory to model the response of the FTR to an external drive and how flux-tuneability can be exploited for quantum-limited parametric amplification.

2.3.1 Distributed circuit model

The device we consider in this work is a $\lambda/4$ coplanar waveguide resonator, which is terminated by a SQUID loop at one end (shorted boundary) and coupled capacitively to a transmission line on the other end (open boundary). As discussed in Sec. 2.2.2, the bare CPW resonator can be modeled as a discrete chain of identical LC oscillators with per-unit inductance L_0 and capacitance C_0. Using this representation, we design an equivalent circuit model of the full circuit by attaching the SQUID to the right end of the chain, as shown in Fig. 2.8.

The following derivation closely follows the treatments in Refs. [101, 102] with elements of Refs. [103] and [104]. It is important to emphasize that we focus on the case of the SQUID being placed at the end of the CPW resonator, at position $x = \ell$. Different resonator designs with the SQUID integrated at varying positions along the CPW can lead to significantly different results, which is comprehensively discussed in Ref. [104].

Initially, we will neglect the coupling capacitance C_{ext} to the transmission line since it is generally negligible compared to the capacitance of the CPW itself. For FTR designs with very large coupling, it can be re-introduced later as a small correction to ω_j and κ_j [102]. Furthermore, since we are in the limit in which the plasma frequency of the SQUID is much larger than the resonance frequency of the CPW resonator, we also neglect the self-capacitance of the SQUID. Under these conditions, the total Lagrangian of the FTR can be written as [102]

$$\mathcal{L} = \int_0^d dx \left\{ \frac{C_0}{2} \left(\frac{\partial \Phi(x)}{\partial t} \right)^2 - \frac{1}{2L_0} \left(\frac{\partial \Phi(x)}{\partial x} \right)^2 \right\} + E_{\mathrm{J}} \cos \left(\frac{\Phi(\ell)}{\varphi_0} \right) , \qquad (2.52)$$

with the reduced flux quantum $\varphi_0 = \hbar/2e$, the Josephson coupling energy E_{J} of the SQUID and the magnetic flux field $\Phi(x)$ at position x along the CPW. The integral corresponds to the contribution of the CPW, while the second term describes the SQUID at position $x = \ell$. Notably, it is irrelevant for the further discussion whether the non-linear inductance arises from a single Josephson junction or a SQUID, so both can be sufficiently described by a single, tuneable Josephson energy E_{J}.

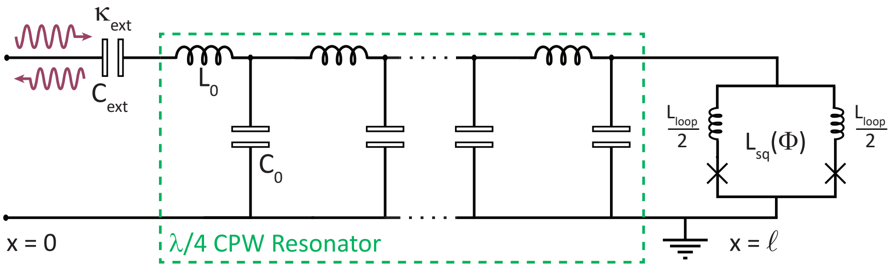

Fig. 2.8.: FTR equivalent circuit diagram. The flux-tuneable resonator (FTR) consists of a $\lambda/4$ CPW resonator terminated on one end via a SQUID. The CPW resonator is represented by a linear chain of lumped element LC oscillators with per-unit inductance L_0 and capacitance C_0. The SQUID attached to the right end has a flux-dependent Josephson inductance $L_{\mathrm{sq}}(\Phi)$ and a static loop inductance L_{loop}, arising from geometric and kinetic inductance contributions. The other end of the CPW is capacitively coupled to a input-output transmission line with the coupling capacitance C_{ext} and coupling rate κ_{ext}.

2.3.2 Flux-dependent resonance frequency

In the limit of a small phase drop across the SQUID, $\Phi(\ell)/\varphi_0 < 1$, i.e. the transport currents remaining small w.r.t. the critical current, we can linearize the SQUID potential by approximating the cosine as a quadratic potential [102]

$$E_\mathrm{J} \cos\left(\frac{\Phi(\ell)}{\varphi_0}\right) \approx \text{const} - \frac{E_\mathrm{J}}{2}\left(\frac{\Phi(\ell)}{\varphi_0}\right)^2 . \tag{2.53}$$

After adjusting the second part of the Lagrangian Eq. (2.52) accordingly, the eigenmodes of the system can be found by solving the Euler-Lagrange equation for the CPW resonator, which is expressed by the wave equation

$$v^2 \frac{\partial^2 \Phi(x)}{\partial x^2} - \frac{\partial^2 \Phi(x)}{\partial t^2} = 0 , \tag{2.54}$$

where $v = 1/\sqrt{C_0 L_0}$ is again the phase velocity based on the characteristic parameters of the distributed circuit model. A general solution can be expressed as

$$\Phi(x) = \sum_{j=0}^{\infty} \phi_j \cos(k_j x) . \tag{2.55}$$

Which wavevectors are valid solutions to Eq. (2.55) depends on the boundary condition given by the $\lambda/4$ CPW design. On the open end, the geometry imposes a vanishing current $\partial_x \Phi(0) = 0$. This is inherently satisfied by the cosine solution in Eq. (2.55). The boundary condition on the end with the SQUID, however, is dynamically influenced by the presence of the Josepshon junctions and can be written as [101]

$$\frac{1}{L_0} \frac{\partial \Phi(\ell)}{\partial x} + \frac{E_\mathrm{J} \Phi(\ell)}{\varphi_0^2} = 0 . \tag{2.56}$$

Interestingly, Eq. (2.56) provides an intuitive understanding of the flux-tuneability provided by the SQUID: Due to the second term of the equation, the flux-dependent Josepshon energy alters the boundary condition of the circuit at its rightmost end. In the first limit, the SQUID exhibits an exceedingly large (effectively infinite) Josephson energy, imposing a node of the flux field at the boundary and preserving the conditions of a $\lambda/4$ resonator. Conversely, in the opposite limit, the Josephson energy is completely nullified, leading to an anti-node boundary condition more akin to a $\lambda/2$ resonator. Theoretically, adjusting the magnetic flux threading the SQUID by half of a flux quantum, $(0 \rightarrow \Phi_0/2)$, should permit variation in the eigenmode frequencies between the range $(\pi v/\ell)n < \omega_n < (\pi v/\ell)(n + 1/2)$. Nevertheless, real-world applications observe more confined ranges due to the non-zero minimum and limited maximum Josephson energies of the SQUID.

Returning to the derivation, we can combine our proposed solution Eq. (2.55) with the boundary conditions and compare coefficients, which results in a transcendental equation for $k_j\ell$ [102]:

$$k_j\ell\tan(k_j\ell) = \frac{L_0\ell E_\mathrm{J}}{\varphi_0^2}\,. \tag{2.57}$$

Equation (2.57) is a dispersion equation with an infinite set of solutions with wavelengths $\lambda = 2\pi/k_j$ and frequencies $\omega_j = k_j v$, corresponding to the normal mode structure of the FTR in the linear regime. In the absence of the SQUID and its Josephson energy E_J, one would simply retrieve the standard $\lambda/4$ harmonic oscillator modes expressed by the poles of $\tan(k_j\ell)$:

$$k_j^{(0)}\ell = \frac{\pi}{2}(1+2j) \text{ with } j \in 0,1,2,3\ldots\,. \tag{2.58}$$

To incorporate the effect of the SQUID inductance, we use the definition for the Josephson energy $E_\mathrm{J} = \varphi_0^2 L_\mathrm{J}$ along with the previously derived SQUID inductance L_sq (Eq. (2.46)) to replace E_J in Eq. (2.57) with the flux-dependent energy of the SQUID and obtain

$$k_j\ell\tan(k_j\ell) = \frac{L_0\ell}{L_\mathrm{sq}(\Phi_\mathrm{ext}) + L_\mathrm{loop}/4} \tag{2.59}$$

where we also take into account the previously discussed self-inductance L_loop of the SQUID loop, which enters with a factor of $1/4$ due to the SQUID geometry [105, 106]. Solving Eq. (2.59) numerically will provide exact solutions to the normal mode structure of the FTR including the contributions of the Josephson inductance and the self-inductance SQUID loop. If one also makes use of Eq. (2.51) to numerically calculate the total flux Φ, the solutions will also reproduce the effects of the flux screening due to the finite loop inductance and make the model compatible to a large range of devices, even with large screening parameters $\beta_\mathrm{L} > 1$. To obtain an analytical expression, we can expand the tangent in Eq. (2.59) around $\pi/2$ and obtain a first-order correction to the wave vectors and an approximate solution [105]

$$k_j(\Phi) \approx k_j^{(0)}\left(1 + \frac{L_\mathrm{sq}(\Phi_\mathrm{ext}) + L_\mathrm{loop}/4}{L_0\ell}\right)^{-1} \tag{2.60}$$

or rewritten in terms of frequencies $\omega_j = k_j v$

$$\omega_j(\Phi) \approx \omega_j^{(0)} \left(1 + \frac{L_{\mathrm{sq}}(\Phi_{\mathrm{ext}}) + L_{\mathrm{loop}}/4}{L_0 \ell}\right)^{-1} \tag{2.61}$$

The simplified expression is accurate when considering only the fundamental mode with $j = 0$ and inductance ratios up to $L_{\mathrm{J}}/L_0\ell \approx 0.5$ [102]. This condition typically holds for the FTRs examined in this study. For scenarios involving higher inductance ratios or when the rich multi-mode architecture of the FTR is of interest, it's crucial to employ the exact formula.

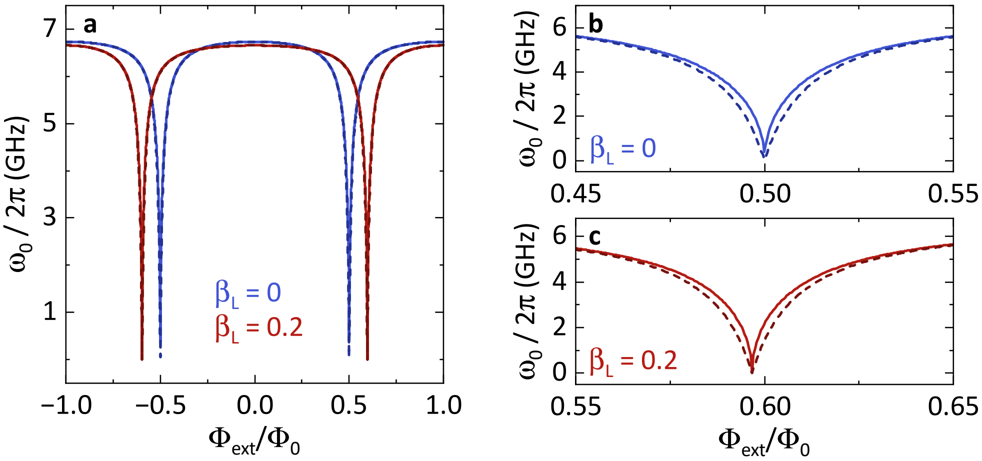

Fig. 2.9.: **FTR flux-dependent fundamental resonance frequency.** The solid lines represent exact, numerically calculated results according to Eq. (2.59) in the case of negligible L_{loop} (blue) and $L_{\mathrm{loop}} = 100\,\mathrm{pH}$ (red). For comparison, dashed lines in darker colors depict the corresponding results of the linearized approximation according to Eq. (2.61). Panels **b** and **c** present zoom-ins of the data shown in **a** to highlight the areas where deviations between the models are discernible. The other parameters used in the calculations are based off real devices and are as follows: $\omega_0^{(0)} = 7\,\mathrm{GHz}$, $I_{\mathrm{c0}} = 2\,\mu\mathrm{A}$, $L_0 = 463\,\mathrm{nH\,m^{-1}}$ and $C_0 = 136\,\mathrm{pF\,m^{-1}}$.

To illustrate the flux-tunability of the FTR and gain an intuitive understanding of the strengths and limitations associated with the different theoretical models, we present a model calculation based on realistic device parameters in Fig. 2.9. In the figure, the exact solutions according to Eq. (2.59) are shown side-by-side with the first order approximation given by Eq. (2.61). Furthermore, we differentiate the distinct scenarios where the self-inductance of the SQUID L_{loop} is considered ($\beta_{\mathrm{L}} > 0$) or neglected ($\beta_{\mathrm{L}} = 0$). It becomes apparent that in the parameter regime of interest the linearized model of the frequency tuning behavior remains accurate, both for negligible and non-negligible L_{loop}. However, the pronounced discrepancy in the shape of the tuning curve between the the calculations with and without loop inductance (see panel **a**) emphasizes the importance of factoring in the SQUID self-inductance in the process of building an accurate tuning model.

Based on the modified wavenumbers k_j obtained from either of the formulas discussed above, we can define effective circuit parameters for the linear components of the flux-tunable circuit. The effective capacitances and inductances are defined as [102]

$$C_j = \frac{C_0\ell}{2}\left(1 + \frac{\sin(2k_j\ell)}{2k_j\ell}\right) \tag{2.62}$$

and

$$L_j^{-1} = \frac{(k_j\ell)^2}{2L_0\ell}\left(1 + \frac{\sin(2k_j\ell)}{2k_j\ell}\right). \tag{2.63}$$

Using the above expressions for C_i and L_i, we have successfully renormalized the circuit parameters to fulfill the resonance frequency definition of a generic LC oscillator

$$\omega_j = k_j v = \frac{1}{\sqrt{L_j C_j}}\,. \tag{2.64}$$

At this point, we have basically reduced the complex circuit consisting of a distributed element CPW resonator and a non-linear SQUID inductance to a linear LC oscillator with modified characteristic parameters. However, it should be clarified that the effective inductance and capacitance do still contain the flux-dependency of the SQUID and need to be (numerically) calculated for the specific external flux Φ_ext.

2.3.3 Non-linear corrections and effective Hamiltonian

In the previous section, which was primarily concerned with the frequency tuning behavior of the FTR, we have treated the system purely classically and also omitted any additional effects that arise from the addition of the inherently non-linear element that is a Josephson junction. In the following, we now reintroduce the nonlinear contributions of the SQUID in order to arrive at a quantum mechanical Hamiltonian description of the flux-tunable microwave resonator.

To this end, we further expand the SQUIDs potential to include the first non-quadratic term:

$$E_{\mathrm{J}} \cos\left(\frac{\Phi(x)}{\varphi_0}\right) = \mathrm{const} - \frac{1}{2} E_{\mathrm{J}} \left(\frac{\Phi(x)}{\varphi_0}\right)^2 + \frac{1}{24} E_{\mathrm{J}} \left(\frac{\Phi(x)}{\varphi_0}\right)^4 + \ldots, \tag{2.65}$$

which we substitute into the Taylor expansion of the Lagrangian together with the normal mode decomposition in Eq. (2.55) [102]:

$$\mathcal{L} = \frac{1}{2} \sum_{i=1}^{\infty} \left(\dot{\phi}_i C_i \dot{\phi}_i - \phi_i L_i^{-1} \phi_i\right) + \sum_{i,j,k,l=1}^{\infty} N_{ijkl} \phi_i \phi_j \phi_k \phi_l \,. \tag{2.66}$$

As discussed above, the first sum encompasses the linear parts of the circuit, portrayed as a set of isolated LC oscillators with effective parameters L_{i} and C_{i}. The second sum, on the other hand, comprises the non-linear properties of the circuit expressed by the coefficients

$$N_{ijkl} = E_{\mathrm{J}} \frac{1}{24} \phi_0^{-4} \prod_{m \in \{i,j,k,l\}} \cos(k_m \ell) \,. \tag{2.67}$$

From the Lagrange function, we derive the Hamiltonian by introducing the conjugate charge variables: $q_i = \partial L / \partial \dot{\phi}_i = C_i \dot{\phi}_i$ and perform a Legendre transformation to obtain the Hamiltonian

$$H = \frac{1}{2} \sum_{i=1}^{\infty} \left(q_i C_i^{-1} q_i + \phi_i L_i^{-1} \phi_i\right) - 3 \sum_{j \neq i} N_{iijj} \phi_i^2 \phi_j^2 + \sum_i N_{iiii} \phi_i^4 \,, \tag{2.68}$$

where we have focused solely on self-interactions and two-mode interactions. Moving to a quantum mechanical picture, q_i and ϕ_i act as operators, satisfying the commutation relation $[\phi_j, q_k] = \delta_{kj} \hbar / i$. Defining the appropriate normal mode annihilation and creation operators yields:

$$\phi_j = i \phi_{\mathrm{zpf},j} (\hat{a}_j^\dagger - \hat{a}_j) \,, \tag{2.69}$$

$$q_j = q_{\mathrm{zpf},j} (\hat{a}_j + \hat{a}_j^\dagger) \,, \tag{2.70}$$

with the zero-point fluctuations

$$q_{\mathrm{zpf},j} = \sqrt{\frac{\hbar \omega_j C_j}{2}} \,, \tag{2.71}$$

$$\phi_{\mathrm{zpf},j} = \sqrt{\frac{\hbar}{2 \omega_j C_j}} \,. \tag{2.72}$$

Finally, we move to a rotating wave approximation and exclude the small photon number-independent frequency shifts due to the nonlinear terms (e.g. Lamb shifts) and obtain:

$$\hat{H} = \sum_{i=1}^{\infty} \hbar\omega_i \hat{a}_i^\dagger \hat{a}_i + \hbar\frac{K_{ii}}{2}\hat{a}_i^\dagger \hat{a}_i^\dagger \hat{a}_i \hat{a}_i + \sum_{j\neq i} \hbar K_{ij} \hat{a}_i^\dagger \hat{a}_i \hat{a}_j^\dagger \hat{a}_j \,, \tag{2.73}$$

with the nonlinearity given by:

$$K_{ij} = -\frac{E_\mathrm{J}}{2\hbar}\left(\frac{\phi_\mathrm{zpf}}{\phi_0}\right)^4 \cos^2(k_i d)\cos^2(k_j d)\,. \tag{2.74}$$

Here, $K_{00} \equiv \mathcal{K}$ represents the Kerr non-linearity of the fundamental mode, which has a profound impact on the behavior of non-linear microwave devices, as we will see in our experiments. The terms proportional to K_{ij} where $i \neq j$ are cross-Kerr interaction terms that couple different modes together. Such cross-Kerr interactions can become relevant depending on the magnitude of the non-linearity and the device's mode structure and can even be exploited to count the number of photons in one mode by probing another mode with a coherent field [107, 108]. However, for our purposes, cross-Kerr terms are usually negligible and will be omitted. Lastly, since we are generally focused on the fundamental mode $j = 0$, we reduce the multi-mode Hamiltonian above to

$$\hat{H} = \hbar\omega_0 \hat{a}^\dagger \hat{a} + \hbar\frac{\mathcal{K}}{2}\hat{a}^\dagger \hat{a}^\dagger \hat{a}\hat{a}\,. \tag{2.75}$$

2.3.4 Response of a non-linear FTR

In real experiments, the properties of microwave resonators are usually probed by studying their response to an external microwave drive. We have briefly discussed the response of a linear CPW resonator in Sec. 2.2.2, arriving at an ideal expression for the scattering parameter S_{21} in Eq. (2.37). Due to the presence of the SQUID and its non-linear inductance, the linear response of a CPW resonator is no longer generally applicable to FTRs. In this section, we will present a partial derivation of the response of a non-linear microwave resonator to an external drive signal, highlighting the most important steps and expressions. For a comprehensive step-by-step derivation, we refer the interested reader to Refs. [109, 110] and the fundamentals of the input-output-formalism in Ref. [111].

Linearized Hamiltonian We begin by extending the non-linear FTR Hamiltonian Eq. (2.75) by an external drive with frequency ω_p and amplitude α_p of the form

$$\hat{H}_\mathrm{d} = \alpha_\mathrm{p} e^{-i\omega_\mathrm{p} t} \hat{a}^\dagger + \mathrm{h.c}\,. \tag{2.76}$$

If we now assume that the system is strongly driven at ω_p, we can decompose the resonator field operators into $\hat{a} = \alpha e^{-i\omega_p t} + \hat{d}$ with a classical amplitude $\alpha = \langle \hat{a} \rangle$ and quantum fluctuations $\hat{d}$ around this amplitude. The resulting linearized Hamiltonian, in a reference frame rotating with ω_p, reads

$$\hat{H}_\mathrm{lin} = -\tilde{\Delta} \hat{d}^\dagger \hat{d} + \frac{1}{2} \left[\Lambda \hat{d}^\dagger \hat{d}^\dagger + \Lambda^* \hat{d} \hat{d} \right] , \tag{2.77}$$

where we have introduced the modified detuning $\tilde{\Delta} \equiv \Delta - 2|\alpha|^2 \mathcal{K}$, the bare detuning $\Delta = \omega_\mathrm{p} - \omega_0$ and the single-mode squeezing strength $\Lambda = |\alpha|^2 \mathcal{K} e^{i\phi_\Lambda}$.

Equations of motion We now use the input-output-formalism [111] to formulate the equations of motion for the classical resonator field amplitude α

$$\frac{d}{dt}\alpha = \left(i\Delta - \frac{\kappa}{2} \right) \alpha - i\mathcal{K}|\alpha|^2 \alpha - \sqrt{\frac{\kappa_\mathrm{ext}}{2}} \alpha_\mathrm{in} \tag{2.78}$$

where κ is the total loss rate, κ_ext the external coupling to input/output ports[2] and α_in the amplitude of the coherent drive. To solve the differential equation, we use the ansatz

$$\begin{aligned} \alpha_\mathrm{in} &= \bar{\alpha}_\mathrm{in} e^{-i\omega_\mathrm{p} t} \,, \\ \alpha &= \bar{\alpha} e^{-i(\omega_\mathrm{p} t + \phi)} \,, \end{aligned}$$

where we allow for a finite phase offset ϕ. The corresponding steady-state solution becomes

$$-\left(i\Delta + \frac{\kappa}{2} \right) \bar{\alpha} + i\mathcal{K}\bar{\alpha}^3 = -\sqrt{\frac{\kappa_\mathrm{ext}}{2}} \bar{\alpha}_\mathrm{in} e^{i\phi} \,. \tag{2.79}$$

---

[2] Here, we assume a resonator in a side-coupled configuration (cf. Fig. 2.4**a**), as used in our experiments. Due to the coupling to a bidirectional transmission line with two ports, energy can couple in and out of the system at both input/output ports, leading to an effectively halved coupling rate of $\kappa_\mathrm{ext}/2$ in the equations of motion.

Multiplication of the steady-state solution with its complex conjugate results in an expression for the average photon occupation number of the microwave resonator mode, which we define as $\bar{n}_\mathrm{c} = |\bar{\alpha}|^2$:

$$\bar{n}_\mathrm{c}\left[(-\Delta + \mathcal{K}\bar{n}_\mathrm{c})^2 + \left(\frac{\kappa}{2}\right)^2\right] = \frac{\kappa_\mathrm{ext}}{2}\bar{n}_\mathrm{in} \tag{2.80}$$

with the corresponding input photon rate $\bar{n}_\mathrm{in} = |\bar{\alpha}_\mathrm{in}|^2$. Equation (2.80) is commonly used in experiments to calculate the photon occupation resulting from a microwave drive using $\bar{n}_\mathrm{in} = P/\hbar\omega$ with the drive frequency ω and the power P in Watts.

Additionally, the phase between drive field and resonator field can be expressed as

$$\tan(\phi) = -\frac{\kappa/2}{-\Delta + \mathcal{K}\bar{n}_\mathrm{c}}\,. \tag{2.81}$$

Using Eq. (2.79) with the input-output relation $\alpha_\mathrm{out} = \alpha_\mathrm{in} + \sqrt{\kappa_\mathrm{ext}/2}\alpha$ gives rise to a modified expression for the scattering parameter of a side-coupled, non-linear cavity

$$S_{21}(\omega) = 1 - \frac{\kappa_\mathrm{ext}/2}{\kappa/2 - i(\Delta + \mathcal{K}\bar{n}_\mathrm{c})}\,. \tag{2.82}$$

Onset of bistability The above equations contain important insights into the response of the non-linear resonator to an external drive field. Comparison of Eq. (2.82) to the linear scattering response given by Eq. (2.37) reveals that the Kerr non-linearity modifies the effective detuning in the denominator according to $\Delta \rightarrow \Delta + \mathcal{K}\bar{n}_\mathrm{c}$, effectively changing the resonance frequency of the resonator. However, the cubic nature of $\bar{n}_\mathrm{c}$, described by Eq. (2.80), leads to an even more complex behavior.

To illustrate this, we plot the solutions of Eq. (2.80) in Fig. 2.10**a** as a function of the detuning Δ and for various drive powers, i.e. input photon rates $\bar{n}_\mathrm{in}$. For small enough powers, Eq. (2.80) has a single, real-valued solution for all detunings and we observe a linear, Lorentzian shaped response in the resulting photon occupation $\bar{n}_\mathrm{c}$. However, as the input power is increased the resonance feature becomes asymmetric and shifts to lower detunings, since we assumed a negative $\mathcal{K}$ (as observed in experiments). This frequency shift is also represented in the linearized Hamiltonian Eq. (2.77) in the form of the modified detuning $\tilde{\Delta} = \Delta - 2\mathcal{K}\bar{n}_\mathrm{c}$.

Once the input photon number surpasses a critical threshold, three simultaneous solutions are found for a certain range of detunings. In this regime, the resonator occupation is *bistable* and can be found in either of the metastable maximum or minimum amplitude states. Only the intermediate solution is unstable and can not be accessed experimentally. In practice, due to the existence of two metastable states, the experimentally observed resonator response is hysteretic and will depend on the sweep direction.

A simulated measurement result is presented in Fig. 2.10**b**. For an experiment with increasing drive frequency the resonator will be found in the low occupation state (dashed line) for most of the detunings, while an otherwise identical experiment sweeping the drive frequency downwards observes the resonator in a higher amplitude state along the same region.

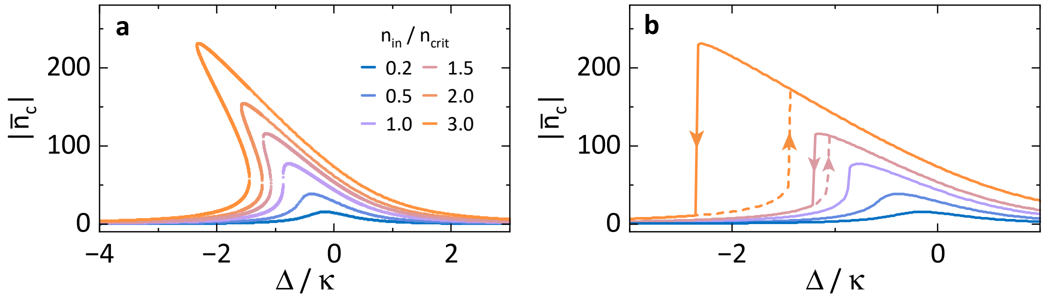

Fig. 2.10.: Response of a resonator with Kerr non-linearity. Average photon occupation $\bar{n}_\mathrm{c}$ of a non-linear resonator as a function of detuning $\Delta = \omega_\mathrm{p} - \omega_0$, plotted for different input powers, expressed as ratio of the critical input photon rate $\bar{n}_\mathrm{in}/\bar{n}_\mathrm{crit}$. The solutions for $\bar{n}_\mathrm{c}$ are calculated according to Eq. (2.80) assuming $\mathcal{K} = -0.1\kappa$ and $\kappa = \kappa_\mathrm{ext}$. **a** As the input power increases, the response deviates from a Lorentzian lineshape and its maximum shifts to lower detunings. Above the critical input power $\bar{n}_\mathrm{in}/\bar{n}_\mathrm{crit} > 1$, the system bifurcates and three solutions appear for a range of detunings. In this regime, the highest and lowest solutions are metastable and can be observed in an experiment, the intermediate solution is not physical. **b** We simulate the experimentally accessible response by plotting the high and low $\bar{n}_\mathrm{c}$ solution as solid and dashed lines, respectively, for selected input powers. In the bifurcation regime the two branches deviate and the direction of the frequency sweep (arrows) determines which branch is observed by the experiment.

Based on the above equations we can analytically determine the threshold where the system transitions from one well-defined state to the bistable regime. This threshold is known as the bifurcation point and characterized by a critical input photon number $\bar{n}_\mathrm{in,crit}$.

Following Ref. [112], we identify $d\bar{n}_{\mathrm{in}}/d\bar{n}_{\mathrm{c}} = 0$ and $d\bar{n}^2_{\mathrm{in}}/d\bar{n}^2_{\mathrm{c}} = 0$ as necessary conditions for the critical point and calculate accordingly:

$$\bar{n}_{\mathrm{in,crit}} = \frac{2}{3\sqrt{3}} \frac{\kappa^3}{|\mathcal{K}|\kappa_{\mathrm{ext}}} , \tag{2.83}$$

$$\omega_{\mathrm{crit}} = \omega_0 - \frac{\sqrt{3}}{2} \frac{\mathcal{K}}{|\mathcal{K}|} \kappa , \tag{2.84}$$

$$\bar{n}_{\mathrm{c,crit}} = \frac{\sqrt{3}}{3} \frac{\kappa}{|\mathcal{K}|} , \tag{2.85}$$

where ω_{crit} is the drive detuning at which bistability emerges if $\bar{n}_{\mathrm{in}} > \bar{n}_{\mathrm{in,crit}}$ and $\bar{n}_{\mathrm{c,crit}}$ is the resulting photon occupation of the resonator mode at this point.

The knowledge of the non-linear photon occupation and the thresholds governing the onset of the bifurcation regime is essential for the effective operation of non-linear resonator devices. This is especially true for multi-tone driving schemes, such as the ones employed in this work in Chap. 5, where the drive detuning $\Delta = \omega_{\mathrm{p}} - \omega_0$ is a crucial parameter that should ideally stay constant. Therefore, experimental drive powers should be carefully calibrated and chosen to operate the resonator in the quasi-linear regime, where no bifurcation appears and the power dependent frequency shift remains smaller than the resonator linewidth κ.

Based on Eq. (2.83), we can further identify a complementary approach at the design stage: The critical photon number and with it the dynamic range of a device can be increased by designing the circuit deliberately to exhibit a smaller non-linearity $\mathcal{K}$, which essentially depends on the ratio of Josephson inductance and total inductance (cf. Eq. (2.74)). However, a reduction of $\mathcal{K}$ can be at odds with other design considerations. We discuss some of the competing design goals related to the non-linearity in Sec. 3.1.

2.4 Parametric amplification with JPAs

Parametric amplification describes the concept of amplifying a weak signal through the periodic modulation of a system's parameter over time. This modulation can affect various system aspects, such as the refractive index within an optical medium [113] or the resonance frequency of either a mechanical oscillator [114] or an electrical circuit [115]. With respect to electrical circuits, the operation of a parametric amplifier can be analogized to a simple, parallel LC circuit. Here, the charge stored on the plates of the capacitor oscillates with the circuit's natural resonance frequency, $\omega_0 = 1/\sqrt{LC}$. Conversely, the current flowing through the inductor performs the same oscillation delayed by a 90° phase shift. Modulating the system's capacitance or inductance in a timed manner, e.g. varying the distance of the capacitor plates in rhythm with the charge oscillation, enables the transfer of energy into the system – or out of it, depending on the modulation's phase and frequency. In the context of superconducting circuits, the parametric modulation of a system parameter can be realized based on the nonlinear inductance inherent to Josephson junctions. The resulting devices are referred to as *Josephson Parametric Amplifiers* (JPAs) [116]. Different types of JPAs are distinguished by their specific circuit implementations and the amplification processes they employ. In the following, we want to provide a brief overview of the most common JPA architectures and their operating principles.

Any parametric amplification process of a microwave signal involves at least three distinct microwave frequencies: the *pump* (ω_P), the *signal* (ω_s), and the *idler* (ω_i), the latter being an inevitable byproduct of the amplification process. The operational differences between devices primarily revolve around whether a *three-wave* or *four-wave* mixing process is utilized [74, 116]. In a *three-wave* mixing process a single photon at the pump frequency is converted into a signal and an idler photon:

$$\omega_\mathrm{P} = \omega_\mathrm{s} + \omega_\mathrm{i}\,. \tag{2.86}$$

A *four-wave* mixing process, on the other hand, requires two pump photons, converting them according to

$$2\omega_\mathrm{P} = \omega_\mathrm{s} + \omega_\mathrm{i}\,. \tag{2.87}$$

Clearly, energy conservation poses considerably different requirements on the frequency detuning between the pump and signal tones for each of the mixing processes, which can have implications for the experimental design. The amplification process possible in a given device is dictated by the symmetry of the nonlinear potential, which can be determined both by circuit design and by choice of experimental protocol. Interestingly, the flux-tunable resonators we have discussed extensively in Sec. 2.3 are capable of supporting both parametric amplification processes, which we will illustrate in the following.

Three-wave mixing: Flux-driven JPA When operated at a flux bias value with a finite flux responsivity $\partial\omega_\mathrm{c}/\partial\Phi$, i.e. a finite slope of the tuning curve shown in Fig. 2.9**a**, a FTR possesses a non-symmetric energy potential that is suitable to implement the three-wave mixing process for parametric amplification. The corresponding devices are commonly referred to as flux-driven JPAs [117], because, in this configuration, the flux-tunable inductance of the SQUID is used as the modulation parameter for the amplification process.

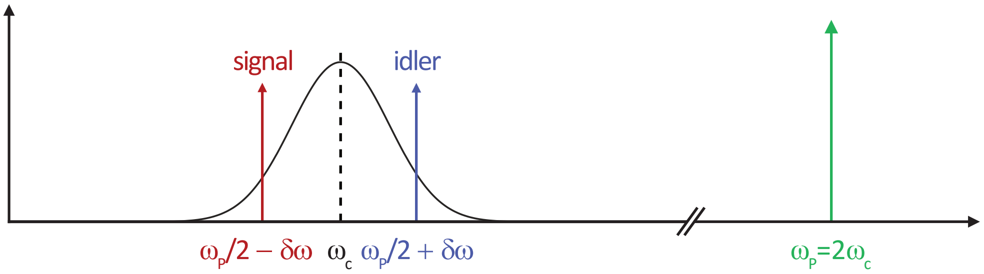

Fig. 2.11.: **Three-wave mixing process with flux-driven JPA.** Schematic illustration of the relevant frequencies for the parametric amplification process using three-wave mixing in a flux-driven JPA. A strong pump tone is applied at twice the JPA resonance frequency $\omega_\mathrm{P} = 2\omega_\mathrm{c}$. This enables a three-wave mixing process that amplifies the input signal at $\omega_\mathrm{s} = \omega_\mathrm{c} - \delta\omega$, while also creating an additional idler mode at $\omega_\mathrm{i} = \omega_\mathrm{c} + \delta\omega$.

To drive the three-wave mixing process, a pump tone, operating at double the circuit's resonance frequency $\omega_\mathrm{P} = 2\omega_\mathrm{c}$, is inductively coupled to the JPA and induces periodic modulations in the flux threading the SQUID loop. This, in turn, modulates the inductance of the SQUID and, with it, the resonance frequency ω_c of the JPA circuit. This parametric modulation leads to the three-wave mixing process that is illustrated in Fig. 2.11. An incoming signal mode at the frequency $\omega_\mathrm{s} = \omega_\mathrm{P}/2 - \delta\omega$, with a detuning $\delta\omega$, is amplified, while an idler mode at frequency $\omega_\mathrm{i} = \omega_\mathrm{P}/2 + \delta\omega$ is created.

Flux-pumped JPAs offer two distinct modes of operation: If the input signal frequency $\omega_\mathrm{s} = \omega_\mathrm{P}/2 - \delta\omega$ has a non-zero offset from half the pump frequency, $\delta\omega \neq 0$, the JPA acts as a *phase-preserving* amplifier that equally amplifies both signal quadratures. This mode inherently introduces a minimum noise equivalent to half a noise photon to the input signal, a property that is called the standard quantum limit for phase-insensitive amplification [74, 118]. Intuitively, the minimum added noise can be understood to be a consequence of the quantum fluctuations at the idler frequency being mixed into the signal mode during amplification. Conversely, if the signal frequency aligns with half the pump frequency ($\omega_\mathrm{s} = \omega_\mathrm{P}/2$), signal and idler modes overlap ($\omega_\mathrm{s} = \omega_\mathrm{i}$) and interfere with a fixed phase relation. This condition enables *phase-sensitive* amplification, where one quadrature experiences amplification, while the other quadrature is deamplified, depending on the relative phase between the input signal and the pump tone. By exploiting this feature, squeezed states of light can be generated [119] and noise performance below the standard quantum limit can be achieved [120].

For a quantitative treatment of the parametric amplification process of flux-driven JPAs based on input-output theory [111] we refer the interested reader to Ref. [118].

Four-wave mixing: Current-driven JPA Modulating the flux threading a SQUID loop is not the only way to modulate the inductance of a JPA. A similar feat can also be achieved by exploiting the inherent current dependency of a Josephson junction: If the current I passing through a Josephson junction is significantly less than its critical current I_{c0}, the junction's inductance can be approximated as $L \approx L_J \left[1 + \frac{1}{6}\left(I(t)/I_{c0}\right)^2\right]$ [102]. Introducing an AC current into the junction through a microwave pump therefore directly induces a time-dependent impedance variation, as required for parametric amplification. Owing to the inductance's quadratic dependence on the current $I^2(t)$, i.e. the symmetric energy potential of the junction, this method can be used to implement a four-wave mixing process. Notably, this amplification protocol can be implemented irrespective of whether a single Josephson junction or a SQUID is used as the non-linear element, allowing our established FTR design to be used in this current-driven JPA configuration.

The four-wave mixing process is illustrated in Fig. 2.12**a**. A strong classical pump tone ω_P is applied near the resonance ω_c of the JPA, and combined with the to-be-amplified signal ω_s. The pump drives the JPA into a non-linear response regime close to the bifurcation point (cf. Sec. 2.3.4), making it exceptionally sensitive to small perturbations. The JPA therefore translates small input fluctuations, such as those introduced by a weak quantum signal, to large changes in the output field [102]. Aside from the input signal at ω_s, also the frequency components at the idler frequency ω_i are amplified, leading to added noise limited by the standard quantum limit as in the case of *phase-preserving* three-wave mixing discussed above. A comprehensive and quantitative treatment of the four-wave mixing process in current-driven JPAs is found in Ref. [102].

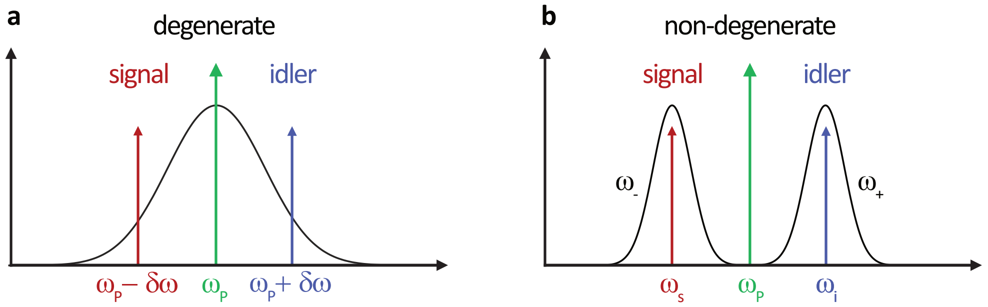

Fig. 2.12.: Degenerate and non-degenerate four-wave mixing processes. Schematic illustration of the relevant frequencies for the parametric amplification process using four-wave mixing. We distinguish degenerate (**a**) and non-degenerate (**b**) cases. In **a**, a strong pump tone is applied close to the JPA resonance frequency $\omega_\mathrm{P} \approx \omega_\mathrm{C}$. This enables a four-wave mixing process that amplifies the input signal at $\omega_\mathrm{S} = \omega_\mathrm{P} - \delta\omega$, while also creating an additional idler mode at $\omega_\mathrm{i} = \omega_\mathrm{P} + \delta\omega$. In **b**, instead of a single resonator mode, a pair of hybridized modes, ω_+ and ω_-, is used. The pump is applied approximately in between the hybridized modes, $\omega_\mathrm{P} \approx (\omega_+ + \omega_-)/2$. As a result, the signal (ω_S) and idler (ω_S) fields of the four-wave mixing process occupy separate resonator modes.

The final concept to be discussed in the classification of parametric amplifiers is *degeneracy*: Amplification processes can be categorized as either non-degenerate or degenerate based on the relationship between the signal and idler fields generated during the mixing process [116]. Degenerate amplification occurs when the signal and idler fields occupy the same physical mode[3]. Both the three- and four-wave mixing examples discussed earlier fall under this category, as they utilize a single mode for amplification. This approach is widely employed in various applications, such as fast qubit state readout [121] and quantum feedback protocols [122]. Conversely, non-degenerate amplification processes separate the amplified signal from the generated idler mode. This separation offers distinct advantages, including effective signal amplification while allowing easy exclusion of the idler from the detection band, simplifying the signal processing chain.

To illustrate non-degenerate amplification, consider the non-degenerate four-wave mixing process depicted in Fig. 2.12**b**. Instead of utilizing a single resonator mode, the amplifier here is designed to feature a pair of hybridized modes (a dimer), denoted as ω_+ and ω_-. By applying the pump tone ω_P in between these two modes, it becomes possible to amplify a signal at ω_s and read it out at one of the hybridized modes, while the idler signal ω_i occupies the second hybridized mode and can be processed separately.

---

[3] Unfortunately, there is no consistent definition of degeneracy in the literature w.r.t. parametric amplification. We follow the convention of Ref. [116] and use the term *non-degenerate* strictly for physically separated modes, not merely for a finite frequency difference between ω_i and ω_S.

In the context of JPAs, a dimer amplifier implementing a non-degenerate four-wave mixing process can be constructed using capacitively shunted arrays of Josephson junctions [123–125]. In this work, we utilize such a device for our experiments in Chap. 5 and present a detailed characterization of its performance in Sec. 4.4.

2.5 Optomechanics with superconducting circuits

The field of optomechanics is focused on the investigation of the interaction between light (or electromagnetic radiation, more generally) and mechanical vibrations [22]. In this section, we first want to introduce the most general Hamiltonian that captures the optomechanical interaction. Subsequently, we explore the specific, flux-mediated coupling that lies at the heart of the electromechanical devices investigated in this work and derive a system-specific Hamiltonian that also incorporates the Kerr non-linearity of the flux-tuneable microwave resonator.

2.5.1 The general optomechanical interaction

For the general model, we simplify the approach to the interaction by considering a singular optical[4] mode and a singular mechanical normal mode. In most situations, due to the linearity of the dynamics and the independent evolution of the normal modes, this model serves as an adequate representation. Formally, the uncoupled optical and mechanical modes are each described by a general quantum harmonic oscillator Hamiltonian (cf. Sec. 2.1)

$$\hat{H} = \hbar\omega_c\hat{a}^\dagger\hat{a} + \hbar\Omega_\mathrm{m}\hat{b}^\dagger\hat{b}\,, \tag{2.88}$$

where $\hat{H}$ represents the energy operator, ω_c and Ω_m are the frequencies of the optical and mechanical modes, respectively, and we omit the constant $1/2$ energy offsets due to zero-point fluctuations. The optomechanical interaction is often realized as a parametric modulation of the resonance frequency of one oscillator depending on the quadrature amplitude (e.g. a displacement) of the other. A common scenario to illustrate this is an optical Fabry-Perot cavity with

---

[4] In optomechanics, the electromagnetic field is generally referred to as *optical*, irrespective of its actual frequency range. As such, the term encompasses both optical and microwave fields.

one stationary mirror and a movable one. The moving mirror's oscillation at frequency Ω_m modulates the cavity frequency ω_c, given the dependency of the resonance condition on the distance between the two mirrors. We can write this dependency in a general form [126]

$$\omega_\mathrm{c}(x) = \omega_\mathrm{c} + x\frac{\partial \omega_\mathrm{c}}{\partial x} + x^2\frac{\partial^2 \omega_\mathrm{c}}{\partial^2 x} + \dots . \tag{2.89}$$

In a majority of experimental setups, it is sufficient to focus on the linear term in the expansion of the cavity resonance frequency and we can define $G = -\partial\omega_\mathrm{c}/\partial x$ as the optical frequency shift per displacement or simply the *cavity responsivity*. The correction to the cavity energy due to the optomechanical interaction is then given by [126]

$$\hbar\omega_\mathrm{c}(x)\hat{a}^\dagger\hat{a} = \hbar(\omega_\mathrm{c} - G\hat{x})\hat{a}^\dagger\hat{a}\,, \tag{2.90}$$

where $\hat{x} = x_\mathrm{zpf}(\hat{b}+\hat{b}^\dagger)$ is the displacement of the moving mirror, with the already introduced zero-point motion x_zpf. At this point it should be noted that the mass m in the definition of x_zpf is not generally equivalent to the real mass of the oscillator (e.g. the mirror). Instead, we replace m by an effective mass m_eff, so $x_\mathrm{zpf} = \sqrt{\hbar/2m_\mathrm{eff}\Omega_\mathrm{m}}$. The effective mass takes into account the actual mode shape of the oscillator in question and is suitably normalized depending on the definition of the displacement $x(t)$ in the specific system. We discuss m_eff of a nanostring oscillator in Sec. 2.2.1 and an in-depth treatment of effective mass in the context of optomechanics is found in Ref. [127]. The system Hamiltonian which combines the uncoupled terms with the interaction reads [22]

$$\hat{H} = \hbar\omega_0\hat{a}^\dagger\hat{a} + \hbar\Omega_0\hat{b}^\dagger\hat{b} - \hbar g_0\hat{a}^\dagger\hat{a}(\hat{b} + \hat{b}^\dagger)\,. \tag{2.91}$$

In this equation, $g_0 = Gx_\mathrm{zpf}$ is defined as the **single-photon coupling strength**. It quantifies the rate at which photons from the cavity are converted into phonons in the mechanical mode – and vice versa. Notably, while the specific definition of g_0 varies based on the system in question, the interaction Hamiltonian remains consistent, making this form generally applicable to describe a variety of systems at largely different mass- and frequency scales.

Furthermore, the relationship between the parameters g_0, Ω_m, Γ_m and the cavity loss rate κ has a profound impact on the physical phenomena that can be explored with any specific optomechanical device. A comprehensive review on the different parameter regimes is found in Ref. [22], but we want to emphasize three distinctive regimes relevant to this work:

Resolved-sideband regime In the case that the cavity loss rate (or linewidth) is significantly smaller than the mechanical frequency ($\kappa \ll \Omega_\mathrm{m}$) the so-called *resolved-sideband* condition is fulfilled. Being in the resolved-sideband regime is often beneficial for experiments. One of the key advantages is that it allows for efficient cooling of the mechanical oscillator using sideband cooling, as we will demonstrate in Sec. 5.3. Using this technique, photons can be used to extract energy from the mechanical oscillator, potentially cooling it down to its quantum ground state [128, 129]. In the opposite case of the unresolved-sideband regime ($\kappa > \Omega_\mathrm{m}$), cooling to the quantum ground state is generally not possible using standard sideband cooling techniques [22].

Quantum cooperativity One can define the quantum cooperativity as

$$C_\mathrm{qu} = 4g_0^2/\kappa\Gamma_\mathrm{m} \cdot \bar{n}_\mathrm{c}/\bar{n}_\mathrm{ph}^\mathrm{th}\,, \tag{2.92}$$

using the photon occupation of the cavity $\bar{n}_\mathrm{c}$ and the thermal occupation of the mechanical mode $\bar{n}_\mathrm{ph}^\mathrm{th} = [\exp(\hbar\Omega_\mathrm{m}/k_\mathrm{B}T) - 1]^{-1}$. It indicates that the optomechanical interaction strength is greater than the combined losses in both the optical and mechanical modes. With $C_\mathrm{qu} > 1$ a coherent transfer of quantum states between the optical and mechanical system becomes possible.

Single-photon strong coupling regime The *single-photon strong coupling* regime is defined by $g_0 > \kappa$, i.e. the single-photon coupling rate exceeding the loss rate of the cavity. In this regime, non-linear quantum effects are predicted to become observable [22], including the resolution of individual photons in a photon stream (*granularity*) [25] and preparation of non-classical mechanical states [43]. Experiments realizing the optomechanical interaction in clouds of ultracold atoms have achieved coupling rates on the verge of this regime [25, 130], but a final demonstration of single-photon strong coupling remains elusive and is one of the long-term goals pursued in this work.

2.5.2 Flux-mediated inductive coupling

Having established a general description of the optomechanical interaction, we now proceed to focus on the specific implementation studied in this work: In our electromechanical system, the *optical* component is realized using an electrical, LC oscillator operating at microwave frequencies. In particular, we

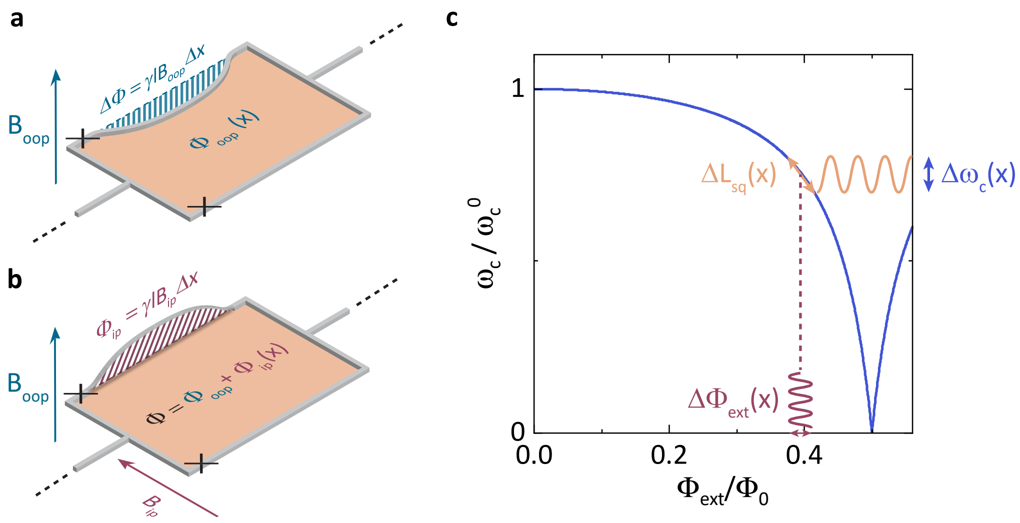

Fig. 2.13.: Flux-mediated inductive coupling with SQUIDs. **a** and **b** show a schematic illustration of a mechanically compliant SQUID, where a part of the loop (left) is released from the substrate and forms a mechanical string oscillator of length l. **a** shows how in an external out-of-plane magnetic field B_{oop}, the in-plane displacement Δx of the oscillating loop section leads to a reduction of the SQUID loop area (dashed blue) and a corresponding flux change $\Delta\Phi = \gamma l B_{\mathrm{oop}} \Delta x$. **b** illustrates the extended scenario including the magnetic field's in-plane component B_{ip}. Here, the out-of-plane displacement of the oscillator introduces an additional in-plane contribution to the flux $\Phi_{\mathrm{ip}} = \gamma l B_{\mathrm{ip}} \Delta x$. The total external flux is then given by $\Phi_{\mathrm{ext}} = \Phi_{\mathrm{oop}} + \Phi_{\mathrm{ip}}$. **c** The blue curve shows the normalized resonance frequency ω_{c} of the FTR as a function of Φ_{ext}. The colored lines graphically illustrate the flux-mediated coupling, which translates the flux modulation $\Delta\Phi$ to a modulation of the SQUID's Josephson inductance ΔL_{sq} and a corresponding modulation of the resonance frequency $\Delta\omega_{\mathrm{c}}$.

employ a frequency tuneable resonator (FTR) based on a SQUID-terminated CPW resonator. We extensively discussed this type of device in Sec. 2.3 and showed that its eigenfrequency ω_{c} depends on the external flux penetrating the attached SQUID, via the latter's non-linear, flux-dependent inductance.

To realize an inductively coupled optomechanical interaction, we follow the theoretical proposal in Refs. [35] and [131] and incorporate a mechanically compliant element into the SQUID by releasing a section of the superconducting loop from the substrate, forming a nanostring oscillator. The arrangement is illustrated in Fig. 2.13.

Coupling mechanism We begin by considering the mechanically compliant SQUID in the presence of an arbitrary magnetic field $\vec{B}_{\mathrm{ext}}$. To understand the geometric effects at play, it is helpful to decompose the magnetic field vector into orthogonal field components $\vec{B}_{\mathrm{ext}} = \vec{B}_{\mathrm{oop}} + \vec{B}_{\mathrm{ip}}$, where we will omit arrows on the vectors from now on. The out-of-plane component B_{oop} is orientied normal to the plane of the SQUID loop, as illustrated in Fig. 2.13**a**. In the figure, we can see how a displacement of the oscillating part of the SQUID in the in-plane direction, i.e. perpendicular to B_{oop}, leads to an effective reduction of the SQUID's loop area by the dashed blue area. Since B_{oop} contributes to the total flux threading the SQUID proportional to the loop area A (orange shading), we can define the flux contribution of the out-of-plane field component as $\Phi_{\mathrm{oop}} = A \cdot B_{\mathrm{oop}}$. Conversely, a change in the loop area A through the displacement of the nanostring also changes the total external flux.

In the same vein, we now focus on the effect of the in-plane field component B_{ip}. Without considering the mechanically compliant nanostring as part of the SQUID, B_{ip} is oriented entirely parallel to the area spanned by the SQUID loop and no flux contribution can be associated with the in-plane field component B_{ip}. However, as we have discussed in Sec. 2.2.1, nanostrings exhibit both an out-of-plane and an in-plane mode at the same time. Therefore, we also need to consider the effect of a non-zero out-of-plane displacement of the nanostring. This case is illustrated in Fig. 2.13**b**: The dynamic out-of-plane displacement of the nanostring opens up an area A_{ip} (red shading) perpendicular to B_{ip} that gives rise to an additional in-plane flux contribution $\Phi_{\mathrm{ip}} = B_{\mathrm{ip}} \cdot A_{\mathrm{ip}}$. The out-of-plane flux contribution Φ_{oop}, as discussed previously, remains unchanged as long as we assume perfectly orthogonal field components. Therefore, the total flux[5] determining the Josephson inductance of the SQUID will have contributions from both field directions

$$\Phi_{\mathrm{ext}} = \Phi_{\mathrm{oop}} + \Phi_{\mathrm{ip}} = B_{\mathrm{oop}} \cdot A_{\mathrm{oop}} + B_{\mathrm{ip}} \cdot A_{\mathrm{ip}} \,. \tag{2.93}$$

Any modulation to this flux by the periodic motion of the mechanical oscillator will be translated by the SQUID into a modulation of its Josephson inductance and therefore affect the resonance frequency of the microwave resonator. This flux-to-frequency modulation is the essence of the flux-mediated coupling mechanism and is schematically illustrated in Fig. 2.13**c**.

Flux-mediated single-photon coupling rate Now, we want to find an analytical expression for the flux-mediated coupling. For this derivation, we work with a general external magnetic field B_{ext} and the corresponding perpendicular oscillator displacement $x(t)$. Based on our previous discussion and Fig. 2.13, it will be applicable to both the out-of-plane case (**a**) with $B_{\mathrm{ext}} = B_{\mathrm{oop}}$ and x the in-

---

[5] As discussed in previous sections, a finite loop inductance of the SQUID will lead to an effective reduction of the total flux due to screening effects. We neglect this effect for the discussion of the coupling mechanism, since flux changes due to the mechanical oscillation are small and the associated screening effects negligible.

plane mode's displacement, as well as the in-plane case (**b**) with $B_{\mathrm{ext}} = B_{\mathrm{ip}}$ and x being the out-of-plane mode's displacement.
We follow the same procedure as in the derivation of the general optomechanical interaction and start with a description of the FTR resonance frequency

$$\omega_{\mathrm{c}}(x) = \omega_{\mathrm{c}}(\Phi_{\mathrm{ext}}) + \partial_x \omega_{\mathrm{c}}(x)|_{x=0}\, x + \ldots \tag{2.94}$$

Here, we have used the fact that the nanostrings' displacement and the change to the flux are small to express ω_{c} by a steady-state value $\omega_{\mathrm{c}}(\Phi(x = 0)) = \omega_{\mathrm{c}}(\Phi_{\mathrm{ext}})$ with the string at $x = 0$ and a linearized perturbation caused by its displacement. The dependency of the change in flux to the displacement of the nanostring can be readily identified by studying the geometry illustrated in Fig. 2.13**a**. It becomes clear that the change in area, and therefore flux, is directly defined by the geometric properties of the displaced nanostring via $\Delta\Phi = B_{\mathrm{ext}}\Delta A = B_{\mathrm{ext}}\gamma l \Delta x$, where l is the length of the string and γ is a geometric factor that accounts for the string's non-uniform displacement along its length [132]. This leads to a displacement dependent frequency shift

$$\partial_x \omega_{\mathrm{c}}(x) = \frac{\partial \omega_{\mathrm{c}}}{\partial \Phi}\frac{\partial \Phi}{\partial x} = \frac{\partial \omega_{\mathrm{c}}}{\partial \Phi}\gamma l B_{\mathrm{ext}}\,. \tag{2.95}$$

Substitution of Eq. (2.95) into Eq. (2.94) and comparison to the general expression in Eq. (2.90) allows us to identify the single-photon coupling strength in the case of flux-mediated coupling

$$g_0 = \partial_\Phi \omega_{\mathrm{c}}(\Phi_{\mathrm{ext}}) B_{\mathrm{ext}} \gamma l x_{\mathrm{zpf}}\,. \tag{2.96}$$

While this derivation might appear rather simplistic, more meticulous treatments arrive at the same result [35, 38, 131].

It is worth emphasizing that the derivative $\partial\omega_{\mathrm{c}}/\partial\Phi$ in the expressions above is the so-called *flux responsivity* of the FTR and corresponds to the slope of its flux-tuning curve (cf. Eq. (2.61) and Fig. 2.9). It is nicely visible in Fig. 2.13**c** that the slope of the curve varies considerably with the external flux between 0 (for $\Phi_{\mathrm{ext}} = 0$) and very large values (for $\Phi_{\mathrm{ext}} \to 0.5$). This observation in combination with Eq. (2.96) makes clear that g_0 can be switched off or adjusted over a large parameter range *in-situ* using the control parameters $\partial\omega_{\mathrm{c}}/\partial\Phi$ and B_{ext}. This capability is one of the main perks of this implementation of flux-mediated optomechanical coupling.

2.5.3 Non-linear optomechanics

In the derivation of the optomechanical interaction Hamiltonian in Sec. 2.5.1, we have treated both the microwave (optical) cavity and the mechanical oscillator as linear harmonic oscillators. However, we have seen in Sec. 2.3 that the inclusion of the SQUID into the circuit of the FTR leads to the appearance of Kerr-type non-linear terms in the system Hamiltonian (cf. Eq. (2.75)) and have discussed the impact of these terms on the FTRs response to an external drive in Sec. 2.3.4. In this section, we build upon these results and extend them by considering the coupling to the mechanical component to develop a suitable description for the complete optomechanical system. The presented derivation closely follows Refs. [131, 133] and, if not explicitly provided, variable definitions are identical to Sec. 2.3.4.

Effective Kerr Hamiltonian To derive the effective system Hamiltonian including the Kerr non-linearity, we combine the general optomechanical Hamiltonian Eq. (2.91) with the non-linear correction term of Eq. (2.75):

$$\hat{H} = \hat{H}_0 - \hbar\frac{\mathcal{K}}{2}\hat{a}^\dagger\hat{a}^\dagger\hat{a}\hat{a} + \hbar g_0\hat{a}^\dagger\hat{a}(\hat{b} + \hat{b}^\dagger) + \hat{H}_\mathrm{p}\,, \tag{2.97}$$

where we have collapsed the linear harmonic oscillator terms into the free Hamiltonian

$$\hat{H}_0 = \hbar\omega_c\hat{a}^\dagger\hat{a} + \hbar\Omega_\mathrm{m}\hat{b}^\dagger\hat{b}\,, \tag{2.98}$$

and have included the same coherent, external drive $\hat{H}_\mathrm{p}$ as introduced in Sec. 2.3.4. Under the assumption of a strong drive, we again perform the displacement transformation $\hat{a} = \alpha e^{-i\omega_p t} + \hat{d}$ with $\alpha = \langle\hat{a}\rangle$ and linearize the Hamiltonian in the rotating frame [133]

$$\hat{H}_\mathrm{eff} = -\tilde{\Delta}\hat{d}^\dagger\hat{d} + \Omega_\mathrm{m}\hat{b}^\dagger\hat{b} - \frac{1}{2}\left[\Lambda\hat{d}^\dagger\hat{d}^\dagger + \Lambda^*\hat{d}\hat{d}\right] + \left(g\hat{d}^\dagger + g^*\hat{d}\right)\left(\hat{b} + \hat{b}^\dagger\right)\,, \tag{2.99}$$

where we have re-used Λ and $\tilde{\Delta}$ as introduced in Eq. (2.77) and additionally defined the photon-enhanced optomechanical coupling strength $g = |\alpha|g_0e^{i\phi_\mathrm{G}}$.

Effects of the Kerr-non-linearity Using the input-output theory [111], we examine the classical part of the system, where $\hat{a} = \alpha$. Staying in the rotating frame around the pump frequency ω_p, the equation of motion is derived as:

$$\frac{d}{dt}\alpha = \left(i\Delta - \frac{\kappa}{2}\right)\alpha - i\mathcal{K}|\alpha|^2\alpha - i\sqrt{2}g_0\langle\hat{q}\rangle\alpha - \sqrt{\frac{\kappa_\mathrm{ext}}{2}}\alpha_\mathrm{in}\,, \tag{2.100}$$

where $\langle\hat{q}\rangle = (\hat{b} + \hat{b}^\dagger)/\sqrt{2}$ denotes the position quadrature of the mechanical resonator. Additionally, we can make use of the classical dynamics of the mechanical mode, written as

$$\frac{d}{dt}\langle\hat{q}\rangle = \Omega_\mathrm{m}\langle\hat{p}\rangle - \frac{\Gamma_\mathrm{m}}{2}\langle\hat{q}\rangle \tag{2.101}$$

$$\frac{d}{dt}\langle\hat{p}\rangle = -\Omega_\mathrm{m}\langle\hat{q}\rangle - \frac{\Gamma_\mathrm{m}}{2}\langle\hat{p}\rangle - \sqrt{2}g_0|\alpha|^2\,, \tag{2.102}$$

where $\hat{p} = i(\hat{b}^\dagger - \hat{b})/\sqrt{2}$ is the momentum quadrature. Note that in the above equations, the sign of the term proportional to g_0 is a matter of convention. In fact, in the flux-mediated coupling architecture studied in this work, both a positive and a negative g_0 can be realized by operating at either the left lobe ($\partial\omega_\mathrm{c}/\partial\Phi > 0$) or the right lobe ($\partial\omega_\mathrm{c}/\partial\Phi < 0$) of the flux tuning curve.

Given that the mechanical resonator has only a weak influence on the cavity field, its long-time limit offers the steady-state solution

$$\langle\hat{q}\rangle_s = -\frac{\sqrt{2}g_0\Omega_\mathrm{m}|\alpha|^2}{\Omega_\mathrm{m}^2 + \Gamma_\mathrm{m}^2/4}\,. \tag{2.103}$$

Incorporating this result back into Eq. (2.100) reveals a dependence $\propto |\alpha|^2\alpha$. Intriguingly, this mirrors the Kerr-term, allowing us to rewrite the equation of motion with an effective Kerr that is modified due to the mechanical interaction:

$$\frac{d}{dt}\alpha = \left(i\Delta - \frac{\kappa}{2}\right)\alpha - i\mathcal{K}_\mathrm{eff}\alpha|\alpha|^2 - \sqrt{\frac{\kappa_\mathrm{ext}}{2}}\alpha_\mathrm{in} \tag{2.104}$$

Here, the effective Kerr constant, $\mathcal{K}_\mathrm{eff}$, is defined as:

$$\mathcal{K}_\mathrm{eff} \equiv \mathcal{K} - \frac{2g_0^2\Omega_\mathrm{m}}{\Omega_\mathrm{m}^2 + \Gamma_\mathrm{m}^2/4} \tag{2.105}$$

In the limit of high-Q mechanical oscillators ($\Omega_\mathrm{m} \gg \Gamma_\mathrm{m}$), the mechanical impact on the Kerr is proportional to g_0^2/Ω_m. This is typically a negligible correction compared to the self-Kerr of non-linear cavities. However, an interesting implication of this result is that even a linear optomechanical system with $\mathcal{K} = 0$ will have a finite Kerr non-linearity $\mathcal{K}_{\text{eff}}$ arising from the coupling to the mechanical resonator.

Finally, multiplying the steady-state solution with its complex conjugate yields for the average photon occupation $\bar{n}_{\text{c}}$:

$$\bar{n}_{\text{c}} \left[(-\Delta + \mathcal{K}_{\text{eff}} \bar{n}_{\text{c}})^2 + \left(\frac{\kappa}{2} \right)^2 \right] = \frac{\kappa_{\text{ext}}}{2} \bar{n}_{\text{in}} \,. \tag{2.106}$$

Notably, the above expression is virtually identical to Eq. (2.80), save for the correction to the non-linearity $\mathcal{K}_{\text{eff}}$, which is negligible for most devices, as discussed above. Based on this quasi-equality, we can immediately conclude that the response of the non-linear resonator and its discussion in Sec. 2.3.4 remain qualitatively valid for the optomechanical system. In particular, this also applies to the analytical expressions for the onset of bifurcation (Eqs. (2.83)ff.), when modified with the effective Kerr factor.

2.6 Quantum acoustics with surface acoustic waves

Surface Acoustic Waves (SAWs) are mechanical waves propagating along the surfaces of solid materials. The first attempt of theoretical description dates back to 1885 when the concept was proposed by Lord Rayleigh [134]. SAWs occur naturally as seismic events such as earthquakes. However, it is their widespread application in signal processing for telecommunication that make them an integral component of modern consumer technology [135, 136]. This section aims to provide a compact overview of the theoretical framework for their description and the working principle of essential components. We will also discuss the behavior of SAWs on more complex, multi-layer substrates, providing theoretical background to the experimental study in Chap. 6.

2.6.1 Introduction to SAWs

One of the key advantages of SAW-based technology stems from the slow propagation speed of sound compared to electromagnetic signals. To put it in perspective, compared to light, SAW wave packets travel roughly five orders of magnitude slower. This results in a substantial reduction in wavelength for a given oscillation frequency, allowing for the creation of resonant structures on a considerably smaller on-chip footprint - a crucial advantage in modern integrated circuit design. The integration of SAW components into electric circuits is made possible due to the piezoelectric effect. Piezoelectric materials, when strained, exhibit a net polarization due to the asymmetric configuration of their electric dipoles. Conversely, introducing a voltage to these materials triggers mechanical deformation. This phenomenon is particularly apparent in insulating materials whose crystal structures do not adhere to inversion symmetry.

Formally, in a piezoelectric material, the mechanical stress tensor **T** relates to the strain **S** via Hooke's law and the electric field $\vec{E}$ as [137]

$$\mathbf{T} = \mathbf{cS} - \mathbf{e}\vec{E}\,, \tag{2.107}$$

where **c** is the elastic stiffness tensor and **e** is the piezoelectric tensor. Additionally, the relation for the electric displacement field $\vec{D}$ differs from the non-piezoelectric scenario and is given by:

$$\vec{D} = \mathbf{cS} + \varepsilon\vec{E}\,. \tag{2.108}$$

Here, ε represents the electric permittivity, which is assumed isotropic. It's worth noting that many tensor elements in **c** and **e** nullify for a majority of solids due to symmetry reasons.
Defining the displacement field $\vec{u}$ in relation to the strain and the coordinates $x = (x_1, x_2, x_3)$ via

$$S_{ij} = \frac{\partial u_i}{\partial x_j}\,, \quad i, k = 1, 2, 3\,, \tag{2.109}$$

we can find SAW modes as the solutions to the elastic wave equation

$$\nabla \cdot \mathbf{T} = \rho \frac{\partial^2 \vec{u}}{\partial t^2}\,, \tag{2.110}$$

requiring they also fulfill Eqs. (2.107) and (2.108). These modes decay into the bulk on a length scale of the SAW wavelength λ and meet the stress-free boundary conditions $T_{iz}|_{z\to-\infty} = 0$.

The resulting wave solutions can exhibit a range of characteristic displacement and propagation profiles and are categorized accordingly. The most significant type of wave for quantum acoustics is the *Rayleigh wave* [134], which we almost exclusively focus on in this work. Rayleigh waves are a blend of longitudinal and transverse acoustic modes, causing particles to move elliptically in planes perpendicular to the surface but parallel to the propagation direction. Other types of waves include *shear, shear-horizontal, Love* and *Lamb* waves. For details and derivations of the various types of surface waves, we refer the reader to Ref. [138–140].

2.6.2 SAWs on multi-layer substrates

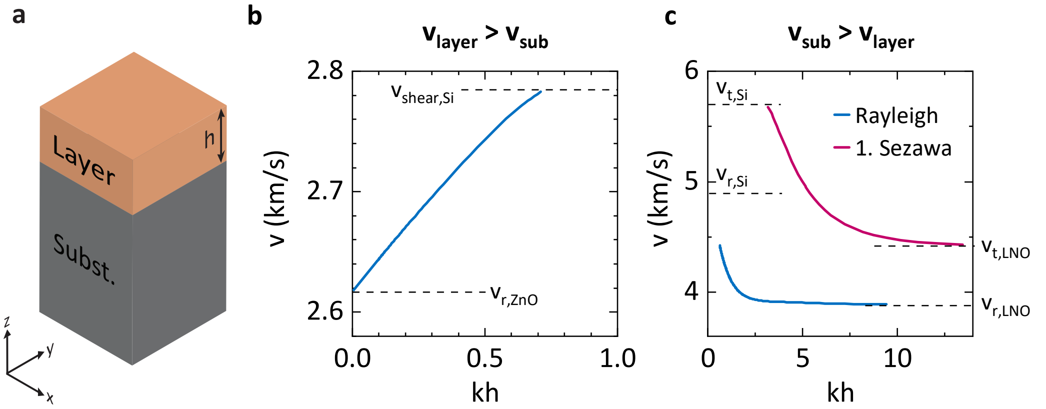

Fig. 2.14.: **SAW phase velocities in a generalized two-layer system of variable thickness. a** Schematic illustration of a generalized two-layer system with an infinitely thick substrate (grey) and an additional top layer of thickness h. **b** Rayleigh phase velocity as a function of wavenumber-thickness-product kh in the case of $v_{\text{layer}} > v_{\text{sub}}$, where we chose Silicon as the layer and ZnO as the substrate for the simulation. v_{r} of the combined system increases with kh until it reaches a cutoff at the layer shear velocity. **c** Rayleigh and Sezawa phase velocities as a function of kh in the case of $v_{\text{sub}} > v_{\text{layer}}$, simulated using Silicon as a substrate and Lithium Niobate (LNO) as the layer. v_{r} of the Rayleigh mode decreases from the substrate value with kh until it becomes asymptotic to the layer velocity. Additionally, higher order modes of *Sezawa*-type appear (see main text).

In most cases, the theory of SAWs is discussed with the assumption of a single-crystalline, piezoelectric and infinitely extended bulk material. However, with the availability of modern nanofabrication techniques, which allow the deposition and patterning of nanometer-scale films and features, it is worthwhile to explore the behavior of SAWs which propagate in or are in contact with thin films. This is especially of interest for the integration of SAW components into electrical circuits, in particular superconducting quantum circuits, where thin films of superconducting metals are an essential building block. In the following, we want to explore some of the properties of SAWs on thin film materials. We will limit the discussion to the results most relevant to the experiments in this study. A comprehensive treatment of SAWs in thin film materials is found in Ref. [137].

For our discussion, we imagine a generalized two-layer material, consisting of a thin layer of variable thickness h on top of a substrate material with quasi-infinite thickness (i.e. $\gg \lambda$), as illustrated in Fig. 2.14**a**. Finding solutions for surface acoustic waves on such multi-layer materials is generally a complex task, but can be accomplished using the *partial waves method* [138] or the *transfer matrix method* [141]. In our case, we use an alternative approach and model the system of interest in a software for Finite Element Method (FEM) simulations [142]. The FEM simulations have the advantage of simultaneously providing visual access to the resulting displacement profiles, which helps to categorize the solutions into the different wave types. A detailed description of our methodology for the FEM simulations is found in Ref. [143].

It appears intuitive that the relevant parameters for the behavior of SAWs in multi layer substrates are the characteristic phonon propagation velocities of the substrate (v_{sub}) and layer (v_{layer}). In our generalized two-layer system, we can find two distinct parameter regimes based on the relationship of the two velocities:

Scenario 1: $v_{\mathrm{layer}} > v_{\mathrm{sub}}$ – Stiffening If the sound velocity in the layer exceeds the one in the substrate, the addition of the layer leads to a *stiffening* of the Rayleigh mode in the combined system. To illustrate this effect, we chose a system of Silicon ($v_{\mathrm{r,Si}} = 4.89\,\mathrm{km/s}$) on ZnO ($v_{\mathrm{r,ZnO}} = 2.65\,\mathrm{km/s}$) [138]. We then simulate the phase velocity of the Rayleigh mode v_{r} as a function of the layer thickness w.r.t. the SAW wavelength, which we express by the product of wavenumber and thickness, $kh = 2\pi h/\lambda$. The results are shown in Fig. 2.14**b**. For small values of kh, i.e. a very thin layer, the phase velocity of the system corresponds to the velocity of the substrate. It then increases monotonically with kh until the shear-wave velocity of the layer is reached. Above this point, the Rayleigh mode in the system ceases to exist. In fact, it can be shown that for this type of two-layer system only a single Rayleigh mode can propagate, and only in this particular range of kh values. No other Rayleigh type solutions exist [138].

Scenario 2: $v_{\mathrm{sub}} > v_{\mathrm{layer}}$ – Loading In the opposite scenario, where the substrate velocity exceeds the layer velocity, the substrate is *loaded* by the addition of the layer, leading to a decrease in effective phase velocity. We exemplify this behavior by simulating the kh dependent phase velocity for a system of Lithium Niobate (LNO, $v_{\mathrm{r,LNO}} = 3.98\,\mathrm{km/s}$) on Silicon ($v_{\mathrm{r,Si}} = 4.89\,\mathrm{km/s}$) and plot the results in Fig. 2.14**c**. In this case, the phase velocity again approaches the substrate velocity for $kh \rightarrow 0$ and decreases with kh until $kh \gg 1$, where it becomes asymptotic with the Rayleigh velocity of the layer. This is intuitive since for large layer thicknesses compared to the SAW wavelength, the substrate ceases to play a role for the waves propagating close to the surface. Another relevant feature in this type of systems is the appearance of higher order Rayleigh-like modes for large values of kh, which are called *Sezawa* modes and are unique to multi-layer materials. An infinite number of these modes appear with increasing kh and all of them have a low frequency cutoff at the transversal velocity of the substrate $v_{\mathrm{t,Si}}$ and become asymptotic to the transversal velocity of the layer for large values of kh [138].

From the perspective of an experimentalist working with SAWs on multi-layer systems, these results emphasize that the thickness and frequency-dependent effective phase velocity of the combined system needs to be considered in the design stage of the experiment. In particular, feature sizes or operating frequencies might have to be adapted and limits to the broadband operation kept in mind. However, the combination of materials with different properties as well as the option to deliberately adjust effective phase velocities also offer significant potential for creative experimental design.

2.6.3 SAW circuit elements

In the following, we will briefly introduce the most essential circuit elements which enable the controlled excitation, confinement and detection of SAWs and therefore form the basis for the integration of SAWs into electrical circuits.

Interdigital Transducers (IDT) The piezoelectric effect, by coupling potential differences (i.e. voltages) in the material to mechanical strain, provides a natural interface between electrical circuits and acoustic waves. The most important component to exploit this interaction is the *Interdigital Transducer* (IDT), which can act both as a transmitter and a receiver of SAW excitations. At its core, the IDT is made up of a periodic array of finger electrodes with width a and pitch (distance between electrodes) p, with alternating connections to a top and a bottom terminal, as illustrated in Fig. 2.15**a**. By applying a voltage between the terminals of the IDT, an electric field is generated between the adjacent electrodes. If the IDT is placed on top of a piezoelectric substrate, the piezoelec-

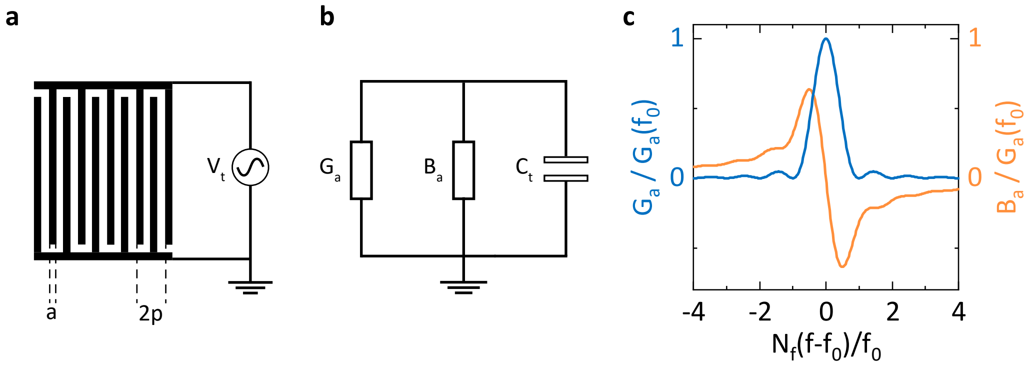

Fig. 2.15.: IDT geometry and equivalent circuit. a Layout of a simple IDT with regular electrodes with width a and pitch p and metallization ratio $\eta = a/p = 50\%$. The electrodes are wired to the top or bottom terminal in alternating order. An AC voltage V_t can be applied between the terminals to excite SAWs in a piezoelectric substrate. **b** Equivalent circuit diagram of the IDT, consisting of acoustic conductance G_a, susceptance B_a and a geometric capacitance C_t in parallel. **c** G_a and B_a as a function of excitation frequency f around the IDT resonance condition at $f_0 = v_\mathrm{p}/2p$, normalized to the conductance on resonance $G_\mathrm{a}(f_0)$.

tric effect translates this electric field to periodic strain at the substrate surface, which can lead to the excitation of SAWs. For the IDT to function most effectively, the periodicity $2p$ of its design must align with the wavelength of the SAW, in which case the elastic perturbations caused by each of the electrodes interfere constructively. This requirement on the SAW wavelength leads to a strong frequency dependence of the transduction process, with maximum efficiency reached for the so-called center frequency of the IDT $f_0 = v_\mathrm{p}/\lambda_\mathrm{SAW} = v_\mathrm{p}/2p$, with v_p being the phase velocity of the SAW in the substrate [139]. The effectiveness of the IDT is also intrinsically tied to the properties of the substrate on which the SAW moves. The strength of the interaction between the IDT and the wave is characterized by an electromechanical coupling coefficient, K^2. The coupling coefficient can be related to the difference in SAW velocity between propagation on a free surface, versus a surface covered by a metallic film via [139]

$$K^2 = 2\frac{v_\mathrm{free} - v_\mathrm{metal}}{v_\mathrm{free}} . \tag{2.111}$$

The underlying cause of this relationship is the piezoelectric effect itself, which translates the electric fields of a propagating SAW to a strain counter to the material strain, leading to additional stiffness in the material. This stiffening effect is reduced by a metallic film which can screen the electric fields, thereby also reducing the SAW velocity.

Formally, the operating mechanism of the IDT can be expressed through transmitter and receiver response functions, denoted as μ and g_m, respectively

[137]. When a SAW wave is emitted from the IDT, its electric potential, represented as ϕ_{out}, is defined by the equation $\phi_{\mathrm{out}} = \mu V_{\mathrm{t}}$, where V_{t} is the voltage applied across the transducer. Conversely, when a SAW is incident on the IDT, the current generated within the circuit is related to the SAW's potential ϕ_{in}, as described by $I = g_{\mathrm{m}}\phi_{\mathrm{in}}$.

To derive the overall IDT response, μ, the superposition of the individual response of every electrode needs to be considered. However, in a simplified picture, where we omit internal reflections within the IDT structure, it's possible to calculate the response of a single finger pair, the *element factor* μ_{e} and multiply it with an *array factor* A, which describes the position, polarity and periodicity of the electrodes. Notably, the array factor is the Fourier transform of the real space arrangement of the electrodes, enabling a very direct optimization process of the frequency response via layout adaption.

For the simplest IDT design with regular electrodes (p and a constant) and a metallization ratio of $\eta = a/p = 50\%$ (cf. Fig. 2.15**a**), the array factor can be simplified to

$$A = \sum_{n=1}^{N_{\mathrm{f}}} \exp\left(2\pi i n \frac{f}{f_0}\right) \approx N_{\mathrm{f}} \frac{\sin X}{X}\,, \tag{2.112}$$

with the number of IDT electrodes N_{f} and $X = N_{\mathrm{f}}\pi(f - f_0)/f_0$. Based on this array factor, the IDT has a sinc-like frequency dependence centered around f_0. It can also be shown that the *element factor* of a regular IDT finger pair with 50% metallization is $\mu_{\mathrm{e}} = 0.8iK^2$ [137], leading us to an expression of the transducer response function [53]

$$\mu = 0.8iK^2 N_{\mathrm{f}} \frac{\sin X}{X}\,. \tag{2.113}$$

For circuit design and especially implementation with more complex electrical circuits, the IDT can be conceptualized as a equivalent circuit model of an acoustic conductance G_{a}, susceptance B_{a} and a capacitance C_{t} in parallel, as shown in Fig. 2.15**b**. The IDT is then characterized by a complex admittance

$$Y_{\mathrm{a}} = G_{\mathrm{a}} + iB_{\mathrm{a}} + 2\pi i f C_{\mathrm{t}}\,. \tag{2.114}$$

Here, G_a depicts the conversion process from electrical current to the SAW and B_a is the Hilbert transform of G_a due to causality. Using Eq. (2.113), we can find approximate expressions for the acoustic parameters of the simple IDT

$$G_\mathrm{a} \approx G_{\mathrm{a},0} \left(\frac{\sin X}{X} \right)^2 \tag{2.115}$$

$$B_\mathrm{a} \approx G_{\mathrm{a},0} \frac{\sin 2X - 2X}{2X^2} \tag{2.116}$$

where the conductance at the IDT's resonance frequency is denoted as $G_{a,0} = G_\mathrm{a}(f_0) \approx \frac{2.87}{2} W N_\mathrm{f}^2 2\pi f_0 K^2$ [139]. The frequency dependencies of G_a and B_a are shown in Fig. 2.15**c**. On the other hand, C_t corresponds to the geometrically determined capacitance of the IDT and can be analytically calculated using conformal mapping techniques, for example using the formulas in Ref. [144].

From the circuit equivalent model we can also estimate the operating bandwidth of the transducer, by finding the 3 dB points where $G_\mathrm{a} = G_{\mathrm{a},0}/2$. The bandwidth Δf between these points is

$$\Delta f \approx \frac{0.9 f_0}{N_\mathrm{f}} \,. \tag{2.117}$$

Finally, for maximally efficient signal conversion the transducer impedance needs to be matched to the connected electrical transmission lines impedance. Assuming the acoustic contributions G_a and B_a are small compared to the capacitance C_t, we can write the relevant acoustic resistance as [139]

$$R_\mathrm{a}(f_0) = \frac{G_{\mathrm{a},0}}{(2\pi f_0 C_\mathrm{t})^2} \,. \tag{2.118}$$

Therefore, by adapting C_t using the geometry, IDTs can often be designed to match the 50Ω impedance of standard electronic components.

Surface Acoustic Wave Resonators Surface acoustic wave resonators represent the elastic-wave analogon of an electromagnetic Fabry-Perot cavity, where a standing surface acoustic wave is confined between two highly reflective mirrors. Here, we consider the most simple implementation of a SAW resonator, the 1-port resonator illustrated in Fig. 2.16 (a). To effectively reflect SAWs, the *mirrors* are in this case distributed Bragg reflectors formed by a large number of periodically arranged parallel metallic strips. Each strip, by altering the local

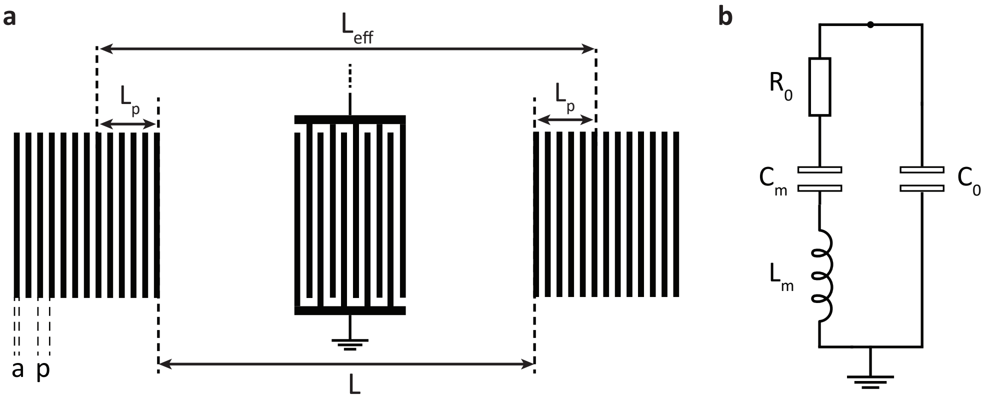

Fig. 2.16.: SAW resonator geometry and equivalent circuit. a Layout of a 1-port SAW resonator. Two Bragg reflectors, each consisting of N_g parallel metallized strips of width a and pitch p, are separated by a distance L and confine acoustic waves within a cavity of effective length L_eff. A single IDT is symmetrically placed in the center to excite and detect SAWs. **b** *Butterworth-van Dyke* equivalent circuit of the 1-port SAW resonator. The acoustic component is modelled in the left branch by a series of resistance R_0, motional capacitance C_m, and motional inductance L_m. The second, parallel branch consists of a single capacitance C_0, which is dominated by the geometric capacitance of the IDT.

propagation speed of an incident SAW, leads to a partial reflection. Similar to the IDT, the pitch p and the line width a define a resonance-like condition at $f_0 = v_\mathrm{p}/2p$, where all partial reflections interfere constructively. The total reflection resulting from the interference can be approximated based on the reflectivity of a single stripe r and the number of stripes N_g by [139]

$$|\Gamma| \approx \tanh(N_\mathrm{g}|r|)\ . \tag{2.119}$$

The reflectivity r is proportional to the piezoelectric coupling strength K^2 of the material and is usually in the range of $0.1 - 1\%$. Therefore, $N_\mathrm{g} > 500 - 1000$ is necessary to reach near-unity reflection $\Gamma \approx 1$. In this limit, we can also approximate the frequency range in which the reflectors provide near-unity reflection to [137]

$$\Delta f_\mathrm{SB} = 2f_0 r/\pi\ . \tag{2.120}$$

This bandwidth is commonly called the mirror's *stop band*, outside of this band, the mirrors are transparent to incoming SAWs.

To build a SAW resonator, two of these mirrors are placed a distance L apart, forming a cavity which confines SAWs. Additionally, an IDT is placed within the cavity to excite and detect the SAWs. Akin to a Fabry-Perot cavity, the SAW resonator supports multiple standing SAW modes within Δf_SB separated in frequency by the so-called free spectral range (FSR) $\Delta f_\mathrm{FSR} = v_\mathrm{p}/2L_\mathrm{eff}$, where

L_eff is the effective cavity length. Defining an effective cavity length is necessary because of the distributed nature of the Bragg reflector, so the reflection of SAWs does not occur immediately upon impact on the first metallic strip, but some penetration distance L_p into the mirror, such that $L_\mathrm{eff} = L + 2L_\mathrm{p}$. In the high reflectivity case $\Gamma \approx 1$, the penetration depth can be well estimated as $L_\mathrm{p} = \lambda/(4|r|)$ [139].

In line with the treatment of the IDT, the 1-port SAW resonator's electrical response can also be represented using an equivalent electrical circuit, which is called the *Butterworth-van Dyke* circuit and shown in Fig. 2.16**b**. The circuit consists of two parallel branches. The right branch contains a capacitance C_0, which is dominated by the the IDT's geometrical capacitance, so that $C_0 \approx C_\mathrm{t}$ as defined previously.

The left branch models the acoustic contributions to the circuit and includes a motional capacitance C_m, a motional inductance L_m, and a series resistance R_0. The resistance accounts for cavity losses, such as the mirror's finite reflectivity or phonon propagation losses. The motional capacitance and inductance describe the presence of acoustic waves in the cavity. Their analytical expressions are [145]

$$R_0 = \frac{1 - |(f)|}{2G_\mathrm{a}(f)} \tag{2.121}$$

$$L_\mathrm{m} = \frac{L_\mathrm{eff}}{4v_\mathrm{p}G_\mathrm{a}(f)} \tag{2.122}$$

$$C_\mathrm{m} \approx 1.8C_\mathrm{t}\frac{L_\mathrm{t}}{L_\mathrm{eff}}\frac{K^2}{2} \tag{2.123}$$

with the transducer length $L_\mathrm{t} = (2N_\mathrm{f} - 1)p/2$. The total admittance of the resonator Y_r can be calculated from the sum of both branches to

$$Y_r = i2\pi f C_\mathrm{t} + \left[i2\pi f Lm - i/(2\pi f C_\mathrm{m}) + R_0\right]^{-1} . \tag{2.124}$$

2.7 TLS losses in superconducting circuits

Research with superconducting quantum circuits, in particular in the direction of quantum computing, has revealed the appearance of uncharacteristically large losses when operating microwave frequency devices at very low powers and temperatures. Such losses reduce the coherence of superconducting quantum circuits and thus present a major challenge on the road to applicable quantum computing. Several studies [86, 146, 147] pinpoint unsaturated Two-Level-Systems (TLS) as the main origin of these losses. While the effect of TLS on the losses in microwave devices is well studied and several comprehensive theories for its description have been developed [148, 149], their microscopic nature is still not fully understood. A selection of commonly suggested culprits are dangling bonds, the collective motion of disordered atoms, hydrogen defects or other specific impurities [150]. The TLS have a probability to tunnel between two distinct states, causing minute energy shifts, often on the level of 10^{-5} eV, which is roughly equivalent to a frequency of 10 GHz, and therefore close to the operating frequency of many quantum circuits. TLS are also found more frequently in amorphous materials than in crystalline ones. Interestingly, the losses of quantum acoustic devices at low powers behave analogously [151], suggesting an interaction of the elastic wave with the same or similar types of TLS. Accordingly, it has been found that phonons can be absorbed and later re-emitted by TLS, which also leads to a power dependence of phonon propagation in the quantum regime [152]. For a more detailed study of phonon interaction with TLS we recommend Ref. [153].

Fortunately, the *standard tunneling model* (STM) [149] that is used to model the effect of TLS losses is very general and assumes a wide spectrum of tunneling states. It can therefore be applied to a multitude of systems, even without distinct knowledge of the underlying mechanism. In conclusion, we refrain from speculating about the microscopic processes that lie at the origin of the TLS related losses and instead focus on the introduction of a suitable phenomenological model. The goal is to be able to quantify the impact of TLS on the properties of superconducting circuits, such as resonance frequency and quality factor, while also differentiating the TLS interaction against other loss mechanisms.

Following the STM, we assume the most general form of a real-valued TLS Hamiltonian:

$$\hat{H}_{\mathrm{TLS}} = \frac{1}{2}\begin{pmatrix} \varepsilon & \Delta_0 \\ \Delta_0 & \varepsilon \end{pmatrix} \tag{2.125}$$

Here, ε symbolizes the energy gap between the two local energy minima, and Δ_0 represents the energy necessary for tunneling across the barrier. Upon diagonalizing the Hamiltonian, we arrive at two eigenfunctions: $|\Phi_+\rangle$ and $|\Phi_-\rangle$, with eigenenergies split by $E = \sqrt{\varepsilon^2 + \Delta_0^2}$. This splitting can be considered the char-

acteristic energy of the TLS. Notably, values for ε and Δ_0 hinge on the specifics of the TLS mechanism. Thus, a diverse ensemble of TLS will yield a wide spectrum of eigenenergies, which can couple to the electric fields of superconducting circuits. A crucial insight from the STM is the power-dependency of the related energy loss. Since a TLS can only absorb energy to be excited into the high-energy state, they become saturated for a duration until they revert to a low-energy state. When the average photon number in a resonator $\bar{n}_\mathrm{c}$ exceeds a critical value n_sat, the TLS related losses become fully saturated.
Based on the calculation in Ref. [85, 154], the resulting power dependency of a resonator's quality factor can be written as

$$\frac{1}{Q_\mathrm{i}} = \frac{1}{Q_\mathrm{i,TLS}} \left(1 + \frac{\bar{n}_\mathrm{c}}{n_\mathrm{sat}}\right)^{-\alpha} + \frac{1}{Q_\mathrm{res}} \,. \tag{2.126}$$

Here, $Q_\mathrm{i,TLS}$ represents the intrinsic loss contribution due to TLS at zero temperature and vanishing photon number $\bar{n}_\mathrm{c}$, i.e. no thermal polarization. Q_res is a summary term for all non-TLS related losses and α is a correction factor that accounts for non-uniform distribution of the electric field, with $\alpha = 1/2$ in the standard model [150, 155].

It appears intuitive that TLS can also become thermally saturated, so it is not surprising that the STM predicts an effect on the loss rate in response to a temperature change, which then modifies the internal Q-factor according to

$$\frac{1}{Q_\mathrm{i}} = \frac{1}{Q_\mathrm{i,TLS}} \tanh\left(\frac{hf_\mathrm{r}(T)}{2k_\mathrm{B}T}\right) + \frac{1}{Q_\mathrm{res}} \,, \tag{2.127}$$

where we have also used the temperature dependent resonance frequency of the resonator $f_\mathrm{r}(T)$, which we will discuss in the following. It can be shown that the power and frequency dependent loss rate is primarily driven by near-resonant TLS, where the energy splitting of the meta-stable states coincides with the operating frequency of the device [85]. However, a second class of TLS with energies *off-resonant* with the operating frequency still has a measurable impact on resonator properties, particularly the resonance frequency f_r. An expression for the temperature-dependent frequency shift due to off-resonant TLS is found to be [85]

$$\Delta f_\mathrm{r}(T) = \frac{1}{\pi Q_\mathrm{i,TLS}} \left[\mathrm{Re}\Psi\left(\frac{1}{2} + \frac{hf_\mathrm{r}(T)}{2\pi i k_\mathrm{B}T}\right) - \ln\left(\frac{hf_\mathrm{r}(T)}{2\pi k_\mathrm{B}T}\right)\right] f_\mathrm{r}(0), \tag{2.128}$$

using the digamma function Ψ. Using the above equations, temperature and power dependent measurements of a resonator's resonance frequency and quality factor can be used to gain detailed insight into the magnitude of TLS related losses in the investigated material. We will employ this technique repeatedly both for superconducting microwave resonators, as well as quantum acoustic devices based on surface acoustic waves.

Device Design and Fabrication

3

The chapter will begin by discussing the design considerations that inform the circuit design for flux-tuneable resonators (FTRs) with mechanically compliant SQUIDs, which are used in the experiments presented in Chap. 5. We will then outline selected stages in the optimization process and elaborate on the reasoning behind the implemented changes. Subsequently, the design process towards surface acoustic wave (SAW) devices for quantum applications, as they are employed in the experiments in Chap. 6, is discussed in an analogous fashion. Finally, we will introduce the nanofabrication techniques employed in the fabrication of the various samples investigated in this thesis and briefly summarize the different processes.

3.1 Design of FTRs with mechanically compliant SQUIDs

From the discussion of the physical phenomena underpinning the flux-mediated coupling in Sec. 2.5.2, it becomes apparent that the realization of the electromechanical interaction places various requirements on the employed devices. In particular, we recall the individual proportionality factors influencing the single-photon optomechanical coupling strength as defined in Eq. (2.96): $g_0 \propto B\partial\omega_c/\partial\Phi l x_{\mathrm{zpf}}$. In the following, we will discuss in detail how each of these factors impacts the device performance and informs the circuit design.

Flux responsivity $\partial\omega_c/\partial\Phi$ and frequency tunability A large flux responsivity is directly correlated with a large frequency tuning range of the microwave cavity. An added advantage of a large tuning range is increased flexibility in the operating frequency of the device. In order to achieve a larger tuning range, the participation ratio of the flux-dependent SQUID inductance L_{sq} to the total inductance L_Σ must be made large. However, with increasing L_{sq}/L_Σ the device will approach the transmon regime, where significant anharmonicity of its energy levels leads to non-linear behaviour, which will limit the applicable operating power (see 2.3.4). Therefore, the critical current I_{c0} of the Josephson junctions, which determines their inductance according to $L_\mathrm{J} = \Phi_0/(2\pi I_\mathrm{c0})$ needs to be chosen carefully. Furthermore, a larger responsivity is inherently associated with larger susceptibility to flux noise, an experimental challenge that is discussed in detail in Sec. 4.3.

SQUID and nanostring geometry At the heart of the flux-mediated electromechanical coupling lies the modulation of the magnetic flux permeating the SQUID loop by the oscillatory motion of the mechanical oscillator. Ideally, in order to maximize the coupling strength, the entire inductance of the SQUID L_sq should be dynamically modulated by the mechanical motion. In reality however, the SQUID inductance also contains a static self-inductance given by the loop geometry L_geo, and a kinetic contribution L_kin from the thin films used in their fabrication. These factors can be summarized as the static loop inductance of the SQUID $L_\mathrm{loop} = L_\mathrm{kin} + L_\mathrm{geo}$ and can be analytically calculated[1]. We have discussed the effect of a non-negligible loop inductance on the SQUIDs behavior in 2.2.4, where we have also introduced the screening parameter β_L to quantify the ratio between loop inductance and Josephson inductance.
For the design of the mechanically compliant SQUID, this means that while long and thin nanostrings are desirable in order to increase the strings zero-point motion and therefore the contribution lx_zpf, care must be taken to not introduce an overly large kinetic inductance L_kin. If the strings are made too thin, L_kin can cause the screening parameter to no longer fulfill $\beta_\mathrm{L} \ll 1$ and the FTR to behave hysteretically [105].

Resilience to external magnetic fields Since g_0 is directly proportional to the magnetic field permeating the SQUID, a straightforward way to increase the coupling strength is to increase the externally applied magnetic field. To make a larger range of magnetic field magnitudes available in the experiment, the superconducting circuit needs to be resilient to those fields without leading to a decrease in device performance or even a breakdown of superconductivity. To this end, selecting materials with a larger superconducting gap and therefore larger critical temperatures and fields is recommended. Furthermore, the orientation of the applied field can significantly alter the effect on the superconducting material. In general, thin films can withstand much larger external fields when they are applied along the film direction as opposed to the film normal [156].

---

[1] The necessary equations and parameters to calculate the loop inductance of a mechanically compliant SQUID are summarized in App. A.3.

FTR quality factor While the quality factor $Q = 1/\kappa$ of the microwave resonator does not directly influence the optomechanical coupling strength, it does determine the quantum cooperativity that can be reached with a given g_0 according to Eq. (2.92) and is (generally) the main limit to overcome when aiming for the single-photon strong coupling regime defined by $g_0 > \kappa$. Therefore, by maximizing the cavity quality factor, one can decrease the requirements on g_0 for achieving full quantum control of the electromechanical device.

3.1.1 Optimization of FTR design and fabrication

Considering the various and sometimes conflicting requirements posed on the design of mechanically compliant FTRs discussed in the previous sections, it is apparent that the realization of a well performing electromechanical device is not a trivial task. Over the course of this thesis, and in previous works before it, different approaches were investigated and iteratively improved upon. In this subsection, we will provide a review of some of the major revisions and elaborate on the underlying reasoning.

Single-step process

The initial device layout at the start of this work was developed in Ref. [158] and is based on a simple, yet effective, all-aluminum, single-step process. The process involves the use of only a single electron beam lithography step, followed by a single shadow evaporation and oxidation of the Josephson junctions along with the entirety of the remaining aluminum circuitry. This results in a straightforward fabrication process with reduced complexity and time consumption. A more detailed description of the employed fabrication techniques is provided in Sec. 3.3.

An exemplary circuit layout for the single-step devices is shown in Fig. 3.1. On the silicon chip, six superconducting $\lambda/4$ CPW resonators are patterned into the aluminum thin film, each designed to a different length and corresponding resonance frequency. Each of the resonators is shunted to ground via a mechanically compliant SQUID, which is shown in the micrograph images in panels **b-d**, forming a flux-tuneable electromechanical device as discussed in Sec. 2.5.2. Between devices, the length of the nanostrings embedded in the SQUID is varied, leading to different mechanical resonance frequencies. Each

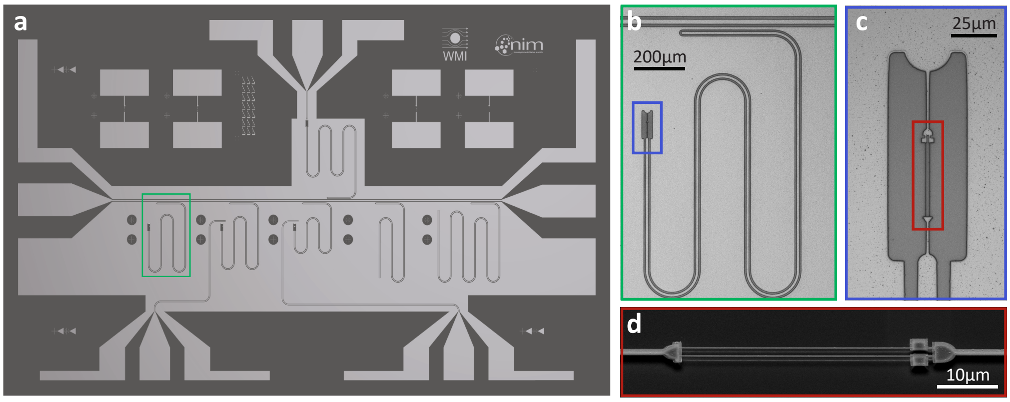

Fig. 3.1.: Nano-electromechanical device fabricated by the single-step process. **a** Illustration of a device layout fabricated with the single-step, all-aluminum process. Aluminum structures are shown in silver, while the silicon substrate is colored in dark grey. A shared feedline connects the short ends of the chip and capacitively couples to six flux-tuneable $\lambda/4$ CPW resonators. The ports on the long side of the chip can be used for additional drive signals. **b** Optical micrograph image of a single, meandering CPW resonator, corresponding to the green box in **a**. **c** Magnified view of the end of a CPW resonator (blue box), where the SQUID that shunts the center conductor of the CPW to ground is visible. **d** Tilted scanning electron micrograph (SEM) image of the suspended SQUID structure that allows for mechanical motion of the nanostrings. A version of the micrograph images was previously published in Ref. [157].

FTR is capacitively coupled to a shared feedline, which serves as a common pathway for the transmission of microwave signals to and from the resonators, allowing for the simultaneous readout of multiple devices (multiplexing). The use of a shared feedline simplifies the device layout and reduces the number of required input and output ports and microwave lines. This advantage is especially pronounced during early stages of design and development, where the yield of functioning structures might be low and multiplexing allows to quickly identify the working FTRs. However, proper care needs to be taken regarding the frequency spacing of the individual FTRs, otherwise the presence or even overlapping of multiple resonance features in the transmission signal can add significant complexity to the analysis. Lastly, compared to a reflection type geometry, the signal available for analysis is generally reduced by a factor of 2 in transmission geometry [159].

Unfortunately, the simplicity of the single-step fabrication process also leads to the most significant downside to this approach: During the shadow evaporation step, aluminum is evaporated, oxidized and evaporated again in order to form the Al/AlO$_x$/Al tunnel barriers that act as the Josephson junctions used in the SQUID (see Sec. 2.2.3). In the single-step approach, the oxidation process results in the formation of an oxide layer not only in the junction area, but also across the entire metal film of the chip. Therefore, instead of a continuous, high-quality aluminum film, the CPW resonators actually consist of an Al/AlO_x/Al tri-layer. The presence of the oxide layer across the entire metal film has several implications for the device performance. Most importantly, the additional interfaces and the introduced dielectric can host a large number of defects and impurities, which can act as two-level-systems (TLS) and can cause noise and energy dissipation in the circuit, as was discussed in Sec. 2.7. Oxides (SiO_x, AlO_x, NbO_x etc.) in particular are known to host a large density of TLS and great efforts across the field are put into minimizing their presence in high-coherence superconducting circuits [80, 160–162]. In our devices fabricated with the single-step process, we find large FTR loss rates on the order of $\kappa/2\pi > 1\,\mathrm{MHz}$, which prevent the devices from operating in the single-photon strong coupling regime $g_0 > \kappa$, even with comparatively large coupling rates exceeding $g_0/2\pi > 50\,\mathrm{kHz}$. We believe TLS in the aluminum oxide layer and associated interfaces to be the main reason for this high loss rate. In addition, the mechanical properties of the nanostring might also be expected to change as opposed to a string made from a single layer of aluminum. However, a detailed comparison of the nanostrings in a SQUID fabricated with the single-step process and pure aluminum strings presented in Ref. [158] did not uncover significant differences.

In summary, while the initial device layout based on a single-step process offers high simplicity and ease of fabrication, it is inherently limited by the presence of oxide layers and interfaces introduced during the fabrication process. These oxide layers can negatively affect the performance of the device, particularly with regards to TLS that can limit the achievable FTR quality factors and therefore the optomechanical cooperativity.

Development of multi-step process

To overcome the aforementioned limitations and improve the performance of the device, a more complex multi-step process has been developed over the course of this work. This process involves multiple layers of different superconducting materials, as well as multiple lithography steps, resulting in a more complex and time-consuming fabrication process, which is detailed in Sec. 3.3. Particular care must be taken to establish proper galvanic contact between the individual metal layers, a challenge we discuss in detail in Sec. 3.1.2. When successfully implemented, the multi-step process allows for greater control

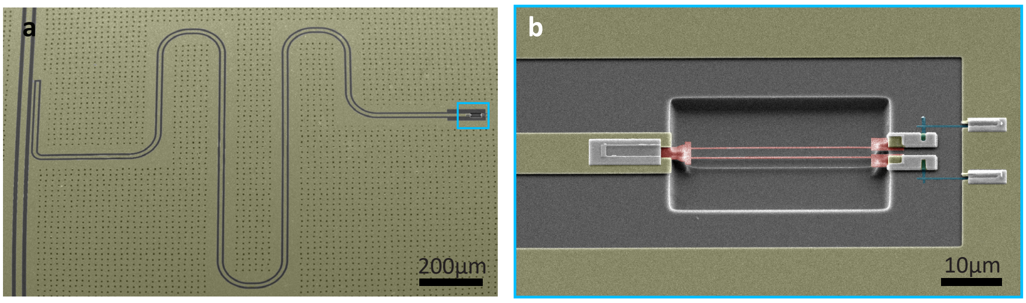

Fig. 3.2.: Nano-electromechanical device fabricated by the new multi-step process. **a** Tilted, false-color SEM image of a device fabricated with the newly developed multi-step process described in the main text. The base wiring (CPW resonator and ground plane) is fabricated using a subtractive etch process out of Niobium (green) on a silicon substrate (dark grey). The SQUID that shunts the CPW resonator to ground is visible on the right and highlighted. **b** Magnified view of the pocket at the end of the CPW resonator (blue box). The mechanically compliant element, featuring two parallel nanostring oscillators, is fabricated from a single layer of aluminum using lift-off and is shown in red. The Al/AlO$_x$/Al Josephson junctions use an angled shadow evaporation process and are false-colored blue. The aluminum bandages that establish galvanic contact between the different metal layers are shown as light grey.

over the fabrication and material composition of the individual components, which can improve their respective performance and opens up additional degrees of freedom in the design process. By choosing appropriate materials, it also enables the introduction of more advanced surface cleaning techniques, which can reliably remove surface oxides as a potential source of TLS losses. Scanning electron micrograph (SEM) images of a nano-electromechanical device fabricated using the newly developed multi-step process are presented in Fig. 3.2.

In our case, we opt for Niobium (Nb) as the material of choice for most of the superconducting circuitry, including the CPW resonators. The fabrication of non-tuneable CPW resonators made of Nb has been carefully optimized at the WMI and internal quality factors exceeding $Q_{\mathrm{int}} = 6 \times 10^6$ were reliably demonstrated [163]. Further, and of high relevance to our experiments with flux-mediated coupling, the quality factors have been shown to remain largely unaffected by external magnetic fields up to $B_{\mathrm{ext}} = 70\,\mathrm{mT}$, when applied along the thin film direction [164]. The higher performance of Nb over Al CPW resonators can be understood primarily as a result of two factors: (i) Nb has a critical temperature of 9.25 K, whereas superconductivity of Al breaks down above 1.19 K [92]. The associated larger superconducting gap of Nb is less susceptible to quasiparticle excitations, which leads to lower resistive losses and better magnetic field resilience. (ii) Highly reactive surface cleaning techniques like *Piranha* and *BOE* (see Sec. 3.3.1) can be applied to the deposited Nb

films and Si surfaces at several points along the fabrication process in order to remove surface oxides (SiO_x, NbO_x) and reduce TLS losses. The same chemical treatments would etch and/or corrode aluminum films and are therefore not applicable.
As such, aluminum structures are only used where Nb is not a suitable alternative. This is the case for the mechanically compliant parts of the SQUID loop, where we rely on a well established deposition and release process to fabricate highly tensile stressed nanomechanical string oscillators with high quality factors [68]. Nanomechanical devices made from pure Nb have been realized, but generally do not match the performance of Al nanostrings [165]. With a similar reasoning, we employ the *Manhattan-style* [166, 167] $Al/AlO_x/Al$ Josephson junctions that are found in the majority of state-of-the-art cQED devices due to their reproducibly high performance and ease of fabrication.

Despite the increased complexity associated with the multi-step process, the opportunity to merge all of these individual high-performance components into a single circuit presents a clear path towards the realization of advanced electromechanical devices. For example, with optomechanical coupling strengths up to $g_0/2\pi \approx 50\,\mathrm{kHz}$ demonstrated in our previous devices, and a typical resonance frequency of 5 GHz of the FTR, the single-photon strong coupling condition $g_0 > \kappa$ would be achievable with quality factors of $Q \approx 1 \times 10^5$, an order of magnitude below the demonstrated values for non-tuneable Nb resonators.

3.1.2 Bandaging optimization

Arguably the primary challenge in realizing a multi-step process for fabricating flux-tuneable electromechanical devices is reliably establishing a galvanic contact between the different metal layers deposited and structured in the different lithography steps. This difficulty arises due to the formation of native, insulating surface oxides (AlO_x, NbO_x) on the metal layers once they are exposed to atmospheric pressures, which prevent the formation of a continuous conducting path.

To overcome this challenge, various techniques have been developed to remove or reduce the oxide layer and establish a good galvanic contact between the metal layers. One common approach is to use an aggressive surface treatment process, such as Argon (Ar) ion milling, to remove the oxide layer and

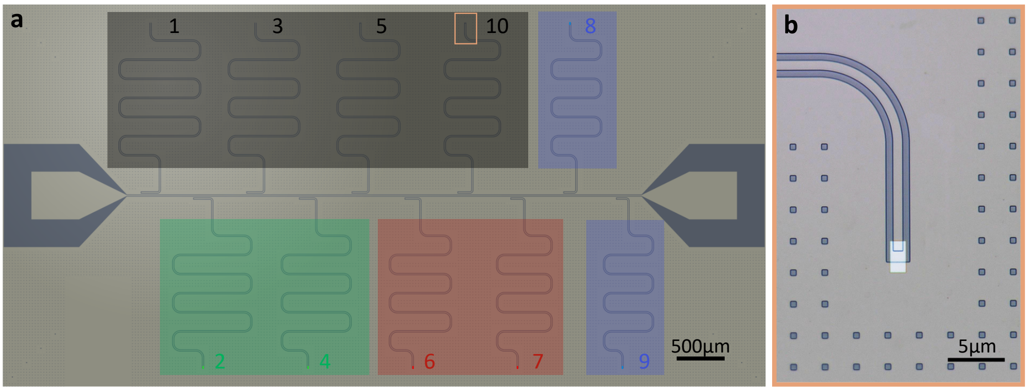

Fig. 3.3.: Device layout for the optimization of the bandaging process. Illustration of the device layout used for the optimization of the Ar-ion milling and bandaging process. The chip contains four standard $\lambda/4$ CPW resonators (shaded black), while the other six resonators are initially fabricated in a $\lambda/2$ configuration, i.e. both ends open. In a second lithography step, the $\lambda/2$ resonators are shorted to ground via an aluminum bandage. An optical micrograph of the resist mask used for the bandaging is shown in **b**. The different shading of the resonators corresponds to the three different milling recipes used.

create a clean metal surface. However, ion milling can lead to Ar ions being implanted into the metal or substrate, which can lead to additional losses that may negatively impact device performance [161, 168]. To circumvent this issue, researchers have explored alternative approaches such as a technique called bandaging [169]. Bandaging separates the milling process spatially from the areas of the substrate where critical circuit components (JJs, nanostrings) are located. To this end, after all relevant structures are successfully defined on the chip and only galvanic contact is lacking, another lithography step is performed. In this step, the resist layer is only selectively removed at small areas where the to-be-connected metal layers overlap, while the critical areas of the device remain covered in resist. The small overlap areas are then milled and a relatively thick layer of newly evaporated metal (the *bandage*) is deposited. This procedure protects the critical structures and the substrate below from the ion milling, while still allowing the oxide layer to be removed at a selected location where the galvanic contact can be established via the bandage. Bandaging has been shown to be an effective way of reducing the impact of ion milling on the performance of quantum circuits, in particular transmon qubits [169].

However, we have found that, for FTRs, the ion milling as part of the bandaging process can still have a significant negative impact on the device loss rates, even though the milling sites are located some distance away from the JJs. Since superconducting qubits fabricated at the WMI with a very similar process do not observe a negative impact from the bandaging [163, 170], we hypothesize that the current distribution in FTRs (and $\lambda/4$ CPW resonators in general) may make them more vulnerable to damages introduced by milling: The ions that are implanted into the metal can create defects which function as scattering centers for charge carriers or pinning centers for vortices. As each vortex carries one quantum of magnetic flux, a Lorentz force is exerted on the vortices when a current passes through the superconductor. This force induces dissipative vortex motion, which leads to additional losses [171]. Due to the current anti-node of the FTRs fundamental mode being located at the SQUID, close to the surfaces treated with milling, we anticipate substantial currents to flow near the pinned vortices. Therefore, additional optimization was required in order to properly tailor the process parameters to the fabrication of flux-tuneable electromechanical devices.

We conduct a systematic investigation to optimize the Ar-ion milling recipe by varying the relevant parameters of the *Kaufman*-type Ar-ion source. A comprehensive description of the *Kaufman* source and its parameters can be found in Ref. [172]. To perform the optimization, we design a test chip with ten resonators (shown in Fig. 3.3**a**), six of which are initially designed in $\lambda/2$ configuration, i.e. with two electrically open ends. In a second lithography step, one end of the $\lambda/2$ resonators is milled and subsequently connected to ground via an evaporated aluminum bandage, re-establishing the $\lambda/4$ boundary condition. The resist mask used for the milling and bandaging is shown in Fig. 3.3**b**. The remaining four resonators on the chip are standard $\lambda/4$ resonators to establish a baseline for loss measurements. Importantly, we investigate three different sets of milling parameters on this device, each set being applied to two adjacent resonators (see shaded areas in Fig. 3.3**a**). The milling parameters used for each resonator are summarized in Tab. 3.1. In this initial optimization step, only the beam current I_{beam} and the duration of the milling process t_{milling}, i.e. the two parameters defining the total number of ions hitting the target, were varied. The beam voltage V_{beam}, which defines the beam energy, and the acceleration voltage V_{acc} was kept constant to limit the available parameter

Recipe	Resonator	V_{beam} (V)	I_{beam} (mA)	V_{acc} (V)	t_{milling} (s)
1	2, 4	400	15	90	180
2	6, 7	400	15	90	360
3	8, 9	400	30	90	180

Tab. 3.1.: Summary of the Ar-ion milling recipes compared during the bandaging optimization. The numbering of resonators refers to the device layout shown in Fig. 3.3.

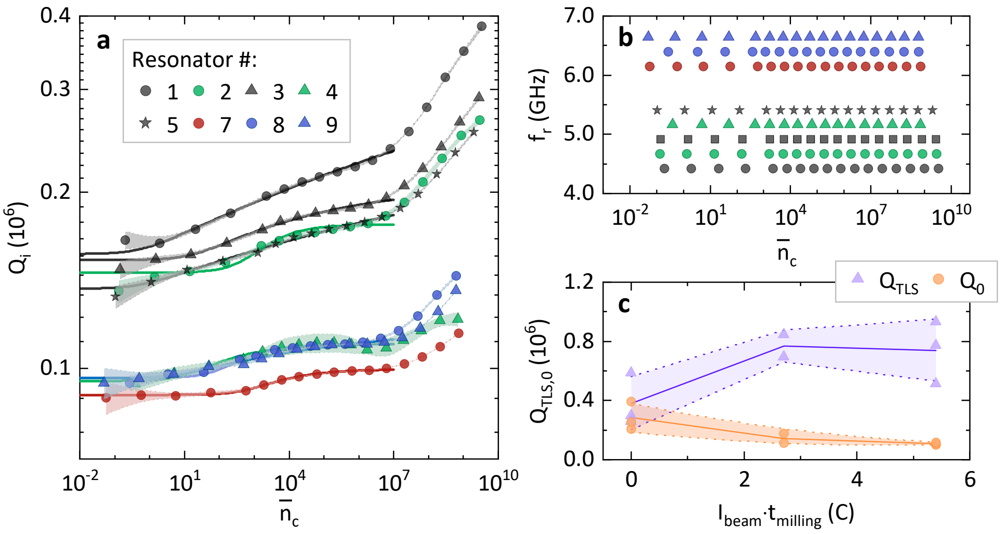

Fig. 3.4.: Resonator measurement results during the bandaging optimization. Intrinsic quality factors Q_i (**a**) and resonance frequencies f_r (**b**) as a function of input power converted to average photon number $\bar{n}_\mathrm{c}$. The values are extracted using the circle fit Eq. (4.1). The resonators are indexed according to the numbering in Fig. 3.3**a** and have been prepared with different milling recipes as listed in Tab. 3.1. Higher Q_i are generally observed for the reference resonators (black) and resonators with less aggressive milling recipes (e.g. green). Uncertainties of the respective fits are illustrated as shaded areas. In **c**, the TLS-associated quality factor Q_TLS and non-TLS quality factor Q_0 were extracted from fits to Eq. (2.126) (solid lines in **a**) and plotted over the total ion charge of the used milling recipe. The solid lines and shaded areas correspond to the mean value and standard deviation respectively. A downward trend in Q_0 with increasing ion charge is discernible.

space. To evaluate the losses incurred on the CPW resonators by the different milling processes we measure the complex microwave transmission parameter S_{21} for each resonator at base temperature $T_\mathrm{base} \approx 20\,\mathrm{mK}$ using a commercial cryostat, while varying the excitation frequency and input power. By fitting the complex transmission data with our circle fit routine (cf. Sec. 4.2.1), we were able to extract the relevant resonator properties, such as the internal quality factors, Q_i and resonance frequencies f_r, for the eight resonators that were measured.

In Fig. 3.4**a**, we present the power dependent internal quality factors for eight of the measured resonators[2], where the input power was converted into the average number of photons occupying the cavity using Eq. (2.80). As might be expected, we observe the highest internal quality factors, ranging from 1.5×10^5 to 4×10^5, for the reference resonators without a bandage (resonators 1, 3 and 5, black symbols in Fig. 3.4**a**). These resonators also display an increase

---

[2] resonators 6 and 10 were excluded as outliers due to uncharacteristically low quality factors

of Q_i with applied power, which is typical for superconducting microwave resonators coupled to a bath of TLS, as described by the model introduced in Sec. 2.7. However, resonator 2 features similarly high Q_i after being exposed to bandaging recipe 1. Resonator 4, which was fabricated with the same parameters as resonator 2, shows significantly smaller Q_i than resonator 2. The reason for this discrepancy in the performance of the nominally identically processed resonators is not clear, but external influences like resist residues close to the bandage might play a role. Resonators 8 and 9, using bandage recipe 3 with an increased I_beam, show reduced Q_i on the order of 10^5, which also remain relatively constant over the range of applied input powers. This could indicate that the dominant loss mechanism can no longer be associated with TLS but rather with the defects related to the milling process such as implanted Ar ions or missing metal atoms. Similar behavior is observed for resonator 7, which was fabricated with a doubled milling time compared to the other resonators. It becomes clear that an increased number of Ar-ions hitting the target area, either due to a higher beam current or longer milling duration, leads to a – sometimes significant – reduction in the internal quality factors of the investigated resonators.

With this observation in mind, we can attempt to further characterize the nature of the additional losses apparently introduced by the more aggressive milling processes. By fitting the data shown in **a** to Eq. (2.126) (solid lines), the TLS model for power-dependent losses introduced in Sec. 2.7, we can extract the quality factor contribution associated with coupling to a bath of TLS Q_TLS and the quality factor due to remaining losses Q_0 for each of the resonators. We note that the linear increase of Q_i at very high input powers ($\bar{n}_\mathrm{c} > 10^7$) is not predicted by the simple TLS model [173] and therefore excluded from the fit. In order to visualize the potential impact of the milling process on the different loss contributions, we plot in Fig. 3.4**c** the extracted TLS losses (Q_TLS) and non-TLS losses (Q_0) as a function of the product $I_\mathrm{beam} \cdot t_\mathrm{milling}$, which corresponds to the total ion charge applied to the milled area over the duration of the process. We find $Q_\mathrm{i} \approx Q_\mathrm{TLS} \approx Q_0$ for the reference resonators, indicating that TLS and non-TLS losses are on the same order of magnitude and neither of them is solely limiting the device performance. However, as we look towards the milled resonators with $I_\mathrm{beam} \cdot t_\mathrm{milling} > 0$, we observe a downward trend in Q_0. At the same time, Q_TLS remains largely constant within the uncertainties, independent of the ion charge. This observation strongly suggests that the milling process introduces significant additional losses, such as the dissipative vortex motion discussed above, which are not related to the coupling to a TLS bath. Therefore, the milling leads to these losses, described by Q_0, becoming the limiting loss contribution as $Q_{\mathrm{TLS}} \gg Q_{\mathrm{i}} \approx Q_0$ for the milled resonators.

Based on these results, it might appear straightforward to decrease the duration and beam current of the milling process even further to minimize the additional losses. However, the number of Ar-ions used in the milling process can not be made arbitrarily small. Otherwise, the milling will no longer be able to serve its intended purpose of removing the surface oxide layers that prevent galvanic contact. In this case, the remaining oxide layer below the bandage would form a superconductor-insulator-superconductor tunnel barrier, i.e. a Josephson junction (cf. Sec. 2.2.3) at the end of the CPW resonator. As discussed in Sec. 2.3.4, the non-linear inductance associated with the Josephson junction would manifest as a power dependency of the resonator's resonance frequency. Therefore, to verify the effectiveness of our milling recipes, we evaluate the resonance frequencies f_{r} extracted from the fits as a function of input power. The results are presented in Fig. 3.4**b** and show power-independent resonance frequencies for all resonators, confirming that all investigated recipes achieve sufficient removal of the surface oxides.

Ultimately, the goal of optimization must be to locate the threshold where milling time and beam current can be chosen as low as possible while the process remains potent enough to penetrate the surface oxides. Therefore, after this initial, promising study, we performed further optimization runs with similar devices, now also with regards to different beam and acceleration voltages, until we arrived at a minimally invasive process that only uses the least amount of energy and number of ions necessary to remove the aluminum and niobium surface oxides. The parameters presently considered optimal and in use for the multi-step fabrication process for flux-tuneable electromechanical devices are $I_{\mathrm{beam}} = 15\,\mathrm{mA}$, $V_{\mathrm{acc}} = 90\,\mathrm{V}$, $V_{\mathrm{beam}} = 300\,\mathrm{V}$ and $t_{\mathrm{milling}} = 180\,\mathrm{s}$.

3.2 Design of SAW devices

As outlined in Sec. 2.6, the characteristics of surface acoustic wave devices, in particular SAW resonators, are largely defined by the employed piezoelectric material and the geometry and placement of the patterned transducers and gratings. In this section, we will introduce the most relevant design parameters and how they are chosen and adapted to reach equivalent device properties on various piezoelectric materials. A detailed description of the investigated material systems along with experimental studies of fabricated devices are found in Chap. 6.

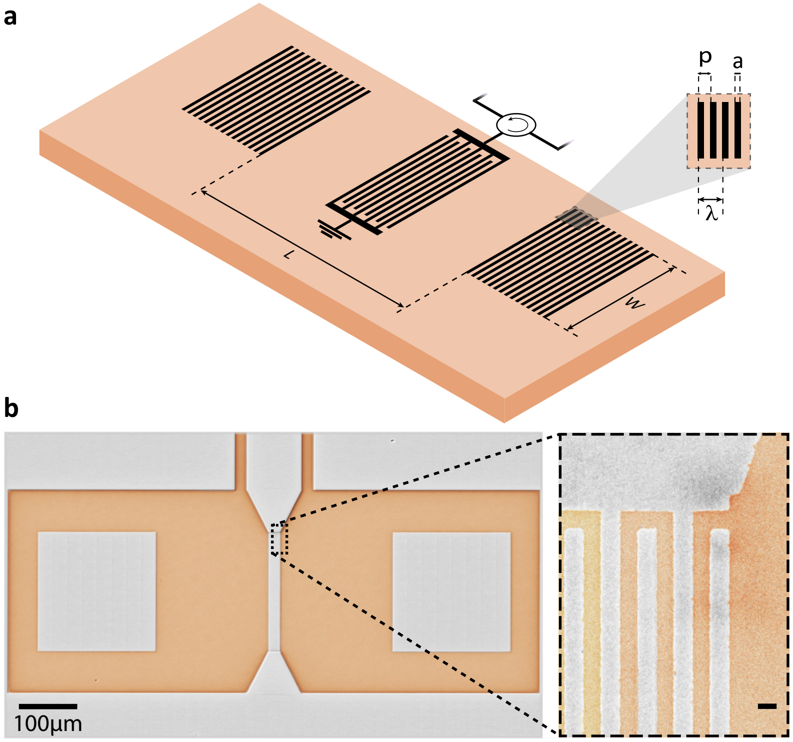

Fig. 3.5.: One-port surface acoustic wave resonator design. a Schematic of the used surface acoustic wave (SAW) resonator geometry, including its relevant design parameters. **b** Optical micrograph of the SAW resonator structure in false color. Aluminum is represented in light gray, while LNO is colored orange. The zoom-in section displays a scanning electron micrograph (SEM) highlighting the individual strips comprising the transducer. The black scale bar corresponds to a length of 200 nm, which is the nominal width of the strips. A version of this figure has been published in Ref. [174].

Since the long-term perspective for quantum acoustics requires integration of the acoustic devices (i.e. SAW resonators) with various superconducting circuit components, every device parameter needs to be designed with compatibility to established quantum circuits in mind. In particular, this requires matching their operating frequencies of several GHz along with efficient transduction of the elastic excitations into electromagnetic signals and vice versa [175].

In our case, we design our SAW resonators to a target frequency of $f_0 \approx 5\,\mathrm{GHz}$ and opt for a standardized one-port resonator geometry, where a single interdigital transducer (IDT) is placed symmetrically in the center of the Bragg reflectors forming the SAW cavity (see Fig. 3.5**a** and **b**). The IDT is formed by periodically patterned aluminum electrodes alternating between signal and ground terminals with a pitch of $p = 400\,\mathrm{nm}$ and a metallization ratio of $\eta = 0.5$, meaning the gaps between electrodes are designed with the same width as the metallized stripes. This transducer layout, commonly referred to as single-electrode IDT [139], offers the advantage of a simple design process and comparatively large feature dimensions on the order 100 nm even at GHz operating frequencies. However, it is important to consider the non-negligible reflection that the single-electrode IDT introduces into the SAW resonator mode volume. To minimize this contribution, we generally choose the number of transducer electrodes N_f to be as small as possible (10 to 100), while still sufficient to provide the necessary transduction efficiency. Since the piezoelectric coupling is material dependent, N_f and the mode volume itself (i.e. the length L and width W) can be optimized individually for any investigated material systems to reach a desired transduction efficiency.

In the context of SAW resonators, the transduction efficiency of the IDT is directly related to the external quality factor Q_e of the device. Therefore, we exploit the strong geometric dependence of Q_e on design parameters $Q_\mathrm{e} \propto L_\mathrm{eff}/(WN_\mathrm{f}^2)$ [53] to engineer Q_e close to critical coupling ($Q_\mathrm{i} \approx Q_\mathrm{e}$) and low transducer reflectivity at the same time. As a side effect of the low number of transducer electrodes, the bandwidth of our IDTs is generally much larger than the mirror stop band of the Bragg reflectors forming the SAW resonator and the transduction efficiency can be considered constant across the narrow frequency band.

In the design of the Bragg reflectors, we utilize $N_\mathrm{g} = 500$ electrically floating aluminum strips with a pitch identical to the value used for the IDT ($p = 400\,\mathrm{nm}$). This pitch defines the SAW wavelength $\lambda = 2p$, which is reflected most effectively, thereby determining the operating frequency of the SAW resonator ($f_0 = v_\mathrm{p}/\lambda$). To ensure consistency and reproducibility in the fabrication process, we keep the pitch constant across all the investigated substrates and devices.

To maximize the constructive interference between differently reflected wave packets within the resonator, the distance between mirrors L and distance between the central IDT and each mirror d_{IDT} are chosen to fulfil

$$L = \left(2n \pm \frac{1}{2}\right)\frac{\lambda}{2}\,, \tag{3.1}$$

$$d_{\mathrm{IDT}} = \left(\frac{n}{2} - \frac{1}{4}\right)\lambda + \frac{\lambda}{8}\,. \tag{3.2}$$

It is important to acknowledge that our resonator geometry has the capability to excite and confine various types of SAWs, including Rayleigh, shear, and Love waves, each with their own distinct phase velocity and corresponding resonance frequency. Additionally, in the context of a multi-layer material system, Sezawa modes need to be taken into account (see Sec. 6.2). However, all of our devices are specifically designed to excite and confine Rayleigh waves and we will largely limit our discussion to this type of SAW.

Lastly, we note that many more complex transducer and resonator geometries have been proposed and demonstrated, which use a combination of non-reflecting [139] or uni-directional IDTs [176], beam-steering [177] and bandgap-engineering [178] to significantly increase the performance of SAW resonators. However, in this work, we deliberately opted for widely established and easily reproducible circuit designs to keep our findings as general as possible and applicable to a broader field of research.

3.3 Nanofabrication Techniques

In this section, we will explore the technical aspects of nanofabrication that are necessary to realize nano-electromechanical and surface acoustic wave based quantum acoustic devices. First, we will briefly discuss the importance of surface cleanliness and the techniques we use to achieve it. Then, we will provide a step-by-step guide to the most relevant sub-processes involved in the fabrication of the various devices studied in this work, detailing the materials and equipment involved.

3.3.1 Surface treatments

For the successful and reproducible fabrication of state-of-the-art superconducting circuits, the quality and cleanliness of the employed materials and processes is paramount [179]. In particular, contamination of surfaces and interfaces between substrate and the superconducting metal has to be minimized in order to avoid the introduction of lossy two level systems (TLS) (see Sec. 2.7). To this end, a variety of chemical surface treatments is available, each targeting a separate class of contaminants [180]. While the specific parameters can be adapted depending on the to-be-fabricated device, we generally employ a combination of two surface treatments, which are briefly introduced in the following:

Piranha etch A solution composed of a mixture of concentrated sulfuric acid (H_2SO_4) and hydrogen peroxide (H_2O_2), which creates a powerful oxidizing environment that is particularly effective at removing organic residues. For our samples, it is generally used at the beginning of the process to strip organic residue present on the raw silicon substrates from protective coatings applied during shipping or wafer dicing. However, Piranha etch will also cause the growth of an oxide layer on the surface of the silicon substrate, which should be removed subsequently.

Buffered Oxide Etch (BOE) A solution of hydrofluoric acid (HF) and ammonium fluoride (NH_4F), which can reliably remove surface oxides of silicon and niobium. The NH_4F acts as a buffer, keeping the pH constant, ensuring a constant and controlled etch rate. The process also passivates the cleaned surfaces against re-oxidation for a limited time [181]. We employ BOE directly after the Piranha etch to remove the oxide layer on the silicon surface. The process can be repeated at later steps to ensure a clean, oxide-free contact surface for the evaporated metal layers. However, aluminum films have to be protected (e.g. by a resist mask), as they are attacked by the BOE.

3.3.2 Multi-step fabrication

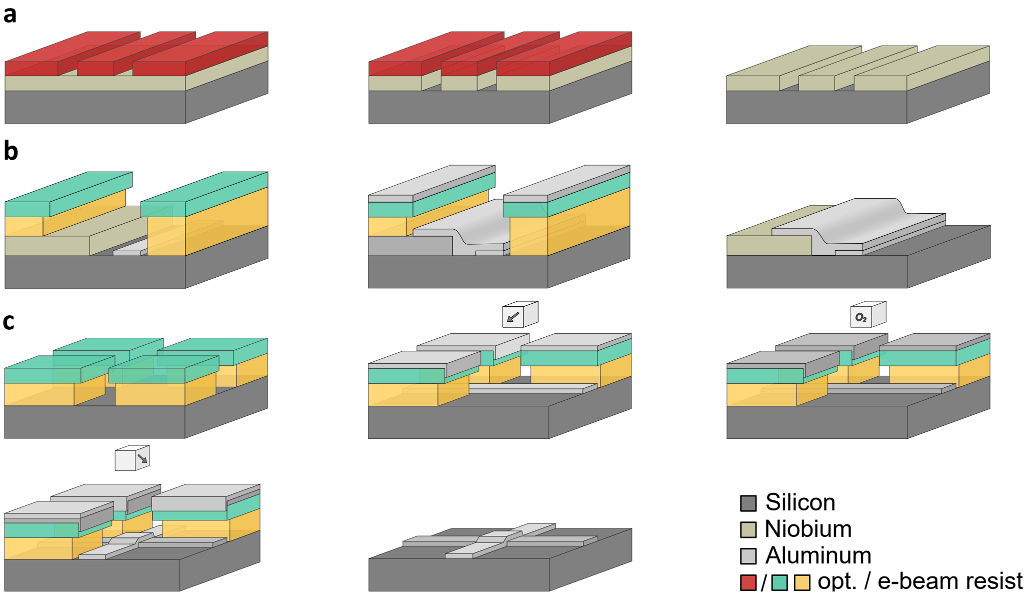

Fig. 3.6.: Graphical illustration of the most relevant nanofabrication steps for samples in this work. **a** Patterning of the base wiring from a Nb thin film using optical lithography and reactive ion etching (RIE). **b** Single step aluminum evaporation after lithography by e-beam. Used for all single layer aluminum structures including bandaging. **c** Double-angle shadow evaporation for Josephson Junction fabrication. Aluminum is evaporated from two different angles (arrows indicate evaporation direction) with a controlled oxidation step in between. A detailed description of the processes is provided in the main text. Adapted from Ref. [182].

The essential techniques of the fabrication process for nano-electromechanical devices are illustrated in Fig. 3.6 and will be discussed step-by-step in the following. Large parts of the process have been developed in parallel to the optimization of the fabrication of high-coherence superconducting qubits at the WMI. In addition to the description provided here, we therefore refer the detail-oriented reader to the very comprehensive description of the qubit process in Ref. [182].

Niobium base wiring The process starts with patterning all circuit components that are made out of Nb using a subtractive process to transfer the intended layout into a previously sputtered Nb thin film (Fig. 3.6**a**). This so-called *base wiring* encompasses ports, signal lines and the CPW resonator geometry, along with alignment markers that can be used for subsequent fabrication steps. For this, the chip is coated with a positive photoresist, followed by a pre-exposure bake. The layout of the base wiring is exposed using a direct laser writer, and a post-exposure bake is performed in order to increase the etch stability of the resist. The resist that was exposed to laser light is removed during a development step, forming a mask for the next step of reactive ion etching (RIE). During the RIE process, the non-protected Nb is chemically and physically etched by a mixture of Ar and SF_6 plasma. After the RIE process, the remaining photoresist is removed by a suitable stripper.

SQUID loop and nanostring (single layer aluminum) In the second step, the main part of the SQUID loop along with the nanostring geometry is fabricated (Fig. 3.6**b**). The sample is spin-coated with a double-layer stack of two different electron beam (e-beam) lithography resists. After the e-beam lithography process and development of the double-layer stack, a single layer of Al is evaporated using an e-beam evaporation system. Prior to evaporation *BOE* can be used to remove residues and oxides from the exposed substrate. Finally, lift-off in aceton and/or a suitable remover removes the non-exposed resist and the excess Al on top of it.

Josephson Junctions In the third step, two Manhattan-type Josephson junctions (JJs) are fabricated. The junctions are defined using the double-layer resist stack and e-beam lithography, followed by development. As already employed in the previous step, a pre-evaporation *BOE* cleaning can be used to ensure a clean and oxide free silicon surface and improve adhesion of the thin junction leads. The shadow-evaporation of the Josephson junctions requires two consecutive evaporation processes. During the first Al evaporation, the sample is tilted by 45° w.r.t. the chip surface, leading the evaporated Al to only coat the substrate along the evaporation direction, while trenches in perpendicular orientation are protected by the tilted resist layer (see Fig. 3.6**c**). The chip is then oxidized under a controlled flow of pure oxygen (dynamic oxidation) leading to the formation of an AlO_x layer. In the second evaporation step, the direction of evaporation is rotated by 90° while the tilt angle of 45° is maintained, so that the second arm of the JJ geometry can be coated with metal. In the small rectangular area where both arms overlap a Josephson junction is formed by the $Al/AlO_x/Al$ tunnel barrier.

Bandaging Next, galvanic contact needs to be established between the three different metal layers deposited in the previous steps using a bandaging approach [169]. Patterning and evaporation of the aluminum bandage follows the single layer evaporation process already discussed in the second step and illustrated in Fig. 3.6**b**. However, prior to evaporation, the native oxides of the different metal layers (AlO_x and NbO_x) are removed by an Ar-ion milling process. The milling has to be performed *in-situ*, immediately followed by the evaporation and without exposing the sample to ambient pressure to prevent re-oxidation. The parameters optimized and used for the bandaging are discussed in detail in Sec. 3.1.2.

Nanostring annealing and release Lastly, the nanostrings need to be released from the substrate, which allows them to perform their oscillatory motion. However, since we aim for high-Q nanomechanical resonators in the MHz frequency range, a highly tensile stressed material is mandatory to reach the necessary pre-stress values (cf. Eq. (2.27)). Since, depending on the deposition parameters, aluminum thin films can be only weakly tensile stressed or even compressively stressed, we incorporate an additional annealing step to introduce the necessary pre-stress in a controlled manner. To this end, the sample is annealed at 350 °C for 30 minutes in vacuum. During the subsequent cooldown back to room temperature, the aluminum film becomes highly tensile stressed due to the different thermal expansion coefficients of aluminum and silicon. This effect becomes even more pronounced once the sample is cooled to cryogenic temperatures. Finally, the nanostring is selectively released by a combination of anisotropic and isotropic RIE processes (Ar and SF_6), which gradually remove the silicon below the string until it is freely suspended. The parts of the chip that are not supposed to be etched are protected by a resist mask during this process, which is patterned using e-beam lithography to accurately define the etch window. As a last step, the etch mask is removed using a suitable remover and the sample is carefully dried using a critical point drier (CPD). More details regarding the fabrication of nanostring oscillators are found in Refs. [68, 183, 184].

3.3.3 Single-step fabrication

The single-step fabrication employed for the earlier generations of electromechanical devices (see Sec. 3.1) is accomplished using only a subset of the tools and sub-processes that were discussed in the previous section for the multi-step process. The complexity of the process is greatly reduced since the patterning of base wiring, SQUID loop, nanostring and Josephson Junctions is combined into a single step of e-beam lithography, shadow evaporation of Al/AlO_x/Al and lift-off (cf. Fig. 3.6**c**). The nanostrings are then annealed and released using RIE as discussed above.

3.3.4 Fabrication of SAW devices

The fabrication of surface acoustic wave resonators, like the one shown in Fig. 3.5**b** is comparatively straightforward compared to the more involved multi-step processes we have discussed above. All structures which form the SAW cavity (IDT, Bragg reflectors) are patterned in a single step of e-beam lithography and e-beam evaporation of 20 nm aluminum, followed by lift-off as illustrated and discussed in Fig. 3.6**b**. The major challenge in the fabrication of GHz frequency SAW resonators is instead the proper calibration of the e-beam lithography itself:

Firstly, since piezoelectric substrates are generally good insulators, they can suffer from localized charging effects when exposed to the electron beam, which can have detrimental effects on the lithography [185]. Secondly, the geometry of the IDTs and Bragg reflectors, each consisting of thin ($\approx$ 200 nm) periodic lines densely arranged across a large area, is very susceptible to the *Proximity Effect* (PE). The PE describes the unintended exposure of resist which is located close to incident electron beam due to (back)scattering in the substrate [185]. This can result in the broadening of lines and the merging of closely spaced features, which can significantly impact the performance of the resulting device.

The problem of charging effects in the substrate can be remedied by applying an additional layer of conductive material on top of the e-beam resist which helps to achieve a sufficient distribution and transport of charges away from the incident beam. We use a very thin (few nm) layer of commercially available conductive resist, which solves the charging problem but otherwise has negligible impact on the exposure properties.

The proximity effect on the other hand is a complex challenge, which has received considerable attention from researchers as well as industry [185, 186]. Fortunately, the scattering process of electrons can be simulated with high accuracy when taking into account the correct material parameters (density, stoichiometry) for the e-beam resist and substrate. Commercial software packages for proximity effect correction (PEC) can perform these simulations and calculate a dynamic adjustment to the exposure dose for each point in the layout depending on its localized scattering environment. In our case, we apply PEC by the software BEAMER[3] to the layouts for SAW devices and successfully compensate for the proximity effect.

---

[3] BEAMER Electron- and Laser-Beam Lithography Software by GenISys GmbH

Experimental Setup and Methods

4

This chapter focuses on the experimental setups and measurement techniques employed for the investigation of electromechanical and acoustic systems in the quantum regime. It begins by introducing the cryogenic measurement setup, which provides the technical foundation for conducting experiments at millikelvin temperatures. The chapter provides a basic description of the crucial microwave components used for signal generation, routing and processing, both within the cryostat and at room temperature. It then delves into a technical description of measurement techniques. We introduce microwave spectroscopy, the main tool to probe electromechanical devices, along with signal analysis methods used to extract their properties and dynamics. In this context, we address two of the main experimental challenges: flux noise and vibrations, and present an active resonator stabilization protocol that was developed to compensate for these disturbances. Finally, the Josephson Parametric Amplifier (JPA) that enables nearly quantum limited amplification in the setup is discussed and characterized.

4.1 Cryogenic measurement setup

In this section, we present a detailed description and visualization of the cryogenic measurement setup utilized in this work. The centerpiece of the experimental setup is a commercial *TRITON* dry dilution refrigerator from Oxford Instruments equipped with a superconducting vector magnet (VM), enabling investigations at ultra-low temperatures with simultaneous 3-axis vector control of an external magnetic field. Additionally, a multitude of microwave components are needed to generate, filter and analyze the low-noise and high-precision signals used in the experiments. An overview of the comprehensive setup is presented in Fig. 4.1. Panel **a** focuses on the wiring of the microwave lines across the various temperature stages within the cryostat, ranging from room temperature (300 K) to 80 mK, the base temperature at the mixing chamber. For our experiments, we use four main microwave lines (A through D),

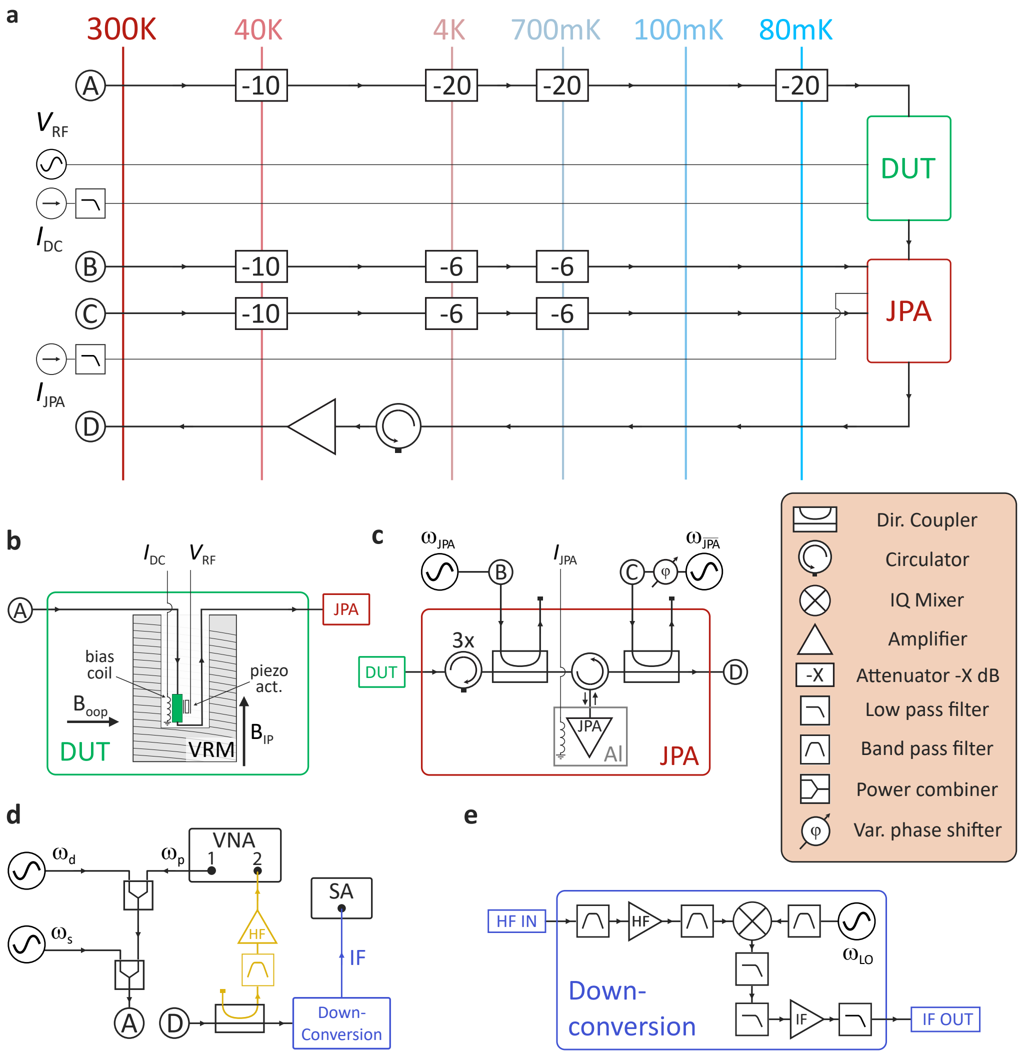

Fig. 4.1.: Schematic of the microwave wiring in the cryogenic measurement setup. **a** Overview of the microwave wiring and installed components across the various temperature stages of the dilution refrigerator used in this work. The symbols for individual microwave components are explained in the legend on the right. The placement and wiring of the device under test (DUT) and the Josephson Parametric Amplifier (JPA) are detailed in **b** and **c**, respectively. The signal processing chain at room temperature is shown in **d** and a detailed illustration of the frequency downconversion setup is provided in **e**. All active microwave components (VNA, SA, signal generators) use a Rubidium frequency standard as common reference clock. A detailed description of the setup is provided in the main text.

where line A is generally used as the input line to the device under test (DUT), B and C are auxiliary inputs necessary for operation of the JPA, which will be discussed later on, and D is the output line routing the transmitted signal from the DUT back to the signal processing chain outside of the cryostat. Additionally, there are low-pass filtered lines to apply DC voltages I_{DC} and I_{JPA} and a radio frequency (RF) voltage V_{RF}. As shown in the figure, the input lines are strongly attenuated by several microwave attenuators at different temperature stages. This is necessary to block thermal radiation from higher temperature stages from reaching the DUT and ensure proper thermalization of the microwave cables. Since each attenuator dissipates heat at its location and introduces thermal noise corresponding to its temperature, it is important to distribute the attenuators across the different temperature stages. The output is not attenuated, consists of superconducting cables where applicable and contains an additional cryogenic HEMT amplifier (High Electron Mobility Transistor) providing 40 dB of gain to minimize signal losses and maximize the signal to noise ratio of the measured signal. A circulator before the HEMT prevents reflected signals as well as thermal radiation from travelling back towards the DUT.

Moving on to panel **b**, we showcase the details of the placement and wiring of the DUT. As illustrated in the figure, the sample packaging (green) is mounted to a cylindrical extension of the mixing chamber plate, such that it is placed in the center of the magnet, which is used to generate the external in-plane magnetic field B_{ip}. Note that the magnet assembly is operating at 4 K and is not thermally connected to the mixing chamber or the sample package. Attached to the package are a small coil, which uses the DC current I_{DC} to generate a bias magnetic field B_{oop}, and a piezoelectric actuator which can be driven by an RF voltage V_{RF} to coherently excite mechanical motion of the sample. The microwave input signal from line A is transmitted through the DUT and routed back out of the magnet to the mixing chamber plate, where it is sent to a Josephson Parametric Amplifier (JPA), which we will discuss in the following. However, at this point, we will limit the discussion to the technical aspects of how we operate our JPA inside the dilution refrigerator, while a characterization of our JPA is presented in Sec. 4.4.

The wiring and signal routing used to operate the JPA for our experiment are illustrated in Fig. 4.1**c**. The to-be-amplified signal arriving from the DUT first passes an array of 3 isolators followed by a directional coupler, where it is combined with the pump tone of the JPA ω_{JPA}, which is generated by a microwave generator at room temperature and sent into the cryostat via line B. The directionality of the coupler (30 dB) and the circulators (3×20 dB) prevent the pump tone from interacting with the DUT, even though the power of the pump tone is several orders of magnitude larger than the microwave tones used in the experiment. As JPAs are generally operated in reflection, the signal then passes another circulator and is reflected off of the JPA, where it is amplified by ca. 20 dB. The JPA is located in a superconducting aluminum housing mounted to the mixing chamber plate, which shields the flux-sensitive amplifier from external magnetic fields to ensure stable operating conditions. Inside the aluminum housing, a superconducting coil is mounted to the JPA package and used to control the flux bias of the JPA via the DC current I_{JPA}. After amplification, the signal then passes a second directional coupler, where a second pump tone, which we denote $\omega_{\overline{\mathrm{JPA}}}$, with a frequency identical to ω_{JPA} but with an added variable phase shift[1] is combined with the signal. If power and relative phase of the second pump tone $\omega_{\overline{\mathrm{JPA}}}$ is chosen correctly, destructive interference between the two pumps leads to a near total cancellation of frequency components at ω_{JPA} after the second directional coupler. Making use of this interference technique called *pump cancellation* is necessary because the high powered pump tone might otherwise saturate amplifiers or mixers in the output line and signal processing chain and lead to non-linear and unintended effects.

Shifting our focus to the microwave electronics located outside the croystat at room temperature, panel **d** gives an overview of the components and interconnections of the signal generation and processing chain used in the microwave spectroscopy experiments. Not shown for simplicity, but crucial for the success of the experiment is a Rubidium frequency standard that acts as common 10 MHz reference clock for all active microwave components (VNA, SA, signal generators). On the input side, the probe signal ω_{p} generated at port 1 of the VNA is combined with two additional microwave tones ω_{d} and ω_{s} using two power combiners in series and finally enters the croystat via microwave line A. All microwave input tones are high frequency signals on the order of several GHz. On the output side, the measurement signal exits the cryostat via microwave line D and first passes a directional coupler, which splits off 1% of the signal and routes it to input port 2 of the VNA, after band-pass filtering and amplification. This high frequency path (HF) from port 1 to port 2 of the VNA is used to measure the microwave response spectrum S_{21} of the DUT. The

---

[1] We use a second microwave generator with an integrated option to set the relative phase of the generated signal. Another approach would be to use a single microwave generator along with a power divider and a variable phase shifter to generate pump and cancellation tones from the same source. However, the added flexibility of a separate microwave generator with variable power and phase enables higher cancellation efficiency, when optimized properly.

main part of the signal passes the directional coupler and enters the analog downconversion stage of the setup, which is illustrated in panel **e**.

In the experiments investigating electromechanical systems, the mechanical subsystem's dynamics, oscillating at MHz frequencies with linewidths in the Hz range, are imprinted onto GHz frequency carrier signals, e.g. ω_d or ω_p (detailed in Sec. 2.5). Conducting precise spectral analysis on GHz signals with Hz resolution is technologically demanding and time-consuming. To address this, we employ frequency downconversion, a technique commonly used in digital communication and signal analysis [187]. This method shifts the GHz carrier signal to a more manageable MHz frequency range, simplifying the signal's digitization and analysis.

The downconversion is executed using an analog IQ-demodulator, which mixes the carrier signal with a local oscillator (LO) to produce a new signal known as an intermediate frequency (IF) signal. Additionally, the downconversion setup, illustrated in Fig. 4.1**e** and elaborated in Ref. [188], encompasses various stages of amplification and filtering for both the high-frequency carrier and the IF signal. These stages aim to reduce noise and enhance the signal-to-noise ratio for subsequent analysis. Ultimately, the downconverted (IF) measurement signal is fed into a spectral analyzer (SA) for processing.

4.2 Experimental techniques

Having established the experimental setup and the essential microwave components, we continue by introducing the experimental methods used to investigate electromechanical devices. First, we focus on the characterization of the flux-tuneable microwave resonators using microwave spectroscopy and provide a step-by-step explanation of the signal analysis procedure to extract the main figures of merit describing their performance. Subsequently, we shift the focus to the mechanically compliant element and detail the measurement and analysis eventually leading to quantitative information about the nanostring oscillator.

4.2.1 Microwave characterization of flux-tuneable resonators

An illustrative explanation of the detailed analysis process and fitting procedure for FTRs is presented in Fig. 4.2. Panel **a** depicts an example for the

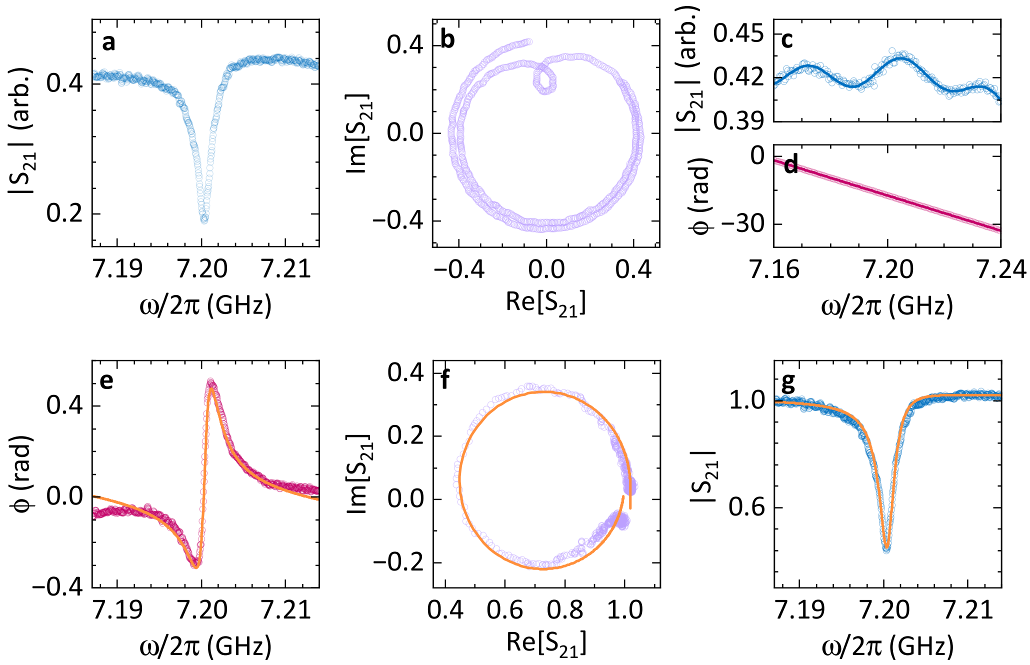

Fig. 4.2.: **Analysis procedure for the characterization of FTRs via microwave spectroscopy.** **a** Raw microwave transmission amplitude $|S_{21}|$ around the resonance frequency of a FTR. **b** shows the same data in the complex plane. A deviation from the ideal circular resonance shape is observed, due to a complex background of the measurement setup. **c** and **d** show the signal background, i.e. S_{21} measured around the same frequency range but with the FTR far detuned, expressed as uncalibrated magnitude (**c**) and unwrapped phase (**d**) along with polynomial fits (solid lines). We correct for the distortion by complex division of the fitted background curves and fit the corrected data with Eq. (4.1). This results in the rescaled and normalized data shown in **e** (phase), **f** (complex response) and **g** (transmission amplitude) along with the fits (orange lines).

raw data captured by a microwave transmission experiment. The experiment was executed using only a VNA (cf. Fig. 4.1**d**), which generates a microwave signal at port 1 and detects the incident voltage at port 2 after passing through the cryostat and the device. The resulting complex transmission parameter $S_{21} = V_2/V_1$ is then determined as a function of the excitation frequency. By plotting the amplitude $|S_{21}|$, one can identify the resonance frequency of the FTR, evident as a dip in transmission. As discussed in Sec. 2.2.2, the shape of this absorption signature is expected to be Lorentzian for an ideal resonator. However, as apparent from **a**, the measured $|S_{21}|$ deviates from this ideal shape, as we observe a slight tilt and unequal transmission on opposite sides of the resonance. This observation is confirmed by visualizing the data in the complex plane, as shown in panel **b**. Here, we observe not only the characteristic circular resonance signature but also additional, smaller circular features and shifts in position and rotation of the circle with respect to the ideal case (more details can be found in Ref. [189]). These perturbations seen in both amplitude and complex representation are a result of the complex background of the measurement setup, including aspects such as electrical delays, impedance mismatches and interference between competing signal paths [87, 189].

Fortunately, the frequency tuneability of the FTR makes it possible to quantify these background contributions and perform a comprehensive correction of their effects. To this end, a separate measurement is conducted with the FTR deliberately detuned far from the region of interest, i.e. the center of the previous measurement. This means that the measurement captures only the background signal, rather than the resonance signature of the FTR. The obtained signal background is expressed as the uncalibrated magnitude in panel **c** and unwrapped phase in panel **d**. We observe several small peaks and dips in the magnitude response, while the phase response is dominated by a linear decrease with frequency, consistent with the effect of a constant electrical delay incurred by the signal propagation in the microwave wiring. In order to correct for the background contribution later on, we first fit the recorded background data with suitable polynomial functions (up to 5th order for magnitude, 1st order for phase), which are shown as solid lines.
Once the background is quantified and approximated by analytical functions, it can be corrected for. This is achieved by conducting a complex division of the fitted background curves from the originally measured data containing the FTR signature. The outcome of this correction is presented in panels **e**, **f**, and **g** as phase, complex plane and magnitude representations, respectively. The phase response now shows the expected phase shift on resonance on a largely flat background. The resonance circle in the complex plane appears rescaled, rotated and translated to intersect the real axis at the canonical off-resonant point at unity, and the corrected magnitude response now resembles an ideal Lorentzian much more closely. Consequently, the plots portray a clearer view of the FTR's response, free from background distortions, thus providing a more accurate representation of its signature.

Finally, to extract the characteristics of the investigated FTR, we fit the corrected data using the *circle fit* model developed by Probst *et al.* [87]

$$S_{21}(f) = Ae^{i\phi}e^{-i2\pi f\tau}\left[1 - \frac{(Q/|Q_\mathrm{e}|)e^{i\theta}}{1+2iQ(f/f_\mathrm{r}-1)}\right]. \tag{4.1}$$

Here, the properties of the resonator are given by the resonance frequency f_r, as well as the internal, external and total quality factors Q_i, Q_e, and $Q = 1/(Q_\mathrm{i}^{-1} +$

Q_e^{-1}), respectively. The model also contains pre-factors in the form of a global amplitude factor A, an added phase ϕ, and an electric delay τ. In addition, the phase θ models the effect of impedance mismatches between input- and output as well as signal paths in parallel to the resonator. It is clear from the presence of these additional terms that the model was developed to fit raw data, with the pre-factors intended to infer and compensate for each of the background effects discussed above. This is necessary for fixed frequency devices, where it is not possible to directly measure the background separately. However, since the subtraction of real background data is feasible for FTRs, it will generally result in better correction results than only applying the fit.

4.2.2 Microwave characterization of the mechanical element

In analogy to the previous discussion of the spectroscopy and data analysis techniques used to characterize microwave resonators, we will introduce the experiments and analysis needed to characterize the mechanical component of an electromechanical system. Unlike the response of the microwave resonator, the resonance condition of the mechanical element is generally not directly observable using a simple microwave transmission experiment as discussed above. Instead, we use a more involved continuous wave (CW) spectroscopy method and process the signal using the full downconversion setup previously described in Fig. 4.1**d,e**. The spectroscopy experiment is schematically illustrated in Fig. 4.3.

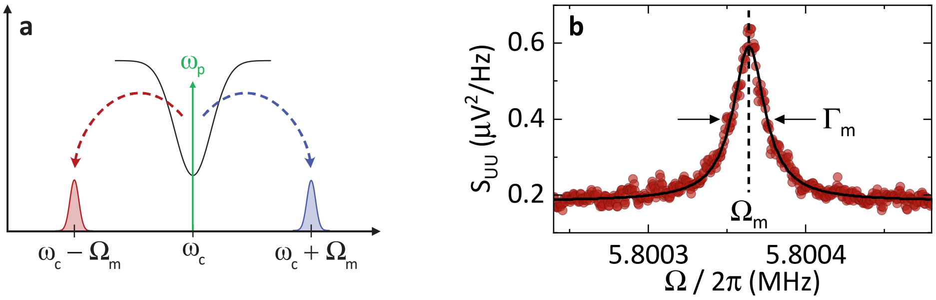

Fig. 4.3.: Microwave spectroscopy of the mechanical oscillator. **a** Schematic illustration of the CW spectroscopy experiment where the system is probed by a microwave tone ω_p and the electromechanical coupling leads to the appearance of sidebands at $\omega_p \pm \Omega_m$. We generally use spectral analysis on the blue-detuned sideband (blue) to determine the properties of the mechanical oscillator. **b** Example of an experimental voltage spectral density $S_{UU}(\Omega)$, acquired by spectral analysis of the downconverted probe tone ω_p. The position and full width half maximum (FWHM) of the spectral density peak corresponds to the resonance frequency Ω_m and loss rate Γ_m of the mechanical oscillator, respectively. Using a fit to a damped harmonic oscillator model Eq. (4.2) (black line), both parameters can be extracted.

In detail, we inject a weak probe tone, which is resonant with the microwave resonator ($\omega_\mathrm{p} = \omega_\mathrm{c}$), into the system[2]. As discussed in Sec. 2.5.2, the electromechanical interaction translates the oscillating displacement of the mechanical resonator into a modulation of ω_c (cf. Fig. 2.13**c**). Since the modulation is periodic with the resonance frequency of the mechanical mode Ω_m, it is represented in frequency space by the appearance of symmetric sidebands at $\omega_\mathrm{p} \pm \Omega_\mathrm{m}$ around the probe tone. In an equivalent scattering picture, these sidebands correspond to the well-known Stokes and anti-Stokes fields. After interaction with the DUT, we use the frequency downconversion path of our experimental setup (cf. Fig. 4.1**e**) to downconvert the signal with a local oscillator ω_LO. In the most common case of *homodyne* downconversion, one sets $\omega_\mathrm{LO} = \omega_\mathrm{p}$, resulting in degenerate Stokes and anti-Stokes fields at the mechanical frequency Ω_m. However, in our experiments, we adopt a *heterodyne* downconversion approach, setting $\omega_\mathrm{LO} = \omega_\mathrm{p} - \delta_\mathrm{het}$. This choice of LO lifts the degeneracy of the sideband frequencies, causing them to manifest in spectral analysis at $\delta_\mathrm{het} \pm \Omega_\mathrm{m}$. This separation allows for the independent investigation of the Stokes and anti-Stokes fields. Unless specified otherwise, we focus our analysis on the anti-Stokes field and we factor the technical frequency offset δ_het into our plots and discussions of the mechanical spectra, i.e. we present our thermal sideband noise spectra relative to the probe tone frequency. In the final stage of the signal processing, the in-phase (I) and out-of-phase (Q) quadrature components of the downconverted probe tone are combined using a 90° hybrid coupler. The signal is then routed to a spectrum analyzer, which evaluates the voltage fluctuations in the signal and computes the voltage spectral density $S_\mathrm{UU}(\Omega)$. This spectral density holds information about the mechanical oscillator responsible for the modulation of the probe signal. An example of an experimentally acquired voltage spectral density is shown in Fig. 4.3**b**.

In the absence of an external driving force, the measured voltage fluctuations $S_\mathrm{UU}(\Omega)$ are proportional to the thermal displacement noise $S_\mathrm{xx}^\mathrm{th}(\Omega)$ of the mechanical oscillator, which we derived in Sec. 2.2.1. The shape and position

---

[2] In the experiments presented later in this work, we often make use of probe tones with a finite detuning $\Delta = \omega_\mathrm{p} - \omega_\mathrm{c}$. However, the signal analysis procedure presented in this section remains unchanged and applicable.

of the peak observed in the voltage spectral density can therefore be fitted by a model based on Eq. (2.31)

$$S_{\mathrm{UU}}(\Omega) = A\frac{2\Gamma_{\mathrm{m}}}{(\Omega^2 - \Omega_{\mathrm{m}}^2)^2 + \Gamma_{\mathrm{m}}^2\Omega^2} + B\,. \tag{4.2}$$

From the fit, the characteristic linewidth Γ_{m} and resonance frequency Ω_{m} of the mechanical element can be extracted, along with an amplitude factor A and a constant background signal B. It is important to note that the variance of the physical displacement of the mechanical oscillator, and accordingly its phonon occupation, is not directly accessible from our measurement observable $S_{\mathrm{UU}}(\Omega)$ as determined above. However, with sufficient knowledge of the experimental setup and a suitable measurement protocol, a calibration can be performed to reveal this information.

4.2.3 Frequency noise calibration

To gain insight into the displacement of the mechanical oscillator, we employ a calibration technique based on frequency modulation, drawing inspiration from established protocols in quantum optics, notably those detailed in Ref. [75]. In the following, we will highlight the most important aspects and equations. A comprehensive derivation can be found in the supplementary material of Ref. [57].

As a starting point, we recall the double-sided displacement spectral density of a harmonic oscillator in thermal equilibrium with a bath of temperature T (cf. Eq. (2.31) in Sec. 2.2.1)

$$S_{\mathrm{xx}}^{\mathrm{th}}(\Omega) = \frac{1}{m_{\mathrm{eff}}}\frac{2\Gamma_{\mathrm{m}}k_{\mathrm{B}}T}{(\Omega^2 - \Omega_{\mathrm{m}}^2)^2 + \Gamma_{\mathrm{m}}^2\Omega^2}\,, \tag{4.3}$$

which is proportional to $S_{\mathrm{UU}}(\Omega)$ (Eq. (4.2)) using a suitable amplitude factor. Further, we know that the electromechanical coupling in our system translates the thermal motion of the nanostring oscillator into a frequency modulation of the microwave resonator. Hence,

$$S_{\omega\omega} = G^2 S_{\mathrm{xx}} \tag{4.4}$$

where $G = g_0/x_{\mathrm{zpf}}$. Using the above expressions and integration over the entire frequency range, we can associate the frequency fluctuations with the average number of phonons occupying the mechanical mode, $\bar{n}_{\mathrm{ph}}$ and the single-photon coupling rate g_0 [75]

$$\langle \delta\omega^2 \rangle = \int_{-\infty}^{+\infty} S_{\omega\omega}(\Omega) \frac{d\Omega}{2\pi} = S_{\omega\omega}(\Omega_{\mathrm{m}}) \frac{\Gamma_{\mathrm{m}}}{2} = 2\bar{n}_{\mathrm{ph}} g_0^2 \,, \tag{4.5}$$

where we have used $\bar{n}_{\mathrm{ph}} \approx k_{\mathrm{B}} T / \hbar \Omega_{\mathrm{m}} \gg 1$ in the last equality. In practice, Eq. (4.5) shows that we can determine $\langle \delta\omega^2 \rangle$ and therefore $\bar{n}_{\mathrm{ph}} g_0^2$ from the integrated peak area, as long as we have access to $S_{\omega\omega}(\Omega)$ experimentally.

In order to make use of this equality, the goal of the frequency noise calibration technique is to establish a relationship between the direct observable of the FTRs resonance frequency fluctuations, denoted as $S_{\omega\omega}(\Omega)$ – or equivalent phase fluctuations $S_{\Psi\Psi}(\Omega)$ – and the measured observable $S_{\mathrm{UU}}(\Omega)$. Formally, we express this relationship by introducing the transfer function K_Ψ via

$$S_{\mathrm{UU}}(\Omega) = K_\Psi(\Omega) S_{\Psi\Psi}(\Omega) = \frac{K_\Psi(\Omega)}{\Omega^2} S_{\omega\omega}(\Omega) \,. \tag{4.6}$$

To gain knowledge about this transfer function experimentally, we introduce an artificial, well-defined frequency fluctuation by frequency-modulating the probe tone ω_{p} with a modulation frequency Ω_{mod} and a frequency deviation Ω_{dev}. The frequency modulation once again is expressed as a phase modulation $S_{\Phi\Phi}$ and becomes converted in our experiment into a measured voltage signal via:

$$S_{\mathrm{UU}}(\Omega) = K_\Phi(\Omega) S_{\Phi\Phi}(\Omega) \,, \tag{4.7}$$

where K_Φ is an additional transfer function. Experimentally, the modulation used for the calibration manifests itself as a second, sharp peak in the down-converted spectroscopy signal at Ω_{mod}, as seen in Fig. 4.4**a**.

As the parameters of the artificial modulation, Ω_{mod} and Ω_{dev}, are known, we can predict the recorded voltage spectral density at the modulation frequency [75]

$$S_{\mathrm{UU}}(\Omega_{\mathrm{mod}}) = \frac{\phi_0^2}{4} \frac{K_\Phi(\Omega_{\mathrm{mod}})}{\mathrm{ENBW}} \,, \tag{4.8}$$

where ENBW is the measurement bandwidth of the spectral analyzer in units of Hz and $\phi_0 = \Omega_{\mathrm{dev}} / \Omega_{\mathrm{mod}}$ is the phase modulation depth. Furthermore, based on Eq. (4.5) we expect at the mechanical frequency [57]

$$S_{\mathrm{UU}}(\Omega_{\mathrm{m}}) = K_\Psi S_{\Psi\Psi}(\Omega_{\mathrm{m}}) = \frac{K_\Psi}{\Omega_{\mathrm{m}}^2} S_{\omega\omega}(\Omega_{\mathrm{m}}) = \frac{K_\Psi}{\Omega_{\mathrm{m}}^2} \frac{4 g_0^2}{\Gamma_{\mathrm{m}}} \bar{n}_{\mathrm{ph}} \,. \tag{4.9}$$

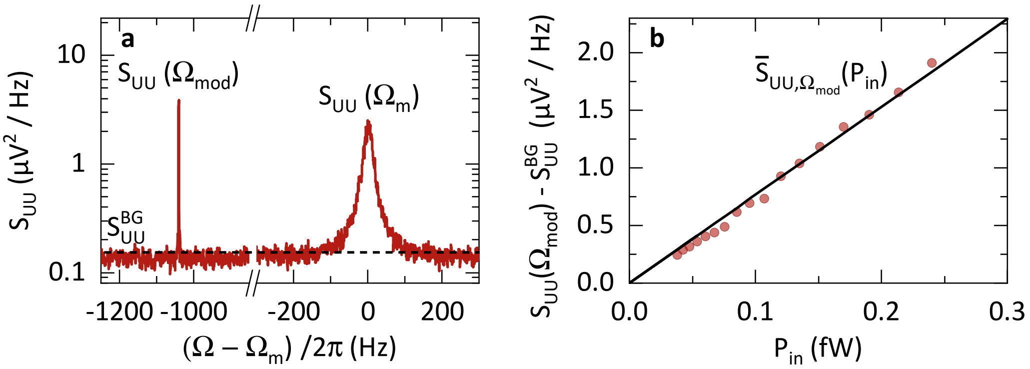

Fig. 4.4.: Exemplary spectrum with calibration peak and mechanical signature. **a** Voltage spectral density spectrum in frequency noise calibration setting. Both the anti-stokes field caused by the mechanical motion of the nanostring $S_{\mathrm{UU}}(\Omega_{\mathrm{m}})$ and a sharp peak arising from the frequency modulation of the probe tone $S_{\mathrm{UU}}(\Omega_{\mathrm{mod}})$ are visible on top of a signal background $S_{\mathrm{UU}}^{\mathrm{BG}}$. **b** Extracted Intensity of the background corrected modulation signal $S_{\mathrm{UU}}(\Omega_{\mathrm{mod}}) - S_{\mathrm{UU}}^{\mathrm{BG}}$ as a function of probe tone power P_{in}. We fit a linear dependence through the origin to extract the corrected modulation amplitude $\bar{S}_{\mathrm{UU},\Omega_{\mathrm{mod}}}$.

Note that both Eq. (4.8) and Eq. (4.9) differ from the expressions found in Refs. [57, 75] by a factor of 2. The reason for this discrepancy is that Gorodetsky et al. [75] developed the calibration for a specific experimental setting of optical homodyning. As discussed in Sec. 4.2.2, homodyne downconversion will lead to the appearance of symmetrical sidebands at $\pm\Omega_{\mathrm{m}}$ in the downconverted probe signal. The spectrum analyzer used to evaluate the signal, however, conventionally displays single-sided spectra, i.e. it will fold negative frequency components onto the positive frequency space. For a symmetrical, double-sided spectral density like $S_{\mathrm{UU}}(\Omega)$, this process effectively leads to multiplication of the measured spectral density by 2. In our experiment, the heterodyne downconversion breaks the symmetry, with sidebands instead appearing at $\delta_{\mathrm{het}} \pm \Omega_{\mathrm{m}}$ in the downconverted signal. With the sideband frequencies not being symmetric w.r.t. zero, the folding of negative frequencies does not result in the overlap of positive and negative frequency components, and only half of the spectral density is recorded, compared to the homodyne case. If properly implemented, the choice of homodyne vs. heterodyne detection and convention of single-sided vs. double-sided spectra does not alter the result of the frequency noise calibration technique. However, care must be taken to adapt all formulas consistently to the implemented measurement protocol. We discuss this challenge in more detail in App. A.2.

A second difference in the measurement protocol is the handling of the artificial frequency modulation. In the optical homodyning experiment, the frequency modulation is applied before the beamsplitter, i.e. the same stimulus, including the frequency modulation, is used to probe the DUT and acts as LO for the downconversion. In such experiments, it can be shown that $K_\Phi = K_\Psi$, leading to the cancellation of the transfer functions [75]. However, for our experiments, where the frequency modulation is only applied to the probe tone and not to the LO, this is not generally the case, and we need to generalize the treatment by introducing the transform factor $\mathcal{Y}$ as

$$K_\Psi = \mathcal{Y} K_\Phi \,. \tag{4.10}$$

Lastly, since our experiment is performed in the microwave domain, the detected signal is the voltage fluctuations present at the I and Q outputs of the mixer that downconverts the probe signal. Therefore, we expect the amplitude of the calibration signal to increase linearly with microwave power ($S_{\mathrm{UU}}(\Omega_{\mathrm{mod}}) \propto P_{\mathrm{in}}$) [57], but find that the power-dependent background $S_{\mathrm{UU}}^{\mathrm{BG}}$ conceals this relationship in many experimental datasets. To adjust for the power-dependent effects, we extract the background-corrected calibration magnitude $S_{\mathrm{UU}}(\Omega_{\mathrm{mod}}) - S_{\mathrm{UU}}^{\mathrm{BG}}$ as a function of microwave power and fit the linear dependence, as illustrated in Fig. 4.4**b**. From the slope of the fit, we calculate the corrected calibration amplitude $\bar{S}_{\mathrm{UU},\Omega_{\mathrm{mod}}}(P_{\mathrm{in}})$ and use it in place of $S_{\mathrm{UU}}(\Omega_{\mathrm{mod}})$.

Using the aforementioned adjustments to the model, together with Eq. (4.9) and Eq. (4.8), we find the desired calibration

$$S_{\omega\omega}(\Omega) = \frac{1}{4}\frac{1}{\mathcal{Y}}\frac{\Omega_{\mathrm{m}}^2\phi_0^2}{\mathrm{ENBW}}\frac{S_{\mathrm{UU}}(\Omega)}{\bar{S}_{\mathrm{UU},\Omega_{\mathrm{mod}}}} \,, \tag{4.11}$$

and accordingly an expression for the optomechanical single-photon coupling rate

$$2\bar{n}_{\mathrm{ph}} g_0^2 = \frac{1}{8}\frac{\Gamma_{\mathrm{m}}}{\mathcal{Y}}\frac{\Omega_{\mathrm{m}}^2\phi_0^2}{\mathrm{ENBW}}\frac{S_{\mathrm{UU}}(\Omega_{\mathrm{m}})}{\bar{S}_{\mathrm{UU},\Omega_{\mathrm{mod}}}} \,. \tag{4.12}$$

In the above equations it is assumed that the transfer functions do not vary significantly in the frequency range of interest, i.e. $K_{\Psi,\Phi}(\Omega) \approx K_{\Psi,\Phi}(\Omega_{\mathrm{m}}) \approx K_{\Psi,\Phi}(\Omega_{\mathrm{mod}})$.

At this point, all of the variables in Eq. (4.11) are known, except for the exact form of the transform factor $\mathcal{Y}$, which can be calculated for the specific experiment using input-output theory to [57]

$$\mathcal{Y} \approx \frac{16\eta^2\kappa^2\Omega_\mathrm{m}^2}{(4|\Delta|^2+\kappa^2)(4(|\Delta|-\Omega_\mathrm{m})^2+(1-2\eta)^2\kappa^2)}\,, \tag{4.13}$$

with the loss rate κ and coupling efficiency $\eta = \kappa_\mathrm{ext}/\kappa$ of the microwave resonator. Note that the calculation of $\mathcal{Y}$ requires extensive knowledge of the FTR properties, which are subject to change based on experimental conditions (e.g. power or temperature). Therefore, in-situ characterization of the FTR and repeated adjustment of $\mathcal{Y}$ for every measurement are generally necessary.

Finally, once g_0 is successfully extracted from the measurement, we can use $S_{\omega\omega}(\Omega)$ together with Eq. (4.4) to access the physical displacement of the mechanical oscillator in the form of the displacement spectral density $S_\mathrm{xx}(\Omega)$ via the optomechanical coupling rate according to

$$S_\mathrm{xx}(\Omega) = \frac{x_\mathrm{zpf}^2}{g_0^2}S_{\omega\omega}(\Omega)\,. \tag{4.14}$$

4.3 The challenge of flux noise in electromechanics

One of the most successful and widespread applications of SQUIDs is in magnetometry, where the extreme sensitivity of a SQUID's inductance to an external flux is exploited to detect even the smallest magnetic signals. That same property of the incorporated SQUID, however, makes the flux-tunable devices used in this work extremely susceptible to the presence of flux noise. Flux noise can originate from external sources and manifest as real change to the flux threading the loop, but can also arise intrinsically from the dynamics within the SQUID itself. In both cases, the flux noise will be translated into an effective change of resonance frequency of the flux-tuneable device via its flux responsivity $\partial\omega_\mathrm{c}/\partial\Phi$. As discussed in Sec. 3.1, a large flux responsivity is generally advantageous for the realization of flux-mediated electromechanical coupling. Therefore, flux noise is a particularly challenging aspect of experimental work with this class of devices.

For the intended operation at GHz frequencies, Johnson-Nyquist noise is generally assumed to be the primary contribution to intrinsic white flux noise in SQUIDs. The microscopic origin of this type of noise can be understood as dissipative quasiparticle currents within the Josephson junctions. The spectral density of Johnson-Nyquist noise can be calculated according to [190]

$$S_\Phi = 4(1+\beta_L)\frac{k_B T L_{\text{loop}}}{\Phi_0 I_{c0} R_n}, \tag{4.15}$$

given in units of Φ_0^2/Hz. Here, we used the Boltzmann constant k_B and the SQUID normal state resistance $R_n = \pi\Delta/(2eI_{c0})$, with the superconducting gap at zero temperature Δ (0.18 meV for aluminum) [91]. Using real parameters of a device investigated in this work ($\beta_L = 0.2$, $I_{c0} = 1.6\,\mu\text{A}$, $L_{\text{loop}} = 130\,\text{pH}$ and $T = 80\,\text{mK}$) we can estimate a RMS flux noise of $\sqrt{S_\Phi} \approx 34\,\text{n}\Phi_0/\sqrt{\text{Hz}}$. Operating at a steep working point with a flux responsivity of $\partial\omega_c/\partial\Phi = 2\pi \times 5.7\,\text{GHz}/\Phi_0$ this would translate to a RMS resonance frequency fluctuation of $\approx 195\sqrt{\kappa/2\pi}$. Based on this result and $\kappa/2\pi \approx 1\,\text{MHz}$ for the same device, the fluctuations are significantly smaller than the linewidth of the FTR and intrinsic flux noise will only have negligible impact on our experiments.

Therefore, we instead focus on external sources of flux noise that affect the experiment. We can further distinguish these sources of noise by their frequency f_{noise} in relation to the FTR loss rate κ and the measurement bandwidth Δf_{meas}. In most cases, high frequency noise that oscillates faster than the FTR loss rate ($f_{\text{noise}} > \kappa$) will not alter the result of a measurement. Low frequency flux noise on the other hand can either manifest as an experimentally observed shift in the FTRs resonance frequency ($f_{\text{noise}} < \Delta f_{\text{meas}}$) or an effective broadening of its linewidth ($f_{\text{noise}} > \Delta f_{\text{meas}}$). The latter category is also known and studied as a source of pure dephasing in superconducting qubits [191]. It turns out that the experiments presented in this work suffer primarily from ultra-low frequency noise that falls into the former category ($f_{\text{noise}} < 1\,\text{Hz}$). In the following, we will identify and investigate the two primary types of flux noise in our experiments and present our approach to a technical solution to accomplish a significant suppression of their impact.

Mechanically induced low-frequency flux noise The first of the challenges we faced during measurements of flux-tuneable electromechanical devices is illustrated exemplary in Fig. 4.5. Panel **a** shows several measurements of the microwave transmission $|S_{21}|$ around the resonance signature of a FTR, while a constant in-plane magnetic field of $B_{\text{ip}} = 1.5\,\text{mT}$ is applied. Periodic oscillations as a function of probe frequency are visible in the transmitted signal. When the measurement is repeated using a different measurement bandwidth

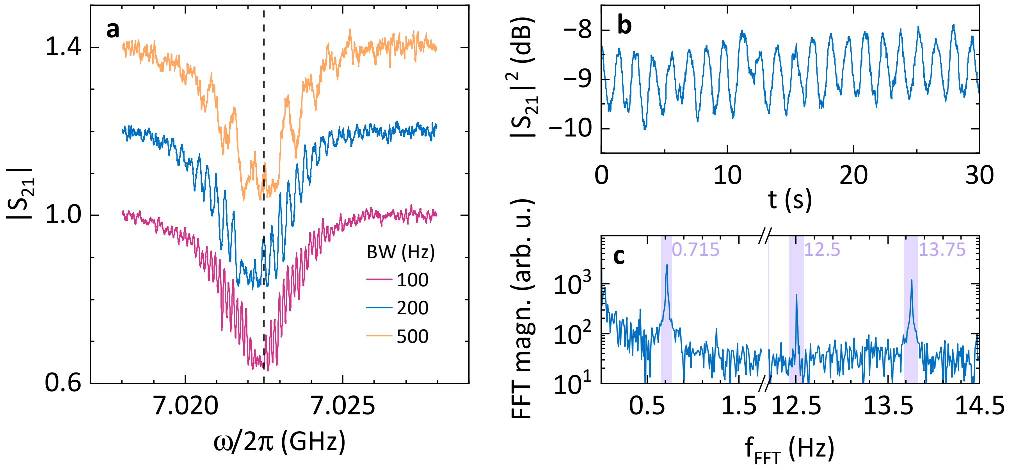

Fig. 4.5.: Oscillatory features associated with external flux noise in FTR spectroscopy. a shows three linescans of $|S_{21}|$ around the resonance signature of a FTR tuned to a highly sensitive working point, each taken with a different measurement bandwidth Δf_{meas}. The traces are offset by 0.2 for clarity. Periodic oscillations are visible in the acquired signal with a period that increases with Δf_{meas}. **b** Excerpt of the time-resolved microwave transmission $|S_{21}(t)|$ measured at a fixed frequency on resonance with the FTR (cf. dashed line in **a**). The measurement is taken using the CW mode of a VNA and $\Delta f_{\mathrm{meas}} = 200\,\mathrm{Hz}$. **c** FFT of the full time domain measurement partly shown in **b**. The largest contribution to the oscillating noise can be identified around $0.7\,\mathrm{Hz}$. The experiments are performed at $T = 80\,\mathrm{mK}$ and $B_{\mathrm{ip}} = 1.5\,\mathrm{mT}$.

of the VNA, the oscillation period in the frequency response appears to change. This implies that the periodic change in $|S_{21}|$ can be associated with a noise source with a defined period $1/f_{\mathrm{noise}}$ which is smaller but on the same order of magnitude as the measurement duration. In order to quantify this type of external flux noise and identify its source, we next perform time-resolved, continuous wave (CW) spectroscopy at a single frequency on resonance with the FTR. The recorded microwave transmission over time $|S_{21}(t)|$ is displayed in panel **b** and clearly shows a periodic oscillation in signal amplitude, which is consistent with a periodic change in the FTRs resonance frequency due to external flux. We then perform a Fast Fourier Transformation (FFT) on the time-resolved measurement to decompose the time series into frequency components (panel **c**) and find the largest contribution at $f_{\mathrm{FFT}} \approx 0.7\,\mathrm{Hz}$. Two other distinct frequencies can be identified at $12.5\,\mathrm{Hz}$ and $13.7\,\mathrm{Hz}$, but it is clear from panel **b** that the slower $0.7\,\mathrm{Hz}$ oscillation dominates the noise in the signal. Other experiments with flux-sensitive electromechanical devices have observed similar oscillatory features and could successfully trace their origin to the mechanical vibrations caused by the pulse tube refrigerators (PTR) which are used for the pre-cooling of dry dilution refrigerators [112, 192]. In these cases, the vibrations, and with them the oscillations in the signal, could be removed by switching off the PTR for the duration of the measurement. However, an analogous attempt in our experiment did not lead to any change in the observed signal oscillations. Furthermore, the PTRs commonly built into dilution refrigerators have repetition rates of 1.2 Hz or 1.4 Hz, but we do not find oscillatory components at those frequencies in our Fourier transformed signal. Therefore, we conclude that vibrations from the pulse tube are not the source of the periodic noise.

However, the periodicity and frequency on the lower Hz regime nevertheless suggests a type of mechanical vibration at the origin of the oscillating noise. The most plausible explanation appears to be the movement of the chip including its packaging with respect to the externally applied magnetic field. We recall the discussion of the experimental setup in Sec. 4.1: The sample is mounted to an extension of the mixing chamber plate of the dilution refrigerator and is positioned into the center of the 3D vector magnet used to generate the in-plane magnetic field. As the sample is not physically anchored to the magnet, it can be displaced with respect to the static magnetic field. Since alignment of the sample holder along the field direction of the vector magnet is done manually and subject to small errors, not only rotation but even displacement along the in-plane field direction can give rise to fluctuating out-of-plane field components, which are translated to a change in resonance frequency of the flux-tuneable device. We perform a rough estimate of the effect of such relative displacement for $B_{\mathrm{ip}} = 1.5\,\mathrm{mT}$ and a high flux sensitivity of $\partial\omega_{\mathrm{c}}/\partial\Phi \approx 2\pi \times 5.7\,\mathrm{GHz}/\Phi_0$ as in the above measurements and find that a tilting of the sample by an angle $\alpha < 0.1^\circ$ w.r.t the magnets in-plane field direction is sufficient to cause frequency shifts up to 1 MHz.

In the short term, the impact of such low-frequency oscillations on the experiments can be minimized by careful choice of measurement parameters. It can already be seen in Fig. 4.5**a** that for low measurement bandwidths the individual oscillations become harder to distinguish as they become fast compared to the dwell time at each frequency. For sufficiently low bandwidths and/or by using the average feature of the VNA the oscillations eventually are averaged out into the shape of a slightly broadened Lorentzian, which can be successfully fitted using the theoretical model introduced in Sec. 2.2.2. The effect of this type of mechanically induced flux noise is then visible as an effective increase of the extracted linewidth κ, but is no longer an immediate hindrance to the measurement procedure or the analysis. In the long term the underlying mechanical vibrations either need to be filtered or the experimental setup needs to be adapted to no longer be susceptible to this type of noise. Unfortunately, at the ultra-low frequency band of interest ($f \approx 0.7\,\mathrm{Hz}$) even very large mechanical low-pass filters such as spring systems generally do not achieve significant attenuation. Therefore, the most promising solution is the development of a different type of (vector) magnet that can be directly anchored to the mixing chamber plate of the cryostat and the sample such that all components react to vibrations in concert and no relative displacement is possible.

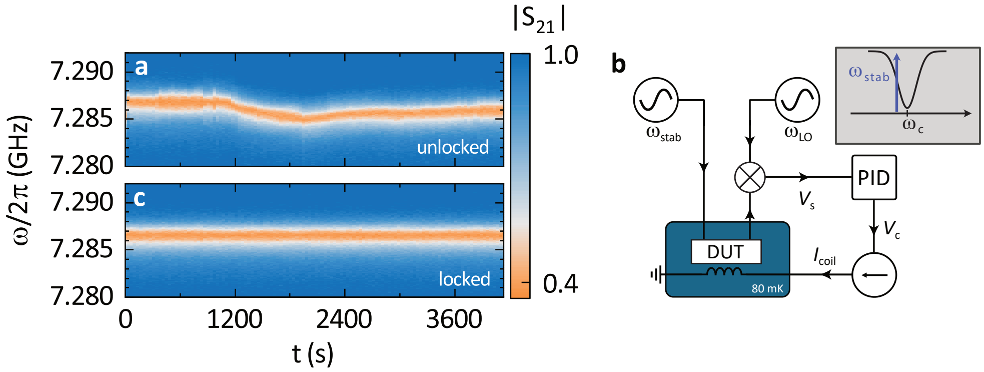

Fig. 4.6.: **Long term resonance frequency drifts. a** Microwave transmission of a FTR repeatedly measured over the course of 1 hour in intervals of $30\,\mathrm{s}$. The resonance signature can be identified as a decrease in $|S_{21}|$, encoded in orange color. Slow drifts across several MHz are visible over the course of the measurement. **b** Schematic of the active feedback circuit used to stabilize the FTR resonance frequency against slow drifts using a PID controller to provide real time feedback via the tuning coil mounted to the DUT. The part of the circuit inside the cryostat is shaded blue and heavily simplified. The top right inset illustrates the off-resonant placement of the stabilization tone ω_{stab}. **c** A long term microwave transmission measurement nominally identical to the one shown in **a**, but with active frequency stabilization enabled. No drifts in resonance frequency are observed over the measurement duration. The experiments are performed at $T = 80\,\mathrm{mK}$ and $B_{\mathrm{ip}} = 1.5\,\mathrm{mT}$.

Long term resonance frequency drifts due to external flux noise The second experimental challenge related to external flux noise is well illustrated in the data shown in Fig. 4.6**a**. In the associated measurement, the microwave transmission of a FTR was repeatedly probed every 30 s over the course of one hour while the in-plane magnetic field B_{ip} was kept constant at 1.5 mT. While the settings and conditions of the repeated linescans remain nominally the same, the frequency of the resonance signature (orange) drifts across a range of several MHz. Such drifts in resonance frequency can be highly problematic, especially for long measurements, as many experiments rely on a careful selection of microwave drive or probe frequencies relative to the resonance frequency of the investigated FTR. The specific origin of the drifts is hard to pinpoint without extensive investigation, but several plausible explanations exist:

First and foremost, it should be noted that in the experimental setup as introduced in Sec. 4.1, no dedicated shielding against external magnetic fields can be employed around the device, since the in-plane magnetic field generated by the vector magnet must not be impaired. Therefore, the complex magnetic field environment in the laboratory, which contains many electronic devices, can reach the sample and lead to fluctuations in the external flux. A second option is the movement of flux vortices across the superconducting thin film. It has been reported that in strong enough magnetic fields, aluminum thin films exhibit a mixed state comparable to type-II superconductors and form vortices through which the field penetrates the thin film [156, 193]. These vortices, also called *fluxons*, will generally distribute themselves across the film in a lattice. The supercurrents around the vortices in proximity to the SQUID can then generate fields that contribute to the external flux penetrating the SQUID [194]. While the vortices generally remain pinned at defect sites, they can stochastically hop between sites, leading to abrupt changes in the flux environment of the SQUID [195]. Improvements to the shielding or packaging of the sample like the magnet arrangement discussed above are promising approaches to reduce the effect of the drifts, but it is likely that some degree of long term instability is unavoidable in any experimental investigation of flux-tuneable devices.

Therefore, instead of attempting to prevent the underlying flux noise entirely, we developed an active feedback system to dynamically compensate for frequency fluctuations. A schematic of its working principle is shown in Fig. 4.6**b**. The feedback system is based on a constant, low-power microwave tone ω_{stab} slightly off-resonant with the to-be-stabilized FTR (i.e. $\omega_{\mathrm{stab}} = \omega_{\mathrm{c}} + \delta_{\mathrm{s}}$). After being sent through the cryostat and the device under test (DUT), downconversion with a local oscillator ω_{LO} converts the transmitted signal at the stabilizer frequency $|S_{21}(\omega_{\mathrm{stab}})|$ into a DC voltage signal V_{s}, which is routed as the input signal to a proportional-integral-derivative (PID) controller. The detuning δ_{s} of the stabilization tone is chosen such that it is placed on the maximum slope of the Lorentzian lineshape of the FTR's resonance signature (see inset). Therefore, a small shift in the resonance frequency of the FTR leads to a relatively large, roughly linear change in the microwave transmission $|S_{21}(\omega_{\mathrm{stab}})|$. In order to lock the frequency of the FTR at the start of a measurement, the momentary value of $V_{\mathrm{s}}(t = 0)$ is set as target value of the PID. The PID is configured to output a control voltage V_{c}, which is proportional to the error $V_{\mathrm{s}}(t) - V_{\mathrm{s}}(0)$.

The control voltage is then attenuated and routed to a voltage-controlled current source, which drives the bias coil attached to the flux-tuneable device. Effectively, V_c is treated as an offset voltage to the internal voltage generator of the current source and dynamically modulates the coil current I_{coil} and with it the out-of-plane bias field B_{oop}. The bias field in turn will shift the resonance frequency of the flux-tuneable device until $V_s(t)$ returns to the target value.

The effect of the active feedback loop can be seen in Fig. 4.6**c** where we show a repetition of the measurement shown in panel **a**, using identical settings and working points, but with the frequency stabilization enabled. Once again we monitor the microwave transmission around the resonance signature of the FTR over the course of one hour. Unlike in the previous measurement, the shape and position of the resonance feature (orange) does not exhibit any discernible drifts, suggesting that the feedback loop successfully compensates any changes in the external flux by adapting the coil current accordingly. To provide a more detailed comparison between the stabilized and non-stabilized case, all individual linescans of both measurements (120 traces each) are plotted in panel Fig. 4.7**a**. Clearly, in the non-stabilized case (blue) multiple overlapping traces with significantly different resonance frequencies are visible. With the FTR locked by the active stabilization loop (red) on the other hand, all 120 traces overlap almost completely and no deviation from the initial resonance frequency and lineshape is discernible by eye. To gain a quantitative understanding of the performance, we fit each of the traces using the circle fit model (see Sec. 4.2.1) and determine the exact resonance frequency. From the extracted frequencies, we calculate the deviation relative to the first linescan and plot their distribution as a histogram in Fig. 4.7**b**. The spread of extracted

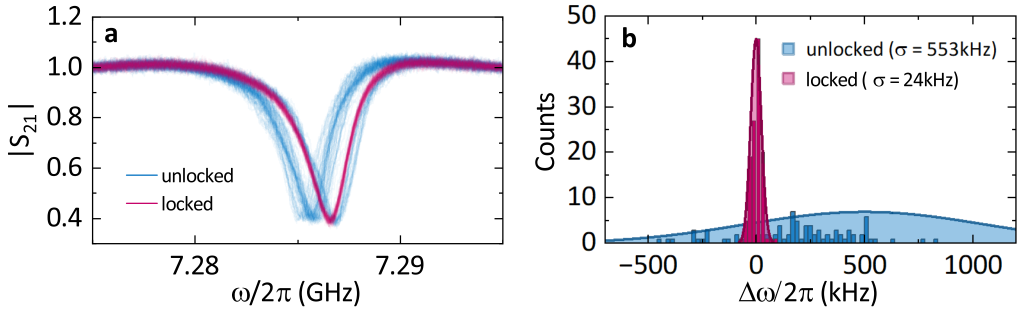

Fig. 4.7.: Active feedback system performance. a Individual traces of two long-term stability experiments of a FTR with (red) and without (blue) frequency locking. Each measurement consists of 120 linescans recorded in intervals of 30 s. **b** Histogram of the resonance frequency distribution with and without frequency locking extracted from fits to the data in **a**. The standard deviation is reduced by a factor of 23 for the frequency locked measurement. The experiments are performed at $T = 80\,\mathrm{mK}$ and $B_{ip} = 1.5\,\mathrm{mT}$.

resonance frequencies is drastically reduced for the measurement with frequency locking enabled. We quantify the stabilization performance further by calculating the standard deviation σ of the Gaussian distributions (shaded areas) and find $\sigma_{\mathrm{unlocked}} = 553\,\mathrm{kHz}$ and $\sigma_{\mathrm{locked}} = 24\,\mathrm{kHz}$, an improvement by a factor of 23.

Clearly the developed frequency stabilization system is capable of almost entirely negating the long term resonance frequency drifts caused by external flux noise and constitutes an essential tool for the investigation of flux-tuneable electromechanical devices. Generally, no adverse effects on the measurement are to be expected with this technique as long as proper care is taken with the choice of frequency and power of the stabilization tone. In particular, ω_{stab} needs to be chosen so that it does not interfere with any of the microwave drives used in the experiment. Further, its power should be kept to the absolute minimum necessary to generate a usable stabilization signal V_{s}. Using too large powers introduces the risk of populating the microwave resonator with additional photons that can interact with the measurement, for example via optomechanical damping or the spring effect (see Sec. 2.5). However, in our experiments, the feedback circuit performed well with stabilization tone powers below 10 aW at the sample, which can be translated with Eq. (2.80) to an average occupation of <1 photon in the FTR, well below where optomechanical effects should become non-negligible.

4.4 Quantum limited amplification using a Josephson Parametric Amplifier

As discussed in the previous sections, the comprehensive characterization of electromechanical devices requires the detection of weak signals caused by the thermal motion of nanoscale mechanical oscillators, sometimes down to the level of individual quanta of motion. When measuring in such highly sensitive regimes, measurement accuracy can quickly become limited by the noise performance of individual components. In the realm of commercially available components for the microwave frequency regime, this often comes down to the noise added by the cryogenic HEMT (high electron mobility transistor) amplifiers, which constitute the first amplification stage of the gain chain. If the detection system is designed appropriately, this amplifier limits the total noise performance and introduces on the order of $n_{\mathrm{add}} = 10$ noise photons to the signal [196]. A solution to this problem is the introduction of quantum limited amplifier designs based on superconducting Josephson circuits, like Josephson Parametric Amplifiers (JPAs) [100] or Travelling Wave Parametric Amplifiers (TWPAs) [197], which in principle are capable of amplification at the standard quantum limit ($n_{\mathrm{add}} = 1/2$) [198] or even beyond it [196].

In our experimental setup, which is detailed in Sec. 4.1, we use a Dimer Josephson Junction Array Amplifier (DJJAA) kindly provided by the Kirchmair Group from the University of Innsbruck [199]. This type of JPA is based on a superconducting circuit implementation of a Bose-Hubbard dimer [123, 124], supplemented by an array of Josephson junctions in order to increase the bandwidth and dynamic range of the amplifier in comparison to the more basic single SQUID designs [125]. Fundamentally, the DJJAA implements a four-wave mixing process to enable non-degenerate, phase-preserving amplification, as introduced in Sec. 2.4. In the following section, we will present dedicated experimental data to characterize the performance of the DJJAA specifically in our setup. A more comprehensive treatment of DJJAA class devices, including theoretical background and noise characterization, is found in Ref. [125], and an investigation of the exact same device used in this work was performed in Ref. [199].

Flux tuneability and non-degenerate gain JPAs make twofold use of the fact that their resonance frequency is flux-dependent. Not only is the periodic modulation of the resonance frequency the fundamental drive behind parametric amplification, but the flux-tuneability itself also allows the device to operate at a broader range of operating frequencies, somewhat compensating for the generally limited bandwidth of JPAs. Accordingly, we begin the characterization of the JPA in our setup by recording a flux tuning curve, i.e. a repeated broadband measurement of the JPA's microwave reflection S_{11} in order to extract the shape and position of its resonance signature as a function of I_{JPA}, the DC-current applied to the bias coil mounted to the JPAs sample packaging. The results of one such measurement are presented in Fig. 4.8**a**. Immediately, a major difference of the employed DJJAA design w.r.t. a standard FTR or single-SQUID JPA presents itself: Not just a single resonance feature, identifiable by dark red color, appears in the plot, but multiple sets of dimers (i.e. two parallel resonance dips) are visible as they exhibit the characteristic

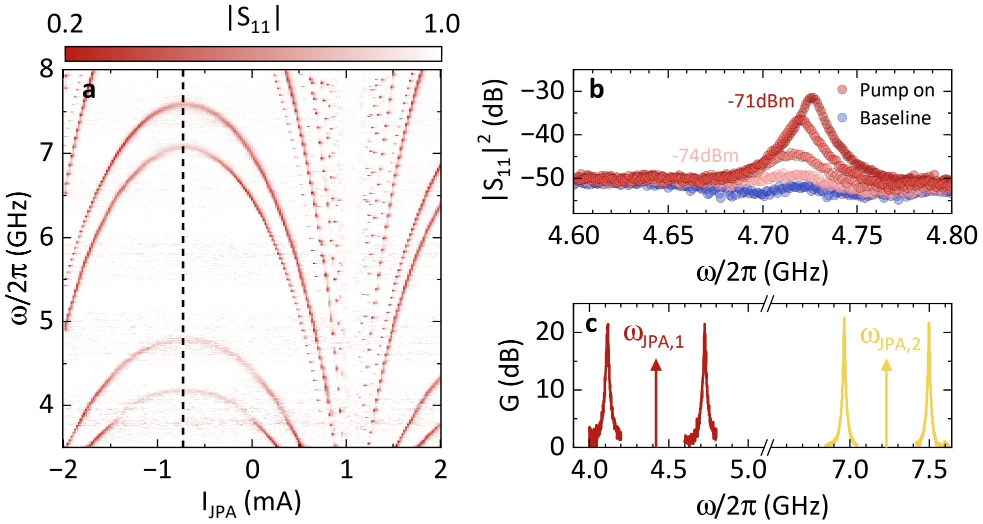

Fig. 4.8.: DJJAA Flux-tuneability and gain profile. a Microwave reflection coefficient $|S_{11}|$ of the DJJA amplifier as a function of DC-current I_{JPA} applied to the bias coil. Two pairs of flux periodic resonance features are visible around $4\,\mathrm{GHz}$ and $7\,\mathrm{GHz}$ as well as indications of higher frequency modes. **b** Effect of parametric pumping of the DJJAA. $|S_{11}|$ measured around the upper mode of the $4\,\mathrm{GHz}$ dimer with a coherent pump signal $\omega_{\mathrm{JPA},1}/2\pi = 4.442\,\mathrm{GHz}$ of increasing power applied (light to dark red) and without pump and the DJJAA far detuned to $I_{\mathrm{JPA}} = 1\,\mathrm{mA}$ (blue). The amplifier gain $G(\omega)$ can be calculated from $|S_{11}|^2$ as the difference between baseline and the response with active pump. **c** Measured gain profiles for pump tones applied at $\omega_{\mathrm{JPA},1}/2\pi = 4.442\,\mathrm{GHz}$ and $\omega_{\mathrm{JPA},2}/2\pi = 7.23\,\mathrm{GHz}$. Gain measurements in **b** and **c** are performed with the DJJAA tuned to a flux bias point of $I_{\mathrm{JPA}} = -730\,\mu\mathrm{A}$ (dashed line in **a**).

cosine-like frequency tuning behavior with the applied flux. This peculiar mode structure is created by the two capacitively coupled Josephson Junction arrays that give the DJJAA its name (see Ref. [125]). Generally, the frequency of the resonance features is closely related to the frequencies for which a JPA can perform parametric amplification. The existence of multiple mode pairs in the DJJAA therefore promises an increased operating range as opposed to standard JPAs. Since many of our microwave components are designed to operate in the 4 GHz to 8 GHz band, we can only make use of the two dimers around 4 GHz and 7 GHz, and therefore limit our discussion to these modes.

Having mapped out the flux dependency of the two dimers' resonance frequencies, the amplification performance can now be investigated. To this end, we operate the DJJAA at a fixed flux bias point, defined by a static coil current $I_{\mathrm{JPA}} = -730\,\mu\mathrm{A}$ (dashed line). Next, we introduce a parametric pump tone, roughly at the center frequency between the two modes of the dimer to be amplified, in this case, $\omega_{\mathrm{JPA},1} = 4.42\,\mathrm{GHz}$. With this pump configuration, one drives a four-wave mixing process leading to phase-preserving, non-degenerate amplification (see Sec. 2.4 and Ref. [200]). The response of the amplifier to the parametric pump is illustrated by the measurements shown in Fig. 4.8**b**. We first acquire a baseline measurement (blue datapoints) with the pump tone disabled and the DJJAA far detuned from the frequency range shown ($I_{\mathrm{JPA}} = 1$ mA). The DJJAA is then tuned back to the operating point and the pump tone is turned on and increased in power from −74 dBm (light red) to −71 dBm (dark red) at the sample. As a result of the four-wave mixing process, a Lorentzian shaped peak appears in the reflected microwave signal, growing in height with increasing pump power until it exceeds the baseline by about 21 dB. The effective gain of the amplifier can now be calculated by dividing the amplified signal (i.e. the Lorentzian peak) by the baseline signal without amplification

$$G(\omega) = |S_{11,\mathrm{on}}(\omega)|^2/|S_{11,\mathrm{base}}(\omega)|^2. \tag{4.16}$$

When using this technique, it is crucial to measure the baseline signal not just with a disabled pump tone, but while the dimer modes are tuned away from the acquired frequency range. Otherwise, the characteristic dips in reflection of the dimer modes will lead to artificial gain in the calculation.

So far, we have only presented the amplification at the upper mode of the 4 GHz dimer. However, the DJJAA is designed to provide roughly symmetric amplification around the parametric pump frequency and a second frequency range of roughly equal gain is expected to form at the lower frequency mode. The corresponding gain profile, as measured for a pump tone $\omega_{\mathrm{JPA},1} = 4.42$ GHz with a power of $P_{\mathrm{JPA},1} = -71$ dBm is shown in Fig. 4.8**b**, where the gain was calculated from the individual reflection measurements as discussed above. As expected, two symmetrical Lorentzian gain profiles appear at 4.1 GHz and 4.7 GHz. An analogous gain profile measurement for a pump tone $\omega_{\mathrm{JPA},2} = 7.23$ GHz, centered between the 7 GHz dimer, with $P_{\mathrm{JPA},2} = -68.8$ dBm is shown in the same plot, demonstrating 22 dB of gain. Lastly, fitting the gain profiles with a simple Lorentzian function allows us to extract the bandwidth B over which the devices provide the measured amplification and find $B/2\pi \approx 10$ MHz. For resonant amplifiers, there is generally a trade-off between high gain and large bandwidth of the form [201]

$$\sqrt{G_0} \times B \approx \kappa_{\mathrm{ext}}, \tag{4.17}$$

where κ_{ext} is the external coupling or loss rate of the device. Therefore, it is useful to state not the individual gain and bandwidth values but instead calculate the so-called Gain Bandwidth Product (GBW), a more general measure of the amplifier performance. In our device, we find $\sqrt{G_0} \times B/2\pi \approx 90\,\mathrm{MHz}$ and 60 MHz for the 4 GHz and 7 GHz dimers, respectively.

Gain mapping In the above discussion, we have illustrated the amplification performance of the DJJAA using two specific pump configurations that were previously identified as suitable to provide more than 20 dB of stable gain. Doing so, however, is not trivial. While in theory the ideal pump frequency for the four-wave mixing is perfectly centered in between the dimer modes, in reality the application of the strong pump itself will lead to frequency shifts in the dimer modes due the Kerr effect present in the non-linear resonator (see Sec. 2.5.3). This in turn will also alter the ideal pump frequency. Furthermore, the power of the pump needs to be carefully calibrated to provide maximum gain without pushing the system into a bistable regime, where reproducible and stable amplification is no longer possible [124]. These requirements lead to a large parameter space of possible pump frequencies and pump powers that needs to be probed in order to find an ideal pump configuration.

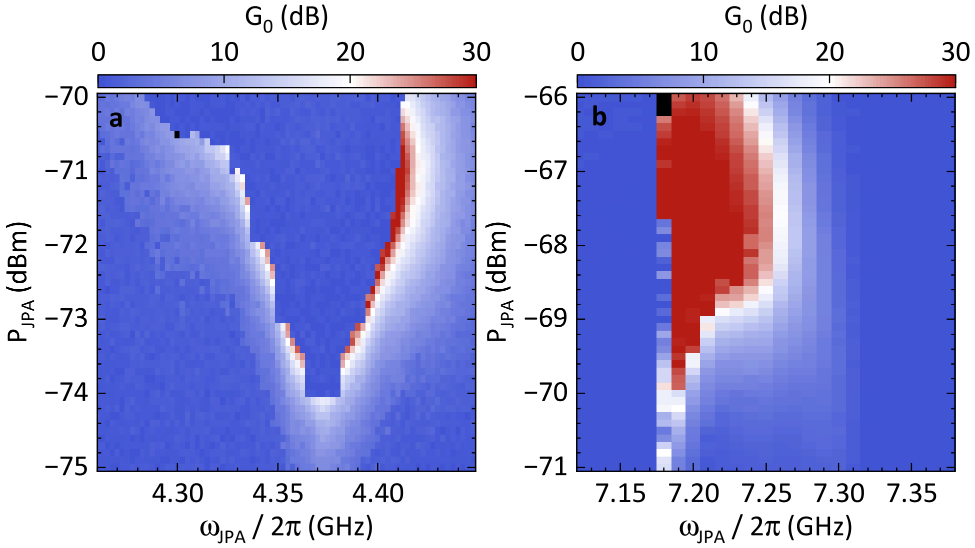

Fig. 4.9.: **DJJAA Gain mappings.** Maximum measured non-degenerate gain G_0 of the DJJAA encoded in color as a function of pump frequency ω_{JPA} and pump power P_{JPA}. **a** shows the gain achieved around 4.1 and 4.7 GHz (exact frequencies vary), when a pump is applied between the modes of the 4 GHz dimer. **b** shows the achieved gain around 6.9 and 7.5 GHz while pumping between the modes of the 7 GHz dimer. The ideal operating conditions, providing 20 dB of stable gain, correspond to the white areas of the colormaps. Configurations with higher gain values (red) are likely to be bistable.

A useful tool to gain an understanding of the suitable pump configurations is the creation of a comprehensive gain mapping, as is shown in Fig. 4.9. The maps display the color coded maximum gain G_0 as a function of pump frequency ω_{JPA} and pump power P_{JPA}. They are created by repeatedly measuring the DJJAA's S_{11} profiles as shown in Fig. 4.8**b** for a given ω_{JPA} and varying P_{JPA} and calculating the maximum gain for this pump configuration according to Eq. (4.16). This procedure is then repeated for various pump frequencies. It is worth noting that gain values exceeding 25 dB (dark red areas in the map) generally correspond to unstable configurations, where repeated measurements will observe either a high gain or zero gain solution. This effect is nicely illustrated when comparing the two shown maps: While the 7 GHz map (**b**) shows a large red area corresponding to > 20 dB gain, the corresponding area in the 4 GHz map (**a**) consists mostly of zero gain measurements. The desired operating regime for low noise experiments, providing a stable and reproducible ≈ 20 dB gain therefore corresponds to the white areas of the map. As apparent from the maps, there exist a multitude of pump configurations which achieve this result, but in general it is advisable to select a configuration with the lowest necessary pump power to minimize non-linear effects in the signal chain. While collecting the data to create the gain mapping, we also extract the frequency f_{gain}, which corresponds to the peak position of the gain profile, for each of the pump configurations, since both pump power and frequency can cause the peak to shift slightly.

We note that the measured gain mapping is only valid for the specific flux bias point, in this case $I_{\mathrm{JPA}} = -730\,\mu\mathrm{A}$. Even more possible configurations need to be considered when the flux-tuneability of the dimers themselves is taken into account. By changing the flux bias of the DJJAA the frequency at which the gain is realized can be shifted and a new gain mapping can be created. Using this additional degree of freedom, suitable pump configurations can be found to effectively enable 20 dB of amplification over a range of more than 1 GHz around the 4 GHz and the 7 GHz dimers [199]. Generally, configurations at flux bias points closer to zero flux (like the one shown above) are preferable, since they are more stable and require lower pump powers.

Pump configuration database To streamline the setup of the DJJAA before a measurement, we have developed a programmatic approach to automatically identify the most suitable pump configuration. All data acquired from the gain mapping measurements is stored in a database structured like Tab. 4.1. When a measurement signal at frequency f is supposed to be amplified, we query the database for pump configurations that provide $G_0 \approx 20$ dB gain at $f_{\mathrm{gain}} = f \pm 10$ MHz. We exclude unstable results with $G_0 > 25$ dB and select the configuration requiring the lowest drive power. The pump tone is then applied us-

f_{JPA}(GHz)	P_{JPA}(dBm)	G_0(dB)	f_{gain}(dB)
7.22	-68.8	23.46	7.486
7.21	-69.1	20.31	7.475
7.22	-68.9	19.28	7.485
7.21	-69.2	17.14	7.473
7.22	-69.0	16.09	7.483
...	...	...	...

Tab. 4.1.: **Excerpt of a gain database table for amplification around the 7GHz dimer.** The data is extracted from the measurements used to construct the gain mapping in Fig. 4.9**b**. Shown is the result of a real search query for suitable pump configurations providing roughly 20 dB of gain at a frequency of $f_{\mathrm{gain}} \approx 7.48\,\mathrm{GHz}$, sorted by gain.

ing the selected configuration and the experiment can proceed. Only when no suitable configuration is found in the database, the flux bias point of the DJJAA is adjusted manually and the procedure repeated until amplification at the intended frequency becomes possible.

Amplifier saturation Another aspect that needs to be considered for the operation of JPAs and amplifiers in general is amplifier saturation, a phenomenon which occurs when the amplifier, tasked with scaling a strong input signal, reaches its output power limit and is no longer able to provide the expected linear voltage amplification [202]. In the case of JPAs, the dynamic range is usually limited by one of two effects: power dependent frequency shifts due to the inherent (Kerr-) non-linearities of the device, and *pump depletion*. While the former type of effect is already discussed in Sec. 2.3.4 in detail, pump depletion appears once the amplified signal becomes comparable in power to the pump signal. In this regime, photon conversion processes become relevant that effectively remove photons from the pump signal, leading to an effectively lower pump power that results in a reduction of the amplifier's gain [102].
A common figure of merit to quantify the onset of amplifier saturation is the *1dB compression point*. This point is defined as the input power level at which the real output power of the amplifier is 1 dB less than the ideal linear extrapolation of the amplifier's gain. In essence, it marks the transition between the linear and non-linear operating regimes of the amplifier. Knowledge of the amplifier's 1 dB compression point is crucial to its proper application in experiments, as it directly relates to the amplifier's ability to faithfully act as a linear amplifier, which is key for the amplification of the signals received from the device under test. Any input signal power beyond the 1 dB compression point can result in a notable distortion of the amplified signal and is therefore to be avoided.

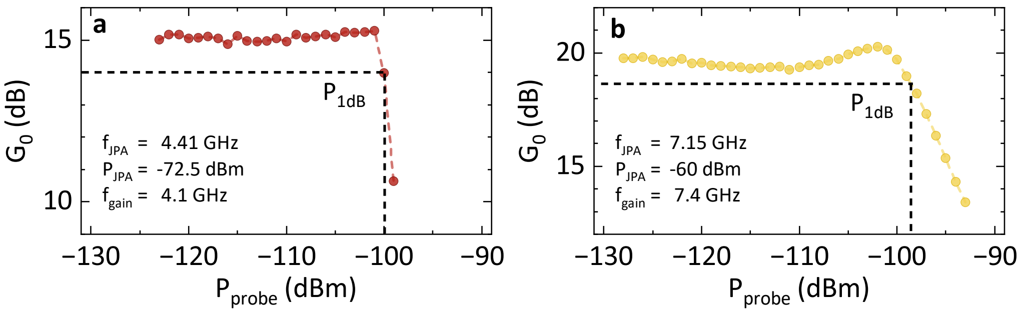

Fig. 4.10.: DJJAA power saturation. Maximum measured non-degenerate gain G_0 of the DJJAA's 4 GHz dimer (**a**) and 7 GHz dimer (**b**) as a function of incident signal power P_{probe} at the input port while ω_{JPA} and P_{JPA} are kept constant (see insets for pump configurations). The connecting lines are guides to the eye. The onset of amplifier saturation leading to a reduction in gain is visible in both measurements. The 1 dB compression points as highlighted by the dashed lines is extracted from the data to $\text{P}_{1\text{dB}}@4G = -100\,\text{dBm}$ and $\text{P}_{1\text{dB}}@7G = -98\,\text{dBm}$.

In order to identify the 1dB compression point experimentally for our Josephson parametric amplifier, we first choose a stable pump configuration from the database and keep the selected ω_{JPA} and P_{JPA} constant. We then perform repeated VNA frequency sweeps of the amplifiers gain profile while gradually increasing the power P_{probe} of the VNA's probe signal, which is incident on the DJJAA's input port. From the gain profile at each input power, we extract the maximum gain G_0 using a Lorentzian fit. In Fig. 4.10, we show the experimentally determined gain as a function of input power for the lower dimer realizing 15.0 dB of gain at 4.1 GHz (**a**) and the upper dimer realizing 19.6 dB of gain at 7.4 GHz (**b**). In both measurements, we observe a nearly constant gain at low input powers, which corresponds to the amplifier providing linear amplification. Therefore, we use the average value of the first 10 data points as a reference value for linear gain. For the measurement of the 7 GHz dimer in **b**, the onset of saturation and gradual decrease of G_0 is clearly visible, allowing us to identify the 1 db compression point ($P_{1\text{dB}}$) as $\text{P}_{1\text{dB}}@7\text{G} = -98\,\text{dBm}$. The slight increase in measured gain shortly before saturation is understood as an effect of the Kerr non-linearity of the device, which shifts the mode frequencies downwards with increasing power, briefly crossing a regime where the pump frequency is placed more ideally than in the starting configuration.

In the compression measurement of the 4 GHz dimer shown in **a**, the decrease in gain appears much more like a sudden collapse than a gradual reduction. This peculiar effect has been observed in other DJJAA type devices [199, 203] and appears to occur specifically when operating the amplifier at flux bias conditions close to zero flux. An explanation for the abrupt collapse is yet to be found. However, for the purpose of our experiments, we can still estimate the equivalent of a 1 dB compression point from the recorded data to $\mathrm{P_{1dB}@4G} = -98\,\mathrm{dBm}$ and use this value as a limit to the dynamic range available for amplification.

In conclusion, we observe the onset of amplifier saturation for both dimers at roughly $-100\,\mathrm{dBm}$ input power, demonstrating that due to the implementation of large SQUID arrays in the DJJAA's design a comparatively high dynamic range can be achieved when compared to single SQUID JPAs [100, 105, 204]. This observation is consistent with theoretical predictions [102, 205] and other experimental realizations of dimer amplifiers [124, 125]. More importantly, the dynamic range of the DJJAA exceeds the regime of linear operation for all of the investigated electromechanical devices in this work, i.e. signal powers are generally limited by the FTR's bistability, not by saturation of the amplifier.

Noise performance The primary appeal of incorporating a JPA into an experimental setup lies in its potential to drastically increase the signal-to-noise ratio (SNR) of the experiment by minimizing the addition of noise during the amplification process. In a practical sense, this means that the JPA can amplify weak quantum signals at ultra low temperatures and with minimal added noise before they are further processed by other, potentially noisier, components of the measurement chain. If the power gain of the JPA is sufficiently large, it can saturate the noise added by subsequent amplifier stages and the SNR becomes dominated by the SNR incident on the JPA. In the following, we are investigating whether the DJJAA used in our experiment accomplishes this feat. To this end, we perform a so-called noise visibility measurement, which we present in Fig. 4.11. To acquire the data shown in panel **a**, we use a spectral analyzer to measure the noise power density around the amplification bandwidth of the DJJAA both during active amplification driven by a suitable pump signal (red) and in the non-driven state, where no amplification is achieved (blue). No other microwave signals are sent to the device during the measurement, so the measured signal is purely determined by the quantum fluctuations incident on the device input. Clearly, the measured power spectral density S_{PP} shows two Lorentzian shaped peaks when the amplifier is driven by a pump which are not present in the noise power measurement in the disabled state. We now calculate the noise visibility ratio

$$\Delta P(\omega) = S_{\mathrm{PP,on}}(\omega)/S_{\mathrm{PP,off}}(\omega) \tag{4.18}$$

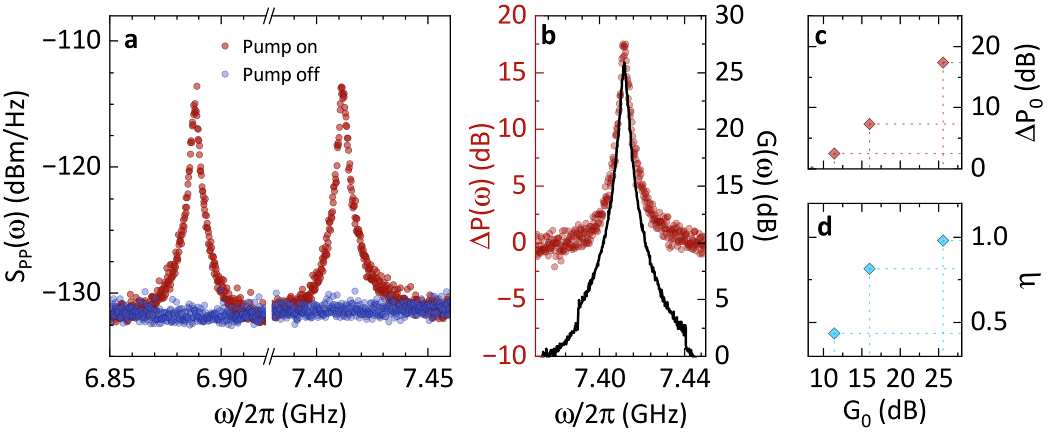

Fig. 4.11.: DJJAA noise visibility. a Power spectral density measured using a spectral analyzer at room temperature with (red) and without (blue) a pump signal applied to the DJJAA. No other input signals aside from the pump are used in the experiment. Peaks in the noise power density are observed within the amplification bandwidth of the amplifier in the measurement with active pump, as the noise at the input of the DJJAA is amplified. **b** Noise visibility ΔP, calculated from the data in **a** according to Eq. (4.18). A separately recorded gain profile of the DJJAA using identical pump settings is shown in black, matching the shape of the increased noise visibility. **c** Maximum noise visibility ΔP_0 as a function of maximum gain G_0 at 3 different pump powers, both maxima are extracted using Lorentzian fits. **d** Contribution by the DJJAA to the quantum efficiency η of the measurement chain for 3 different pump powers, plotted over the corresponding gain. All experiments use $f_{\mathrm{JPA}} = 7.05\,\mathrm{GHz}$ and $P_{\mathrm{JPA}} = -60.5\,\mathrm{dBm}$ to $-60.0\,\mathrm{dBm}$.

and compare it in **b** with the gain profile of the DJJAA, which was measured under the same pump configuration by a VNA directly after the noise visibility measurement. The gain provided by the DJJAA coincides in shape and bandwidth with the observed increase in the noise power, further indicating that during active operation the noise power becomes dominated by the DJJAA. Next, we vary the applied pump power and for each configuration use Lorentzian fits to extract the maximum noise visibility ΔP_0 (from the spectral analyzer data) and the maximum gain G_0 (from the VNA gain profiles). The results are shown in Fig. 4.11**c**. For the investigated pump configurations, we find gain values ranging from $G_0 = 11.0\,\mathrm{dB}$ to $25.5\,\mathrm{dB}$ and corresponding noise visibilites $\Delta P_0 = 2.5\,\mathrm{dB}$ to $17.3\,\mathrm{dB}$.

By comparing the gain provided by the amplifier with the noise visibility, one can estimate the factor by which the SNR of the experiment can be improved due to the addition of the parametric amplifier. For the largest gain value of $G_0 = 25.5\,\mathrm{dB}$ and the corresponding $\Delta P_0 = 17.3\,\mathrm{dB}$, we find by division (in linear units) a potential improvement up to a factor of $G_0/P_0 = 6.65$. Furthermore, we can estimate the contribution of the DJJAA to the quantum efficiency η of the experimental amplification chain using [203, 206]

$$\eta = 1 - 10^{(-\Delta P/10)}. \tag{4.19}$$

The resulting values of η for the investigated pump configurations are plotted in Fig. 4.11**d**, reaching up to $\eta = 0.97$ for the highest gain. In other words, the contribution of the remaining amplifier stages, in particular the HEMT, to the noise measured at room temperature is reduced to only 3%. This makes clear that the DJJAA's own added noise has now become the limiting factor in the amplifier chain.

However, the noise visibility measurements are not sufficient to quantify the noise added by the DJJAA itself and the upper bound to the efficiency above can only be reached when the amplifier operates at the theoretical quantum limit of 0.5 added noise photons. Extracting the amplifier's added noise requires careful calibration of the entire measurement setup using a precisely known input power incident on the DJJAA. Various approaches to a proper input power calibration exist, making use of qubits [207], shot noise [208] or a *hot load*, i.e. the known black body radiation emitted by a heatable microwave attenuator [204, 209]. Performing this calibration exceeds the scope of this work, but fortunately has already been completed for our device in Ref. [199] using the hot load method, obtaining $n_{\mathrm{add}} \approx 1.5$ for operation of the 7 GHz dimer. Accordingly, we can expect the DJJAA to operate close to but not at the quantum limit of $n_{\mathrm{add}} = 0.5$. However, when compared against the setup's HEMT amplifier with a specified noise temperature of 2.3 K, corresponding to 6.85 photons at 7 GHz, an added noise of $n_{\mathrm{add}} \approx 1.5$ would present an improvement by a factor of 4.56, which agrees reasonably well with the SNR improvement of 6.65 calculated from noise visibility.

Inductively Coupled Electromechanics

5

This chapter provides a comprehensive presentation and analysis of the experimental research into inductively coupled electromechanical devices performed over the course of this work. Throughout the chapter, we make extensive use of the theoretical background on microwave resonators (Sec. 2.2.2), optomechanics (Sec. 2.5), and the flux-mediated electromechanical coupling mechanism (Sec. 2.5.2), as well as the experimental methods and analysis techniques introduced in Sec. 4.

In the first section, we discuss the pre-characterization of the electromechanical device used in our experiments. Key parameters such as flux-tuneability, Kerr non-linearity, and quality factors are investigated, followed by a characterization of the mechanical response of the nanostring oscillator. This preliminary characterization sets the stage for the in-depth investigation of the system's behavior in subsequent experiments. The next section revolves around the optomechanical single-photon coupling strength g_0. We report unprecedentedly high values of g_0 achieved in the investigated device and use a combination of different experiments and analysis techniques to independently verify the validity of the results.

We then investigate the device's capabilities with regards to low-power optomechanical sideband cooling, with the goal of bringing the mechanical system close to its quantum ground state. We provide a brief introduction of the experimental cooling protocol and then present and discuss the latest experimental results. In this context, we analyze the role of the device's Kerr non-linearity in the cooling process and emphasize which limits and opportunities arise from its presence.

Finally, we explore backaction in the electromechanical system as a means of mechanical frequency control. We present a novel technique for in-situ control of the resonance frequency of the mechanical oscillator, detailing the tuning protocol and results, and investigate the potential influence of flux vortex formation in the superconducting thin film.

5.1 Device characterization

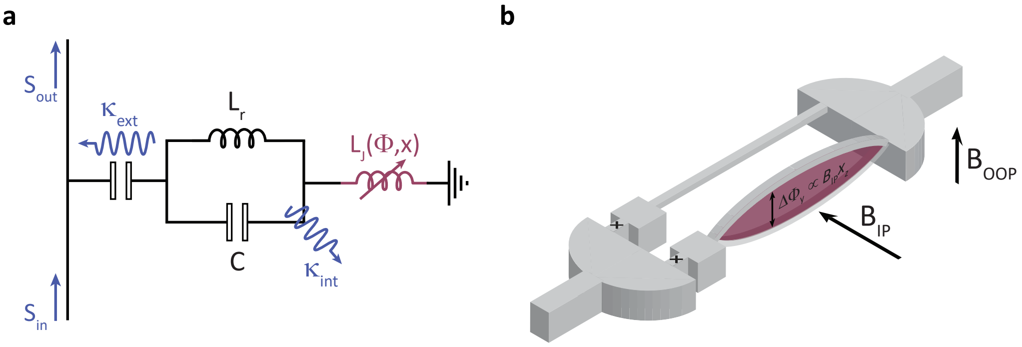

Fig. 5.1.: Flux tuneable CPW resonator with mechanically compliant SQUID. a Equivalent circuit representation of an inductively coupled electromechanical device. The CPW microwave resonator is described by means of a lumped element model as effective capacitance C and inductance L_r. It is coupled capacitively to a feedline with the external coupling rate κ_ext. Additionally, the circuit contains a dynamic inductance (purple), whose magnitude depends on the time-varying displacement $x(t)$ of the mechanical element, and which forms the basis for the electromechanical coupling. **b** Schematic illustration of the mechanically compliant SQUID with incorporated nanostrings and relevant magnetic field directions. The shading illustrates how the motion of the nanostring modulates the flux-threaded area of the SQUID-loop due to an in-plane magnetic field B_ip. The second, weaker magnetic field component B_oop is used to control the effective flux bias Φ_b of the SQUID. A version of this figure was published in Ref. [157].

The nano-electromechanical device investigated in this study is based on a superconducting quantum interference device (SQUID), incorporated into a coplanar waveguide (CPW) microwave resonator. Design and fabrication are based on the first generation single-step process, which is detailed in Sec. 3.1.1 along with micrographs of a fabricated sample, and a summary of all design parameters is found in App. A.1. Figure 5.1**a** presents an equivalent circuit representation of the device. The CPW resonator is modeled using a lumped element framework and depicted by an effective capacitance C and inductance L_r. It is capacitively coupled to a microwave feedline with an external coupling rate κ_ext. Uniquely, the circuit comprises a dynamic inductance, highlighted in purple, which is contingent on the time-varying displacement, $x(t)$, of the mechanical element. In our case, the dynamic inductance is provided by a mechanically compliant SQUID, which can be viewed as a nonlinear, flux-controllable inductor with a mechanical degree of freedom. The SQUID element is schematically depicted in Fig. 5.1**b**, with Josephson junctions, the integrated nanostrings and pertinent magnetic field directions highlighted. The diagram illustrates how the nanostring's movement modulates the flux-threaded area of the SQUID-loop w.r.t. to an in-plane magnetic field, B_ip, and thus the magnitude of the Josephson inductance $L_\mathrm{J}(\Phi)$, implementing the flux-mediated electromechanical interaction we have discussed in Sec. 2.5.2. We note that the nanostrings support both out-of-plane (OOP, shown) and in-plane (IP) flexural modes. In this experiment, we focus on the string's OOP mode, interacting with a strong in-plane magnetic field B_ip, since the in-plane field orientation supports a much higher critical magnetic field compared to the OOP direction [156]. Additionally, a secondary, weaker magnetic field component, B_oop, is employed to control the effective flux bias, Φ_b, of the SQUID. A change to the flux bias Φ_b (via B_oop) causes the flux-dependent Josephson inductance of the SQUID to change as well, causing a shift in the resonance frequency of the circuit.

5.1.1 Flux tuning behavior

We start by characterizing the microwave response of the flux-tuneable CPW resonator (FTR) at $B_\mathrm{ip} = 0$, effectively turning off the electromechanical interaction. To this end, we use standard microwave transmission experiments performed in the cryogenic measurement setup introduced in Sec. 4.1 using only the VNA and the corresponding high frequency signal path. The JPA is detuned from the region of interest for the measurement since the additional amplification is not necessary for the initial characterization. In the first experiment, we record the frequency-dependent microwave transmission for various OOP flux bias values Φ_b. The results in Fig. 5.2**a** demonstrate the flux-tuneability of the system. The resonance frequency ω_c of the FTR is visible as a dark blue feature in the calibrated transmission $|S_{21}|$. We can observe a significant and controllable shift in the resonance frequency from $\omega_\mathrm{c} = 7.45\,\mathrm{GHz}$ to $6.7\,\mathrm{GHz}$. This effect is periodic in Φ_b with a periodicity of Φ_0 as expected for non-hysteretic FTRs (see Sec. 2.3). Additionally, a constant parasitic resonance feature is detectable around 7.3 GHz, which can be attributed to a second, non-tuneable CPW resonator coupled to the same feedline (cf. the multiplexed chip layout discussed in Sec. 3.1.1). It should be noted that the FTR and the parasitic resonator are non-negligibly coupled via the shared feedline. As such, caution must be taken when operating the FTR at frequencies close to 7.3 GHz, as complex effects can arise.

Next, we turn to quantitative investigation of the flux-tuneability. As detailed in Sec. 4.2.1, we use background correction and the circle fit method (Eq. (4.1)) to fit the data and extract the exact resonance frequency ω_c as a function of the applied bias flux. The extracted values for ω_c are shown in Fig. 5.2**b** and confirm

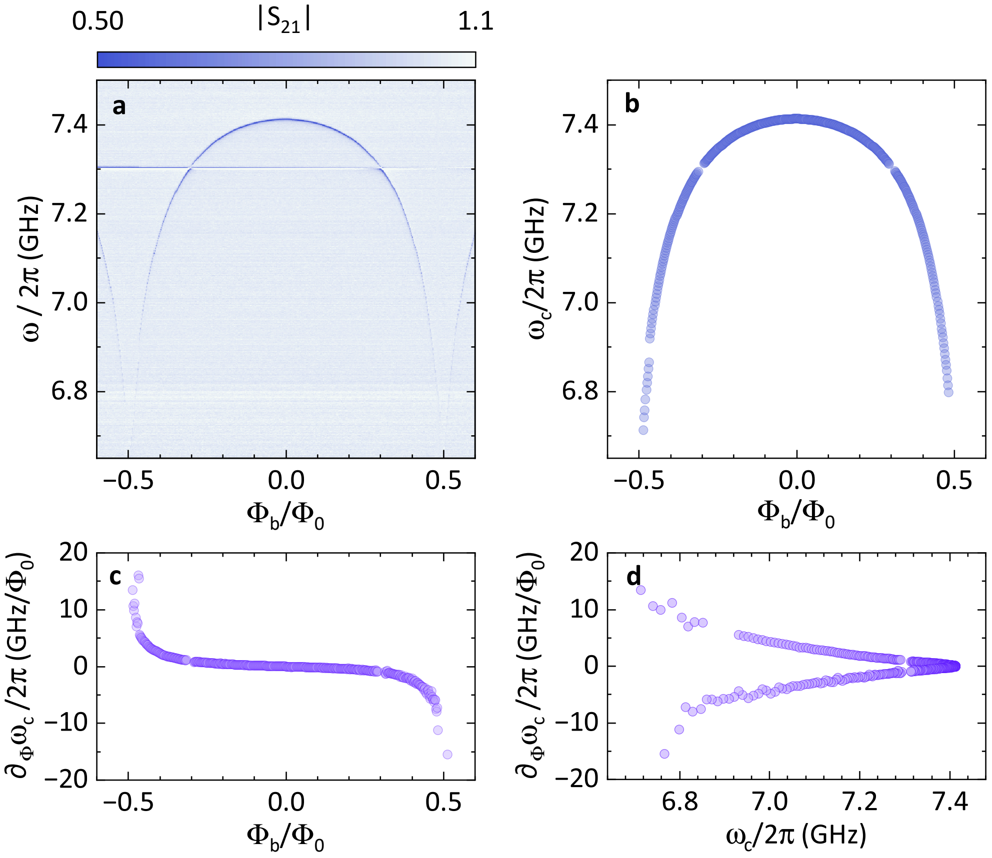

Fig. 5.2.: Flux tuning and flux dependent device parameters. a Calibrated microwave transmission magnitude $|S_{21}|$ at zero field ($B_{\mathrm{ip}} = 0$) as a function of the normalized flux bias Φ_{b}/Φ_0. The flux-dependent inductance of the circuit leads to a controllable shift in its resonance frequency (dark blue) from 7.45 GHz to 6.6 GHz. A parasitic resonance is visible around 7.3 GHz and discussed in the main text. **b** Flux dependent FTR resonance frequency ω_{c}, extracted from the measurement shown in **a** using fits to Eq. (4.1). **c,d** Flux responsivity $\partial\omega_{\mathrm{c}}/\partial\Phi$ as a function of **c** flux bias Φ_{b} and **d** FTR resonance frequency ω_{c}. The flux responsivity is calculated numerically as the derivative of the data in **b**.

the large and continuous flux tuneability over a range of roughly 750 MHz. The determined resonance frequencies then serve as a basis to gain insight into the flux responsivity $\partial\omega_{\mathrm{c}}/\partial\Phi$, i.e. the change in resonance frequency with change of bias flux through the SQUID loop. To this end we apply the central difference method [210] to numerically compute the first partial derivative of the resonance frequency with respect to the flux bias from the data in panel b and present the result in Fig. 5.2**c**. While the flux responsivity effectively vanishes at the zero flux point $\Phi_{\mathrm{b}}/\Phi_0 \approx 0$, or the so-called *sweet spot*, our data shows a gradual and then exponential increase in magnitude as the flux bias is increased towards $|\Phi_{\mathrm{b}}/\Phi_0| \approx 0.5$, with maximum values around $|\partial\omega_{\mathrm{c}}/\partial\Phi| \approx 2\pi \cdot 15\,\mathrm{GHz}/\Phi_0$. We also visualize the same numerically calculated data for

$\partial\omega_c/\partial\Phi$ as a function of the corresponding FTR resonance frequency ω_c at the same flux bias point in panel **d**. Due to the symmetric shape of the flux tuning curve around $\Phi_b/\Phi_0 = 0$, two responsivity solutions with different sign exist for every value of ω_c. The frequency representation provides a clearer picture on the vast range of experimental working points, i.e. available combinations of resonance frequency and flux responsivity, especially in the moderate region with $|\partial\omega_c/\partial\Phi| < 2\pi \cdot 10\,\mathrm{GHz}/\Phi_0$, where we observe a roughly linear relationship between $\partial\omega_c/\partial\Phi$ and ω_c. Also, in practice, since ω_c is generally more directly observable in the experiment compared to Φ_b, the data in **d** can serve as a look-up-table to quickly identify the associated value of $\partial\omega_c/\partial\Phi$ for experiments and data analysis. Lastly, we recall from Sec. 2.5.2 that the electromechanical single-photon coupling strength g_0 is directly proportional to $\partial\omega_c/\partial\Phi$, which has two wide ranging implications: First, the flux responsivity data shows that the device indeed has the predicted ability to control g_0 in-situ and quasi continuously over a wide range of working points via control of Φ_b. Second, the experimentally observed $|\partial\omega_c/\partial\Phi|$ of more than $2\pi \cdot 10\,\mathrm{GHz}/\Phi_0$ in our device exceeds any previously reported values for inductively coupled electromechanical devices by several orders of magnitude [56, 58], suggesting a potential for similar improvements regarding the single-photon coupling strength g_0.

Quality factors and loss rates As introduced in Sec. 2.2.2, the quality factors, or Q-factors, are one of the most important and widely used figures of merit in the evaluation of the performance of microwave resonators. Furthermore, we have discussed in Sec. 3.1 how the quality factors and associated loss rates of the FTR component play a significant role in determining the operating conditions of nano-electromechanical devices. It is plausible to expect that changing the resonance frequency of a flux-tuneable resonator by several hundreds of MHz might also have a noticeable effect on the losses that determine its Q-factors. Therefore, the subsequent section is dedicated to the exploration of the impact of the flux tuning protocol on the quality factors and loss rates of the investigated FTR.

For the quality factor analysis, we employ the same dataset discussed in the previous section, where we have already extracted the flux dependent resonance frequency of the FTR (cf. Fig. 5.2**b**) using a fit of the individual microwave transmission response $|S_{21}|$ to Eq. (4.1). From the same fits to the data, we extract the internal and external quality factors (Q_i and Q_e) and loss rates (κ_{int} and κ_{ext}) for every flux bias point. The results are presented in Fig. 5.3.

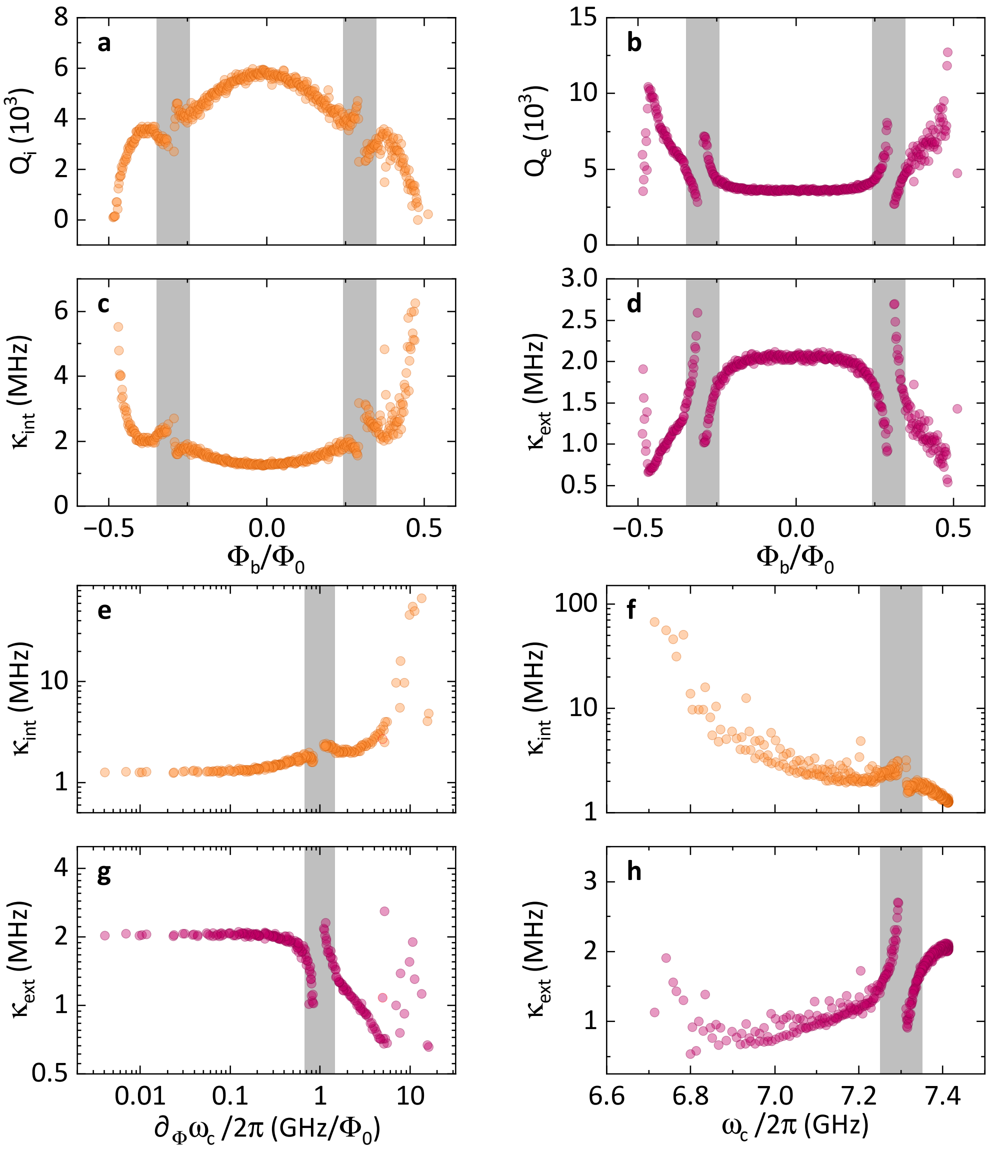

Fig. 5.3.: Flux dependency of FTR quality factors and loss rates. a-d Internal and external quality factors (Q_i, Q_e) and loss rates (κ_int, κ_ext) of the investigated FTR as a function of the normalized flux bias Φ_b/Φ_0. **e,g** The same data for κ_int and κ_ext as a function of the corresponding flux responsivity $\partial\omega_\mathrm{c}/\partial\Phi$. **f,h** Loss rates κ_int and κ_ext over the corresponding FTR resonance frequency ω_c. All quality factors and loss rates are extracted from the flux tuning curve measured at zero in-plane field and shown in Fig. 5.2**a** using fits to Eq. (4.1). In all panels, the grey shading highlights regions where the FTR resonance frequency $\omega_\mathrm{c}/2\pi \approx (7.30 \pm 0.05)\,\mathrm{GHz}$ and coupling to a parasitic mode leads to additional features.

It becomes clear from the quality factor data that the bias flux applied to the SQUID loop does indeed have an effect on the loss behavior of the FTR. Unfortunately, the data is dominated by large features appearing at $\Phi_\mathrm{b}/\Phi_0 \approx \pm 0.25$ (grey shaded areas). Recalling Fig. 5.2, we find that the features coincide exactly with the region where the flux-tuneable resonator becomes resonant with the parasitic resonator mode at 7.3 GHz. Due to the coupling to a shared feedline, the two modes interact and the theoretical model of a single resonator underpinning Eq. (4.1) is no longer fully valid. Since the coupling of two microwave resonators is generally well understood and not the focus of this work, we will neglect these features in our discussion.

For the internal Q-factor shown in panel **a**, a broad maximum of $Q_\mathrm{i} \approx 6 \times 10^3$ is observed around the zero flux point, while its value decreases drastically towards larger flux bias values. This behavior can most likely be understood as an increase in the susceptibility of the device to external flux noise, which we discussed in detail in Sec. 4.5 and the following sections. The flux responsivity $\partial\omega_\mathrm{c}/\partial\Phi$ translates a given change in external flux to a change in the resonance frequency of the flux-tuneable device. High frequency flux noise will therefore present as an effective broadening of the resonance feature, i.e. a higher loss rate and lower quality factor. Assuming that the flux noise itself is frequency independent, a change in flux responsivity should translate directly to a corresponding change in the internal loss rate $\kappa_\mathrm{int} = \omega_\mathrm{c}/Q_\mathrm{i}$. We have shown in our analysis of the flux responsivity in Fig. 5.2**c** that $\partial\omega_\mathrm{c}/\partial\Phi$ increases exponentially for flux bias values approaching $\Phi_\mathrm{b}/\Phi_0 \approx 0.5$, which is also the region where observe a drastic increase in κ_int to values above $2\pi \cdot 6\,\mathrm{MHz}$ (cf. panel **c**). The link between the increased intrinsic losses and the flux responsivity is further solidified when we examine Fig. 5.3**e**, where the internal loss rate κ_int is extracted from the same data and plotted as a function of $\partial\omega_\mathrm{c}/\partial\Phi$. In this visualization, we see that for low responsivities, κ_int remains largely constant, suggesting that in this regime the intrinsic loss rate of the FTR is dominated by other loss channels, e.g. two-level systems. As the flux responsivity increases above $\partial\omega_\mathrm{c}/\partial\Phi > 2\pi \cdot 1\,\mathrm{GHz}/\Phi_0$, the loss rate rises exponentially, suggesting the onset of a flux noise dominated regime. This pattern is consistent with our conjecture based on the influence of high-frequency flux noise. Moreover, the results suggest that operating the device at a flux bias with high flux responsivity, while desirable to reach high optomechanical coupling rates, makes the device susceptible to flux noise, which manifests in the form of a lower Q_i. This trade-off needs to be carefully considered.

The external quality factor Q_e on the other hand is primarily determined by the capacitive coupling between the CPW resonator and the transmission line. The strength of this coupling is in turn clearly defined by geometric parameters, in particular distance and length of the CPW section that runs in parallel to the transmission line. Therefore, one might intuitively expect a near constant value of Q_e and no significant effect of the flux bias. However, from the data shown in panels **b** and **d**, we see that Q_e and κ_ext only remain constant in a limited range around the zero flux point. Towards higher flux bias values, we first encounter anti-crossing like features in the shaded region, which can be attributed to coupling to the parasitic mode as discussed above. At even higher flux bias, however, we find a significant, roughly linear decrease in κ_ext. Interestingly, κ_ext eventually returns to the zero flux value as $\Phi_\mathrm{b}/\Phi_0 \approx -0.5$ is approached, an effect that is not visible for positive flux bias values. A likely explanation for the decreasing κ_ext is that the capacitive coupling between CPW resonator and transmission line is frequency dependent [84]. This explanation is supported by panel **h**, where we plot κ_ext as a function of the FTR resonance frequency ω_c. We can identify a linear dependence of κ_ext on ω_c between 6.9 and 7.2 GHz with κ_ext increasing towards higher frequencies. This observation agrees with the theoretical prediction of the frequency dependent coupling to a transmission line $\kappa_\mathrm{ext} \propto \omega_\mathrm{c}$ [124]. For lower frequencies, the data becomes scattered and no clear pattern is discernible. It is likely that in this regime a second effect becomes dominant: As established previously, the internal quality factors become very small for $|\Phi_\mathrm{b}/\Phi_0| \approx 0.5$, which eventually places the device in the undercoupled regime with $Q_\mathrm{e} \gg Q_\mathrm{i}$. In this limit, the fitting algorithm is generally no longer able to accurately disentangle internal and external losses, leading to unreliable results [87]. This conjecture is also supported by our earlier observation that the extracted κ_ext values in the limit of $|\Phi_\mathrm{b}/\Phi_0| \approx 0.5$ do not behave symmetrically w.r.t. the sign of the flux bias.

SQUID properties Recalling the theoretical models introduced in Sec. 2.3, we have established that the frequency tuning behavior of FTRs is inherently determined by the relationship between the static linear inductance of the CPW resonator and the SQUID acting as a flux-controlled variable inductance. Therefore, one can gain insight into the characteristic properties of the SQUID by quantitative analysis of the observed tuning behavior. Based on the analytical model given in Eq. (2.61), a total of 4 variables are used in order to fully describe the flux-tuneable circuit: The critical current of a single Josephson junction I_c0, the loop inductance L_loop, the CPW inductance $L_\mathrm{r} = L_0\ell$ and the bare resonance frequency $\omega_0 \equiv \omega_{j=0}^{(0)}$. Ensuring a proper fit to the tuning data can therefore be challenging without prior knowledge of at least some of the parameters. Fortunately, based on the geometry of the investigated device, analytical calculations can be used to confine the available parameter space. First of all, the inductance of a CPW resonator is determined by its line inductance, i.e. by the self-inductance of the central conductor per unit length. For our CPW geometry the line inductance can be calculated [211] to 463 pH/mm, which we multiply by the design length of the center conductor to receive $L_\mathrm{r} = 463\,\mathrm{pH/mm} \times 3.95\,\mathrm{mm} = 1.832\,\mathrm{nH}$. Also, we have previously discussed in Sec. 2.2.4 how L_loop contains contribution of a kinetic inductance L_kin and a geometric inductance L_geo, both of which can be calculated based on the known dimensions and materials of the SQUID loop. For our device, we obtain $L_\mathrm{kin} = 90\,\mathrm{pH}$, $L_\mathrm{geo} = 46\,\mathrm{pH}$ (details on the calculation are found in App. A.3). Since we are confident in the accuracy of the analytic calculations of these two values, we prevent the fitting algorithm from varying them and use only ω_0 and I_c0 as free fit parameters. At this point, we want to point out that we expect the device to have a total loop inductance of $L_\mathrm{loop} = 136\,\mathrm{pH}$. This level of loop inductance gives rise to non-negligible self screening effects in the SQUID, which lead to a significant deviation of the tuning behavior, as we have calculated in Sec. 2.3.2. We incorporate these effects into our tuning model not only via the inclusion of L_loop in Eq. (2.61), but also via numerical calculation of the total flux Φ in the presence of screening currents according to Eq. (2.51). Furthermore, we limit our analysis to data in the range $|\Phi_\mathrm{b}| < 0.4$ as the first order approximation used to derive Eq. (2.61) shows larger deviations around half a flux quantum (cf. Fig. 2.9). The previously discussed experimental tuning curve along with the fitted model is presented in Fig. 5.4**a**.

We find that the experimentally observed tuning behavior is well described by the fit. From the fit to the data acquired in zero field, we extract $\omega_0/2\pi = 7.964\,\mathrm{GHz}$ and $I_\mathrm{c0} = 1.63\,\mu\mathrm{A}$, which corresponds to a screening parameter of $\beta_\mathrm{L} = 0.214$. The tuning analysis confirms that one of the important design goals postulated in Sec. 3.1 was met: By appropriately balancing the SQUID and loop inductance, we were able to achieve a low screening parameter $\beta_\mathrm{L} < 0.5$, which gives the device a non-hysteretic, easily controllable frequency tuning behavior with a clearly defined periodicity of $1\Phi_0$.

Magnetic field dependence Given that the flux-mediated inductive coupling scheme in this study relies on external magnetic fields, it’s crucial to explore their impact on the properties of the SQUID and, consequently, the FTR.

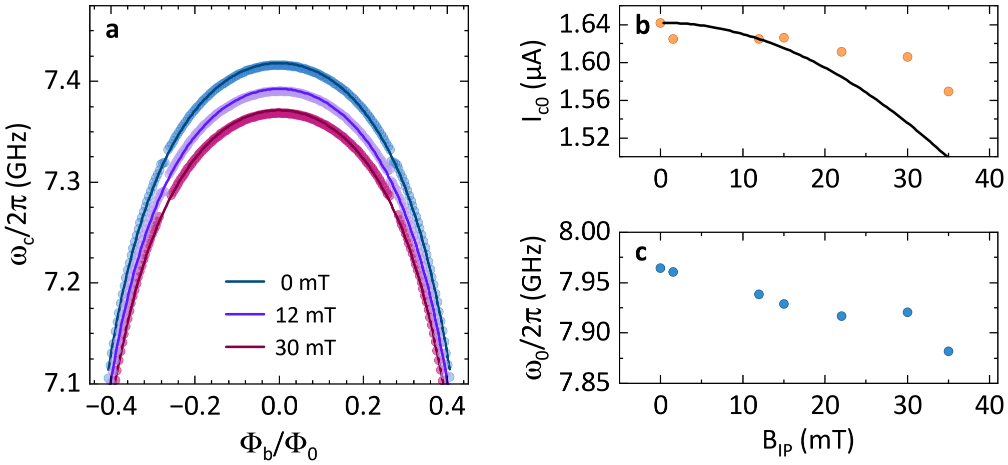

Fig. 5.4.: Extraction of field dependent SQUID parameters via fit of the tuning behavior. **a** Experimentally determined FTR resonance frequencies ω_c as a function of normalized bias flux Φ_b/Φ_0, for varying in-plane fields B_ip. The data for each in-plane field is fitted to Eq. (2.61) in order to extract the device parameters I_c0 and ω_0. **b,c** Field dependent single junction critical current I_c0 (**b**) and bare resonance frequency ω_0 (**c**) extracted from fits to tuning curves as shown in **a**. The black line is a model calculation using Eq. (2.41) with the real geometric parameters of the device (details in main text).

To this end, we apply a constant external magnetic field B_ip in the in-plane direction and repeat the tuning measurement by sweeping the out-of-plane bias flux Φ_b. The flux-dependent resonance frequencies in in-plane fields of 12 mT and 30 mT, extracted as before from microwave transmission spectra, are plotted along the zero-field data in Fig. 5.4**a**, along with fits to Eq. (2.61). Evidently, the maximum resonance frequency decreases towards larger magnetic fields, indicating an increased total inductance of the FTR circuit. From fits to the shown tuning curves and analogous measurements at further field values, we extract the single junction critical current I_c0 and the bare resonance frequency ω_0, plotted as function of the in-plane field B_ip in Fig. 5.4**b** and **c**, respectively.

We observe a decline in both I_c0 and ω_0 with increasing external field. The decrease in critical current is anticipated since the external magnetic field affects the phase difference across the Josephson junction, a phenomenon briefly discussed in Sec. 2.2.3 and described by Eq. (2.41). Based on the London penetration depth of Aluminum $\lambda_\mathrm{L} = 50\,\mathrm{nm}$, the length of the junction perpendicular to the field $L_\mathrm{JJ} = 150\,\mathrm{nm}$, and an estimated AlO$_\mathrm{x}$ thickness of $d_\mathrm{ox} = 2\,\mathrm{nm}$, we calculate the expected magnetic field dependency of I_c0 for our junction geometry and plot the result as a black line in panel **b**.

In comparison to values extracted from the fits, the model appears to overestimate the decrease in I_{c0}. Several factors might contribute to this discrepancy. For instance, the magnetic field dependence of the London penetration depth is not considered in our calculation. However, the change in λ_L has been found to be on the order of 10^{-3} even in larger external fields approaching the critical field of Aluminum [212], which is not sufficient to explain the observed discrepancy. A more likely explanation is that Eq. (2.41) neglects the fields generated by currents threading the junction electrodes, a valid simplification only for junction dimensions below the London penetration depth of the material [92]. With $\lambda_L = 50\,\text{nm}$, this condition is not strictly met in our case, potentially leading to a more complex behavior not described by the model.

Another intriguing feature is the decrease of ω_0 shown in panel **c**. The bare resonance frequency ω_0 represents the linear part of the FTR unaffected by the flux-dependent Josephson inductance. A decreasing ω_0 with external magnetic field suggests an additional effect not fully explained by the increase in junction inductance alone. Most likely, the additional frequency shift arises from an increase in kinetic inductance due to Cooper-pair-breaking induced by the external magnetic field. This effect would affect both the superconducting nanostrings in the mechanically compliant SQUID, increasing the loop inductance L_loop, and the entire CPW section of the FTR, increasing L_r. Field dependent frequency shifts due to kinetic inductance have been observed in nanowires [213] and CPW resonators [214] made from high kinetic inductance materials like Niobium or Niobium-Titanium-Nitride (NbTiN), where they can be exploited for targeted frequency tuning [214] and parametric amplification [215]. While the kinetic inductance of aluminum is comparatively small, it's reasonable to expect a frequency shift given the large external fields.

In summary, while the dependence of the Josephson inductance and FTR frequency on externally applied magnetic fields follows theoretical expectations qualitatively, the interplay of multiple effects is too complex to be quantitatively predicted by our simple model at this stage. Consequently, we primarily rely on experimentally determined values of I_{c0} and ω_0 for analysis and model calculations in this thesis.

5.1.2 Kerr non-linearity

In the discussion of non-linear microwave resonators in Sec. 2.3.4, it becomes clear that the Kerr non-linearity $\mathcal{K}$ is an important parameter for the operation of flux-tuneable resonators. It will influence how the average photon occupation in the FTR is calculated according to Eq. (2.80) and determines the input power that will lead to the onset of bifurcation (Eq. (2.85)), which poses a fundamental limit for many experimental applications.

To determine the value of the Kerr non-linearity for the device in this study, we primarily have two options: First, we can rely on our knowledge of the design parameters of the microwave circuit, like its inductance L, capacitance C and length ℓ, in order to calculate the Kerr analytically using the expression we derived earlier, Eq. (2.74). Second, we can experimentally probe the device for the effects of the non-linearity, in particular the characteristic photon number dependent frequency shift.
In the following, we want to pursue both avenues – hopefully validating the analytical expression with our experimental data – and combine their results with the goal of developing a reliable and adaptable toolset to calculate the Kerr non-linearity in flux-tuneable microwave resonators.

To experimentally extract the Kerr non-linearity of the studied electromechanical device, we perform power-dependent single-tone spectroscopy [216]. The complex microwave transmission $|S_{21}|$ of the FTR close to resonance is recorded using a VNA and a single probe tone ω_p. The measurement is then repeated for increasing microwave powers P_p of the probe tone. As the microwave power is increased, the average photon occupation of the FTR mode $\bar{n}_\mathrm{c}$ is expected to increase as well. As discussed in Sec. 2.3.4, the Kerr non-linearity of the device then leads to a shift of the effective resonance frequency that is proportional to $\bar{n}_\mathrm{c}$ (cf. the modified detuning $\tilde{\Delta}$ in Eq. (2.77)), which can be quantitatively evaluated. The results of a single-tone experiment, performed at a working point of $\omega_\mathrm{c} = 7.25\,\mathrm{GHz}$ and an in-plane field of $B_\mathrm{ip} = 30\,\mathrm{mT}$, are shown in Fig. 5.5.

In the colorplot in panel **a**, the resonance condition of the FTR is visible as a bright orange feature. We observe a pronounced downshift in the resonance frequency by several MHz as the probe power P_p is increased. The direction of the shift towards lower frequencies indicates a negative Kerr coefficient $\mathcal{K} < 0$ of the studied device, which is in agreement with the prediction of

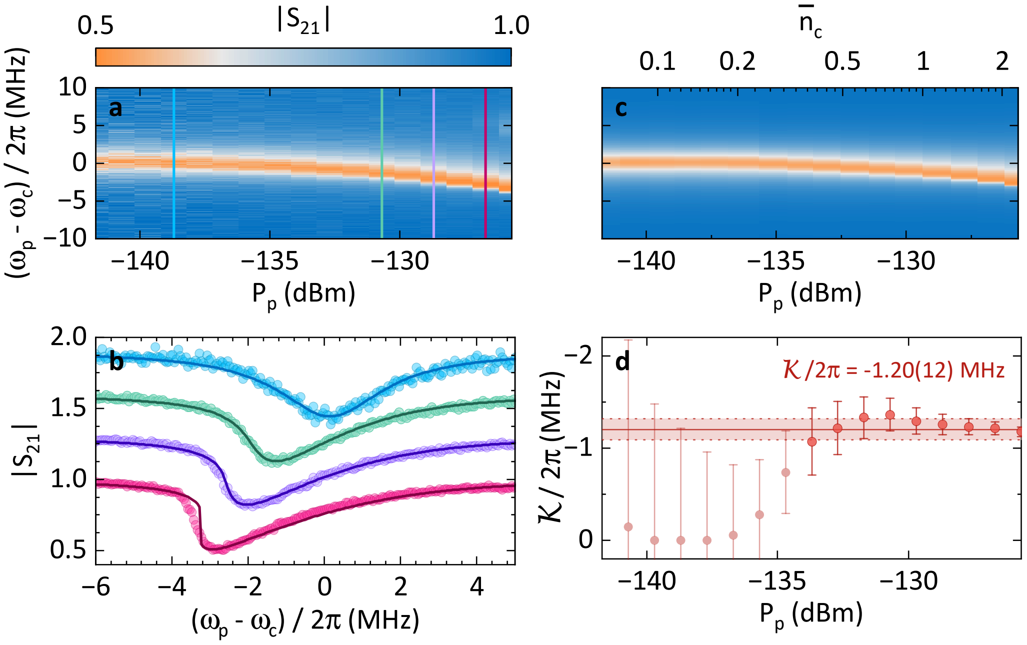

Fig. 5.5.: Power-dependent microwave spectroscopy to extract the Kerr non-linearity. a Microwave transmission $|S_{21}|$ of a FTR, probed by a probe tone ω_p around the resonance frequency ω_c for increasing microwave power levels P_p at the sample (attenuation included). With increasing P_p, a downward shift of the resonance signature by several MHz is observable, consistent with a Kerr-type non-linearity. **b** Linescans of the measurement data shown in **a** at selected microwave powers (see matching colored lines). Solid lines are best fits to the non-linear transmission model Eq. (5.1). **c** Best fits of the experimental data from **a** to Eq. (5.1), presented as a colorplot using the same colorscale. For the upper x-axis, the Kerr non-linearity $\mathcal{K}$ extracted from the fit is used to convert the incident microwave power P_p to an average photon occupation of the FTR $\bar{n}_\mathrm{c}$ according to Eq. (2.80). **d** $\mathcal{K}$ as a function of microwave power, extracted from the fits to Eq. (5.1). Error bars are the uncertainty from the fit in extracting the resonance frequency f_r, propagated to a uncertainty in $\mathcal{K}$. From the high-power range, where errors become reasonable, we extract a mean value of $\mathcal{K}/2\pi = (-1.20 \pm 0.12)\,\mathrm{MHz}$, transparent points are neglected for the mean value calculation. The measurements are performed at a working point of $\omega_\mathrm{c}/2\pi = 7.25\,\mathrm{GHz}$ and $B_\mathrm{ip} = 30\,\mathrm{mT}$.

the circuit model Eq. (2.74). When studying the individual frequency sweeps at a given power (panel **b**), we also find that the Kerr non-linearity leads to a change in the shape of the resonance feature away from an ideal Lorentzian to an asymmetric feature, as expected from the theory presented in Sec. 2.3.4. The deviation from a Lorentzian lineshape, however, means that the standard linear fit model Eq. (4.1) can no longer be used to reliably extract the resonance frequency of the FTR at high input powers. To address this issue, we instead use an improved fitting model for non-linear microwave resonators [217].

$$S_{21}(f) = Ae^{i\phi}e^{-i2\pi f\tau}\left\{1 - \frac{(Q/|Q_\mathrm{e}|)e^{i\theta}}{1 + 2iQ\,[f/(f_\mathrm{r} + \mathcal{K}\bar{n}_\mathrm{c}) - 1]}\right\}, \tag{5.1}$$

which can be recognized as a modification of the circle-fit model Eq. (4.1). Due to the power-dependent modification of the resonance frequency $f_\mathrm{r} \rightarrow f_\mathrm{r} + \mathcal{K}\bar{n}_\mathrm{c}$, where the power enters via the average photon occupation $\bar{n}_\mathrm{c}$, the model can fit the microwave transmission response of the non-linear FTR, including the effects of the Kerr non-linearity, and allows us to extract $\mathcal{K}$, as long as $\bar{n}_\mathrm{c}$ is known. We emphasize that $\bar{n}_\mathrm{c}$ is a frequency-dependent quantity, calculated from the cubic equation Eq. (2.80) with the detuning $\Delta/2\pi = f - f_\mathrm{r}$ and taking the input attenuation of the experiment into account. Since $\bar{n}_\mathrm{c}$ is itself dependent on $\mathcal{K}$, the fitting procedure needs to be performed iteratively until it converges at a solution that fully reproduces the frequency shift and the asymmetric lineshape of a non-linear resonator.

The best fits of Eq. (5.1) to our experimental data are shown as solid lines in Fig. 5.5b and reproduce the measured resonance signatures well, even at high microwave powers where the response deviates significantly from the linear case. Additionally, we present the fits to the entire power-dependent dataset in **c** as a color plot for direct comparison with the data in **a** and find excellent agreement. To put the power levels into perspective, we also use $\mathcal{K}$ extracted from the fits to express the incident power P_p in terms of the average photon occupation of the FTR, $\bar{n}_\mathrm{c}$, as plotted on the top x-axis. The extracted values of $\mathcal{K}$ are presented in Fig. 5.5d. We find values close to zero for low microwave powers, while $\mathcal{K}/2\pi$ appears to saturate around $-1.2\,\mathrm{MHz}$ towards higher powers. This observation can be explained by the fact that in the low-power limit, with $\bar{n}_\mathrm{c} \ll 1$ photons occupying the resonator mode, its response is still approximately linear, and the Kerr-induced frequency shift given by the product $\mathcal{K}\bar{n}_\mathrm{c}$ is extremely small, potentially even smaller than the accuracy with which the resonance frequency f_r can be determined by the fit. The error bars in Fig. 5.5d, calculated by propagating the fitting uncertainty of f_r to $\mathcal{K}$, reflect this effect and show large errors in the low-power regime. Phrased differently, the low-power, linear response regime is almost entirely $\mathcal{K}$-independent and not suited to extract dependable values for $\mathcal{K}$. Therefore, we neglect the values acquired at low power (transparent points) and calculate the mean value in the region of higher powers, extracting a Kerr non-linearity of $\mathcal{K}/2\pi = (-1.20 \pm 0.12)\,\mathrm{MHz}$ at this working point, where the uncertainty is the standard deviation of the considered data points.

Having established the methodology for the experimental extraction of the Kerr non-linearity, the next objective is to evaluate whether an analytical approach can faithfully replicate our experimental observations. Access to such

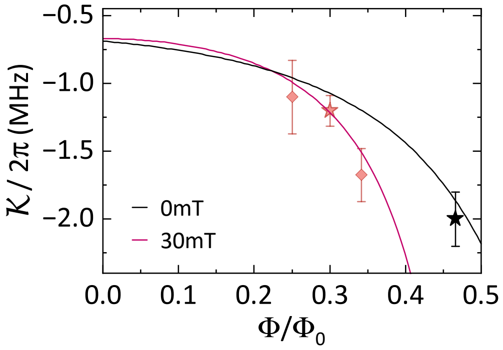

Fig. 5.6.: Calculated Kerr non-linearity based on the circuit model. Kerr non-linearity $\mathcal{K}$ as a function of normalized flux-bias Φ/Φ_0 for in plane fields $B_{\mathrm{ip}} = 0\,\mathrm{mT}$ (black) and $B_{\mathrm{ip}} = 30\,\mathrm{mT}$ (red). $\mathcal{K}$ is calculated numerically according to Eq. (2.74) with the circuit parameters (I_{c0}, β_{L}, L_{loop}) as extracted from the flux tuning curves. Datapoints are experimentally determined values of $\mathcal{K}$ using power-dependent spectroscopy as introduced above, the error bars are the standard deviation. The red star represents the measurement presented in Fig. 5.5, and the black star references a measurement of the same device published in Ref. [57]. We find agreement between the experiments and the theoretical model within their uncertainties.

an analytical framework would be of immense value for the efficient characterization of non-linear resonators because the Kerr non-linearity determined experimentally is inherently specific to the precise operational conditions under which it was measured. From the analytical expression Eq. (2.74), it is clear that $\mathcal{K}$ depends on the ratio of static inductance L to the Josephson inductance L_{J}, which depends on the flux-bias value Φ_{b} of the working point. Furthermore, we have studied the magnetic field dependence of the FTR's tuning behavior in Sec. 5.1.1 and found a non-negligible impact of the in-plane magnetic field B_{ip}. Accordingly, both parameters can be expected to influence $\mathcal{K}$, and a proper characterization of $\mathcal{K}$ across the device's entire operating regime would require a large number of repeated experiments at different operating points.

For the analytical computation of the Kerr non-linearity, we employ Eq. (2.74), incorporating parameters such as the line inductance L_0, line capacitance C_0, and the CPW resonator's design length ℓ, in conjunction with the magnetic field-dependent attributes of the SQUID – I_{c0}, β_{L}, and L_{loop} – derived from the frequency tuning analysis discussed in the previous section. The model's calculations, presented for two distinct in-plane magnetic fields ($B_{\mathrm{ip}} = 0\,\mathrm{mT}$ and $B_{\mathrm{ip}} = 30\,\mathrm{mT}$), are illustrated as solid lines in Fig. 5.6. These calculations highlight the pronounced dependency of $\mathcal{K}$ on both the flux bias point Φ_{b} and the in-plane magnetic field B_{ip}, as anticipated from our discussions on the Josephson inductance. Along these model calculations, we plot experi-

mental $\mathcal{K}$ values, obtained at various flux bias points for $B_{\mathrm{ip}} = 30\,\mathrm{mT}$ through power-dependent spectroscopy measurements. Additionally, we reference values from Ref. [57], where the device under examination was previously investigated at $B_{\mathrm{ip}} = 0\,\mathrm{mT}$. The comparative analysis reveals good agreement between the experimentally determined values and our analytical model within their respective uncertainties across all evaluated operational points.
This result gives confidence in the analytical model's reliability for predicting the Kerr non-linearity at any selected operational point of the device, eliminating the need for dedicated experiments to re-determine $\mathcal{K}$ with each adjustment of the flux bias or external magnetic field. Consequently, we rely on analytically computed $\mathcal{K}$ values for the analysis of subsequent experiments within this work, unless explicitly stated otherwise.

5.1.3 Mechanical response

Having completed a basic field- and flux-dependent characterization of the microwave properties of the electromechanical system, we now shift our focus to the mechanically compliant element. We recall from Sec. 3.1.1 that the mechanical oscillator in the investigated device is formed by the release of two parallel aluminum nanostrings that are part of the SQUID loop. Accordingly, we expect a total of 4 mechanical modes to be present in the system, since each nanostring is capable of performing both in-plane (IP) and out-of-plane (OOP) oscillations (cf. Sec. 2.2.1). Fortunately, the device used in this chapter has already been investigated regarding its mechanical properties in Refs. [57, 158], particularly in the larger context of aluminum nanostrings and their properties at low temperatures. Therefore, we will refrain from repeating the full analysis and instead focus on the aspects that differ from the previous studies:
In the aforementioned experiments, the device was operated with a single control field in out of plane direction. Accordingly, the main contribution to the flux-mediated coupling mechanism was provided by the mechanical in-plane modes of the nanostrings, making them the focus of the study. Moreover, the applied field strengths were subject to a limitation to about 1 mT, imposed by the degradation of the microwave resonator performance in larger fields, originating from the creation of flux lines penetrating the aluminium thin film.

In this work, we operate the device with a strong in-plane field B_{ip} provided by an external vector magnet. This allows us to apply larger field strengths of up to $\approx 100\,\mathrm{mT}$, where the applicable field range is limited by the material

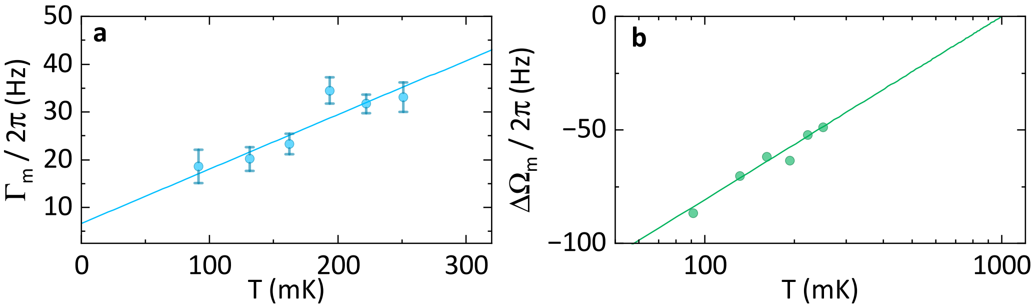

Fig. 5.7.: Temperature dependence of the nanostring oscillator properties. Mechanical linewidth Γ_{m} (**a**) and change of resonance frequency $\Delta\Omega_{\mathrm{m}}$ (**b**) as a function of cryostat temperature, extracted using microwave spectroscopy and fits of Eq. (4.2) to the voltage spectral density. In **a**, we observe and fit a linear dependence (solid line) and extrapolate to 0K for the intrinsic linewidth $\Gamma_0/2\pi = (6.7 \pm 5.0)\,\mathrm{Hz}$. In **b**, the change in $\Delta\Omega_{\mathrm{m}}$ is plotted relative to the extrapolated value for $T = 1\,\mathrm{K}$. We find a logarithmic dependence following Eq. (5.3) with $C = (6.05 \pm 0.07) \times 10^{-6}$. Each data point corresponds to the average of multiple measurements acquired with different probe tone powers. The errors indicate the standard deviation from the averaging. All measurements are performed in an in-plane field of $B_{\mathrm{ip}} = 15\,\mathrm{mT}$.

of the microwave resonator, in particular, the critical field expected for thin film aluminum of 100 nm thickness [156]. In the in-plane field configuration, the out-of-plane mechanical mode of the nanostring is dominating the flux-mediated coupling. Therefore, we need to re-verify the basic properties of the investigated OOP mechanical mode, specifically its intrinsic linewidth Γ_0 and resonance frequency Ω_{m} under the influence of stronger magnetic fields. These parameters will be used extensively in model calculations, fits, and analysis, so their exact determination in the current experimental setup is crucial.

To characterize the properties of the mechanical subsystem at elevated magnetic fields of $B_{\mathrm{ip}} = 15\,\mathrm{mT}$, we make use of the microwave spectroscopy technique introduced in Sec. 4.2.2 to extract Γ_{m} and Ω_{m} from the recorded voltage spectral densities of a weak probe signal by fitting it to the Lorentzian lineshape given by Eq. (4.2). We repeat the measurements for increasing cryostat temperatures and average over a range of probe powers to reduce statistical effects. The results are shown in Fig. 5.7. In the measured linewidth of the nanostring oscillator, shown in panel **a**, we find a linear increase with temperature of the form

$$\Gamma_{\mathrm{m}}(T) = \Gamma_0 + \gamma_{\mathrm{m}} T\,, \tag{5.2}$$

where we define the intrinsic linewidth as $\Gamma_0 = \Gamma_{\mathrm{m}}(T = 0)$. From a linear fit to the data we receive $\Gamma_0/2\pi = (6.7 \pm 5.0)\,\mathrm{Hz}$ and a temperature dependent damping of $\gamma_{\mathrm{m}}/2\pi = (113.5 \pm 2.7)\,\mathrm{Hz/K}$.

Physically, the changing loss rate of the nanostring at cryogenic temperatures can be explained by scattering of phonons at two-level-system (TLS) defects, which influences both relaxation rates and the effective sound velocity found in the material [218]. The underlying models originate from the study of amorphous insulators (e.g. glasses) at low temperatures [149], but prove well applicable to polycristalline aluminum nanostrings [218]. Based on the same model, we expect a logarithmic temperature dependence of the material's sound velocity, which translates to a change of the nanostrings resonance frequency according to [218]

$$\Delta\Omega_\mathrm{m}/\Omega_\mathrm{m} = C \cdot \ln\left(T/T_0\right) . \tag{5.3}$$

In the above equation, T_0 must not be confused with the critical temperature of superconducting aluminum, but instead is a *transition temperature* used in the TLS-scattering model to describe the crossover point between low-temperature and high-temperate behavior. This transition was found to occur at $T_0 = 1\,\mathrm{K}$ for aluminum nanostrings [218].

In panel **b**, we fit the model Eq. (5.3) to the experimentally observed change in Ω_m in reference to the extrapolated value at $1\,\mathrm{K}$ and extract a constant $C = (6.05 \pm 0.07) \times 10^{-6}$. Both the values and the temperature dependence of Γ_m and Ω_m agree well with the observations on the nanostrings' out-of-plane mode in small magnetic fields in Ref. [158]. It also confirms that the nanostring oscillator thermalizes well to the environment over the entire range of experimental cryostat temperatures.

5.2 The electromechanical single-photon coupling rate

With the previous experiments providing a good understanding of the basic properties of both the microwave and mechanical components of the electromechanical device, we proceed with a focused study of the electromechanical single-photon coupling rate g_0 that can be achieved. To this end, we employ two complementary methods to investigate and validate the value of g_0, ensuring a thorough understanding of both the experimental setup and device functionality. The first method, a thermal noise calibration technique, studies the temperature dependence of the phonon occupation of the mechanical mode, enabling a study that is independent of the photon number in the microwave circuit and robust against deviations from the thermal equilibrium.

The second set of experiments investigates the phenomenon of Electromechanically Induced Transparency (EMIT), which serves to validate the g_0 values obtained from the first method and correlates them with the actual photon occupation of the microwave resonator. Together, these methods not only disclose the electromechanical interaction strength but also significantly reduce the uncertainty related to the photon number calibration of the experimental setup, providing a solid base for subsequent experiments presented in this work. Finally, this two-pronged determination of g_0 is repeated for increasingly large external magnetic field values, in order to validate the expected magnetic field dependence of the single-photon coupling strength.

5.2.1 Thermal noise calibration

Background The first approach to determine g_0 is based on the frequency noise calibration technique described in Sec. 4.2.3. However, as discernible from Eq. (4.12), even with the calibration, insight into the coupling rate is initially limited to the product $\sqrt{\bar{n}_\mathrm{ph}}g_0$. Under the assumption of thermal equilibrium, $\bar{n}_\mathrm{ph} = k_\mathrm{B}T/\hbar\Omega_\mathrm{m}$ can be calculated and g_0 extracted, but full thermalization of the nanometer-scale oscillator in a complex cryogenic setup is not self-evident. Furthermore, the optomechanical interaction itself is fundamentally linked to photon-phonon conversion processes, which means any microwave drive applied to the device has the potential to create or annihilate phonons in the mechanical mode, disturbing the equilibrium.

To overcome this uncertainty, we make use of the temperature dependence of the phonon occupation. Experimentally, we perform frequency noise calibrated microwave spectroscopy experiments at a fixed working point and a series of different cryostat temperatures and repeatedly determine $\bar{n}_\mathrm{ph}g_0^2$. Since g_0 remains fixed by the working point, this will allow us to access and calibrate the temperature-dependence of $\bar{n}_\mathrm{ph}$.

Experiment As preparation for the experiment, we select a fixed bias field and working point at which g_0 shall be investigated, in this case $B_\mathrm{ip} = 15\,\mathrm{mT}$ and $\omega_\mathrm{c}/2\pi \approx 6.9\,\mathrm{GHz}$ for all measurements shown in this section. We then use a quick VNA scan of the microwave transmission around the FTR resonance to perform a first circlefit and exactly determine ω_c. Based on the fit result, a weak stabilization tone is applied at $\omega_\mathrm{s} = \omega_\mathrm{c} - 500\,\mathrm{kHz}$ and used to frequency-lock

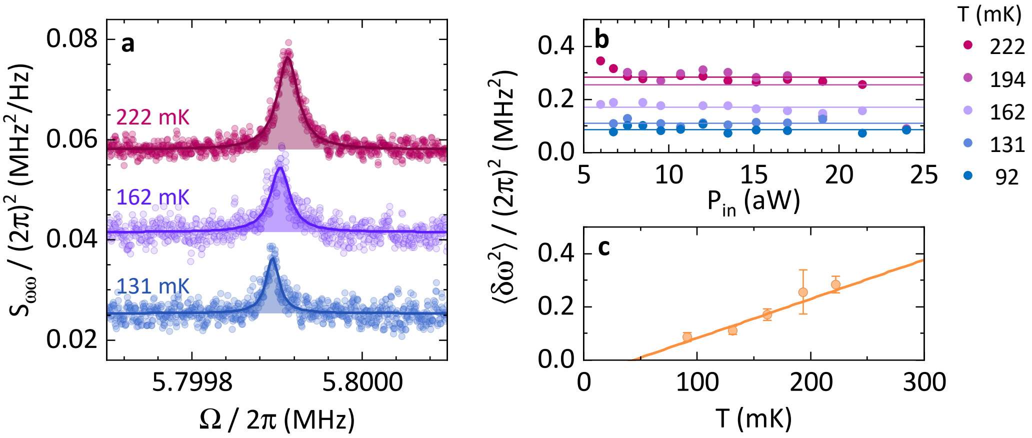

Fig. 5.8.: Extracting the electromechanical coupling rate from frequency fluctuations. a Frequency spectral density $S_{\omega\omega}(\Omega)$ calibrated using the frequency noise calibration protocol for different cryostat temperatures and a fixed microwave power of $P_\mathrm{d} = 15\,\mathrm{aW}$. Towards higher temperatures, an increase in peak area (shaded) is observed. Solid lines are fits to Eq. (4.2). The traces are offset for clarity. **b** Integrated frequency fluctuations $\langle\delta\omega^2\rangle$ at each temperature as a function of probe power. Solid lines illustrate the mean value for each temperature. No change with probe power is observed, confirming the absence of optomechanical cooling or heating effects. Statistical errors are smaller than the symbol size. **c** Integrated $\langle\delta\omega^2\rangle$ as a function of temperature, averaged over all drive powers (error bars are standard deviations). $\langle\delta\omega^2\rangle$ shows a linear temperature dependence as it is proportional to the thermal phonon number $\bar{n}_\mathrm{ph}$. From the slope of the linear fit (solid line) we extract a single-photon coupling rate $g_0/2\pi = (14.31 \pm 1.20)\,\mathrm{kHz}$ (see main text).

the FTR (cf. Sec. 4.3). The frequency-lock will remain enabled for the entire duration of the measurement and over all investigated cryostat temperatures. Small frequency shifts that would arise from the temperature change are compensated by the active feedback loop. For each temperature, we now repeat an identical measurement protocol:

First, the cryostat's temperature is set to the target value using resistive heaters mounted on the mixing chamber plate. After a wait time sufficient to thermalize the DUT (verified by a temperature sensor), the probe tone is applied with the lowest microwave power at $\omega_\mathrm{p} - \Omega_\mathrm{m}$, where Ω_m is known from previous characterization measurements at the exact working point. We choose the red-sideband configuration for the probe tone because it has proven to be the most stable against small frequency drifts that are not compensated by the active feedback. For this reason, we also do not generally assume the detuning $\Delta = \omega_\mathrm{p} - \Omega_\mathrm{m}$ to remain constant over the course of the experiment. Instead we re-record the microwave transmission around the FTR resonance before and after each individual measurement and extract the momentary detuning. Then, using the downconversion path of the experimental setup discussed in Sec. 4.1, the voltage spectral density $S_{\omega\omega}(\Omega)$ of the downconverted probe signal around the mechanical resonance frequency Ω_m is recorded by a spectral analyzer for a series of increasing microwave probe powers. With the frequency noise calibration procedure, introduced in Sec. 4.2.3, we transform the measured voltage spectral density to a calibrated frequency spectral density $S_{\omega\omega}(\Omega)$, which contains all necessary information about $\bar{n}_\mathrm{ph}$ and g_0.

A set of frequency spectral density traces recorded at three different temperatures, but the same microwave power, are shown in Fig. 5.8**a**. As the temperature is increased, the peak area increases as well, consistent with a larger mechanical displacement due to an increase in the thermal occupation of the coupled mode. We quantify the data by fitting the Lorentzian peaks with Eq. (4.2) to determine $S_{\omega\omega}(\Omega_\mathrm{m})$ along with Ω_m and Γ_m. From the fit results, the peak area, or total mean square frequency fluctuations $\langle\delta\omega^2\rangle$ can be directly calculated using Eq. (4.5) to

$$\langle\delta\omega^2\rangle = S_{\omega\omega}(\Omega_\mathrm{m})\frac{\Gamma_\mathrm{m}}{2}\,, \tag{5.4}$$

or alternatively, by numerical integration of the raw data[1].

Repeating the measurement for multiple probe powers per temperature is necessary for the frequency noise calibration, but also gives us the opportunity to verify the measurement backaction of our protocol: In Fig. 5.8**b**, we plot $\langle\delta\omega^2\rangle$ as a function of power for every temperature and find that the values are probe-power independent. This provides a strong indication that optomechanical heating or cooling effects driven by the probe tone do not affect the phonon population of the mechanical element. Furthermore, with the knowledge that the probe power does not affect the result of the measurement, we can average over all measurements taken at the same temperature and plot the integrated frequency fluctuations as a function of temperature in Fig. 5.8**c**. The frequency fluctuations increase linearly with temperature, which is consistent with the expectation since $\langle\delta\omega^2\rangle \propto \bar{n}_\mathrm{ph}$ and $\bar{n}_\mathrm{ph} \propto T$ for $k_\mathrm{B}T \gg \hbar\Omega_\mathrm{m}$, which is fulfilled for our parameters. Less intuitive is the observation that the extrapolation of the linear behavior has a finite offset at $T = 0$. However, this offset, called *backaction-equivalent-temperature*, T_ba, has been observed in other experiments with electromechanical systems and is attributed to the backaction of the microwave circuit on the mechanical element [30].

---

[1] We use both techniques in parallel and check for sufficient agreement to exclude fitting errors.

We fit the temperature dependence to a linear function of the form

$$\langle \delta\omega^2 \rangle / (2\pi)^2 = s(T) T + c_{\mathrm{ba}} \tag{5.5}$$

using a weighted fit based on the statistical deviations of each $\langle \delta\omega^2 \rangle$ value. From our experimental data, we extract $s(T) = (1.47 \pm 0.24) \times 10^{12}\,\mathrm{Hz}^2/\mathrm{K}$ and $c_{\mathrm{BA}} = (-6.5 \pm 3.4) \times 10^{10}\,\mathrm{Hz}^2$, or translated to a temperature offset $T_{\mathrm{ba}} = (-44 \pm 30)\,\mathrm{mK}$.
Since $\langle \delta\omega^2 \rangle = 2 g_0^2 \bar{n}_{\mathrm{ph}}$ (Eq. (4.9)) and g_0 is independent of temperature, the slope describes exactly the increase in thermal phonon occupation and we can write

$$\bar{n}_{\mathrm{ph}} = \frac{k_{\mathrm{B}} T}{\hbar \Omega_{\mathrm{m}}} (T + T_{\mathrm{ba}}) \tag{5.6}$$

and use it to extract the optomechanical single-photon coupling rate

$$\frac{g_0}{2\pi} = \sqrt{\frac{s(T) \hbar \Omega_{\mathrm{m}}}{2 k_{\mathrm{B}}}} = (14.31 \pm 1.20)\,\mathrm{kHz}\,. \tag{5.7}$$

Finally, we can compare the experimentally observed value to the theoretical prediction via Eq. (2.96). At this point, all of the variables are known: $\Omega_{\mathrm{m}}/2\pi = 5.7999\,\mathrm{MHz}$ from the measurement, $x_{\mathrm{zpf}} = \sqrt{\hbar/(2 m_{\mathrm{eff}} \Omega_{\mathrm{m}})} = 40\,\mathrm{fm}$ calculated from geometric parameters, and the flux responsivity $\partial\omega_{\mathrm{c}}/\partial\Phi = 2\pi \cdot 5.5\,\mathrm{GHz}/\Phi_0$ extracted from the tuning curve. Assuming a geometric factor of $\gamma = 0.9$ [57, 219], we expect theoretically

$$g_0^{\mathrm{theory}}/2\pi = 43.40\,\mathrm{kHz}\,, \tag{5.8}$$

which is more than a factor of 3 larger than the experimentally observed value. For now, we will postpone the discussion of this discrepancy and first employ the second approach in our toolbox to evaluate the validity of the extracted g_0.

5.2.2 Electromechanically Induced Transparency (EMIT)

Background Our second experimental technique for the extraction of the single-photon coupling strength is based on Electromechanically Induced Transparency (EMIT). EMIT is the circuit equivalent of Electromagnetically Induced Transparency (EIT) [220], a phenomenon in quantum optics experiments with multilevel atoms, where the interference of electromagnetic fields manifests as a cancellation of the absorption of the probe field. EMIT explores a similar transparency induced through electromechanical interactions of microwave fields.

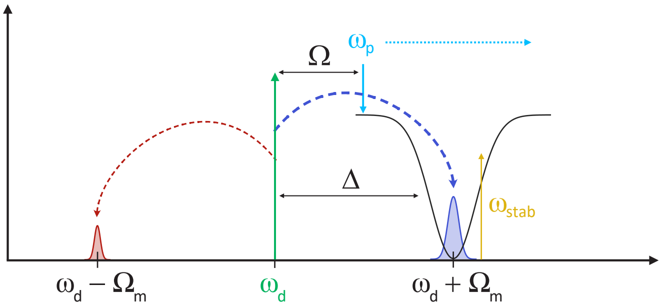

Fig. 5.9.: Schematic illustration of the EMIT experiment. A strong microwave drive ω_d is applied at the ideal detuning $\Delta = \omega_\mathrm{d} - \omega_\mathrm{c} = \Omega_\mathrm{m}$ relative to the FTR resonance frequency ω_c . A second, weaker probe tone ω_p is scanned across the resonance (described by a detuning Ω w.r.t the drive). The anti-Stokes field generated from the drive due to the electromechanical coupling at $\omega_\mathrm{d} + \Omega_\mathrm{m}$ appears within the FTR resonance signature and destructively interferes with the probe tone, leading to the appearance of a transparency window. A very weak stabilization tone at $\omega_\mathrm{stab} = \omega_\mathrm{c} + 500\,\mathrm{kHz}$ is used for active stabilization of the FTR.

Specifically, EMIT is observed when the system is exposed to a strong drive tone ω_d at a specific detuning $\Delta = \omega_\mathrm{d} - \omega_\mathrm{c} \approx -\Omega_\mathrm{m}$, i.e. red-detuned from the FTR resonance by the resonance frequency of the mechanical subsystem, as illustrated in Fig. 5.9. A second, weaker probe tone ω_p is injected into the system and scanned across the frequency range of the FTR resonance to probe the response of the FTR. The simultaneous presence of the drive and the probe tone results in a radiation pressure force oscillating at $\Omega = \omega_\mathrm{p} - \omega_\mathrm{d}$. When the beating frequency Ω matches the mechanical resonance frequency Ω_m, the mechanical system is driven resonantly and a coherent oscillation is induced. In frequency space, this leads to the emergence of sidebands, the Stokes and anti-Stokes fields, symmetrically around the strong driving field. In the resolved-sideband regime ($\Omega_\mathrm{m} > \kappa$), the response of the microwave resonator acts as a narrow-band filter for these fields and strongly suppresses the Stokes peak, as it is far detuned from the resonance condition ($\omega_\mathrm{d} - \Omega_\mathrm{m} \approx \omega_\mathrm{c} - 2\Omega_\mathrm{m}$). In contrast, the anti-Stokes field is roughly on resonance with the microwave resonator ($\omega_\mathrm{d} + \Omega_\mathrm{m} \approx \omega_\mathrm{c}$) and is moreover phase coherent with the probe drive ω_p that scans across the cavity response. This leads to destructive interference of the two fields, suppressing the build-up of the intra-cavity probe field. Simply put, the number of probe photons entering the microwave resonator is reduced and the number of photons transmitted is increased, making the system appear more *transparent* to the probe field. In the cavity response, this effect manifests itself as an enhanced cavity transmission up to unity compared to the feed line.

A quantitative description of the EMIT signature as a function of drive power (expressed as photon occupation $\bar{n}_\mathrm{c}$), drive detuning Δ and probe detuning $\Omega = \omega_\mathrm{p} - \omega_\mathrm{c}$ can be found based on the full optomechanical interaction hamiltonian in presence of a drive field (cf. Eq. (2.97)). Using input-output theory, one finds for the response of a side-coupled microwave resonator in the resolved sideband regime including EMIT [32, 66]

$$S_{21}(\Omega) = \left| 1 - \frac{\kappa_\mathrm{ext}/2}{-i(\Delta+\Omega) + \kappa/2 + \frac{g_0^2 \bar{n}_\mathrm{c}}{-i(\Delta-\Omega_\mathrm{m})+\Gamma_\mathrm{m}/2}} \right| . \qquad (5.9)$$

Intuitively, the above expression can be understood as the response of the microwave resonator to the probe tone, modified by an additional term in the denominator that resembles a Lorentzian function defined by the properties of the mechanical oscillator (linewidth Γ_m and resonance frequency Ω_m) and proportional to the photon-enhanced electromechanical interaction $g_0^2\bar{n}_\mathrm{c}$. Consequently, in the absence of electromechanical coupling ($g_0 = 0$), we recover the response of a simple, linear microwave resonator (cf. Eq. (2.37)).

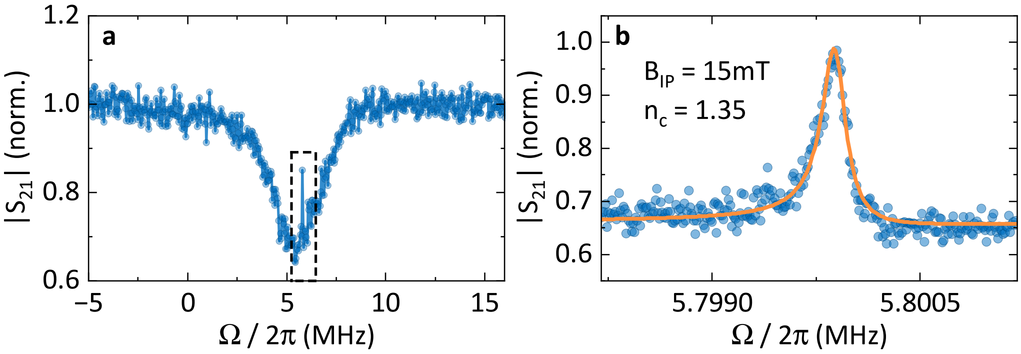

Fig. 5.10.: Microwave response of the electromechanical system in EMIT configuration. a Wideband VNA scan of the FTR response in the presence of a strong drive at $\omega_\mathrm{d} = \omega_\mathrm{c} - \Omega_\mathrm{m}$. **b** Detailed, low-bandwidth scan of the frequency range around $\Omega = \Omega_\mathrm{m}$ (dashed area in **a**). A peak in the microwave transmission appears as the detuning coincides with the mechanical resonance frequency, the transparency signature of EMIT. The peak is fitted to Eq. (5.9) assuming a coupling rate $g_0/2\pi = 9.73\,\mathrm{kHz}$ to extract the cavity photon occupation $\bar{n}_\mathrm{c} = 1.35$. The shown measurements are performed in an in-plane field of $B_\mathrm{ip} = 15\,\mathrm{mT}$ and with a drive power of $P_\mathrm{d} = 0.95\,\mathrm{fW}$.

Experiment To observe the EMIT signature experimentally, we initially bias the device at the desired value of B_ip and tune the FTR to a suitable working point. For the presented experiment, we choose $B_{\mathrm{ip}} = 15\,\mathrm{mT}$ and $\omega_{\mathrm{c}}/2\pi \approx 7\,\mathrm{GHz}$, to allow direct comparison with the previous frequency noise calibration experiment. Subsequently, we conduct a simple microwave transmission scan with the VNA to record the resonance response of the FTR and use our standard fitting procedure to extract ω_{c} and the linewidths κ_{int},κ_{ext} at the specific working point. Based on this data, we frequency-lock the cavity and apply the ideally detuned drive tone at $\omega_{\mathrm{d}} = \omega_{\mathrm{c}} - \Omega_{\mathrm{m}}$.

With the strong drive now interacting with the device, we repeat the microwave transmission measurement around resonance. An exemplary trace is depicted in Fig. 5.10**a**, where a sharp peak is visible within the absorption dip of the FTR resonance. This reduction of absorption is the signature of EMIT. However, to properly resolve and analyze the EMIT signal, we conduct a more detailed VNA scan with a low measurement bandwidth (1 Hz to 10 Hz) across a small frequency window centered around $\omega_{\mathrm{d}} + \Omega_{\mathrm{m}}$. The result of the detailed scan is shown in Fig. 5.10**b**, where a Lorentzian peak in the microwave transmission is discernible. For both scans, we perform the background correction discussed in Sec. 4.2.1.

To quantify the effect and the underlying electromechanical interaction, we repeat the experiment for a range of microwave drive powers from $P_{\mathrm{d}} = 0.1\,\mathrm{fW}$ to $1\,\mathrm{fW}$ and fit the measured traces to Eq. (5.9) using the FTR parameters extracted from fits to the wideband scans[2] (cf. panel **a**) and the mechanical parameters Ω_{m} and Γ_{m} determined in Sec. 5.1.3. Notably, we have two options regarding the choice of free fit parameters:

1. **Assuming photon number $\bar{n}_{\mathrm{c}}$:** Without prior knowledge of the single-photon coupling rate g_0, it is common to assume knowledge of the photon occupation $\bar{n}_{\mathrm{c}}$, based on the knowledge of the experimental setup's attenuation chain, and use fits of Eq. (5.9) to the EMIT response to extract g_0.

2. **Assuming the coupling rate g_0:** Since we have already determined a value for g_0 using the thermal noise calibration (Sec. 5.2.1), we can assume g_0 to be known and use fits of Eq. (5.9) to the EMIT response to extract $\bar{n}_{\mathrm{c}}$ at each microwave power.

---

[2] To extract the FTR parameters (κ,κ_{ext}), we fit the wideband scans using the circle-fit Eq. (4.1). Alternatively, Eq. (5.9) with $g_0 = 0$ can be used as fit model. We have compared both models on experimental data and verified that they return equivalent results. The circle-fit proved more reliable due to the additional background correction terms.

If the resulting values for $\bar{n}_c$ and g_0 from both approaches show agreement, this would indicate that the underlying assumptions are consistent, in particular with respect to the photon number calibration. Crucially, the comparison of the two methods can only yield reliable results if the initial assumptions can be considered independent. In our case, since the thermal noise calibration does not depend on knowledge of $\bar{n}_c$, this requirement is in principle fulfilled.

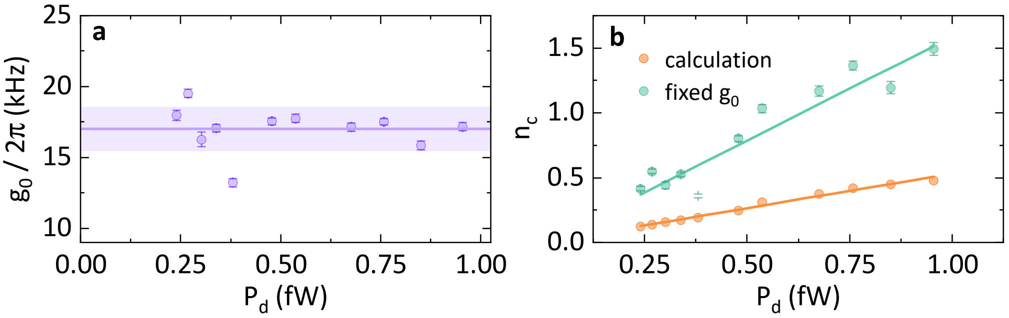

Fig. 5.11.: Fit results of power-dependent EMIT signatures under different initial assumptions. **a** Single-photon coupling rate g_0 extracted from EMIT signatures at various drive powers P_d using fits to Eq. (5.9). In **a**, $\bar{n}_c$ is treated as a known input parameter, calculated according to Eq. (2.80). The solid line and shaded area illustrate the mean value and standard deviation, respectively. In **b**, we analyze the same dataset, but treat $\bar{n}_c$ as a free fit parameter and g_0 as a known input with $g_0/2\pi = 9.73\,\mathrm{kHz}$, as extrapolated from the thermal calibration. Additionally, the calculated values for $\bar{n}_c$, as used as input parameters in **a**, are shown in orange for comparison. Solid lines are linear fits to the data. Error bars are uncertainties of the fits. FTR parameters (κ, κ_{ext}) used in the model are extracted for each power by circle fits to the resonance signature. Other parameters are re-used from previous measurements: $\mathcal{K}/2\pi = -2.87\,\mathrm{MHz}$ and $\Gamma_m/2\pi = 15\,\mathrm{Hz}$. The measurements are performed at $B_{\mathrm{ip}} = 15\,\mathrm{mT}$ and $\omega_c/2\pi \approx 7\,\mathrm{GHz}$.

We first perform the EMIT analysis using the first approach, where we assume knowledge of the photon number and use it as a fixed input parameter. To this end, we calculate $\bar{n}_c$ for each input power according to Eq. (2.80), where we assume a total attenuation to the sample of 86.2 dB and a Kerr non-linearity of $\mathcal{K}/2\pi = -2.87\,\mathrm{MHz}$. The extracted values for the electromechanical single-photon coupling rate g_0 are presented in Fig. 5.11**a** and remain largely constant as a function of the used input power. From the mean value of the power series we extract a coupling rate of $g_0/2\pi = (17.02 \pm 1.57)\,\mathrm{kHz}$.

For the second approach, we need to calculate the expected value of g_0 based on the thermal noise measurement. In order to make a valid prediction, we need to take the different working points of the two experiments into account ($\omega_c/2\pi = 7\,\mathrm{GHz}$ for EMIT vs. $6.9\,\mathrm{GHz}$ for the thermal noise measurement). To this end, we rescale the previous result by the flux responsivity $\partial\omega_c/\partial\Phi$ at the working point it was acquired, which we look up from the flux-tuning curves in Sec. 5.1.1, and receive $g_0^{\mathrm{th}}/2\pi = (14.31 \pm 1.18)\,\mathrm{kHz} \cdot \frac{3.74}{5.5} = (9.73 \pm 0.80)\,\mathrm{kHz}$. Subsequently, we repeat the analysis and fit Eq. (5.9) to the experimental EMIT data, now using $g_0^{\mathrm{th}}/2\pi = 9.73\,\mathrm{kHz}$ as a fixed input parameter and finding the best fit value for $\bar{n}_\mathrm{c}$. The results are presented in Fig. 5.11**b**, along with the calculated values of $\bar{n}_\mathrm{c}$ according to Eq. (2.80) for comparison.

We now compare the values of $\bar{n}_\mathrm{c}$ that were extracted using the second approach to the calculated values from the first approach in order to evaluate whether the results are in agreement. We observe linear scaling of the photon number $\bar{n}_\mathrm{c}$ with power in both datasets and generally higher photon numbers extracted from the fits compared to the calculation. From linear fits to the data, we find slopes of $1.61\,\mathrm{fW}^{-1}$ and $0.53\,\mathrm{fW}^{-1}$ for the fitted and calculated values, respectively. Division of the two slopes reveals that the results of the two methods differ by a factor of 3. If we attribute the entire discrepancy to a wrongly assumed attenuation, it would translate into a real attenuation that is $4.7\,\mathrm{dB}$ smaller than assumed for the calculation. This deviation significantly exceeds what can be considered a reasonable uncertainty in the estimation of the attenuation chain or what would be caused by a wrongly estimated Kerr non-linearity. Moreover, the photon numbers based on the thermal calibration would imply a real attenuation that is *smaller* than what is specified for the used microwave components, which appears unlikely. Therefore, we conclude that there is likely a physical explanation for the discrepancy between the coupling rates extracted by the two different experimental approaches. This aspect will be further explored in the next section.

To conclude the introduction of the EMIT experiment, we evaluate the single-photon coupling rate extracted from EMIT against the theoretical prediction. Using Eq. (2.96) once more, with identical parameters aside from an adjusted flux responsivity $\partial\omega_\mathrm{c}/\partial\Phi = 2\pi \cdot 3.74\,\mathrm{GHz}/\Phi_0$, we calculate the expected g_0 to

$$g_0^{\mathrm{theory}}/2\pi = 29.52\,\mathrm{kHz}\,. \tag{5.10}$$

Compared to the result of the thermal noise calibration experiment, we find a less severe but still significant deviation from the theoretically expected value.

5.2.3 Magnetic field scaling

Having introduced both experimental approaches for determining g_0, we now investigate the evolution of the electromechanical coupling strength – and potentially, the discrepancies between the two experimental techniques previously observed – with increasing external magnetic fields. The expectation is straightforward: According to Eq. (2.96) we anticipate g_0 to scale linearly with the externally applied field B_{ip}. In fact, the prospect of achieving single-photon coupling rates exceeding hundreds of kHz simply by subjecting a device to a strong enough magnetic field has been a key motivation for the realization of inductively coupled electromechanical devices. Initial experimental realizations have indeed confirmed the linear scaling of g_0 for externally applied fields up to 10 mT [56, 57]. However, combining ever stronger magnetic fields and superconducting circuits is bound to be a non-trivial task, especially as the employed field strengths approach the critical fields of the superconducting material. Having confirmed that the aluminum superconducting CPW resonators used in our device can in principle withstand in-plane fields upwards of 100 mT [158] and with our setup's 3D-vector magnet being ideally suited to apply strong magnetic fields without heating the DUT, we want to take the opportunity to extend the investigation to magnetic fields exceeding the previously studied 10 mT range.

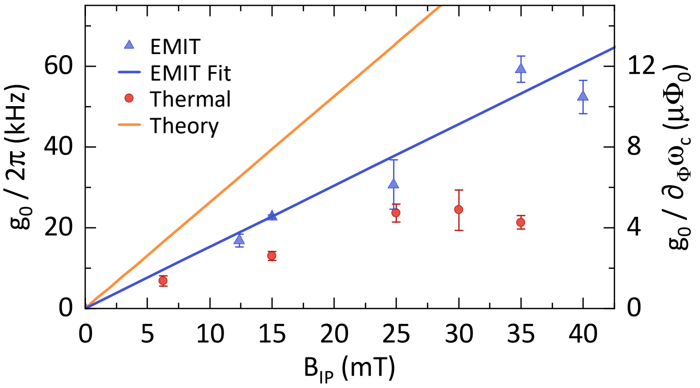

Fig. 5.12.: Electromechanical coupling rate in high magnetic fields. Single-photon coupling rate g_0, extracted from EMIT (blue) and thermal noise (red) measurements at magnetic fields up to 40 mT. The left axis shows all values rescaled to a flux-responsivity of $\partial\omega_c/\partial\Phi = 2\pi\cdot 5\,\mathrm{GHz}/\Phi_0$, while on the right axis the values are normalized by their respective $\partial\omega_c/\partial\Phi$. The orange line is a theoretical prediction calculated according to Eq. (2.96) with the device parameters listed in the main text, resulting in a slope of $2\pi\cdot 2.63\,\mathrm{kHz/mT}$. The blue line is a linear fit to the EMIT data with a slope of $2\pi\cdot 1.52\,\mathrm{kHz/mT}$. We generally observe lower coupling rates than theoretically predicted and find an increased discrepancy between the two measurement methods towards high fields.

To this end, we perform both thermal calibration measurements as discussed in Sec. 5.2.1 and EMIT measurements as introduced in Sec. 5.2.2 at various in-plane magnetic fields ranging from $B_{\mathrm{ip}} = 6.2\,\mathrm{mT}$ to 40 mT. The coupling rates extracted from each of the measurements are summarized in Fig. 5.12, along with a theoretical prediction according to Eq. (2.96). To ensure a valid comparison between different experiments and operating points, we rescale all coupling rates to a flux responsivity of $\partial\omega_{\mathrm{c}}/\partial\Phi = 2\pi \cdot 5\,\mathrm{GHz}/\Phi_0$ on the left axis and normalize them by $\partial\omega_{\mathrm{c}}/\partial\Phi$ on the right axis. This step is crucial to account for the field-dependent inductances that alter the flux-tuning behaviour of the FTR, as discussed in Sec. 5.1.1. Due to the change in inductance, even measurements conducted at nominally identical operating frequencies ω_{c} do not correspond to the same flux bias Φ_{b} and flux responsivity $\partial\omega_{\mathrm{c}}/\partial\Phi$, when a different B_{ip} is applied.

From Fig. 5.12, we make two primary observations: First, while EMIT and thermal calibration measurements exhibit reasonable agreement at low fields, they quickly begin to diverge significantly as B_{ip} is increased. In particular, the coupling rates observed in thermal calibration experiments seem to saturate around 25 mT and do not increase further. The g_0 values determined by EMIT on the other hand show an approximately linear increase until 35 mT, reaching a maximum coupling rate of $g_0/2\pi = (53.71 \pm 2.91)\,\mathrm{kHz}$, or $(59.22 \pm 3.21)\,\mathrm{kHz}$ when rescaled to a flux responsivity of $\partial\omega_{\mathrm{c}}/\partial\Phi = 2\pi \cdot 5\,\mathrm{GHz}/\Phi_0$. This is, to the best of our knowledge, the highest single-photon coupling strength reported in an electromechanical system to date. Increasing B_{ip} further to 40 mT leads to stronger signs of degradation in the flux-tuneable resonator, manifested as rising loss rates and an increasingly challenging stabilization against flux noise. Consistent with this observation is the reduced electromechanical coupling strength extracted from the EMIT experiment at $B_{\mathrm{ip}} = 40\,\mathrm{mT}$.

The second notable observation from the field dependent analysis is that, irrespective of measurement type and even for relatively small magnetic fields ($B_{\mathrm{ip}} < 10\,\mathrm{mT}$), experimentally determined values for g_0 remain significantly below the theoretical predictions. According to Eq. (2.96), we expect g_0 to scale linearly with B_{ip} at a rate of $2\pi \cdot 2.63\,\mathrm{kHz/mT}$ (illustrated by the orange line)[3]. However, fitting the EMIT data with a linear function yields a best fit of

$$g_0^{\mathrm{EMIT}}/2\pi = 1.52\,\mathrm{kHz/mT} \cdot B_{\mathrm{ip}}\,, \tag{5.11}$$

i.e. only 52% of the expected value.

Based on the experience gathered through the experiments of this work, we hypothesize that the lower-than-expected coupling rates are related to fast external flux noise, which the active feedback system does not fully compensate. Both measurement techniques rely on precise placement of a drive tone with a fixed detuning Δ relative to the FTR resonance. If flux noise causes rapid and temporary shifts in the FTR's resonance frequency, Δ will change as well, potentially affecting measurement outcomes. Since both techniques require a significant number of averaged samples to achieve sufficient signal-to-noise ratios, temporary shifts in the effective detuning due to flux noise may not immediately cause the measurement to fail in an obvious fashion, but rather add incrementally to missing or lower signals in individual samples, which can eventually translate to a smaller effective coupling rate in the averaged result. The thermal calibration technique is likely to suffer more severely from this effect, since the measurement duration and average counts are generally much larger compared to EMIT. To provide an intuition: For the thermal calibration method, data acquisition at a single temperature point can take up to 3 hours, while a power-dependent EMIT measurement like the one shown in Fig. 5.11 takes roughly 1 hour to complete.

In summary, it appears that the experimentally determined coupling rates are not fundamentally limited to values far below the theoretical prediction but suffer from a lack of short-term stability in experimental conditions. Faster measurements with fewer averages seem better suited to recover the actual coupling rate. In our case, this observation partly reaffirms the advantage of having two complementary methods to determine g_0. The thermal calibration can be used at small B_{ip} to verify EMIT results and achieve an accurate photon number calibration. Once the relevant photon numbers are calibrated, EMIT measurements, with their shorter duration, are the preferred tool to extract g_0 at higher fields.

---

[3] For the model calculation, we have used $\Omega_{\mathrm{m}}/2\pi = 5.81\,\mathrm{MHz}$, $x_{\mathrm{zpf}} = 40\,\mathrm{fm}$, $\partial\omega_{\mathrm{c}}/\partial\Phi = 2\pi \cdot 5\,\mathrm{GHz}/\Phi_0$ and $\gamma = 0.9$.

5.3 Low-power sideband cooling to the single-phonon level

Due to the versatile nature of the optomechanical interaction, a vast array of implementations have shown considerable success in the investigation and control of mechanical oscillations near the fundamental quantum limits [22]. However, even with this large trove of experience to build upon, bringing mechanical systems into the quantum regime, where the mode population approaches individual quanta of motion, remains a non-trivial task. Due to the comparatively low frequencies of most mechanical oscillators, they exhibit a high thermal population on the order of several hundred phonons, even at millikelvin temperatures. In combination with the low single-photon coupling rates achieved even by state-of-the-art optomechanical devices, this makes relatively large pump powers necessary to reach a sufficient interaction strength [32]. However, considering the potential of devices implementing flux-mediated inductive coupling to realize significantly higher single-photon coupling rates than previously possible, cooling to the quantum ground state using much lower pump powers becomes theoretically feasible.

In this section, we introduce the optomechanical sideband cooling protocol commonly used to achieve ground state preparation, provide a quantitative description for its effects and implement it experimentally on our SQUID-based electromechanical device. Thanks to the unprecedentedly large single-photon coupling strength of up to $g_0/2\pi \approx 53\,\mathrm{kHz}$, we demonstrate cooling of a nanostring's mechanical motion down to individual quanta of motion with ultra-low powers equivalent to less than a single photon occupying the microwave cavity.

5.3.1 Cooling protocol

The experimental protocol to perform optomechanical sideband cooling is illustrated schematically in Fig. 5.13. A strong microwave drive tone ω_d is applied at the ideal red-sideband detuning $\Delta = -\Omega_\mathrm{m}$ relative to the FTR resonance frequency ω_c. The configuration of microwave tones is nominally identical to the EMIT experiment discussed in Sec. 5.2.2, and in fact, both experiments rely on the same underlying scattering process. The electromechanical coupling between the electromagnetic field in the FTR and the mechanical motion of the

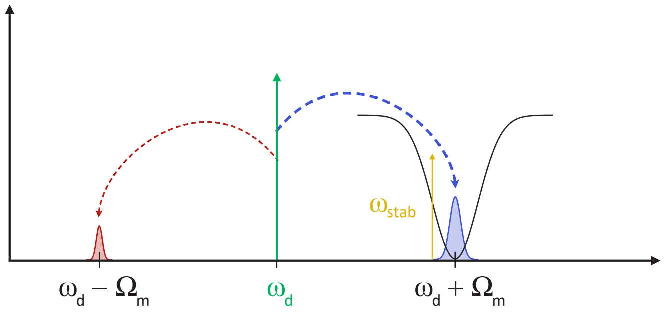

Fig. 5.13.: Schematic illustration of optomechanical sideband cooling. A strong microwave drive tone ω_d is applied at the ideal red-sideband detuning $\Delta = -\Omega_\mathrm{m}$ relative to the FTR resonance frequency ω_c. The anti-Stokes field at $\omega_\mathrm{d} + \Omega_\mathrm{m}$ is generated by inelastic scattering of the drive photons due to the electromechanical coupling. The scattering rate of the underlying process is enhanced by the density of states of the microwave resonator, leading to an asymmetric scattering rate that prefers the anti-Stokes over the Stokes process. Since every upconverted photon removes the energy $\hbar\Omega_\mathrm{m}$ from the mechanical mode, it is effectively cooled to a lower mode temperature. A very weak stabilization tone at $\omega_\mathrm{stab} = \omega_\mathrm{c} - 500\,\mathrm{kHz}$ is used for active stabilization of the FTR.

nanostring oscillator enables a phonon-photon scattering process. Photons at the drive frequency ω_d can be inelastically scattered to either $\omega_\mathrm{d} - \Omega_\mathrm{m}$ or $\omega_\mathrm{d} + \Omega_\mathrm{m}$, creating or annihilating a phonon of frequency Ω_m in the process.

In frequency space, this scattering process manifests itself as the appearance of sidebands symmetrically placed around the drive frequency at the aforementioned frequencies. Due to red-detuned placement of the driving tone, the anti-Stokes sideband, comprising the upconverted photons at frequency $\omega_\mathrm{d} + \Omega_\mathrm{m}$, coincides with the resonance signature of the microwave resonator. On resonance, the photon density of states available for the scattering process is significantly increased compared to the off-resonant case. Therefore, the probability for a drive photon to be upconverted via the anti-Stokes process is significantly higher than the reverse process of Stokes scattering to lower frequencies. Since the energy needed for the upconversion process is provided by the phonons populating the mechanical mode, every upconverted photon removes the energy $\hbar\Omega_\mathrm{m}$, or one quanta of motion, from the coupled mode of the mechanical oscillator.

In this way, the microwave drive can be used to reduce the mechanical mode population and cool the effective mode temperature. Conveniently, because the scattered photons have interacted with the mechanical oscillator via the optomechanical coupling, they are imprinted with information on the position of the mechanical oscillator [74]. This information can be retrieved by suitable analysis of the photons at the output of the device.

5.3.2 Quantitative description

For a quantitative description of the sideband cooling protocol it is sensible to describe the energy loss induced by the optomechanical interaction as an additional loss rate Γ_{opt} of the mechanical system, such that

$$\Gamma_{\mathrm{eff}} = \Gamma_{\mathrm{m}} + \Gamma_{\mathrm{opt}} \tag{5.12}$$

where we use Γ_{m} as before as the undisturbed damping rate in the absence of any drives.

Based on the optomechanical interaction hamiltonian in presence of a drive field (cf. Eq. (2.97)), a quantitative expression for the additional damping rate can be derived [22]

$$\Gamma_{\mathrm{opt}} = g^2 \left[\frac{\kappa}{(\Delta + \Omega_{\mathrm{m}})^2 + \kappa^2/4} - \frac{\kappa}{(\Delta - \Omega_{\mathrm{m}})^2 + \kappa^2/4} \right] , \tag{5.13}$$

where $g^2 = g_0^2 \bar{n}_{\mathrm{c}}$ is the photon-enhanced coupling rate, proportional to $\bar{n}_{\mathrm{c}}$, the microwave power expressed as average photon occupation of the FTR. We see from Eq. (5.13) that the induced damping can become negative for positive detunings, i.e. a blue-sideband drive. In this case, the scattering process will introduce additional phonons into the mechanical mode, effectively heating the system.

Additionally, one finds that the same interaction will also lead to a frequency shift of the mechanical resonance, called the *optomechanical spring effect*

$$\Delta\Omega_{\mathrm{m}} = g^2 \left[\frac{(\Delta - \Omega_{\mathrm{m}})}{(\Delta - \Omega_{\mathrm{m}})^2 + \kappa^2/4} - \frac{(\Delta + \Omega_{\mathrm{m}})}{(\Delta + \Omega_{\mathrm{m}})^2 + \kappa^2/4} \right] . \tag{5.14}$$

Notably, Eq. (5.14) vanishes entirely for a perfect detuning $\Delta = \pm\Omega_{\mathrm{m}}$.

In order to predict the cooling effect on the mechanical mode, one can use a simple, classical model of a harmonic oscillator which has an initial thermal occupation $\bar{n}_{\mathrm{ph}}^{\mathrm{th}}$ and is subject to power-dependent additional damping Γ_{opt}. The mode occupation will be cooled to [22]

$$\bar{n}_{\mathrm{ph}} = \bar{n}_{\mathrm{ph}}^{\mathrm{th}} \frac{\Gamma_{\mathrm{m}}}{\Gamma_{\mathrm{m}} + \Gamma_{\mathrm{opt}}} . \tag{5.15}$$

However, as soon as quantum fluctuations and shot noise begin to become relevant at low effective temperatures, this simple model reaches its limits.

To faithfully describe the cooling experiments including those limiting effects, a full quantum mechanical model can be derived, yielding [32, 221]

$$\begin{aligned}\bar{n}_{\mathrm{ph}} = \bar{n}_{\mathrm{ph}}^{\mathrm{th}} &\left(\frac{\Gamma_{\mathrm{m}}\kappa}{4g^2} + \frac{\kappa^2}{4g^2+\kappa\Gamma_{\mathrm{m}}}\right)\left[1 + \frac{g^2}{\Omega_{\mathrm{m}}^2}\frac{4g^2+\kappa\Gamma_{\mathrm{m}}}{4g^2+\kappa^2}\right] \\ &+ \bar{n}_{\mathrm{c}}\left(\frac{4g^2}{4g^2+\kappa\Gamma_{\mathrm{m}}}\right)\left[1+\frac{8g^2+\kappa^2}{8\Omega_{\mathrm{m}}^2}\frac{4g^2+\kappa\Gamma_{\mathrm{m}}}{4g^2}\right] \\ &+ \frac{8g^2+\kappa^2}{16\Omega_{\mathrm{m}}^2}. \qquad (5.16)\end{aligned}$$

Interestingly, the last term in Eq. (5.16) places a temperature-independent, fundamental limit on the achievable mode occupation, representing heating from quantum backaction noise. As a consequence, ground state cooling is only achievable for devices operating in the resolved-sideband regime ($\Omega_{\mathrm{m}} > \kappa$). For our device, we find the last term to be on the order of 10^{-3} and expect only a negligible contribution from it.

5.3.3 Experimental cooling results

Experimentally, we follow a procedure similar to the EMIT experiments discussed in the previous section. After flux- and field-biasing the device to the desired configuration of B_{ip} and Φ_{b}, we use a fast VNA scan to locate the exact resonance frequency of the FTR via the fitting routine. Subsequently, the frequency-lock is enabled based on the stabilizer tone $\omega_{\mathrm{stab}} = \omega_{\mathrm{c}} - 500\,\mathrm{kHz}$ and the drive tone is applied at (nominally) $\omega_{\mathrm{d}} = \omega_{\mathrm{c}} - \Omega_{\mathrm{m}}$. We emphasize that we generally do not assume the detuning $\Delta = \omega_{\mathrm{d}} - \omega_{\mathrm{c}}$ to be exact or constant across the duration of the experiments. The frequency-locking is not perfect and small drifts or constant offsets can appear. Therefore, we record and fit the FTR resonance signature before and after every measurement, and verify that we conduct the analysis using the correct detuning.

In order to extract information about the state of the mechanical oscillator, we employ heterodyne downconversion of the transmitted drive tone and perform spectral analysis of the anti-Stokes field. As previously described in Sec. 5.2.1, we make use of the frequency noise calibration procedure to transform the measured voltage spectrum into a calibrated frequency spectral density $S_{\omega\omega}(\Omega)$. Subsequently, the spectra are transformed once more to displacement spectral densities $S_{\mathrm{xx}}(\Omega)$ based on Eq. (4.4) and the previously determined values of g_0.

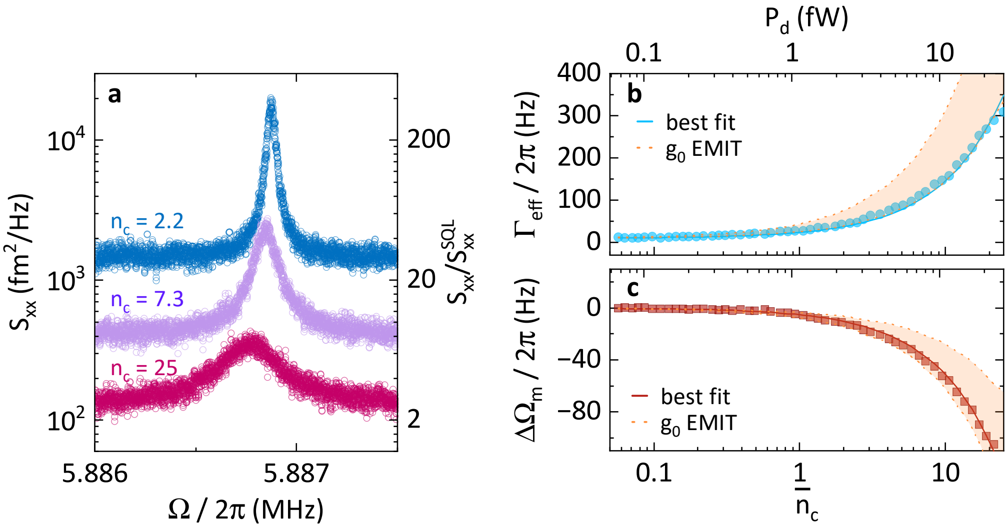

Fig. 5.14.: Optomechanical damping of the mechanical mode. a Thermal displacement spectral densities $S_{xx}(\Omega)$ of the investigated nanostring oscillator during a sideband cooling experiment for three different drive powers, corresponding to $\bar{n}_c = 2.2$, 7.3, and 25 photons, respectively. The peak area decreases with drive power, indicating successful cooling of the mode. The spectra are not artificially offset, the decreasing background is a feature of the power-dependent imprecision noise (see main text). **b,c** Effective mechanical damping rate Γ_{eff} (**b**) and relative frequency shift $\Delta\Omega_m$ (**c**), extracted from fits of the displacement spectra to Eq. (4.2) and shown as a function of drive power P_d and corresponding resonator occupation $\bar{n}_c$. The orange shaded areas show the range predicted by model calculations according to Eq. (5.13) (**b**) and Eq. (5.14) (**c**), assuming $g_0/2\pi = (3.739 \pm 0.741)$ kHz, taking the uncertainty into account. The solid lines are best fits to the data with g_0 as a free fit parameter. The measurement is performed at $B_{ip} = 22$ mT.

For the first sideband cooling experiment we select an in-plane magnetic field strength of $B_{ip} = 22$ mT and a relatively flat working point of $\omega_c/2\pi \approx 7.284$ GHz. Based on EMIT measurements at 24.75 mT, we interpolate the expected single-photon coupling rate to $g_0/2\pi = (3.739 \pm 0.741)$ kHz. We employ the analysis procedure detailed above and retrieve the displacement spectral density $S_{xx}(\Omega)$, which contains information about the displacement and mode occupation of the nanostring, as a function of increasing drive power. Three exemplary spectra are presented in Fig. 5.14**a**, where the corresponding powers are expressed as the average resonator photon occupation $\bar{n}_c$, calculated via Eq. (2.80). We observe a reduction in peak area of the displacement spectra with increasing drive power. As the peak area is proportional to the number of phonons occupying the mechanical mode, this reduction already indicates successful cooling.

To quantify the cooling effect, we fit the spectra to a Lorentzian lineshape Eq. (4.2) and extract the effective damping rate Γ_{eff} and mechanical resonance frequency Ω_m, illustrated in panels **b** and **c**, respectively. The substantial increase in Γ_eff by more than an order of magnitude is consistent with a significant additional energy dissipation due to optomechanical cooling. To validate the quantitative description provided by the expressions for optomechanical damping and spring effect, we perform model calculations (orange) according to Eq. (5.13) and Eq. (5.14) and compare them with the experimental data. The calculations incorporate the interpolated single-photon coupling rate $g_0/2\pi = (3.739 \pm 0.741)\,\mathrm{kHz}$. To validate the interpolated value, we also perform a fit to the same equations with g_0 being a free fit parameter (solid lines). In panel **b**, we observe reasonable agreement between the calculation and the data, with most measured Γ_eff values falling within the uncertainty range of the model. The best fit is achieved for $g_0/2\pi = 2.856\,\mathrm{kHz}$, which is slightly lower than the interpolated value, even considering its uncertainties. The change in resonance frequency, presented in **c**, is well predicted by the theoretical model and the best fit is achieved for $g_0/2\pi = 3.752\,\mathrm{kHz}$, almost identical to the interpolated value. The fact that the theoretical models for optomechanical damping and spring effect, which arise from the same derivation, show different degrees of consistency with a single dataset, extracted from a single fit, might appear surprising. However, as discernible from the form of Eq. (5.13) and Eq. (5.14), and demonstrated in the comprehensive study in Ref. [31], both optomechanical effects show a complex behaviour around the ideal detuning $\Delta = \pm\Omega_\mathrm{m}$, which makes the models very susceptible to small errors in Δ in this regime. Although we attempt to determine Δ for the calculation as accurately as possible, even a small relative frequency shift, i.e. due to the flux-noise-related effects discussed throughout this work, can lead to noticeable deviations.

Before proceeding with further analysis of the sideband cooling results, we want to go on a brief excursion focused on noise levels and measurement sensitivity in the previously presented cooling measurement. In the experimental data presented in Fig. 5.14**a**, we observe a decrease in the background level of the acquired displacement spectra with increasing drive power. This is a consequence of the imprecision noise of the optomechanical measurement, caused by shot noise in the detection process and expressed by the imprecision spectral density $S_\mathrm{xx}^\mathrm{imp}(\Omega)$, which is known to decrease with larger powers according to $S_\mathrm{xx}^\mathrm{imp} \propto 1/P_\mathrm{d}$ [196]. The fact that we observe this decrease implies that our measurement still operates in the imprecision-limited regime, where the total added noise is dominated by $S_\mathrm{xx}^\mathrm{imp}$. By further increasing the drive power, we would expect the total added noise to reach a minimum fundamentally limited by the standard quantum limit (SQL), given by $S_{\mathrm{xx}}^{\mathrm{SQL}} = \hbar/(m_{\mathrm{eff}}\Omega_{\mathrm{m}}\Gamma_{\mathrm{m}})$ [222]. Going beyond this minimum towards even higher powers, backaction forces acting on the mechanical oscillator will cause the noise background to increase again. For the highest drive power available in the presented experiment ($\bar{n}_{\mathrm{c}} = 25$), the background of the displacement spectral density is found at a level of

$$129\,\mathrm{fm}^2/\mathrm{Hz} = (2.55 \pm 0.27) \times S_{\mathrm{xx}}^{\mathrm{SQL}}\,, \tag{5.17}$$

proving that our nano-electromechanical system is capable of performing near quantum-limited displacement detection only a few quanta above the SQL. Furthermore, with the imprecision noise being reduced to such low levels, the nanostring turns into an extremely sensitive force sensor [223]. The sensitivity to forces can be quantified as $S_{\mathrm{FF}}(\Omega) = 2S_{\mathrm{xx}}(\Omega)/|\chi(\Omega)|^2$ [196] with the mechanical susceptibility $\chi(\Omega)$. At the highest measured drive power, we find a maximal on-resonance force sensitivity of

$$\sqrt{S_{\mathrm{FF}}(\Omega_{\mathrm{m}})} = 1.36\,\mathrm{aN}/\sqrt{\mathrm{Hz}} \tag{5.18}$$

for a drive power of 24 fW. This value is close to the theoretical limit for the force sensitivity on resonance, given by $\sqrt{S_{\mathrm{FF}}^{\mathrm{min}}} = \sqrt{4k_{\mathrm{B}}Tm_{\mathrm{eff}}\Gamma_{\mathrm{m}}} = 0.5\,\mathrm{aN}/\sqrt{\mathrm{Hz}}$. The demonstrated force sensitivity is comparable to other published results of electromechanical devices [30, 196, 222]. However, due to the high single-photon coupling rate in the kHz regime, we achieve these results with ultra-low drive powers on the order of fW, several orders of magnitude lower than the pW drives that were used in comparable experiments with capacitively coupled electromechanical devices.

Returning to the discussion of the cooling experiment at hand, the significant increase in the effective mechanical damping rate and the qualitative agreement with the theoretical model strongly suggests that the cooling protocol is effective and the energy in the mechanical mode is gradually depleted as the drive power of the red-sideband tone is increased. Now, to gain direct access to the phonon occupation $\bar{n}_{\mathrm{ph}}$, we recall from Eq. (4.5) that the area of the mechanical resonance signature in $S_{\omega\omega}(\Omega)$ can be related to the phonon occupation of the mechanical mode according to $S_{\omega\omega}(\Omega_{\mathrm{m}})\frac{\Gamma_{\mathrm{m}}}{2} = \langle\delta\omega^2\rangle = 2g_0^2\bar{n}_{\mathrm{ph}}$. Since we now have some confidence in the interpolated value of g_0, we can use it as an input parameter to calculate $\bar{n}_{\mathrm{ph}} = \langle\delta\omega^2\rangle/(2g_0^2)$ for each of the applied drive powers and quantify the effect of the optomechanical cooling. We also know from a previous temperature dependent study that the mechanical oscillator does thermalize with the cryostat down to the lowest temperature (cf. 4.2.2), allowing us to calculate the thermal equilibrium occupation

$$\bar{n}_{\mathrm{ph}}^{\mathrm{th}} = \left[\exp\left(\hbar\Omega_{\mathrm{m}}/k_{\mathrm{B}}T\right) - 1\right]^{-1} = 283 \tag{5.19}$$

and use it as reference. The results of the calculation are presented in Fig. 5.15.

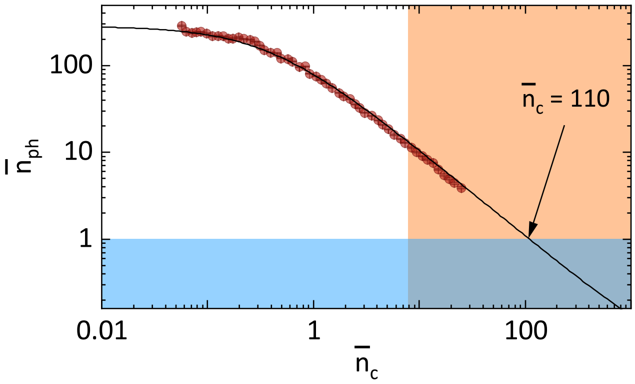

Fig. 5.15.: Sideband cooling to individual quanta of motion. Average phonon occupation $\bar{n}_{\mathrm{ph}}$ of the nanostring's out-of-plane mode as a function of applied drive power, expressed as photon occupation of the microwave resonator $\bar{n}_{\mathrm{c}}$. The mode starts out in thermal equilibrium with the cryostat at $T = 80\,\mathrm{mK}$ and $\bar{n}_{\mathrm{ph}} = 283$ and is gradually cooled to a minimum of $\bar{n}_{\mathrm{ph}} = 3.92 \pm 0.46$. We model the power-dependent occupancy according to Eq. (5.16) using only device parameters and $g_0/2\pi = 3.739\,\mathrm{kHz}$, as extracted from EMIT experiments, and find excellent agreement. We extrapolate the model to higher powers and find that $\bar{n}_{\mathrm{c}} = 110$ would be necessary to cool the mechanical mode to the quantum ground state $\bar{n}_{\mathrm{ph}} < 1$ (blue shaded area). The orange shaded area signifies powers exceeding the bifurcation treshold $\bar{n}_{\mathrm{c,crit}} = 7.87$ of the non-linear microwave resonator, according to Eq. (2.85).

We find that the investigated mode of the nanostring oscillator has been cooled to an average occupation $\bar{n}_{\mathrm{ph}} = 3.92 \pm 0.46$, using a drive power equivalent to $\bar{n}_{\mathrm{c}} = 25$ photons. We compare the experimental result to a model calculation using Eq. (5.16), where we input the experimentally determined properties of the FTR and the mechanical oscillator, and again assume the interpolated coupling rate $g_0/2\pi = 3.739\,\mathrm{kHz}$. The theoretical model shows excellent quantitative agreement with the experimental data. By extrapolating the model towards higher powers, we can estimate the power necessary to cool the mechanical mode to $\bar{n}_{\mathrm{ph}} < 1$ phonon, i.e. to its motional quantum ground state. For our experiment, the model suggests that a drive power equivalent to 110 photons would be sufficient to breach this threshold.

This result is noteworthy, as even with the relatively moderate coupling rate chosen at this working point, the necessary power would be several orders of magnitude lower than commonly employed to cool electromechanical systems into the quantum ground state [31]. Unfortunately, as discussed in Sec. 2.3.4 the inherent non-linearity of our device sets a limit to the applicable power, as the non-linear microwave resonator becomes bistable and shifts in frequency, eventually causing the frequency stabilization to fail. We have calculated the onset of bistability for our device and the current working point with $\mathcal{K}/2\pi = -986\,\mathrm{kHz}$ using Eq. (2.85) and highlighted the bifurcation regime in the plot. It is apparent that some of the experimental data points already lie above the bifurcation point, but still follow the theoretical cooling model. This observation indicates that operation of the device in a small region above bifurcation is possible and the critical photon number given by Eq. (2.85) does not constitute a hard limit. However, further investigation is required to evaluate and quantify the influence and limits placed on the optomechanical cooling protocol by the Kerr non-linearity.

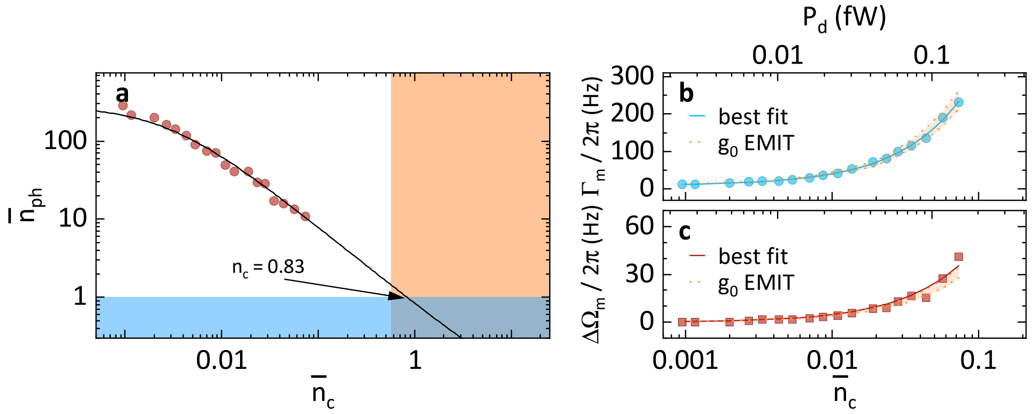

Fig. 5.16.: Low-power sideband cooling. a Average phonon occupation $\bar{n}_{\mathrm{ph}}$ of the mechanical mode as a function of applied drive power, expressed as photon occupation $\bar{n}_{\mathrm{c}}$. The mode starts out in thermal equilibrium at $T = 80\,\mathrm{mK}$ and $\bar{n}_{\mathrm{ph}} = 286$ and is cooled to a minimum of $\bar{n}_{\mathrm{ph}} = 10.82 \pm 0.80$. We model $\bar{n}_{\mathrm{ph}}$ according to Eq. (5.16) using $g_0/2\pi = 55.157\,\mathrm{kHz}$, and find excellent agreement. We extrapolate the calculation and find that $\bar{n}_{\mathrm{c}} = 0.84$ would be necessary to cool the system to the quantum ground state $\bar{n}_{\mathrm{ph}} < 1$ (blue shaded area). The orange shaded area signifies the bifurcation regime of the FTR, according to Eq. (2.85). **b,c** Effective mechanical damping rate Γ_{eff} (**b**) and relative frequency shift $\Delta\Omega_{\mathrm{m}}$ (**c**) as a function of drive power P_{d} and photon occupation $\bar{n}_{\mathrm{c}}$. The orange shaded areas show the range predicted by model calculations according to Eq. (5.13) (**b**) and Eq. (5.14) (**c**), assuming $g_0/2\pi = (55.157 \pm 2.986)\,\mathrm{kHz}$, taking the uncertainty into account. The solid lines are best fits with g_0 as a free fit parameter. The measurement is performed at $B_{\mathrm{ip}} = 35\,\mathrm{mT}$.

For a second experimental run of the cooling protocol we change the operating conditions of the device to produce a significantly higher single-photon coupling strength. In particular, we increase the in-plane field to $B_{\mathrm{ip}} = 35\,\mathrm{mT}$ and move to a steep working point $\omega_{\mathrm{c}}/2\pi \approx 6.9\,\mathrm{GHz}$. Under these conditions, we expect $g_0/2\pi = (55.157 \pm 2.986)\,\mathrm{kHz}$, as interpolated from an EMIT experiment at an adjacent working point. Apart from the changed working point, the experiment is repeated exactly as described above. The final occupation number of the mechanical mode for each drive power is then once again extracted from the peak area of the frequency spectral densities and plotted in Fig. 5.16**a**, along with a model calculation according to Eq. (5.16).

With the even larger interaction strength achieved in this experimental setting, the mechanical motion is cooled to an occupation of 10 phonons, using a drive power equivalent to 0.76 photons or 0.1 fW. By extrapolation of the model calculation, we predict the device to be able to prepare the quantum ground state of the mechanical oscillator with a drive power equivalent to just 0.83 photons (or $\approx$ 1 fW), again demonstrating the remarkable low power capabilities offered by the inductively coupled device due to the large single-photon coupling rates. According to our calculation via Eq. (2.85) using the analytically calculated Kerr non-linearity $\mathcal{K}/2\pi = -3.395\,\mathrm{MHz}$, the relevant photon numbers in this experiment do not exceed the bifurcation threshold of the non-linear device. It is therefore likely that the enhanced sensitivity to external flux noise at the highly responsive working point leads to a premature failure of the stabilization protocol, which limits the applicable powers in this experiment.

We also compare the evolution of the effective damping rate Γ_{eff} and the resonance frequency change $\Delta\Omega_{\mathrm{m}}$ in Fig. 5.16**b** and **c** to their respective theoretical models and find good agreement for both properties. In fact, the best fits to Γ_{eff} and Ω_{m} return single-photon coupling rates of $g_0/2\pi = (55.794 \pm 0.245)\,\mathrm{kHz}$ and $g_0/2\pi = (59.067 \pm 1.114)\,\mathrm{kHz}$, respectively, demonstrating good agreement with the interpolated value $g_0/2\pi = (55.157 \pm 2.986)\,\mathrm{kHz}$. Contrary to the previous experiment, we find an increase in Ω_{m} with drive power. This is a consequence of the detuning, which in this experiment is slightly less red-detuned than the ideal detuning (i.e. $\Delta > -\Omega_{\mathrm{m}}$), leading to an opposite spring effect compared to the previous experiment. This emphasizes the significance of the knowledge and stable control over Δ for the sideband cooling experiment and reinforces that our dynamic determination of κ and Δ allows our analysis to perform well even in non-ideal scenarios.

5.3.4 Conclusion

The two experiments presented in this section demonstrate the versatility and potential of the inductively coupled architecture: Using the two independent control fields, Φ_b and B_ip, the fundamental properties of the device, including the electromechanical coupling strength, can be tuned over several orders of magnitude. The different regimes of interaction strengths directly translate into different power ranges becoming accessible to the experimentalist. In particular, due to the high single-photon coupling strength that can be achieved in the device, we could demonstrate cooling of a nanomechanical oscillator to the regime of individual quanta with unprecedentedly low microwave powers on the order of a single photon, several orders of magnitude below what is commonly required. While the actual preparation of a quantum mechanical ground state in the electromechanical system remains currently limited by technical obstacles, a clear path forward can be identified: External flux noise limiting both long term stability and achievable coupling rate can be remedied with improved shielding, which the device currently operates without. Additionally, the Kerr non-linearity of next generation of devices can be engineered to a lower value in order to increase the dynamic range available to the device, hopefully pushing it beyond what is necessary to reach the quantum ground state. Adjustment of the dynamic range can for example be achieved by replacing the single SQUID by a linear array, which dilutes the non-linearity [124].

5.4 Exploiting backaction for mechanical frequency control

In the previous experiments and discussions, we have focused our attention on the effects that the addition of a mechanically compliant SQUID and its non-linear inductance has on a microwave resonator, in particular how the mechanical oscillation leads to a dynamic modulation of the FTR resonance frequency via flux-mediated inductive coupling. In these discussions, the focus was placed on the response and dynamics of the microwave component, since this is the element that is actively probed in experiments via external microwave drive signals. However, we can also consider how the mechanical resonator in the coupled system is affected via the optomechanical interaction when we use said microwave tones to measure the state of the system. Such effects of the measurement field on the individual system components are commonly referred to as *backaction*.

In this section, we present a focused investigation into backaction effects in the previously studied SQUID-based nano-electromechanical device. We show that the resonance frequency of the mechanically compliant string embedded into the SQUID loop can be controlled in two different ways: (i) the bias magnetic flux applied perpendicular to the SQUID loop, (ii) the magnitude of the in-plane bias magnetic field contributing to the electromechanical coupling. These findings are quantitatively explained by the Lorentz-force based inductive interaction contributing to the effective spring constant of the mechanical resonator. In addition, we observe a residual field dependent shift of the mechanical resonance frequency, which we attribute to the finite flux pinning of vortices trapped in the magnetic field biased nanostring. To gain a deeper understanding of the vortex formation in the complex geometry of the multilayered nanostring, we conduct additional experiments into the magnetic field dependence of the observed flux-pinning effect. Finally, we report on early indications that the investigated electromechanical system is potentially sensitive enough to detect the formation or movement of individual flux vortices.

Parts of the results presented in this section have been published in *Mechanical frequency control in inductively coupled electromechanical systems.* T. Luschmann *et al.* Scientific Reports **12** 1608 (2022) [157]. Some of the figures and text have been adapted from the publication.

5.4.1 Lorentz force backaction on the nanostring oscillator

Backaction can take many forms and is found in a variety of different systems: From photon radiation pressure in optical [224] or microwave [31] cavities to electron tunneling in single-electron transistors [29] or carbon nanotubes [225]. In this section, we will explore a more system-specific backaction effect based on the Lorentz force, which arises from the geometry of the mechanically compliant SQUID in the flux-mediated coupling scheme architecture: As we have discussed in Sec. 2.2.4, a SQUID is fundamentally a superconducting loop, which – in order to fulfill boundary conditions imposed by fluxoid quantization – is threaded by shielding currents, whose polarity and magnitude depend on the external flux currently present in the SQUID loop. Since the source of the external flux is generally an associated magnetic field, the leads of the SQUID are current carrying conductors in an external magnetic field. It is clear that the charge carriers must be subject to the classical Lorentz force $F_\mathrm{L} = B_\mathrm{ip} l I(\Phi)$ proportional to the flux-dependent circulating current $I(\Phi)$ and the length of the string l. In a standard, non-mechanically compliant SQUID, this force is compensated by the superconductors attachment to the substrate. However, in our scenario, the SQUID consists of freely suspended nanostrings, whose equilibrium position will be influenced by the presence of the additional force. Moreover, as the area of the SQUID perpendicular to B_ip and therefore the total flux Φ is modulated by the mechanical motion of the nanostring, the Lorentz force will not remain static, but itself become displacement-dependent, leading to a restoring force on the motion of the nanostring. This constitutes an effective change in the string's stiffness and hence a modification of the mechanical resonance frequency.

To obtain a quantitative description of the Lorentz force backaction on the nanostring, we follow Ref. [38] and describe the electromechanical system in terms of the mechanical displacement X and the center-of-mass coordinate $\varphi_+ = (\phi_1 + \phi_2)/2$ of the SQUID, where ϕ_1 and ϕ_2 are the phase differences across the Josephson junctions. The resulting Hamiltonian can be written as

$$H = \frac{m_\mathrm{eff}\dot{X}^2}{2} + \frac{m_\mathrm{eff}\Omega_\mathrm{m}^2 X^2}{2} + \frac{C\Phi_0^2}{2(2\pi)^2}\dot{\varphi_+}^2 + E(\varphi_+, X)\,. \tag{5.20}$$

Here, $E(\varphi_+, X)$ represents the potential energy of the SQUID, while other variables are defined as before. As the resonance frequency of the microwave cavity is much larger than the mechanical resonance frequency ($\omega_\mathrm{c} \gg \Omega_\mathrm{m}$), the system operates in the dispersive limit and the mechanical displacement along with the corresponding flux change can be considered as static on the timescales relevant for the SQUID dynamics. In this limit, the SQUID can be approximated as a harmonic oscillator and an expansion of its potential energy in terms of the phase up to second order can be performed. The resulting phase-dependent terms describe the dynamic interaction of the electromechanical system, which eventually lead to the radiation pressure interaction, which we already discussed in Sec. 2.5.2. To investigate the mechanical resonance frequency, we instead focus on the phase-independent term in the expansion, which induces a static, but flux-dependent shift of the uncoupled mechanical resonance frequency Ω_0 towards an effective frequency Ω_m. Therefore one obtains [38]

$$\Omega_\mathrm{m} = \sqrt{\Omega_0^2 + \frac{4E_\mathrm{J}\pi^2 B_\mathrm{ip}^2 l^2 \gamma^2 (1-\alpha^2)[\cos^4(\phi_\mathrm{b}) - \alpha^2 \sin^4(\phi_\mathrm{b})]}{m_\mathrm{eff} S_0^3}}. \tag{5.21}$$

Here, $E_\mathrm{J} = \hbar(I_1 + I_2)/4e$ is the SQUID average Josephson energy with $I_{1,2}$ representing the critical currents of the individual Josephson junctions, m_eff the effective mass of the string and γ its shape factor, as already used in Eq. (2.96). Furthermore, we have introduced $S_0 = \sqrt{\cos^2(\phi_\mathrm{b}) + \alpha^2 \sin^2(\phi_\mathrm{b})}$ with the normalized bias flux $\phi_\mathrm{b} = \pi\Phi_\mathrm{b}/\Phi_0$, which is generated by the control field B_OOP. The asymmetry parameter $0 < \alpha < 1$ accounts for non-identical Josephson junctions in the SQUID and is defined by $I_1 = I_0(1-\alpha)$ and $I_2 = I_0(1+\alpha)$ with the average critical current $I_0 = (I_1+I_2)/2$. We want to emphasize strongly that this type of backaction is different from the shift in Ω_m caused by the opto-mechanical interaction [22, 31].

5.4.2 Experiment and initial results

In order to investigate the impact of the electromechanical system on the mechanical subsystem's frequency, we need to analyze the properties of the mechanical resonator as function of Φ_b and the in-plane bias field B_ip. To this end, we first bias the device at the desired B_ip and then perform microwave spectroscopy at different working points (i.e. values of Φ_b). The spectroscopy experiments are performed as discussed in Sec. 4.2.2, with a probe tone resonant with the microwave resonator ($\omega_\mathrm{p} = \omega_\mathrm{c}(\Phi_\mathrm{b})$). The on-resonance configuration of the probe tone is used to avoid any frequency shifts due to the optomechanical spring effect (as evaluated in Sec. 5.3). Additionally, the weak stabilizer tone, which forms the basis for the frequency locking technique is applied at $\omega_\mathrm{stab} = \omega_\mathrm{c}(\Phi_\mathrm{b}) + 500\,\mathrm{kHz}$. The resulting thermal displacement spectrum, in the form of the voltage spectral density $S_\mathrm{UU}(\Omega)$ is then fitted to 4.2 to extract the mechanical resonance frequency Ω_m.

Fig. 5.17**a** shows the recorded voltage spectral density for various flux bias points and a fixed B_ip of 35 mT. Additionally, we illustrate the flux-tuning behaviour of the microwave resonator in panel **b**, with the flux bias points corresponding to the spectra shown in **a** highlighted with matching lines. Based on Eq. (5.21), we expect an evolution of Ω_m with flux bias Φ_b, and indeed, similar to the behavior of the FTR, the position of the peak, i.e. the mechanical resonance frequency, appears to shift towards lower frequencies as the flux bias applied to the SQUID is increased.

To quantify the effect with respect to both the in-plane magnetic field and bias flux applied to the device, we repeat the previously described experiment at various

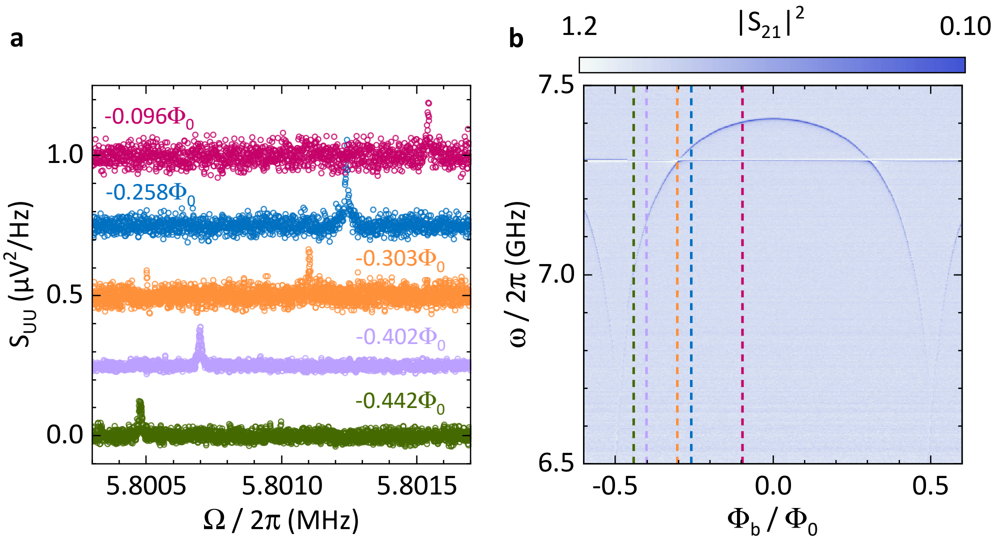

Fig. 5.17.: **Flux-dependent mechanical frequency shift.** **a** Voltage power spectral density of the demodulated probe tone, analyzed around its anti-Stokes peak at various flux bias points (see labels next to the data trace) for a fixed in-plane field of $B_\mathrm{ip} = 35\,\mathrm{mT}$. The spectra are offset by $0.3\,\mu\mathrm{V}^2/\mathrm{Hz}$ for clarity. The Lorentz-shaped mechanical resonance features shift to higher frequencies by roughly $1\,\mathrm{kHz}$ as the normalized flux bias is decreased. **b** Calibrated microwave transmission magnitude $|S_{21}|^2$ of the FTR as a function of the bias Φ_b/Φ_0. The FTR's resonance signature is visible as a dark blue feature. Colored dashed reference lines correspond to the flux bias points at which the mechanical spectra are analyzed in detail and presented in **a**.

flux bias points Φ_b covering the full periodicity of the microwave resonator frequency. In addition, we repeat these flux sweeps for various in-plane magnetic fields ranging from 6.2 mT to 35 mT. The extracted mechanical resonance frequencies are plotted in Fig. 5.18**a**. We note that the electromechanical coupling is strongly suppressed at small flux bias ($|\Phi_\mathrm{b}/\Phi_0| < 0.1$). Therefore, to verify the data in this regime, a piezoelectric actuator attached to the sample was used to resonantly drive the mechanical motion and increase the signal strength.

From the plotted experimental data, we see that Ω_m approximately shows a parabolic tuning behavior with respect to the applied flux bias. We find a maximum tuning of roughly 1 kHz at the maximum applied in-plane field, $B_\mathrm{ip} = 35\,\mathrm{mT}$. We compare these results with the theoretical prediction by fitting the data to Eq. (5.21), choosing E_J and Ω_0 as the only free fit parameters. The SQUID asymmetry is fixed to a small value of $\alpha = 1\%$ to account for minor fabrication deviations of the Josephson junctions, while the remainder of the device parameters is re-used from the previously presented experiments (cf. App. A.1). The resulting model precisely describes our experimental findings, confirming the hypothesis that the shift of the mechanical resonance frequency Ω_m is indeed caused by the Lorentz force acting on the nanostring within the SQUID. The good reproduction of the data by the model also suggests that the mechanical resonance frequency can be tuned quasi-continuously to any point described by Eq. (5.21). However, an analysis of the determined fit parameters plotted in Fig. 5.18**b** reveals that the uncoupled resonance frequency Ω_0 increases by several hundred Hz as B_{ip} is increased, an effect that is not accounted for by the theoretical description of the electromechanical system.

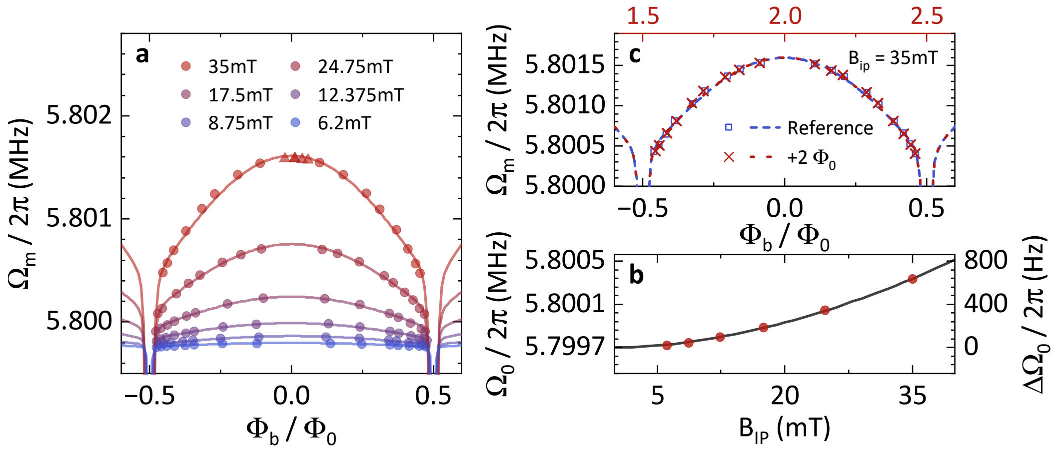

Fig. 5.18.: Quantitative investigation of the frequency tuning. Extracted mechanical resonance frequency Ω_{m} as a function of Φ_{b}, measured at different in-plane fields B_{ip} ranging from $6.2\,\mathrm{mT}$ to $35\,\mathrm{mT}$. Open circles correspond to thermal motion measurements, while triangular data points are acquired with a piezoelectric actuator resonantly driving the mechanical motion. Lines are fits to the data according to Eq. (5.21). **b** Ω_0 (and $\Delta\Omega_0$ in reference to the value at zero-field) extracted from the fits along with a power-law fit (black line) revealing $\Omega_0 \propto B^{1.81}$. The increase suggests an additional contribution not included in the presented model and is discussed in the main text. **c** Re-measured flux-dependency of Ω_{m} at $B_{\mathrm{ip}} = 35\,\mathrm{mT}$ for a reference measurement (blue squares), and second measurement (red crosses) where Φ_{b} was increased such that the SQUID loop contains two additional flux quanta Φ_0. Both datasets were fitted independently according to Eq. (5.21) (dashed lines). In all panels, statistical error bars are smaller than the symbol size.

We want to emphasize the distinction between this unpredicted in-plane magnetic field dependence in Ω_0 and the frequency tuning behaviour attributed to the Lorentz force: The change in mechanical frequency depending on the bias flux Φ_{b}, as measured and modelled in Fig. 5.18**a**, is well understood as a consequence of the Lorentz force acting on the oscillating nanostring. It can be described either by Eq. (5.21) or using a slightly different derivation as found in Ref. [56]. Both descriptions share the same physical origin, i.e. a change in the SQUID's circulating current due to the displacement of a mechanical element, which in turn experiences an effective spring stiffening.

Our comprehensive study of the mechanical resonance frequency as function of both the in-plane bias field and the bias flux controlling the inductance of the SQUID allows us to quantitatively account for this Lorentz force based mechanism. By comparing this quantitative model with our experimental data, we can distinguish and extract the additional, field-dependent shift of Ω_0, which is not accounted for by either of the above mentioned theoretical models. Consequently, we calculate $\Delta\Omega_0$, using $\Omega_0(0\,\mathrm{mT})$ as a reference and present the result in Fig. 5.18**b**.

5.4.3 Residual frequency shift

Confronted with the unknown physical origin of the additional mechanical frequency shift, we investigate various scenarios which could lie at the origin of the B_{ip}-dependence of Ω_0. In the following we elaborate on each of the hypotheses and our conclusions:

Hypothesis 1: Volume change One possible mechanism to influence the mechanical resonance frequency is given by the volume change observed in superconductors, as the externally applied field approaches the critical field of the respective material [226]. In this case, a change in the length of the superconducting aluminum string would translate linearly to a change of resonance frequency according to Eq. (2.27). However, the commonly reported length changes on the order of $\Delta V/V \approx 10^{-8}$ [226] are several orders of magnitude too small to explain the observed frequency shifts $\Delta\Omega_{\mathrm{m}}/\Omega_{\mathrm{m}} \approx 10^{-4}$. More critically, one would expect the length of the superconductor to increase with the applied field, and therefore reduce the string's resonance frequency, contrary to the observed effect, leading us to rule out this theory.

Hypothesis 2: Higher order optomechanical interactions In our discussion of the optomechanical coupling in Sec. 2.5.1, we have limited the discussion to interaction terms linearly proportional to the mechanical displacement $(b^\dagger + b)$. However, based on the theoretical description, higher order terms do exist, in particular the *quadratic* coupling, which links the frequency shift of the microwave resonator to the square of the displacement $(b^\dagger + b)^2$ via the coupling rate $g_0^{(2)}$ [227]. The quadratic coupling in our system is generally much smaller than the first-order radiation pressure coupling that we focus on, and it can be challenging to decouple both effects in the analysis. Nonetheless, it can be observed experimentally, particularly in membrane-in-the-middle experiments, where the quadratic term is dominant due to geometry [224]. Translated to our case of flux-mediated electromechanical coupling, the corresponding quadratic interaction would result in a quadratic dependence of Ω_0 on B_{ip}, as observed in our experiment. However, for our device parameters, we can calculate the expected coupling rate $g_0^{(2)}$ to be on the order of few Hz. Conversely, to explain the observed frequency shift would require a coupling $g_0^{(2)}$ on the order of MHz. Hence, we conclude this hypothesis to be implausible.

Hypothesis 3: Magnetic torque We also consider that the flux captured by the SQUID loop and the corresponding magnetic moment could give rise to a modification of the mechanical frequency if the device acts as a torque magnetometer. In this scenario, the flux captured by the SQUID loop would interact with the external magnetic field via its own magnetic moment m_{SQ}. This could lead to effects within the device known from cantilever torque magnetometry [228–230]. The loop, which can be well approximated as a single square coil, hosts a magnetic moment m_{SQ} due the presence of captured flux. This m_{SQ} points along the out-of-plane direction of the chip [231]. Under the assumption of a slightly imperfect alignment of the magnetic field, which we already established to be very likely in our setup (cf. Sec. 4.3) the torque $\tau = m_{\mathrm{SQ}} \times B_{\mathrm{ip}}$ can be associated with a position dependent force on the string, which could be responsible for the shift in resonance frequency. Since the magnetic moment arises from the flux captured in the SQUID, the effect of this torque would be expected to depend on the number of flux quanta in the SQUID loop.

To investigate this hypothesis, we perform additional measurements probing the mechanical frequency of the system at different flux bias points, separated by more than $1\,\Phi_0$, which correspond to a different number of flux quanta present in the SQUID loop. The data is presented in Fig. 5.18**c**. The resulting $\Omega_0/2\pi = 5.800\,36\,\mathrm{MHz}$, again extracted from fits to Eq. (5.21), is identical for both datasets, suggesting that the observed frequency shift does not depend on the number of flux quanta in the SQUID loop, invalidating the magnetic torque hypothesis.

Hypothesis 4: Flux-line-lattice elasticity Finally, we find parallels in our experimental observations to the results of vibrating reed experiments, which were able to measure the stiffness of the flux line lattice (FLL) in type-II superconductors and its influence on mechanical properties [232, 233]. In particular, the FLL can exhibit quasi-elastic properties, couple to the motion of the atomic lattice and hence influence the mechanical resonance frequency. The underlying mechanism can be explained as follows:

In type-II superconductors, in the presence of a sufficiently strong external magnetic field, magnetic flux penetrates the material in the form of flux lines [234]. This phenomenon is observed when the external fields lie between B_{c1} and B_{c2}, representing the lower and upper critical fields, respectively. Each of these flux lines manifests itself by a normal conducting core enveloped by circulating currents. Notably, every flux vortex carries exactly one quantum of flux, Φ_0. Within the material, these flux lines anchor themselves at pinning sites, typically impurities or defects in the crystal lattice, forming a structured flux line lattice. As the superconductor moves within the external field, the anchored flux lines bend in response. This bending elongates the field lines, increasing the magnetic energy, which can also be expressed as a magnetic line tension or energy per unit length. This tension introduces an additional restoring force, elevating the mechanical resonance frequency. For flux lines that are rigidly pinned, the line tension and the subsequent frequency increase are directly proportional to B^2 [235]. However, if the flux lines are allowed to shift relative to their pinning centers, the frequency increase is less pronounced.

The interaction strength between the flux lines and the atomic lattice is captured by the Labusch parameter (or elastic constant) $\alpha_{\mathrm{L}}(B,T)$. This parameter can be visualized as the spring constant of a combined system of flux line and pinning site. For minimal pinning forces, the resonance frequency Ω_{m} of a reed in an external field was found to follow [233]

$$\Omega_{\mathrm{m}}^2 = \Omega_0^2 + \frac{\alpha_{\mathrm{L}}(B,T)}{\rho}\,. \tag{5.22}$$

Here, Ω_0 denotes the resonance frequency without an external field, and ρ is the material's density. This equation underscores that the field-dependent frequency shift solely stems from the Labusch parameter's dependence on B, offering insights into the pinning forces experienced by the flux lines [235]. According to the theory of flux line lattice elasticity, the field-dependence of $\alpha_\mathrm{L}(B)$ exhibits a power-law behavior $\alpha_\mathrm{L}(B) \propto B^k$ where k can vary significantly across materials.

While we are not aware that this effect has been reported for aluminium, this is likely due to the fact that bulk aluminium is generally considered a type-I superconductor. However, it is widely reported that sufficiently thin aluminium films can behave in ways characteristic of type-II superconductors [193, 236]. Studies of other type-II superconductors find a range of exponents $k \approx 2 \pm 0.2$ and $\alpha_\mathrm{L} \approx 10^{12}$ to $10^{15}\,\mathrm{N/m^4}$ [233, 235, 237]. Fitting our experimental data with a power-law (Fig. 5.18**b**) we find $k \approx 1.81$ and $\alpha_\mathrm{L}(35\,\mathrm{mT}) = 7.88 \times 10^{14}\,\mathrm{N/m^4}$, in line with the reported values.

Given the promising agreement of the experimental data with the FLL theory, we identify flux line pinning as a plausible origin of the mechanical frequency shift. However, since this explanation relies heavily on the assumption to treat the aluminum film as a type-II superconductor in the Shubnikov phase, we want to adhere to due diligence and re-evaluate this claim:

The distinction between type-I and type-II superconductors is primarily determined by the Ginzburg-Landau parameter, κ_GL, defined as [92]

$$\kappa_\mathrm{GL} = \frac{\lambda_L}{\xi_{GL}} \,. \tag{5.23}$$

Here, λ_L is the London penetration depth and ξ_{GL} is the Ginzburg-Landau coherence length. A material is classified as a type-I superconductor when $\kappa_\mathrm{GL} < 1/\sqrt{2}$ and as a type-II superconductor when $\kappa_\mathrm{GL} > 1/\sqrt{2}$ [234].

In the context of thin films, both the penetration depth and coherence length deviate from their bulk values, λ_L^∞ and ξ_GL^∞, due to the influence of a finite mean free path, l_f. For Al, bulk values from literature are found to be $\lambda_\mathrm{L}^\infty = 50\,\mathrm{nm}$ and $\xi_\mathrm{GL}^\infty = 1600\,\mathrm{nm}$ [92]. Given that our Al thin film is polycrystalline with SEM-verified grain sizes on the order of 10 nm, we use this as an approximation for l_f. In scenarios where l_f is significantly smaller than ξ_GL^∞, the penetration depth and coherence length are expressed as [92]

$$\lambda_L = \lambda_L^\infty \left(1 + \frac{\xi_\mathrm{GL}^\infty}{l_\mathrm{f}}\right)^{1/2} , \tag{5.24}$$

$$\xi_\mathrm{GL} = \xi_\mathrm{GL}^\infty \left(1 + \frac{\xi_\mathrm{GL}^\infty}{l_\mathrm{f}}\right)^{-1/2} \tag{5.25}$$

From the above equations, we derive $\kappa_\mathrm{GL} \approx 5$, suggesting that our thin film can plausibly exhibit type-II superconducting behavior. Furthermore, our calculated coherence length, $\xi_{GL} = 126\,\mathrm{nm}$, is comparable to the nanostring's thickness of 110 nm. Given that the diameter of a vortex is approximately ξ_{GL} [92], this implies that vortices can indeed be accommodated within the nanostring.

5.4.4 Indications of flux vortex formation

In the preceeding section, after evaluation of all initially plausible hypotheses, we come to the conclusion that a coupling of the atomic lattice to the lattice of flux vortices permeating the superconducting material is the most likely explanation of the experimentally observed frequency shift. This conjecture, however, has interesting implications regarding the sensing capabilities of the studied electromechanical device.

Very naively, one can estimate the number of flux vortices inside the nanostring simply by the flux associated with a local magnetic field B_{loc} in the cross-sectional area of the nanostring, $t \cdot l$, divided by the flux carried by a single vortex, which we know is Φ_0. Accordingly, we find for the number of vortices per field

$$\frac{n}{B_{\mathrm{loc}}} = \frac{tl}{\Phi_0} \approx 1.66\,\mathrm{mT}^{-1}\,, \tag{5.26}$$

implying a number of flux vortices on the order of 10 to 50 for the magnetic fields of 1 mt to 35 mT used in our study. Note that this estimate is the most crude variant, as it does not account for effects like field displacement in nano-scale systems.

If the previously discussed hypothesis holds, and the number of involved flux vortices is so low, the mechanical frequency should exhibit a step-like increase each time an additional flux line forms in the nanostring, revealing the quantization of magnetic flux. In order to investigate whether such step-like discontinuities in the frequency shift are indeed present, we repeat the flux- and field-dependent experiments presented in Fig. 5.18 on a larger scale, with a significantly improved sampling resolution w.r.t. the external magnetic field B_{ip}. Specifically, we sweep B_{ip} from 12 mT to 30 mT in steps of 0.25 mT and for each field determine the evolution of the flux-dependent mechanical resonance frequency $\Omega_{\mathrm{m}}(\Phi_{\mathrm{b}})$ at various working points along the flux-periodicity. The frequency tuning behavior is then fitted to Eq. (5.21) in order to extract Ω_0 at the respective in-plane field.

The summarized results of the measurements are plotted in Fig. 5.19. The data is derived from two separate measurement runs, with in-plane fields ranging from 12 mT to 20 mT in the first, and 20 mT to 30 mT in the second. After the first run, the sample was exposed to ambient pressure, causing a shift in $\Omega_0/2\pi$ from roughly 5.864 MHz to about 5.887 MHz. To ensure consistency, we've plotted both datasets relative to the mechanical frequency measured at $B_{\mathrm{ip}} = 20\,\mathrm{mT}$, $\Omega_0^{20\mathrm{mT}}$, which was recorded in both runs. From the experimental data, we find Ω_0 exhibits an upward trend with the in-plane field B_{ip}, interrupted by distinct discontinuities, which are highlighted by arrows at 15 mT, 19.5 mT, 22 mT and 23.75 mT and potentially 26 mT.

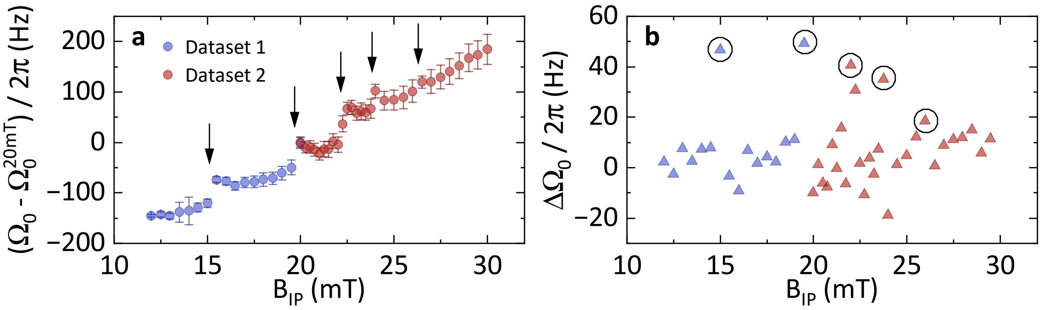

Fig. 5.19.: Discontinuities in the field-dependent frequency shift. a Bare mechanical resonance frequency Ω_0 relative to the value at $B_{\mathrm{ip}} = 20\,\mathrm{mT}$, as a function of the applied in-plane field B_{ip}. Ω_0 is extracted at each field from fits to Eq. (5.21). Five discontinuities that are potential indications for the formation of an additional flux vortex are highlighted. The error bars combine the statistical uncertainty of the fit and propagated uncertainties. **b** Change in Ω_0 between adjacent measurements. The changes correspond to the discontinuities in **a** are circled.

To confirm the location of the discontinuities, we illustrate the step-by-step variation between measurements, $\Delta\Omega_0$, in Fig. 5.19**b**. Most of the discontinuities correspond to frequency shifts around 40 Hz, providing a clear contrast to the typical frequency variations of roughly ±10 Hz between adjacent in-plane fields.

The appearance of such distinct discontinuities in the otherwise very steady evolution of the mechanical resonance frequency could plausibly be an indication for the formation of additional flux vortices at these specific in-plane field values. Curiously, the discontinuities don't follow any recognizable periodic pattern, as one would naively expect from a flux-quantized process, but the intervals between them, ranging from 2 mT to 5 mT, as well as the magnitude of the abrupt changes appear to diminish as the applied field intensifies. Furthermore, we also recall that a naive estimation using Eq. (5.26) predicted more than one vortex to be formed per mT of applied field, which would result in a much smaller interval. These discrepancies raise additional questions and prohibit a clear conclusion at this point.

Therefore, to rule out measurement errors or artifacts arising from the fact that we combine two different datasets for the analysis, we perform another validation experiment in a seperate cooldown, aiming to reproduce our findings as independently as possible. For this measurement, B_{ip} is swept up from 18 mT to 35 mT in a continuous measurement and the bare resonance frequency Ω_0 is extracted using the same analysis and fitting procedure as introduced previously. The resulting data is summarized in Fig. 5.20. Once again we observe an increase in Ω_0 as B_{ip} is increased, interrupted by four to five identifiable discontinuities. However, the sudden changes in Ω_0 are not found at the exact same values of B_{ip} as in the previous measurement run. Instead, the discontinuities are now found at in-plane fields of 20.5 mT, 22 mT, 26.5 mT, 31 mT and potentially 32 mT with corresponding changes $\Delta\Omega_0$ between 24 Hz and 75 Hz, i.e. on the same order, but not identical to the previous observations.

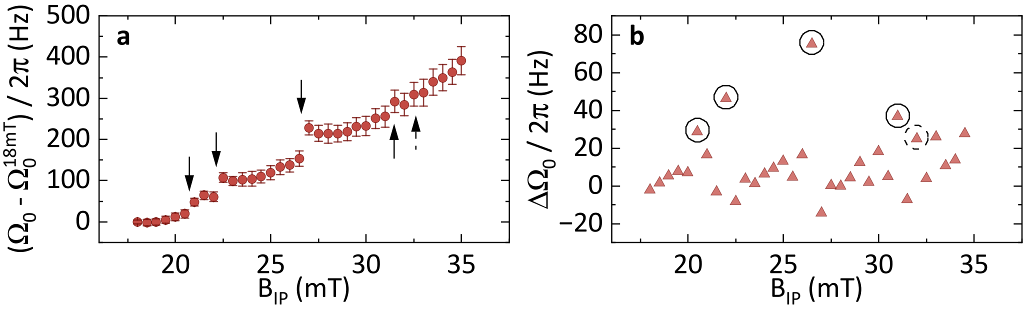

Fig. 5.20.: Validation of the discontinuous field-dependence. Repetition of the measurement shown in Fig. 5.19, performed in a different cooldown. **a** Ω_0 relative to the value at $B_{\mathrm{ip}} = 18\,\mathrm{mT}$, as a function of the applied in-plane field B_{ip}. As before, four or five discontinuities can be identified and are highlighted. The error bars combine the statistical uncertainty of the fit and propagated uncertainties. **b** Change in Ω_0 between adjacent measurements. The large changes that correspond to the discontinuities in **a** are circled.

Finally, we want to evaluate whether the observed frequency changes are in agreement with the previously identified theory of flux line lattice elasticity. From a macroscopic viewpoint, we test compatibility with the theory by comparing the newly acquired, more detailed data with the previous data on the in-plane field dependence and the model Eq. (5.22), which we have used to describe the experimental data via a power-law (cf. Fig. 5.18**c**). We plot the new data juxtaposed with the previously acquired data in Fig. 5.21 and also include the earlier fit $\Omega_0 \propto B_{\mathrm{ip}}^{1.81}$. We find good agreement between both datasets and the model, indicating that the envelope of the field dependence does indeed follow the flux line lattice elasticity model, with the high resolution features, like the observed discontinuities, being contained within.

The fact that two independent measurements exhibit the same number of qualitatively similar discontinuities in the magnetic field dependence of the mechanical resonance frequency constitutes strong evidence that a real physical effect is at play. Moreover, since the overall field dependence still follows the previously observed power-law behaviour, the discontinuities can be interpreted as a microscopic substructure to the macroscopic model of flux-line-lattice elasticity, that only becomes visible at sufficient field resolution on the order of individual flux quanta. In this context, it appears likely that the discontinuities are related to the formation of individual flux vortices in the superconducting nanostring. However, the complex periodicity and unexpectedly large spacing of the discontinuities make clear that a comprehensive understanding of the effect remains elusive. It is likely that only a microscopic model of flux vortex formation in the specific nanostring geometry would be able to predict the discontinuities quantitatively.

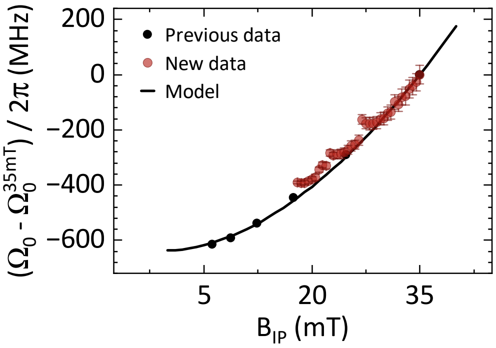

Fig. 5.21.: Validity of the FLL model. Summary of the high-resolution and overview measurements to determine Ω_0 as a function of in-plane field B_{ip}. Black dots and line correspond to the data presented and discussed in Fig. 5.18**c** and the fit to Eq. (5.22), respectively. Red dots are acquired from the more recent high-resolution measurement. Values for Ω_0 are plotted relative to their respective values at $B_{\mathrm{ip}} = 35\,\mathrm{mT}$.

5.4.5 Conclusion

In summary, we present a detailed study of frequency tuning mechanisms affecting a nanostring in an electromechanical system. We find a pronounced shift ($> 50\,\Gamma_{\mathrm{m}}$) in the mechanical resonance frequency as function of the flux bias condition of the SQUID. This Φ_{b}-dependent frequency shift is distinct from frequency shifts based on the optomechanical interaction and is quantitatively explained by an interaction induced by the SQUID via the Lorentz force. The ability to shift the mechanical resonance frequency using the flux bias of the SQUID allows for fast in-situ frequency modulation, which could be employed e.g. for parametric driving of the mechanical element.

Furthermore, our detailed modelling reveals a previously unobserved field-dependent frequency shift that we attribute to the additional mechanical stiffness induced by the flux line lattice in the aluminum nanostring. This underlines the mechanical sensing capabilities of nanostrings and poses the question whether the studied electromechanical system might allow the investigation of the mechanical properties of few or individual flux lines: Using additional, higher-resolution measurements, we attempt to resolve the formation of individual flux vortices in the superconducting nanostring and indeed observe discontinuities in the field-dependence of the mechanical resonance frequency, which are reproducible and consistent with the reordering of the underlying flux line lattice upon vortex formation. However, the experimental signature lacks a defined periodicity and is therefore not consistent with a naive expectation of a quantized formation of vortices in response to the external field. We remain optimistic that with additional investigations – potentially using devices with different geometries and materials – electromechanical devices have the potential to provide insight into the microscopic structure of the flux line lattice in nanoscale superconducting circuits.

6

Surface Acoustic Wave Resonators on Thin-Film Piezoelectric Substrates for Quantum Acoustics

Lithium Niobate (LNO) is a well established material for Surface Acoustic Wave (SAW) devices including resonators, delay lines and filters. Recently, multi-layer substrates based on LNO thin films have become commercially available. In this chapter, we present a systematic low-temperature study of the performance of SAW devices fabricated on LNO-on-Insulator (LNOI) and LNO-on-Silicon substrates and compare them to bulk LNO devices. The goal of the study is to assess the performance of these substrates for quantum acoustics, i.e. the integration with superconducting circuits operating in the quantum regime. To this end, we design surface acoustic wave resonators with a target frequency of 5 GHz and perform experiments at millikelvin temperatures and microwave power levels corresponding to single photons or phonons. The devices are investigated regarding their internal quality factors as a function of the excitation power and temperature, which allows us to characterize and quantify losses and identify the dominating loss mechanism.

Parts of the results presented in this chapter have been published in *Surface acoustic wave resonators on thin film piezoelectric substrates in the quantum regime*. T. Luschmann *et al.* Materials for Quantum Technology **3** 021001 (2023) [174]. Some of the figures and text have been adapted from the publication.

6.1 Introduction

Surface acoustic waves (SAWs) are highly versatile with applications ranging from sensing (air pressure, magnetic resonance) [238], signal processing (GHz filters for mobile communications) [136] to the sorting of bio-molecules [239]. Recently, an additional research direction has been added to this list: quantum applications. In this field, quantized elastic and acoustic excitations are discussed for information storage due to their expected long lifetimes [46, 48–51, 240]. Furthermore, novel interaction regimes are explored in the giant atom limit [52–55], where the wavelength of the interacting wave becomes comparable to the dimensions of the (artificial) atom. These perspectives inspired the sub-field called circuit quantum acousto-dynamics (cQAD) [45]. In addition, within cQAD, applications such as quantum signal filters or microwave-to-optics conversion schemes based on the electro-optic properties of piezoelectric materials are considered [241–244]. Other applications are related to superconducting quantum circuits and in particular quantum bits which require the efficient transduction of electromagnetic to elastic excitations and vice versa. However, while materials with large piezoelectric coupling rates are desired as substrates for high performance SAW devices, the same piezoelectric coupling constitutes a critical loss channel limiting the performance of superconducting qubits below state-of-the-art values achieved for devices fabricated e.g. on silicon [45, 245]. One approach to overcome these ostensibly conflicting conditions is to physically separate the microwave quantum circuit from the acoustic component of the circuit by locating them on two different substrates and mediate the coupling e.g. using a flip-chip assembly in combination with inductive couplers [50].

Alternatively, the recent advent of commercially available thin film lithium niobate on insulator (LNOI) wafers enables the exploration of additional routes like the planar integration of microwave and mechanical elements on the same chip in a spatially separated fashion. The present LNOI platforms are fabricated in an "ion-slicing"-enhanced wafer-bonding process [246] and have been adopted quickly by the integrated photonics community [247], realizing waveguides [248], cavities [249], as well as electro-optical [250] and optomechanical [251] interfaces. Moreover, thin film LNO-on-silicon (without a SiO_x buffer layer) has recently become a subject of interest with respect to suspended SAW systems [252, 253] as well as microwave-to-optical frequency transduction [254] and investigations of mechanical systems in the quantum regime [255]. Previous investigations into the behavior and performance of SAW devices based on thin film piezoelectric platforms proved their general viability, but found considerable differences with respect to their bulk counterparts, which need to be considered in the context of potential applications [256–258]. In particular, a comprehensive study of the performance and loss mechanisms of SAW devices on thin film lithium niobate in the quantum regime, evaluating their viability for applications in quantum acoustics, is still missing. In the following, we present an experimental investigation of the suitability and performance of LNOI and thin film

LNO-on-silicon platforms for SAW-based applications in quantum acoustics. To this end we quantitatively analyze the performance of one of the key building blocks for cQAD, namely GHz-frequency SAW resonators, at conditions typical for the operation in superconducting cQAD architectures. Specifically, this requires studying their properties at millikelvin temperatures and at an average signal power corresponding to the single microwave-frequency photon/phonon level. As a reference point to established SAW technology, we also study devices fabricated on bulk LNO under the same conditions.

6.2 Thin-film material systems

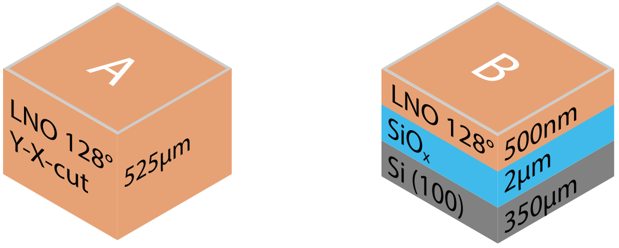

Fig. 6.1.: Investigated SAW material systems. Illustration showcasing the composition of the three different material stacks for sample types A (Bulk LNO), B (LNOI), and C (LNO on silicon) investigated in this study.

As a starting point for the comparative study, the standardized single-port SAW resonator design, which is introduced and discussed in Sec. 3.2, was fabricated on two different multi-layer material systems as well as bulk LNO. The compositions of the three used sample types A, B and C, are schematically illustrated in Fig. 6.1. Sample type A is based on a 128°-rotated Y-X-cut lithium niobate (LNO) crystal. In the bulk, LNO is an established SAW material widely and commercially employed in SAW resonators and radio frequency filters [136, 139] and will act as our reference material for the more complex multi-layer substrates. For type B, we use a lithium niobate on insulator (LNOI) stack, composed of a 500 nm thin 128°-rotated Y-X-cut LNO thin film on a 2 μm SiO$_x$ buffer layer on a 350 μm Si(100) substrate. Lastly, type C is another multi-layer stack composed of 300 nm X-Y-cut LNO on a 500 μm thick Si(111) substrate, without a buffer layer in between.

At this point, it is worth to recall the discussion of SAWs in multi-layer systems in Sec. 2.6.2, where we have shown that the phase velocity v_p is generally not constant across different multi-layer materials and can even exhibit a frequency dependence. This is due to the evanescent nature of the surface wave, where the properties of the underlying layer contribute to v_p. For frequencies around 5 GHz one can estimate a

SAW penetration depth of approximately 320 nm. We exclusively work with thin film thicknesses close to this value, so the majority of modes can be maintained in the LNO layer, which results in a high effective elastic mode filling factor and only minor modifications to v_p and the designed f_0 due to the influence of underlying layers.

6.3 Concept and methods

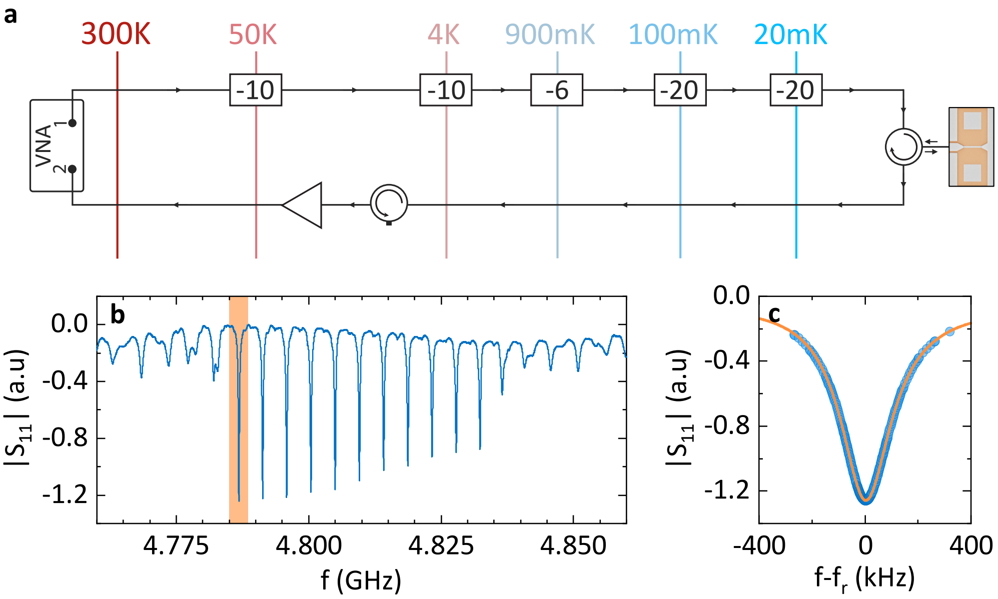

Fig. 6.2.: Measurement setup and analysis procedure. a Illustration of the cryogenic microwave spectroscopy setup used to investigate the performance of SAW resonator devices. **b** Typical reflection spectrum of a single-port SAW resonator. Shown is the normalized amplitude $|S_{11}|(f)$, measured at $T = 20\,\mathrm{mK}$ on a device fabricated on the LNO/Si multi-layer stack (sample type C illustrated in Fig. 6.1). **c** Isolated resonance signature of one selected mode (orange area in **a**) shown along with a fit to Eq. (6.1) (solid line). The fit is used to extract the resonance frequency f_r and the internal and external quality factors Q_i and Q_e.

The SAW resonators are investigated using microwave spectroscopy in a cryogenic measurement setup that is schematically illustrated in Fig. 6.2**a**. The setup is comparable to the one shown and described in Sec. 4.1, but we make use of a specialized cryostat optimized for fast sample exchange (FSE) to reduce cycling times between characterization of the different sample types. The FSE cryostat reaches a base operating temperature of $T_{\mathrm{base}} \approx 20\,\mathrm{mK}$ and does not contain a JPA or a vector magnet, both of which are not necessary for the study presented here. Another difference to the experiments on FTRs presented in the previous section is that due to the single-port design, the investigated SAW resonators can only be probed in reflection. To this end, we employ an additional cryogenic circulator at the mixing chamber stage of the cryostat to spatially separate the heavily attenuated (−66 dB) input signal from the signal reflected off the DUT, which is instead routed through a low loss, amplified output line. This way, we can use a simple VNA measurement to quantify the complex microwave reflection amplitude $S_{11}(f)$ (cf. Ref. [259]). The result of a typical reflection spectroscopy measurement of a SAW resonator is shown in Fig. 6.2**b**, where we plot the normalized magnitude of the scattering parameter $|S_{11}(f)|$. The multiple narrow and equally spaced absorption features are identified as the standing SAW resonator modes with a characteristic frequency spacing given by the free spectral range Δf_{FSR}. We analyze each SAW resonator mode of the investigated sample types A, B, and C individually by fitting its isolated absorption signature using the *circle fit* method to extract the resonance frequency f_{r} and the internal and external quality factors Q_{i} and Q_{e}. The resonance signature of one exemplary mode along with the fit is shown in Fig. 6.2**c**.

The fitting procedure closely follows the process which we introduced in the context of FTR analysis in Sec. 4.2.1. However, three important distinctions need to be made. First, since the SAW resonators are probed in a reflection geometry as opposed to transmission in the FTR case, the fitting function needs to be adapted to model the reflection coefficient S_{11}. This results in the adapted model [87, 189]

$$S_{11}(f) = Ae^{i\phi}e^{-i2\pi f\tau}\left[1 - \frac{2(Q/|Q_{\mathrm{e}}|)e^{i\theta}}{1 + 2iQ(f/f_{\mathrm{r}} - 1)}\right]. \tag{6.1}$$

It is apparent that the model represented by Eq. (6.1) differs only by a factor of 2 from the transmission model Eq. (4.1). The pre-factors A, τ, ϕ and θ remain the same, intended to correct for various signal distortions as discussed in Sec. 4.2.1. Since no frequency tuneability is given for the resonance frequency of the SAW resonators, the comprehensive background correction using real background data used for FTRs is not applicable in this case. Instead, the background contribution can only be inferred from the measurement data using best fits of the above mentioned correction terms. Lastly, the expression to calculate the average photon (or phonon) occupation of a resonator needs to be altered (compared to Eq. (2.80)) to reflect the coupling to a single input/output port, yielding

$$\bar{n}_{\mathrm{ph}} = \frac{\kappa_{\mathrm{ext}}}{\Delta^2 + (\kappa/2)^2}\bar{n}_{\mathrm{in}} = \frac{\kappa_{\mathrm{ext}}}{\Delta^2 + (\kappa/2)^2}\frac{P}{hf}, \tag{6.2}$$

for a microwave signal incident at the sample with power P and frequency f. Here, we also used the fact that SAW resonators are linear devices and do not exhibit a Kerr non-linearity ($\mathcal{K} = 0$).

In order to avoid effects of frequency dependent piezoelectric coupling on mode quality factors, we restrict our analysis to resonances in a narrow band with $|f_{\mathrm{r}} - f_0| < 2.5\Delta f_{\mathrm{FSR}}$ located in the center of the stop band, where we estimate f_0 by taking the average frequency of all visible resonance features. We also extract the effective length L_{eff} of each SAW resonator using $\Delta f_{\mathrm{FSR}} = v_{\mathrm{p}}/2L_{\mathrm{eff}}$, where v_{p} is given by the center frequency f_0 of the stop-band. The difference between the designed resonator length

L (distance between mirrors) and L_{eff} allows us to determine the reflectivity r of a single strip of width a using [139]

$$r = 2a/(L_{\mathrm{eff}} - L)\,. \tag{6.3}$$

6.4 Results

device	orientation	L (mm)	W(μm)	N_{f}	r (%)	$\bar{Q}_{\mathrm{e}}(10^3)$	$\bar{Q}_{\mathrm{i,HP}}(10^3)$
A1	90°	0.7	391	11	1.6	60.0 ± 6.8	52.8 ± 5.9
A2	90°	0.4	140	31	1.6	61.1 ± 7.9	238.4 ± 94.4
A3	90°	0.3	258	17	1.9	39.6 ± 1.8	59.6 ± 3.0
A4	90°	0.2	406	11	2.0	33.4 ± 1.1	64.1 ± 6.9
B1	0°	0.7	285	51	0.7	13.6 ± 2.6	10.3 ± 1.0
B3	90°	0.3	110	151	0.6	18.6 ± 1.4	20.4 ± 1.6
C1	90°	0.8	502	21	0.9	78.1 ± 1.4	21.0 ± 0.9
C2	90°	1.2	388.5	27	0.7	96.0 ± 1.4	16.6 ± 0.3
C3	0°	0.8	388.5	27	0.4	35.9 ± 5.1	7.9 ± 1.4
C4	0°	1.2	388.5	27	0.3	63.3 ± 0.7	10.4 ± 0.2

Tab. 6.1.: **Device design parameters and high power quality factors.** Devices are labeled by sample types A, B and C as illustrated in Fig. 6.1. Design parameters are discussed and illustrated in Sec. 3.2. The mean internal ($\bar{Q}_{\mathrm{i,HP}}$) and external ($\bar{Q}_{\mathrm{e,HP}}$) high power quality factors are calculated from the 5 center-most resonance dips around the stop band center frequency f_0 and are listed along with their standard deviation. The individual values are extracted using fits to Eq. (6.1). All devices operate at $f_0 \approx 5\,\mathrm{GHz}$. The orientation refers to the in-plane propagation direction of SAWs within the resonators w.r.t. the standard propagation direction of the respective cut (i.e. for $128°$-rotated Y-X-cut LNO, $0°$ corresponds to X-propagation). All measurements were performed at $T_{\mathrm{base}} \approx 20\,\mathrm{mK}$ and with microwave powers equivalent to a resonator phonon occupation of $\bar{n}_{\mathrm{ph}} \approx 10^5$.

Quality factors in the high power limit We begin the study with spectroscopy measurements using relatively high microwave probe powers corresponding to an average phonon occupation of $\bar{n}_{\mathrm{ph}} \approx 10^5$ in the SAW resonator. In this regime, the signal-to-noise ratio is large and measurements can be completed quickly, so that sufficient statistics can be collected regarding the basic properties of the SAW devices. A summary of the experimental analysis for high power measurements on 10 different devices across the three sample types is presented in Tab. 6.1, along with design parameters of each device (cf. Sec. 3.2). Note that the shown quality factors $\bar{Q}_{\mathrm{i,HP}}$ and $\bar{Q}_{\mathrm{e,HP}}$ are mean values calculated over the 5 center-most modes around the center frequency of the mirror stop band f_0. We find average internal quality factors on the order of $\bar{Q}_{\mathrm{i,HP}} \approx 10^4$ across all 10 devices and three sample types, with the reference devices on bulk LNO generally performing better and some individual modes of device A2 reaching values up to 3×10^5. However, the spread of quality factors between the modes of A2 is extremely large (60×10^3 to 380×10^3), which translates to a considerable standard deviation of the average $\bar{Q}_\mathrm{i}$. We attribute this to a strongly frequency dependent coupling to parasitic box modes in this particular sample. With respect to the external quality factors $\bar{Q}_\mathrm{e}$ we observe good agreement with our considerations in the design stage (see Sec. 3.2) and find all of the devices to fall roughly into the regime of critical coupling ($Q_\mathrm{i} \approx Q_\mathrm{e}$).

When working with SAW resonators, a multitude of loss mechanisms contribute to the experimentally observed internal quality factor, in particular the phonon propagation loss, diffraction in the anisotropic substrate and finite reflectivity of the Bragg gratings [139, 143, 145]. From the experimentally determined internal quality factors, we can draw some conclusions regarding individual loss contributions: Due to the high operating frequency of the investigated devices, the confined wavelengths are small compared to the dimensions of the resonators (i.e. $W, L \gg \lambda$). In this limit, losses due to diffraction and reflection usually remain negligible, which leads us to the assumption that the loss due to phonon propagation in the substrate constitutes the limiting factor in our devices [143, 151]. Under this assumption, we can calculate the phonon propagation loss according to

$$\alpha_\mathrm{P} = \frac{\pi}{\lambda \bar{Q}_\mathrm{i,HP}} \tag{6.4}$$

and place an upper bound on the phonon propagation losses to $\alpha_\mathrm{P,A} = 0.018\,\mathrm{dB/mm}$, $\alpha_\mathrm{P,B} = 0.024\,\mathrm{dB/mm}$ and $\alpha_\mathrm{P,C} = 0.025\,\mathrm{dB/mm}$ for sample types A[1],B and C, respectively. The corresponding mean free path lengths l_f before a phonon gets scattered are $l_\mathrm{f,A} = 14.98\,\mathrm{mm}$, $l_\mathrm{f,B} = 3.91\,\mathrm{mm}$ and $l_\mathrm{f,C} = 3.56\,\mathrm{mm}$. The extracted values for the propagation loss in bulk LNO are comparable with literature values observed for ST-X-Quartz at low temperatures [151]. With respect to the other sample types, it appears plausible that the presence of additional interfaces and secondary materials in the multi-layer systems leads to an increased scattering probability of propagating phonons and therefore higher lossesn and lower mean free path lengths.

For the single electrode reflectivity r, we calculate values around 2% for all of the bulk LNO devices, which is in good agreement with literature [139]. For the remaining sample types on the other hand we observe decreased reflectivities below 1%. Since electrode reflectivity is proportional to the piezoelectric coupling strength of the material [139], we can infer that the multi-layer materials exhibit a lower piezoelectric coupling compared to the bulk system. This observation agrees with predictions by finite element simulations [143] and can likely be attributed to the reduced mode filling factor in the thin films as opposed to bulk LNO.

Quality factors in the quantum regime The average quality factors extracted from the fast, high power measurements provide a useful baseline to the performance of SAW devices on the investigated substrate. However, as discussed in Sec. 2.7, one important

---

[1] Device A2 was excluded from the calculation of the average phonon propagation loss for sample type A due to the uncharacteristically large spread of observed quality factors.

contribution to the intrinsic losses of solid-state based resonators are the losses due to so-called two-level-systems (TLS), which become especially relevant at low powers. In particular, in electromagnetic CPW resonators, as investigated in the other chapters of this work, TLS losses are commonly identified as the limiting factor for the resonator performance in the quantum regime such that $Q_\mathrm{i} \approx Q_\mathrm{TLS}$ [155]. Therefore, we proceed to analyze the quality factors of SAW resonators also in the low power or single excitation limit as this regime is the most relevant for quantum acoustic applications.

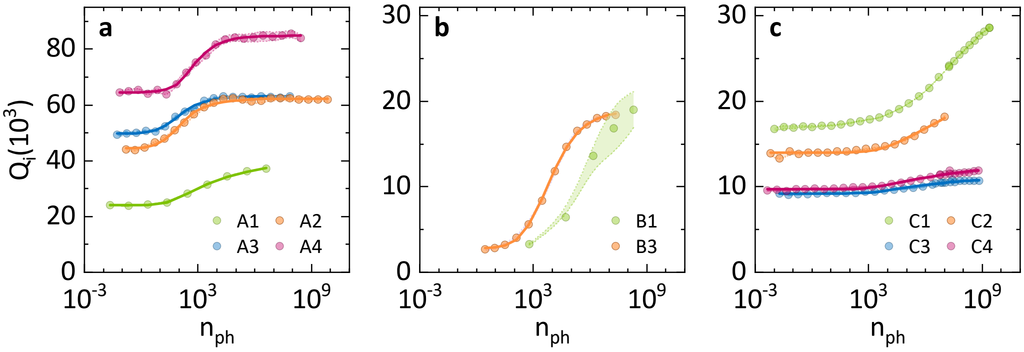

Fig. 6.3.: Power dependency of internal quality factors. Internal quality factors Q_i as a function of the average resonator phonon occuopation $\bar{n}_\mathrm{ph}$, extracted by fits to Eq. (6.1) for various samples of types A (bulk LNO, **a**), B (LNOI, **b**), and C (thin film LNO, **c**) (sample details listed in Tab. 6.1). For each resonator, the mode with the best ratio of intrinsic quality Q_i factor to its uncertainty $Q_\mathrm{i}/\Delta Q_\mathrm{i}$ was selected. Uncertainties are illustrated as shaded areas around the data points as output by the fitting algorithm. Where possible, the power-dependency of Q_i has been fitted to a TLS based model given by Eq. (2.126) (solid lines) and the corresponding TLS contribution Q_TLS was extracted and is summarized in Tab. 6.2. While the devices on bulk LNO (**a**) show a clear saturation behavior for high and low average phonon numbers $\bar{n}_\mathrm{ph}$, devices on LNOI (**b**) and on LNO thin films (**c**) show only partial saturation.

To characterize the impact of TLS losses on the low-power performance of the investigated SAW resonators, we perform power-dependent measurements of the devices' quality factors. To this end, we record the microwave reflection amplitude S_{11} around individual resonance features for varying VNA probe powers and extract Q_i as a function of microwave power. Since measurements in the low power limit of individual phonon excitations are very time consuming, we decide to focus the investigation on a single mode per device instead of calculating a mean value from multiple modes. Specifically, we identify from the high power measurements the mode with the best ratio of intrinsic quality factor to its uncertainty (i.e. $Q_\mathrm{i}/\Delta Q_\mathrm{i}$) and investigate only the selected mode for its power dependent behavior. The experimental results are summarized in Fig. 6.3.

In the figure, the microwave power incident at the sample is expressed in the form of an average phonon occupation $\bar{n}_\mathrm{ph}$ in the respective resonator mode via Eq. (6.2). We observe an increase in Q_i with increasing drive power for all investigated devices. This behavior is expected where TLS losses dominate and commonly associated with the

device	$Q_\mathrm{i}(10^3)$	$Q_\mathrm{TLS}(10^3)$	$Q_0(10^3)$	$Q^\mathrm{T}_\mathrm{TLS}(10^3)$	
A1	24.0 ± 0.5	61.2 ± 1.7	39.5 ± 0.5	-	
A2	44.4 ± 0.5	154.7 ± 4.3	62.2 ± 0.2	-	
A3	49.8 ± 0.5	234.8 ± 7.1	63.2 ± 0.3	189.1 ± 6.0	
A4	64.6 ± 0.6	270 ± 6.8	84.9 ± 0.3	-	-
B1	-	-	-	-	-
B3	2.6 ± 0.1	3.3 ± 0.1	18.9 ± 0.1	3.7 ± 0.1	
C1	16.8 ± 0.2	-	-	36.2 ± 0.2	
C2	14.0 ± 12.7	14.1 ± 7.6	$10^7 \pm 10^{15}$	-	
C3	9.4 ± 1.7	35.5 ± 12.3	12.8 ± 1.5	-	
C4	9.7 ± 1.2	35.7 ± 7.8	13.4 ± 1.0	-	

Tab. 6.2.: **Low power analysis of quality factors and TLS contribution.** Experimentally determined low power internal quality factors Q_i along with the TLS contribution Q_TLS and residual contribution Q_0. The values listed for Q_i are determined by measurements at $T_\mathrm{base} = 20\,\mathrm{mK}$ and low power with an average resonator phonon occupation $\bar{n}_\mathrm{ph} < 1$. Q_TLS and Q_0 are extracted from fits to Eq. (2.126) of the data shown in Fig. 6.3. Conversely, $Q^\mathrm{T}_\mathrm{TLS}$ are the results from fits to Eq. (2.128) of the data shown in Fig. 6.4. Device B1 could not be measured in the low power regime, thus the missing values (-). Design parameters for the investigated devices are listed in Tab. 6.1.

coupling of the resonator field to a bath of TLS, which are increasingly saturated with increasing excitation number. To quantify this effect, we compare the experimental data with Eq. (2.126), the empirical model for the loss caused by a TLS bath which we have introduced in Sec. 2.7. Many of our devices exhibit the characteristic saturation behavior (see Fig. 6.3**a** and **b**) although the impact of TLS losses is less significant compared to their high performance electromagnetic counterparts [80]. However, for the SAW resonators fabricated using LNO thin films on Si (sample type C), we observe a qualitatively different behavior, where saturation is not apparent for average phonon numbers up to 10^9. The behaviour of this set of devices is not fully described by the power-dependent TLS theory. For the remaining devices, we use fits to Eq. (2.126) (solid lines) to extract the contribution of TLS related losses Q_TLS to the internal quality factor of the respective device. The results are listed in Tab. 6.2.

The observed lack of a clear saturation of Q_i with power is commonly associated with off-resonant TLS, which due to their large detuning from the resonator frequency, do not saturate even at high drive powers [85]. Fortunately, it is possible to gain further insight into the properties of off-resonant TLS using temperature dependent measurements. To this end, we choose one device per investigated sample type and study the resonance frequency f_r and the internal quality factor Q_i as a function of temperature for the same mode that was previously investigated regarding its power dependence. The measurements are performed at temperatures between $T = 20\,\mathrm{mK}$ to $1000\,\mathrm{mK}$ with constant microwave powers corresponding to $\bar{n}_\mathrm{ph} \approx 10^5$. The results are presented in Fig. 6.4.

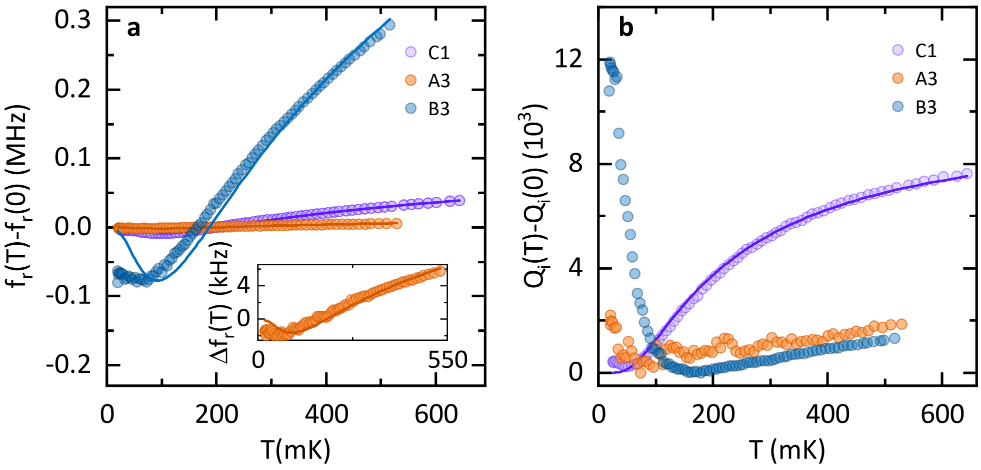

Fig. 6.4.: Temperature dependency of resonance frequency and internal quality factors. Experimentally observed change in (**a**) resonance frequency $f_\mathrm{r}(T) - f_\mathrm{r}(0)$ and (**b**) intrinsic quality factor $Q_\mathrm{i}(T) - Q_\mathrm{i}(0)$ as a function of temperature, shown for one selected resonator mode per substrate, labeled as shown in Tab. 6.1. The measurements are performed with a constant microwave power corresponding to $\bar{n}_\mathrm{ph} \approx 10^5$. Solid lines in **a** are fits to Eq. (2.128). The inset shows the same experimental data along with the fit for resonator A3 rescaled to make the much smaller effect visible. In **b**, the change in Q_i is plotted relative to the intrinsic quality factor at zero temperature $Q_\mathrm{i}(0)$. Fits of $Q_\mathrm{i}(T)$ to Eq. (2.127) (solid lines) are only possible for the data of resonator C1, while the other two resonators show behavior that is not fully described by the presented TLS model (see Sec. 2.7 and Ref. [85]). Uncertainties as provided by the fit models are smaller than the symbol size.

Pronounced changes in f_r as well as Q_i are observed for devices C1 and B3, i.e. on LNO thin film sample types, while device A3 fabricated on bulk LNO shows significantly weaker temperature dependence. Therefore, it can be assumed that thermal TLS do not contribute as strongly to the losses in bulk LNO. This is expected from the observation made from Fig. 6.3**a**, where a clear saturation of Q_i as a function of power suggests that the most relevant loss mechanisms for SAW resonators on bulk LNO are well described by Eq. (2.126) even without considering thermally excited TLS. It is notable, however, that our data of resonator B3 deviates significantly from the behavior predicted by the off-resonant TLS model for temperatures below 100 mK. An unexpected and large increase in Q_i is observed, as well as a constant f_r where a characteristic local minimum is expected. We believe that this behavior can be attributed to an additional effect, which is not considered by either of the applied theoretical models:

The coherence time of resonant TLS is temperature dependent and increases with decreasing T. This in turn leads to a decrease of saturation energy and more TLS being saturated at constant microwave power, effectively increasing Q_i towards very low temperatures [173]. Due to the low overall quality factor of the LNOI resonator B3, which also appears to be heavily TLS limited ($Q_\mathrm{i} \approx Q_\mathrm{TLS}$), this effect appears especially pronounced. A full description of this behavior would require a more extensive theory considering coherent exchange of excitations with TLS, which would exceed the scope of this work.

Despite this discrepancy, by fitting the temperature dependence of devices A3, B3 and C1 to Eq. (2.128), we extract equivalent quality factors $Q^{\mathrm{T}}_{\mathrm{TLS,A3}} = (189.1 \pm 6.0) \times 10^3$, $Q^{\mathrm{T}}_{\mathrm{TLS,B3}} = (3.7 \pm 0.1) \times 10^3$ and $Q^{\mathrm{T}}_{\mathrm{TLS,C1}} = (36.2 \pm 0.2) \times 10^3$ for the thermal TLS contribution. Further, a fit to Eq. (2.127) for device C1 results in $Q^{\mathrm{T}}_{\mathrm{TLS,C1}} = (49.3 \pm 0.4) \times 10^3$. These extracted quality factors show good agreement with the previous analysis of power-dependency. The results of both measurement approaches are summarized in Tab. 6.2.

6.5 Discussion

Analyzing the results of the various measurements performed during the study as summarized in Tab. 6.2, we observe $Q_{\mathrm{TLS}} \approx Q^{\mathrm{T}}_{\mathrm{TLS}} \gg Q_{\mathrm{i}}$ for devices fabricated on bulk LNO, suggesting that TLS are not dominating the losses of these devices and other mechanisms, e.g. acoustic losses to bulk waves, play a larger role. This conjecture is in agreement with our previous discussion about the limiting phonon propagation losses in the context of the high power measurements. Conversely, for the investigated devices fabricated on LNOI (sample type B), we observe $Q_{\mathrm{TLS}} \approx Q^{\mathrm{T}}_{\mathrm{TLS}} \approx Q_{\mathrm{i}}$, which is consistent with TLS currently limiting the performance of LNOI devices. We attribute this difference in loss behavior to the additional interfaces associated with the multi-layer structure. Studies from cQED show that interfaces and, in particular, surface oxides can lead to large TLS losses in coplanar waveguide resonators [80]. For LNOI, this is especially expected due to the introduction of the silicon dioxide buffer layer, which is known to be a lossy dielectric. It is worth noting that there are experiments performed at room temperature which have found SAW devices on LNOI films to exhibit higher quality factors compared to devices on bulk LNO [258], in contrast to the results of our study. This underscores the dominating effect of TLS-related losses for devices operating in the quantum regime, whereas TLS are expected to be fully saturated at room temperature, rendering the associated losses negligible.

The picture for thin film LNO on silicon (sample type C) is less definitive. Clearly, the observed TLS quality factors Q_{TLS} are greatly reduced compared to the devices fabricated on bulk LNO, suggesting a significant increase in the losses to a bath of TLS. However, only device C2 can be considered fully TLS limited with $Q_{\mathrm{TLS}} \approx Q_{\mathrm{i}}$. For the remaining devices, the experimentally observed internal quality factors at low power are better described by $Q_{\mathrm{TLS}} > Q_0 \approx Q_{\mathrm{i}}$, although all three values reside in the same order of magnitude. This observation suggests that while TLS losses play a considerable role, other loss channels, consolidated in Q_0, are the limiting factor in most of our investigated thin film LNO devices. In order to fully understand the behavior of these devices, a detailed study of the LNO-Si interface is most likely necessary. We suspect that during the wafer-bonding process used to fuse thin film LNO to silicon, a non-negligible thermal oxide layer is formed in between the two layers. The additional interfaces produced by the bonding process might not only host a significant amount of TLS, but also have direct impact on the propagation properties of phonons.

Investigation of thin film LNO crystal quality To gain further insight into possible causes for the non-TLS related losses in the thin film LNO devices, we perform a *X-ray diffractometry* (XRD) study of the multi-layer material itself. In the following we will provide a brief introduction to XRD and the experiments performed. However, a comprehensive treatment of the underlying physical concepts and experimental details exceeds the scope of this work and we refer the interested reader to Refs. [260, 261].

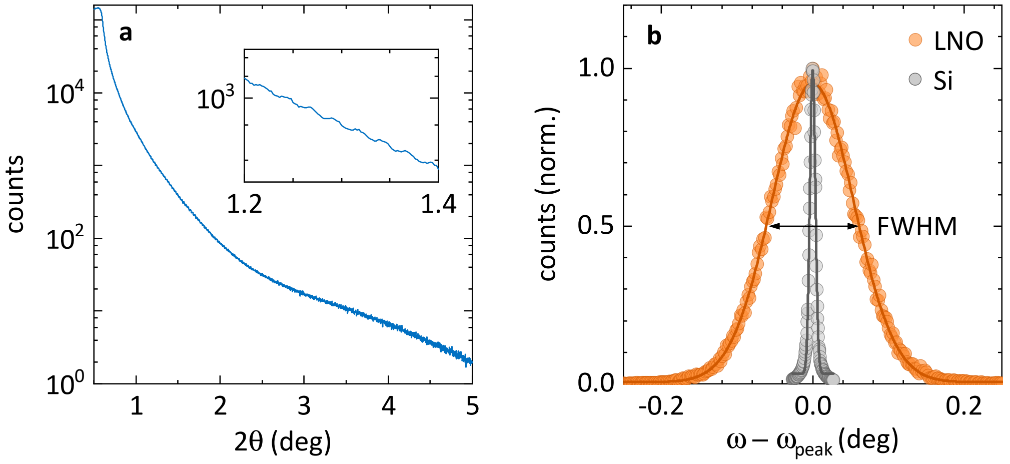

Fig. 6.5.: XRD study of the thin film LNO on silicon material system. a X-ray reflectometry (XRR) measurement for small detector angles $2\theta = 0.5\,°$ to $5\,°$. The inset magnifies a section of the same data to highlight the appearance of Kiessig fringes. **b** Rocking curve measurement to determine the crystallinity of both the LNO (orange) and the silicon (grey) layers. The counts for both curves are normalized to unity and fitted using a gaussian distribution (solid lines). From the fits we extract FWHM of $0.108°$ for LNO and $0.008°$ for Si.

The principle behind XRD is based on the interaction of X-rays with the crystal lattice. When a beam of X-rays strikes a crystal, it interacts with the periodically spaced atoms in the lattice. Upon impact, the X-rays scatter in various directions and are subject to interference conditions depending on the relation between the X-ray wavelength and the length scales of the material's atomic lattice. Therefore, a characteristic diffraction pattern is formed, which contains information about lattice spacing, crystal orientation, crystal quality, and other important characteristics of the material under investigation [261]. A common approach to study diffraction patterns is the 2θ measurement. In this technique, a sample is placed in the path of an incident X-ray beam, and a detector is positioned on the other side of the sample to collect the diffracted X-rays. The term 2θ refers to the angle between the incident X-ray beam and the detector. It is twice the angle of the diffraction, where the diffraction angle is the angle between the incident beam and the diffracted beam. The 2θ angle is used because it simplifies the geometry and allows for easier data analysis. To perform the experiment, the sample is mounted on a sample holder, which can be tilted by an angle ω, while the detector simultaneously moves to an angle 2θ.[2] The X-ray source remains fixed while sample and detector scan a range of angles and the corresponding intensities are recorded.

In Fig. 6.5**a** we show the result of a X-ray reflectometry (XRR) measurement performed on one of the thin-film LNO on silicon samples. XRR is a special case of the 2θ measurement introduced above, where only angles of 2θ between 0.5° and 5° are investigated. For these small angles, the X-rays are reflected at the sample surface as well as at interfaces with a different refractive index. Constructive and destructive interference between the differently reflected rays give rise to so-called *Kiessig* fringes in the diffraction pattern. The shape and periodicity of the fringes can be matched to simulations and therefore provide information about the different layers and their respective thicknesses in a multi-layer material [261]. In the case of the measured thin film LNO sample, the fringes are particularly visible for $2\theta = 1\,°$ to $2\,°$ (see magnified section in inset). Using the *LEPTOS* software [262] we match the observed fringes to a LNO layer thickness of $t_{\mathrm{LNO}} \approx 350\,\mathrm{nm}$, which is a non-negligible deviation from the nominal thickness of 300 nm specified for the source material. The XRR measurement is also in principle capable of testing our conjecture regarding the presence of a $\mathrm{SiO_x}$ layer in between the silicon and LNO films. A thin interface layer of $\mathrm{SiO_x}$ would result in a beating in the measured XRR signal intensity. While indications of a beating might be discernible in the measurement shown in Fig. 6.5**a**, the signal-to-noise ratio towards larger angles is not sufficient for the software to perform a reliable fit.

A second XRD experiment that can be performed is a *rocking curve* measurement, as shown in Fig. 6.5**b**. Here, the detector position is fixed to the value of 2θ where the crystallographic peak of interest appears in an initial 2θ measurement and the incident angle ω is varied slightly, so that the shape of the peak can be studied in detail. Generally a low linewidth of the peak corresponds to a high crystalline quality and homogeneity of the investigated material [261]. In the figure, we compare the peak corresponding to the LNO thin film (orange) to the peak associated with the underlying silicon layer (grey) in the same sample. Using gaussian fits to the data, we find a FWHM of 0.108° for LNO compared to 0.008° for silicon. The sharp silicon peak suggests a high quality, single-crystalline wafer was used in the wafer bonding process. The much wider LNO peak on the other hand points to a much less ideal crystal structure with a higher mosaicity (spread of crystal plane orientations) [260]. Based on these results, it is plausible that the imperfections in the LNO thin films crystal quality and thickness are related to the large non-TLS losses observed for SAW devices in the previous experiments.

---

[2] For this brief excursion into XRD measurements, we adapt the standard notation used in literature, using ω and 2θ for the incident and detector angle, respectively. These symbols are not to be confused with their usage in other chapters of this work, in particular ω as the angular frequency.

6.6 Conclusion

In the presented study, we have investigated surface acoustic wave resonators fabricated on thin film lithium niobate and lithium niobate on insulator (LNOI) samples and compared their performance at millikelvin temperatures and in the quantum regime to reference devices fabricated on the well established piezoelectric LNO (bulk). As a figure of merit, we focus on the internal quality factor Q_i of the resonators, which can be used as an indication for the losses that might limit quantum applications of the SAW devices. We find that internal quality factors of the devices fabricated on multi-layer substrates are generally lower than of those fabricated on bulk LNO, but remain roughly in the same order of magnitude. Subsequently, we used power- and temperature-dependent measurements to gain further insight into the underlying loss mechanisms present in the different substrates, with particular focus on the contribution of two-level systems (TLS), which are often limiting the performance of electromagnetic resonators used in circuit electrodynamics. Using two different models based on thermal and non-thermal TLS, we are able to describe our experimental result and extract the contribution of these TLS to the total losses of the devices. We find TLS losses to be the limiting factor in SAW devices fabricated on LNOI, while other loss channels dominate in the reference devices fabricated on bulk LNO. In the case of thin film LNO on silicon, TLS contribute significantly to the losses, but can not be identified as the sole limiting factor. Instead, we hypothesize based on XRD experiments that the quality of the material itself and defects introduced in the wafer bonding process negatively impact the performance of these devices. However, even with the slightly increased loss rates compared to bulk LNO devices, SAW resonators on thin film LNO demonstrate performance in the single-phonon regime that is comparable to devices on bulk LNO, which are successfully used in quantum acoustic circuits [50, 51]. Moreover, potential advantages in scalability and versatility by avoiding flip-chip assemblies might favor the use of thin film SAW resonators over established bulk devices for particular applications.

Conclusion

7

7.1 Summary of findings

In this thesis, we have conducted comprehensive investigations into both the fabrication processes and the experimental operation of inductively coupled electromechanical circuits and surface acoustic wave based quantum acoustic devices.

Regarding the fabrication, significant efforts have been invested to re-think the processes used to manufacture nano-electromechanical circuits from the ground up to improve their microwave properties, specifically the intrinsic loss rates κ_{int}. As a result, a new multi-step process was developed that allows for the independent optimization of materials and process steps in order to reduce the main cause of microwave losses in superconducting quantum circuits: two-level-systems (TLS). Based on the newly developed process, a new generation of electromechanical devices is being developed that has the potential to approach the single-photon strong coupling regime of optomechanics (first results see Sec. 7.2).
Experimentally, we have studied the electromechanical single-photon coupling rate in inductively coupled devices and its predicted scaling towards significantly larger external magnetic fields. We employed a two-pronged approach of complementary methodologies to independently verify the achievable coupling rates in the studied device. Our investigation revealed a significant disagreement between the different experimental methods, as well as coupling rates that generally remain below those predicted by a theoretical model. Both effects become more pronounced as the magnetic field strength is increased. Based on our experimental data, we attribute the discrepancies to the influence of flux noise and the associated frequency fluctuations of the flux-tunable device. Although an active feedback protocol has been developed for this work to stabilize the experiment against frequency shifts, it proved primarily effective against low-frequency components of the flux-noise. The remaining high-frequency noise, in combination with the long measurement duration required to record microwave signals in the quantum regime, likely leads to an effective reduction of the measured coupling rates g_0. This indicates that future experiments might benefit from methods with shorter measurement duration and fewer averages to more accurately capture g_0, especially at higher magnetic fields. Additionally, methods to shield or compensate the high-frequency flux noise are likely to prove beneficial to future experiments (see Sec. 7.2). Notwithstanding these challenges, our investigated device demonstrated a maximum single-photon coupling strength of $g_0/2\pi = (53.72 \pm 2.91)$ kHz at $B_{\mathrm{ip}} = 35$ mT, exceeding any previously reported value.

Simultaneously, our work on low-power sideband cooling demonstrated the adaptability of the inductively coupled architecture, which allows in-situ tuning of key parameters like the optomechanical coupling strength over a wide range of accessible values. Exploiting the record-high single-photon coupling strength attained in our device, we demonstrated sideband cooling of a nanomechanical oscillator to near-single-phonon occupation with a remarkably low microwave power on the order of a fraction of a single photon. While the quantum mechanical ground state remains elusive for now, we identified concrete limitations such as the device's inherent Kerr non-linearity, which can be selectively addressed in the next iteration of the experimental design (see Sec. 7.2).

Further, we investigated how backaction in the electromechanical system can be exploited for mechanical frequency control of a nanostring. We demonstrated a significant in-situ tuning range of the mechanical resonance frequency, spanning more than 50 mechanical linewidths, and successfully replicated the experimental data with a model based on the Lorentz force acting on the string. The findings also revealed unexpected indications of flux vortex formation in the superconducting nanostring. While further research is needed to fully understand these phenomena, their observation underscores the sensing capabilities of electromechanical devices and suggests exciting possibilities for exploring the mechanical properties of individual flux lines.

Complementing these studies, our research on SAW resonators on thin-film lithium niobate (LNO) and lithium niobate on insulator (LNOI) substrates compared their performance at millikelvin temperatures with devices fabricated from traditional bulk LNO. Our detailed analysis of loss mechanisms, particularly focusing on the role of TLS, revealed that TLS losses are a significant limiting factor in thin-film substrates, while other loss channels dominate in bulk LNO. While the internal quality factors in multi-layer substrates generally fell short of those in bulk LNO, the potential scalability and versatility of thin-film SAW resonators, despite slightly increased loss rates, make them a viable alternative for certain quantum acoustic applications.

7.2 Future directions

Based on the results of this work, two avenues of future experimental work can be identified that could help to push the limits on what is currently possible with inductively coupled electromechanical devices.

Towards lower loss rates First and foremost, the high intrinsic loss rate $\kappa_{\mathrm{int}}/2\pi > 1\,\mathrm{MHz}$ of the flux-tuneable microwave resonator studied in this work currently poses the main obstacle to the single-photon strong coupling regime. The multi-step process

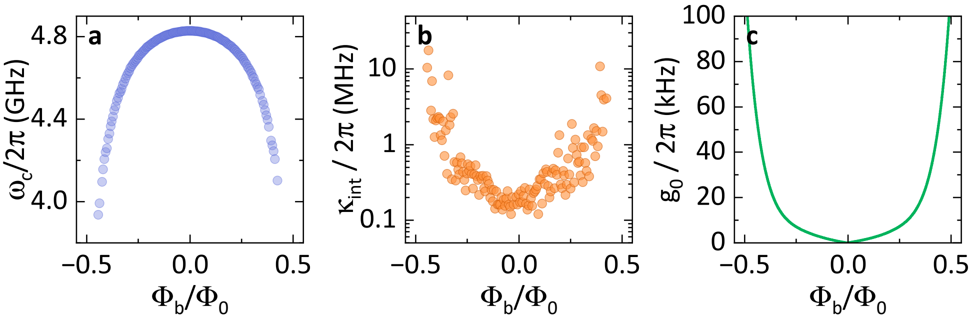

Fig. 7.1.: **First results of next generation electromechanical device.** **a** FTR resonance frequency ω_c, and **b** internal loss rate $\kappa_{\rm int}$ as a function of applied flux bias Φ_b, measured in absence of an in-plane field $B_{\rm ip} = 0$. **c** Expected single-photon coupling strength g_0 of the device, calculated according to Eq. (2.96) using the parameters $\Omega_m/2\pi = 5.7266\,$MHz, $l = 30\,\mu$m, $\gamma = 0.9$, $B_{\rm ip} = 15\,$mT, and $\partial\omega_c/\partial\Phi$ computed numerically from the data in **a**. The investigated device was fabricated using the multi-step process developed over the course of this work and presented in 3.3.2. Sample fabrication and measurement by Korbinian Rubenbauer.

presented in Sec. 3.3.2 was developed to face this challenge and considerably reduce the impact of TLS-related microwave losses in the next generation of electromechanical devices. The first devices based on the newly developed process have been fabricated and measured recently. We present a summary of early results in Fig. 7.1.

As seen in panel **a**, the new device demonstrates a large flux-tuneability of 800 MHz comparable to the previous device. More importantly, the internal loss rate of the device, as shown in panel **b**, was found as low as $\kappa_{\rm int}/2\pi = 120\,$kHz at the sweet spot and $\kappa_{\rm int}/2\pi \approx 300\,$kHz at moderate flux bias points. This corresponds to a quality factor of $Q_i = 20 \times 10^3$ to 40×10^3 and constitutes an improvement by a factor of 10 compared to the previously investigated device. Based on the frequency tuning behavior, we can extract the flux responsivity $\partial\omega_c/\partial\Phi$ and predict the achievable coupling strength g_0 of the device at moderate fields of $B_{\rm ip} = 15\,$mT according to Eq. (2.96) and expect coupling rates in the range up to 80 kHz to be accessible (panel **c**). Due to the increased quality factors, a coupling rate of $g_0/2\pi = 40\,$kHz as already demonstrated for the previous device, would approach $g_0/\kappa \approx 0.33$ and a quantum cooperativity of $C_{\rm qu} = 4g_0^2/(\kappa\Gamma_m) \cdot \bar{n}_c/\bar{n}_{\rm ph}^{\rm th} > 7$ at $\bar{n}_c = 1$, which would allow the coherent transfer of quantum information between the mechanical and the electrical subsystems. With continued efforts to further optimize the quality factors of subsequent devices, even the single-photon single-phonon strong coupling regime can likely become within reach.

Combating flux noise In addition to improving the intrinsic properties of the electromechanical devices, efforts are underway to mitigate adverse external factors, in particular the effects of high-frequency flux noise on future experiments. Ongoing projects involve shielding the cryostat with Cryoperm shields, where first results demonstrating an increased frequency stability have been achieved. Furthermore, a redesign of the magnet and sample assembly to be less susceptible to mechanical vibrations might be promising in minimizing the impact of external disturbances on device performance. These approaches aim to enhance the stability and reliability of future experiments, ultimately enabling higher electromechanical coupling rates to be measured and exploited.

Appendix

A

A.1 Summary of nano-electromechanical device parameters

	parameter	value	comment
CPW	Eigenfrequency	$\omega_c/2\pi = 7.4\,\mathrm{GHz}$	
	Length	$\ell = 3.95\,\mathrm{mm}$	
	Dimensions (width, gap)	$w_c = 10\,\mu\mathrm{m}$, $g_c = 8\,\mu\mathrm{m}$	
	Linear inductance	$L_r = 1.832\,\mathrm{nH}$	
	Linear capacitance	$C = 545\,\mathrm{fF}$	
SQUID	Loop inductance	$L_{\mathrm{loop}} = 136\,\mathrm{pH}$	see App. A.3
	Loop area	$A_{\mathrm{loop}} = 47.7\,\mu\mathrm{m}^2$	
	Critical current	$I_{c0} \approx 1.6\,\mu\mathrm{A}$	
	Screening parameter	$\beta_L \approx 0.2$	
	Eigenfrequency	$\Omega_m \approx 5.8\,\mathrm{MHz}$	out-of-plane mode
String	String length	$l = 30\,\mu\mathrm{m}$	
	Dimensions (width, thickness)	$w = 200\,\mathrm{nm}$, $t = 110\,\mathrm{nm}$	
	Tensile pre-stress	$\sigma_0 = 170\,\mathrm{MPa}$	Ref. [57]
	Shape factor	$\gamma = 0.9$	Ref. [219]

Tab. A.1.: **Summary of electromechanical device parameters.** The parameters are categorized into the sub-components of the electromechanical device: the coplanar waveguide resonator (CPW), the superconducting quantum interference device (SQUID) and the mechanical oscillator, i.e. nanostring (String).

In Tab. A.1, we summarize the most relevant design parameters for the electromechanical device used in the experimental study in Chap. 5. The device was fabricated using the single-step process detailed in Sec. 3.1.1 and Sec. 3.3.3. Due to the nature of the single step process, the coplanar waveguide resonator (CPW) and the nanostring both consist of a Al/AlO$_x$/Al tri-layer of 110 nm thickness.

A.2 Note on the use of single-sided and double-sided spectra for frequency noise calibration

Throughout literature [32, 74, 75], different conventions are used for the definition of displacement and force spectral densities in optomechanical experiments. As with all competing conventions, their results should be equivalent, if consistently used. In our experiment, an additional complication arises due to the use of a heterodyne detection scheme (details in Sec. 4.2.3), which requires careful consideration of the spectral density convention for the experimental analysis. In this section, we provide a detailed comparison of the *single-sided* and *double-sided* convention for spectral densities and how they affect our measurements.

Double-sided convention We use the convention of double-sided spectra throughout this work, so the expressions in the following part are identical to the ones used in the main text. We nevertheless repeat the key parts of the treatment to allow for a direct comparison later on.

Double-sided spectral densities $S_{\mathrm{xx}}^{\mathrm{DS}}(\Omega)$ are defined such that the mean square fluctuations of their corresponding variable x are found by integration over the entire frequency space, i.e.

$$\langle x^2 \rangle = \int_{-\infty}^{+\infty} S_{\mathrm{xx}}^{\mathrm{DS}}(\Omega) \frac{d\Omega}{2\pi}\,, \tag{A.1}$$

specifically also $\langle \delta\omega^2 \rangle = \int_{-\infty}^{+\infty} S_{\omega\omega}^{\mathrm{DS}}(\Omega) \frac{d\Omega}{2\pi}$. This normalization leads to a corresponding driving force spectral density exerted by a thermal bath of temperature T given by [73, 74]

$$S_{\mathrm{FF}}^{\mathrm{DS}}(\Omega) = 2 m_{\mathrm{eff}} \Gamma_{\mathrm{m}} k_{\mathrm{B}} T\,. \tag{A.2}$$

Accordingly, we calculate the (double-sided) thermal displacement spectral density of a mechanical oscillator to [73, 75]

$$S_{\mathrm{xx}}^{\mathrm{DS}}(\Omega) = |\chi_{\mathrm{m}}(\Omega)|^2\, S_{\mathrm{FF}}^{\mathrm{DS}}(\Omega) \approx \frac{k_{\mathrm{B}} T}{m_{\mathrm{eff}}} \frac{2\Gamma_{\mathrm{m}}}{(\Omega^2 - \Omega_{\mathrm{m}}^2)^2 + \Gamma_{\mathrm{m}}^2 \Omega^2}\,. \tag{A.3}$$

We also recall Eq. (4.4), which relates displacement spectral densities and frequency spectral densities via the optomechanical coupling rate g_0

$$S_{\omega\omega} = G^2 S_{\mathrm{xx}} \tag{A.4}$$

where $G = g_0/x_{\mathrm{zpf}}$.

Now we find for explicit integration of $S_{\mathrm{xx}}^{\mathrm{DS}}(\Omega)$ in the high-Q limit ($\Omega_{\mathrm{m}} >> \Gamma_{\mathrm{m}}$)

$$\int_{-\infty}^{+\infty} S_{\mathrm{xx}}^{\mathrm{DS}}(\Omega) \frac{d\Omega}{2\pi} = \frac{k_{\mathrm{B}} T}{m_{\mathrm{eff}}} \cdot \frac{1}{\Omega_{\mathrm{m}}^2} = S_{\mathrm{xx}}^{\mathrm{DS}}(\Omega_{\mathrm{m}}) \frac{\Gamma_{\mathrm{m}}}{2}\,. \tag{A.5}$$

Inserting into the definition of mean square frequency fluctuations from above

$$\langle \delta\omega^2 \rangle = \int_{-\infty}^{+\infty} S_{\omega\omega}^{\mathrm{DS}}(\Omega) \frac{d\Omega}{2\pi} = \int_{-\infty}^{+\infty} \frac{g_0^2}{x_{\mathrm{zpf}}^2} S_{\mathrm{xx}}^{\mathrm{DS}}(\Omega) = \frac{g_0^2}{x_{\mathrm{zpf}}^2} \frac{k_{\mathrm{B}} T}{m_{\mathrm{eff}}} \cdot \frac{1}{\Omega_{\mathrm{m}}^2} = 2 g_0^2 \bar{n}_{\mathrm{ph}} \tag{A.6}$$

where we use $x_{\mathrm{zpf}} = \sqrt{\hbar / 2 m_{\mathrm{eff}} \Omega_{\mathrm{m}}}$ and $\bar{n}_{\mathrm{ph}} \approx k_{\mathrm{B}} T / \hbar \Omega_{\mathrm{m}}$. The above expression was already found in Eq. (4.5) and is the main tool used to extract the single-photon coupling rate g_0 based on the measured mean square frequency fluctuations, i.e. the peak area of the mechanical signatures in the frequency spectral densities.

Single-sided spectra In the single-sided convention, spectral densities are defined such that the mean square fluctuations of a variable x are recovered by the integration of their spectral density $S_{\mathrm{xx}}^{\mathrm{SS}}$ over only positive frequencies, i.e.

$$\langle \delta x^2 \rangle = \int_0^{+\infty} S_{\mathrm{xx}}^{\mathrm{SS}}(\Omega) \frac{d\Omega}{2\pi} . \tag{A.7}$$

One advantage of this convention is that it recovers the familiar result of the classical equipartition theorem for the driving force spectral density exerted by a thermal bath of temperature T

$$S_{\mathrm{FF}}^{\mathrm{SS}}(\Omega) = 4 m_{\mathrm{eff}} \Gamma_{\mathrm{m}} k_{\mathrm{B}} T . \tag{A.8}$$

Based on the thermal force density, this definition alters also the thermal displacement spectral density of a mechanical oscillator to

$$S_{\mathrm{xx}}^{\mathrm{SS}}(\Omega) = |\chi_{\mathrm{m}}(\Omega)|^2 \, S_{\mathrm{FF}}^{\mathrm{SS}}(\Omega) \approx \frac{k_{\mathrm{B}} T}{m_{\mathrm{eff}}} \frac{4\Gamma_{\mathrm{m}}}{(\Omega^2 - \Omega_{\mathrm{m}}^2)^2 + \Gamma_{\mathrm{m}}^2 \Omega^2} . \tag{A.9}$$

Using the single-sided definitions, we find for explicit integration of $S_{\mathrm{xx}}^{\mathrm{SS}}(\Omega)$ in the high-Q limit ($\Omega_{\mathrm{m}} >> \Gamma_{\mathrm{m}}$)

$$\int_0^{+\infty} S_{\mathrm{xx}}^{\mathrm{SS}}(\Omega) \frac{d\Omega}{2\pi} = \frac{k_{\mathrm{B}} T}{m_{\mathrm{eff}}} \cdot \frac{1}{\Omega_{\mathrm{m}}^2} = S_{\mathrm{xx}}^{\mathrm{SS}}(\Omega_{\mathrm{m}}) \frac{\Gamma_{\mathrm{m}}}{4} . \tag{A.10}$$

Notably, the simplified relation between the integration result and the value on resonance differs from the double-sided convention, but the explicit result of integration remains equivalent, which also leads to a familiar result for the mean square frequency fluctuations

$$\langle \delta\omega^2 \rangle = \int_0^{+\infty} S_{\omega\omega}^{\mathrm{SS}}(\Omega) \frac{d\Omega}{2\pi} = \int_0^{+\infty} \frac{g_0^2}{x_{\mathrm{zpf}}^2} S_{\mathrm{xx}}^{\mathrm{SS}}(\Omega) = \frac{g_0^2}{x_{\mathrm{zpf}}^2} \frac{k_{\mathrm{B}} T}{m_{\mathrm{eff}}} \cdot \frac{1}{\Omega_{\mathrm{m}}^2} = 2 g_0^2 \bar{n}_{\mathrm{ph}} . \tag{A.11}$$

Clearly, if the expressions are adapted consistently, both conventions arrive at the same expression that links the mean square frequency fluctuations to the opto-mechanical vacuum coupling rate.

However, a second pitfall presents itself in the handling of acquired experimental data. To generate valid results for g_0 with the frequency noise calibration it is crucial to understand the nature of the spectra that are acquired and use the corresponding models to fit and describe them.

Homodyne detection As discussed in 4.2.3, most commercial spectrum analysers display single-sided spectra. Therefore, in the case of homodyne detection, negative frequency components are folded onto the positive frequency space and effectively lead to a multiplication of the resulting spectral density by 2. This effect is included in the

single-sided displacement spectral density $S_{\mathrm{xx}}^{\mathrm{SS}}$.
To generate valid results, the experimental spectra have to be fitted with Eq. (A.9) and processed using the formulas described above under **single-sided spectra**. Fitting a single-sided spectrum with the displacement spectral density of a double-sided spectrum will effectively lead to a multiplication of the extracted $\langle \delta\omega^2 \rangle$ by a factor of 2 and an overestimation of the optomechanical coupling rate g_0. Numerical integration of the measured spectra can be used as an alternative to fits. In this case, it is important to remember that the entire signal is already represented in the positive frequency space and in a single peak area and does not need to be multiplied or otherwise modified any further.

Heterodyne detection In the case of heterodyne detection, commercial spectrum analyzers will still display single-sided spectra and fold negative frequency components onto the positive frequency space. However, due to the heterodyne detection, the symmetry of the displacement spectral density is broken, and no overlap and multiplication of the signals takes place. Accordingly, the measured spectral density effectively presents like the positive frequency range of a double-sided spectrum and must be fitted with Eq. (A.3) and processed using the formulas described above under **double-sided spectra**. Doing otherwise will lead to half of the frequency fluctuations being discarded and the optomechanical coupling rate being underestimated. In the case of numerical integration, one must be aware that integrating the measured spectral density around a single peak will only encompass half of the real fluctuations. For example, if one numerically integrates 100 linewidths around a peak of a spectrum acquired by heterodyne detection

$$\int_{\Omega_\mathrm{m}-100\Gamma_\mathrm{m}}^{\Omega_\mathrm{m}+100\Gamma_\mathrm{m}} S_{\omega\omega}(\Omega)\frac{d\Omega}{2\pi} \approx \frac{\langle \delta\omega^2 \rangle}{2}\,, \tag{A.12}$$

under the assumption that the underlying spectrum is perfectly symmetrical.

A.3 Geometric and kinetic inductance of a mechanically compliant SQUID

In the following we will present the necessary equations and variables to calculate the geometric and kinetic inductance contributions of a mechanically compliant SQUID.

Kinetic Inductance The kinetic inductance of our SQUID design is dominated by the constrictions that the thin and long nanostring oscillators present. The nanostrings can be approximated as nanoinductors in the *dirty limit* (mean free path much smaller than the superconducting coherence length) with a kinetic inductance following [263]

$$L_{\mathrm{kin}} = \frac{\hbar \rho_{\mathrm{n}} \ell}{\pi \Delta_0 w t}\,. \tag{A.13}$$

In the above equation, ρ_{n} and Δ_0 are the superconductor's normal state resistivity and energy gap at zero temperature, respectively, and w, t, and ℓ describe the nanostring geometry as introduced in Sec. 2.2.1. With the input parameters $(w, t, \ell) = (0.2, 0.11, 30)\,\mu\mathrm{m}$, $\rho_{\mathrm{n}} = 2.82 \times 10^{-3}\,\Omega\,\mathrm{m}$ [264], and $\Delta_0 = 0.18\,\mathrm{meV}$ [91], we calculate a kinetic inductance of 45 pH for a single nanostring. As the SQUID loop contains two identical strings, its total kinetic inductance is $L_{\mathrm{kin}} = 90\,\mathrm{pH}$. Note that, by definition, the kinetic inductance of the SQUID is simply the sum of these contributions. The exact geometry of the SQUID loop, which for example leads to a reduction of parallel inductances, is considered separately (cf. Eq. (2.61)).

Geometric Inductance The geometric contribution to the inductance of the SQUID loop can be modeled using the classical theory of self inductance of a round conducting wire forming a rectangular loop [265]

$$\begin{aligned} L_{\mathrm{geo}} = \left(\frac{\mu_0}{\pi}\right) \Bigg[&-2(W+H) + 2\sqrt{H^2+W^2} - H \ln\left(\frac{H + \sqrt{H^2+W^2}}{W}\right) \\ &- W \ln\left(\frac{W + \sqrt{H^2+W^2}}{H}\right) + H \ln\left(\frac{2H}{d/2}\right) + W \ln\left(\frac{2W}{d/2}\right) \Bigg] \end{aligned} \tag{A.14}$$

Here, W and H are the width and height of the loop, respectively, and d is the diameter of the conducting wire. To approximate the nanostring as a round wire, we use $d = \sqrt{t^2 + w^2}$. Using $W = 24.24\,\mu\mathrm{m}$ and $H = 1.97\,\mu\mathrm{m}$ from our design together with the string geometry from above, we calculate $L_{\mathrm{geo}} = 46\,\mathrm{pH}$. Alternatively, the geometric inductance can be calculated using FEM electromagnetic simulations. We find good agreement between the value calculated with the above equation and a simulation performed with *Ansys Electronics Desktop*. Curiously, we find that using common formulas that specifically focus on loops of *rectangular* wires does not agree with the results of the above equation or the FEM simulation and instead significantly overestimates the geometric inductance of the loop. It appears plausible that the model based on round wires provides a more realistic approximation at the very high aspect ratios of nanometer cross-sections versus micrometer lengths.

Overall the calculations result in a loop inductance of the mechanically compliant SQUID of

$$L_{\mathrm{loop}} = L_{\mathrm{kin}} + L_{\mathrm{geo}} = 136\,\mathrm{pH}\,. \tag{A.15}$$

Bibliography

[1] A. Einstein, B. Podolsky, and N. Rosen, "Can Quantum-Mechanical Description of Physical Reality Be Considered Complete?" Phys. Rev. **47**, 777 (1935) `10.1103/PhysRev.47.777`.

[2] E. Schrödinger, "Die gegenwärtige Situation in der Quantenmechanik," Naturwissenschaften **23**, 807 (1935) `10.1007/BF01491891`.

[3] J. S. Bell, "On the Einstein Podolsky Rosen paradox," Physics Physique Fizika **1**, 195 (1964) `10.1103/PhysicsPhysiqueFizika.1.195`.

[4] F. Hund, "Zur Deutung der Molekelspektren. III.," Z. Physik **43**, 805 (1927) `10.1007/BF01397249`.

[5] P. C. Lauterbur, "Image Formation by Induced Local Interactions: Examples Employing Nuclear Magnetic Resonance," Nature **242**, 190 (1973) `10.1038/242190a0`.

[6] A. Filler, "MR Neurography and Diffusion Tensor Imaging: Origins, History & Clinical Impact of the first 50,000 cases with an Assessment of Efficacy and Utility in a Prospective 5,000 Patient Study Group," Neurosurgery **65**, A29 (2009) `10.1227/01.NEU.0000351279.78110.00`.

[7] J. Canales, "Navigating the history of GPS," Nat. Electron. **1**, 610 (2018) `10.1038/s41928-018-0187-9`.

[8] R. P. Feynman, "Simulating physics with computers," Int. J. Theor. Phys. **21**, 467 (1982) `10.1007/BF02650179`.

[9] "40 years of quantum computing," Nat. Rev. Phys. **4**, 1 (2022) `10.1038/s42254-021-00410-6`.

[10] P. W. Shor, "Polynomial-time algorithms for prime factorization and discrete logarithms on a quantum computer," SIAM J. Comput. **26**, 1484 (1997) `10.1137/S0097539795293172`.

[11] A. J. Leggett, "Testing the limits of quantum mechanics: motivation, state of play, prospects," J. Phys.: Condens. Matter **14**, R415 (2002) `10.1088/0953-8984/14/15/201`.

[12] H. Everett III, "The theory of the universal wave function," Ph.D. Thesis (Princeton University, 1956).

[13] B. S. DeWitt, "Quantum mechanics and reality," Physics Today **23**, 30 (1970) `10.1063/1.3022331`.

[14] M. Schlosshauer, J. Kofler, and A. Zeilinger, "A snapshot of foundational attitudes toward quantum mechanics," Stud. Hist. Philos. Sci. A **44**, 222 (2013) `10.1016/j.shpsb.2013.04.004`.

[15] W. H. Zurek, "Decoherence, einselection, and the quantum origins of the classical," Rev. Mod. Phys. **75**, 715 (2003) `10.1103/RevModPhys.75.715`.

[16] G. Jaeger, “What in the (quantum) world is macroscopic?” Am. J. Phys. **82**, 896 (2014) `10.1119/1.4878358`.

[17] F. Karolyhazy, “Gravitation and quantum mechanics of macroscopic objects,” Nuovo Cimento A (1965-1970) **42**, 390 (1966) `10.1007/BF02717926`.

[18] L. Diósi, “Gravitation and quantum-mechanical localization of macro-objects,” Physics Letters A **105**, 199 (1984) `10.1016/0375-9601(84)90397-9`.

[19] S. L. Adler and A. Bassi, “Is Quantum Theory Exact?” Science **325**, 275 (2009) `10.1126/science.1176858`.

[20] M. Aspelmeyer, “New Frontiers in Quantum Optomechanics: from levitation to gravitation,” in Front. Opt. 2016 2016 Pap. FF3D1 (2016), FF3D.1, `10.1364/FIO.2016.FF3D.1`.

[21] R. Kaltenbaek, M. Arndt, M. Aspelmeyer, et al., “Research campaign: Macroscopic quantum resonators (MAQRO),” Quantum Sci. Technol. **8**, 014006 (2023) `10.1088/2058-9565/aca3cd`.

[22] M. Aspelmeyer, T. J. Kippenberg, and F. Marquardt, “Cavity optomechanics,” Rev. Mod. Phys. **86**, 1391 (2014) `10.1103/RevModPhys.86.1391`.

[23] S. G. Hofer and K. Hammerer, in *Advances In Atomic, Molecular, and Optical Physics*, Vol. 66, edited by E. Arimondo, C. C. Lin, and S. F. Yelin (Academic Press, 2017), pp. 263–374, `10.1016/bs.aamop.2017.03.003`.

[24] S. Barzanjeh, A. Xuereb, S. Gröblacher, et al., “Optomechanics for quantum technologies,” Nat. Phys. **18**, 15 (2022) `10.1038/s41567-021-01402-0`.

[25] K. W. Murch, K. L. Moore, S. Gupta, and D. M. Stamper-Kurn, “Observation of quantum-measurement backaction with an ultracold atomic gas,” Nat. Phys. **4**, 561 (2008) `10.1038/nphys965`.

[26] N. Brahms, T. Botter, S. Schreppler, D. W. C. Brooks, and D. M. Stamper-Kurn, “Optical Detection of the Quantization of Collective Atomic Motion,” Phys. Rev. Lett. **108**, 133601 (2012) `10.1103/PhysRevLett.108.133601`.

[27] C. Whittle, E. D. Hall, S. Dwyer, et al., “Approaching the motional ground state of a 10-kg object,” Science **372**, 1333 (2021) `10.1126/science.abh2634`.

[28] B. P. Abbott et al., “Observation of Gravitational Waves from a Binary Black Hole Merger,” Phys. Rev. Lett. **116**, 061102 (2016) `10.1103/PhysRevLett.116.061102`.

[29] A. Naik, O. Buu, M. D. LaHaye, et al., “Cooling a nanomechanical resonator with quantum back-action,” Nature **443**, 193 (2006) `10.1038/nature05027`.

[30] C. A. Regal, J. D. Teufel, and K. W. Lehnert, “Measuring nanomechanical motion with a microwave cavity interferometer,” Nat. Phys. **4**, 555 (2008) `10.1038/nphys974`.

[31] J. D. Teufel, J. W. Harlow, C. A. Regal, and K. W. Lehnert, “Dynamical Backaction of Microwave Fields on a Nanomechanical Oscillator,” Phys. Rev. Lett. **101**, 197203 (2008) `10.1103/PhysRevLett.101.197203`.

[32] J. D. Teufel, D. Li, M. S. Allman, et al., “Circuit cavity electromechanics in the strong-coupling regime,” Nature **471**, 204 (2011) `10.1038/nature09898`.

[33] T. A. Palomaki, J. D. Teufel, R. W. Simmonds, and K. W. Lehnert, “Entangling mechanical motion with microwave fields,” Science **342**, 710 (2013) `10.1126/science.1244563`.

[34] S. Kotler, G. A. Peterson, E. Shojaee, et al., “Direct observation of deterministic macroscopic entanglement,” Science **372**, 622 (2021) `10.1126/science.abf2998`.

[35] M. P. Blencowe and E. Buks, “Quantum analysis of a linear dc SQUID mechanical displacement detector,” Phys. Rev. B **76**, 014511 (2007) `10.1103/PhysRevB.76.014511`.

[36] E. Buks, S. Zaitsev, E. Segev, B. Abdo, and M. P. Blencowe, “Displacement detection with a vibrating rf superconducting interference device: Beating the standard linear limit,” Phys. Rev. E **76**, 026217 (2007) `10.1103/PhysRevE.76.026217`.

[37] P. D. Nation, J. Suh, and M. P. Blencowe, “Ultrastrong optomechanics incorporating the dynamical Casimir effect,” Phys. Rev. A **93**, 022510 (2016) `10.1103/PhysRevA.93.022510`.

[38] O. Shevchuk, G. A. Steele, and Ya. M. Blanter, “Strong and tunable couplings in flux-mediated optomechanics,” Phys. Rev. B **96**, 014508 (2017) `10.1103/PhysRevB.96.014508`.

[39] A. P. Reed, K. H. Mayer, J. D. Teufel, et al., “Faithful conversion of propagating quantum information to mechanical motion,” Nat. Phys. **13**, 1163 (2017) `10.1038/nphys4251`.

[40] A. Nunnenkamp, K. Børkje, and S. M. Girvin, “Single-Photon Optomechanics,” Phys. Rev. Lett. **107**, 063602 (2011) `10.1103/PhysRevLett.107.063602`.

[41] M. Ludwig, B. Kubala, and F. Marquardt, “The optomechanical instability in the quantum regime,” New J. Phys. **10**, 095013 (2008) `10.1088/1367-2630/10/9/095013`.

[42] U. Akram, W. P. Bowen, and G. J. Milburn, “Entangled mechanical cat states via conditional single photon optomechanics,” New J. Phys. **15**, 093007 (2013) `10.1088/1367-2630/15/9/093007`.

[43] J. Qian, A. A. Clerk, K. Hammerer, and F. Marquardt, “Quantum Signatures of the Optomechanical Instability,” Phys. Rev. Lett. **109**, 253601 (2012) `10.1103/PhysRevLett.109.253601`.

[44] P. Rabl, “Photon Blockade Effect in Optomechanical Systems,” Phys. Rev. Lett. **107**, 063601 (2011) `10.1103/PhysRevLett.107.063601`.

[45] R. Manenti, A. F. Kockum, A. Patterson, et al., “Circuit quantum acoustodynamics with surface acoustic waves,” Nat. Commun. **8**, 975 (2017) `10.1038/s41467-017-01063-9`.

[46] Y. Chu, P. Kharel, W. H. Renninger, et al., “Quantum acoustics with superconducting qubits,” Science **358**, 199 (2017) `10.1126/science.aao1511`.

[47] M. Bild, M. Fadel, Y. Yang, et al., “Schrödinger cat states of a 16-microgram mechanical oscillator,” Science **380**, 274 (2023) `10.1126/science.adf7553`.

[48] A. D. OConnell, M. Hofheinz, M. Ansmann, et al., “Quantum ground state and single-phonon control of a mechanical resonator,” Nature **464**, 697 (2010) `10.1038/nature08967`.

[49] C. T. Hann, C.-L. Zou, Y. Zhang, et al., “Hardware-Efficient Quantum Random Access Memory with Hybrid Quantum Acoustic Systems,” Phys. Rev. Lett. **123**, 250501 (2019) `10.1103/PhysRevLett.123.250501`.

[50] K. J. Satzinger, Y. P. Zhong, H.-S. Chang, et al., “Quantum control of surface acoustic-wave phonons,” Nature **563**, 661 (2018) `10.1038/s41586-018-0719-5`.

[51] A. Bienfait, K. J. Satzinger, Y. P. Zhong, et al., “Phonon-mediated quantum state transfer and remote qubit entanglement,” Science **364**, 368 (2019) `10.1126/science.aaw8415`.

[52] A. Frisk Kockum, P. Delsing, and G. Johansson, “Designing frequency-dependent relaxation rates and Lamb shifts for a giant artificial atom,” Phys. Rev. A **90**, 013837 (2014) `10.1103/PhysRevA.90.013837`.

[53] T. Aref, P. Delsing, M. K. Ekström, et al., in *Superconducting Devices in Quantum Optics*, edited by R. H. Hadfield and G. Johansson, Quantum Science and Technology (Springer International Publishing, Cham, 2016), pp. 217–244, `10.1007/978-3-319-24091-6_9`.

[54] G. Andersson, B. Suri, L. Guo, T. Aref, and P. Delsing, “Non-exponential decay of a giant artificial atom,” Nat. Phys. **15**, 1123 (2019) `10.1038/s41567-019-0605-6`.

[55] L. Guo, A. F. Kockum, F. Marquardt, and G. Johansson, “Oscillating bound states for a giant atom,” Phys. Rev. Res. **2**, 043014 (2020) `10.1103/PhysRevResearch.2.043014`.

[56] I. C. Rodrigues, D. Bothner, and G. A. Steele, “Coupling microwave photons to a mechanical resonator using quantum interference,” Nat. Commun. **10**, 5359 (2019) `10.1038/s41467-019-12964-2`.

[57] P. Schmidt, M. T. Amawi, S. Pogorzalek, et al., “Sideband-resolved resonator electromechanics based on a nonlinear Josephson inductance probed on the single-photon level,” Commun. Phys. **3**, 233 (2020) `10.1038/s42005-020-00501-3`.

[58] D. Zoepfl, M. L. Juan, C. M. F. Schneider, and G. Kirchmair, “Single-Photon Cooling in Microwave Magnetomechanics,” Phys. Rev. Lett. **125**, 023601 (2020) `10.1103/PhysRevLett.125.023601`.

[59] T. Bera, S. Majumder, S. K. Sahu, and V. Singh, “Large flux-mediated coupling in hybrid electromechanical system with a transmon qubit,” Commun. Phys. **4**, 12 (2021) `10.1038/s42005-020-00514-y`.

[60] P. A. M. Dirac, *The Principles of Quantum Mechanics* (Clarendon Press, Oxford, 1981).

[61] E. I. Green, “The Story of Q,” Am. Sci. **43**, 584 (1955).

[62] A. V. Bakshi and U. A. Bakshi, *Network Analysis* (Technical Publications, Pune, 2006).

[63] U. Vool and M. Devoret, “Introduction to quantum electromagnetic circuits,” Int. J. Circuit Theory Appl. **45**, 897 (2017) `10.1002/cta.2359`.

[64] A. Blais, A. L. Grimsmo, S. M. Girvin, and A. Wallraff, “Circuit quantum electrodynamics,” Rev. Mod. Phys. **93**, 025005 (2021) `10.1103/RevModPhys.93.025005`.

[65] S. Timoshenko, *Vibration problems in engineering* (D. Van Nostrand Company, Inc., New York, 1937).

[66] F. J. Hocke, "Microwave circuit-electromechanics in a nanomechanical hybrid system," Ph.D. Thesis (Walther-Meissner-Institut and Technische Universität München, München, 2013).

[67] K. D. Sattler, (Ed.), *Handbook of nanophysics: Functional nanomaterials* (CRC Press Taylor & Francis Group, Boca Raton, 2011).

[68] M. Pernpeintner, "Nanomechanical hybrid systems," Ph.D. Thesis (Walther-Meissner-Institut and Technische Universität München, München, 2016).

[69] S. S. Verbridge, J. M. Parpia, R. B. Reichenbach, L. M. Bellan, and H. G. Craighead, "High quality factor resonance at room temperature with nanostrings under high tensile stress," J. Appl. Phys. **99**, 124304 (2006) `10.1063/1.2204829`.

[70] A. N. Cleland, *Foundations of Nanomechanics* (Springer, Berlin, Heidelberg, 2003), `10.1007/978-3-662-05287-7`.

[71] H. B. Callen and T. A. Welton, "Irreversibility and Generalized Noise," Phys. Rev. **83**, 34 (1951) `10.1103/PhysRev.83.34`.

[72] L. Boltzmann, "Einige allgemeine Sätze über Wärmegleichgewicht," Wien. Berichte **63**, 679 (1871).

[73] P. R. Saulson, "Thermal noise in mechanical experiments," Phys. Rev. D **42**, 2437 (1990) `10.1103/PhysRevD.42.2437`.

[74] A. A. Clerk, M. H. Devoret, S. M. Girvin, F. Marquardt, and R. J. Schoelkopf, "Introduction to quantum noise, measurement, and amplification," Rev. Mod. Phys. **82**, 1155 (2010) `10.1103/RevModPhys.82.1155`.

[75] M. L. Gorodetsky, A. Schliesser, G. Anetsberger, S. Deleglise, and T. J. Kippenberg, "Determination of the vacuum optomechanical coupling rate using frequency noise calibration," Opt. Express **18**, 23236 (2010) `10.1364/OE.18.023236`.

[76] N. T. Bronn, Y. Liu, J. B. Hertzberg, et al., "Broadband filters for abatement of spontaneous emission in circuit quantum electrodynamics," Appl. Phys. Lett. **107**, 172601 (2015) `10.1063/1.4934867`.

[77] D. I. Schuster, A. Wallraff, A. Blais, et al., "Ac Stark Shift and Dephasing of a Superconducting Qubit Strongly Coupled to a Cavity Field," Phys. Rev. Lett. **94**, 123602 (2005) `10.1103/PhysRevLett.94.123602`.

[78] M. Hofheinz, H. Wang, M. Ansmann, et al., "Synthesizing arbitrary quantum states in a superconducting resonator," Nature **459**, 546 (2009) `10.1038/nature08005`.

[79] D. M. Pozar, *Microwave engineering*, 4th ed (Wiley, Hoboken, NJ, 2012).

[80] C. R. H. McRae, H. Wang, J. Gao, et al., "Materials loss measurements using superconducting microwave resonators," Rev. Sci. Instrum. **91**, 091101 (2020) `10.1063/5.0017378`.

[81] R. N. Simons, *Coplanar Waveguide Circuits, Components, and Systems*, red. by K. Chang, Wiley Series in Microwave and Optical Engineering (John Wiley & Sons, Inc., New York, USA, 2001), `10.1002/0471224758`.

[82] S. Gevorgian, L. Linner, and E. Kollberg, “CAD models for shielded multilayered CPW,” IEEE Trans. Microwave Theory Techn. **43**, 772 (1995) `10.1109/22.375223`.

[83] E. Chen and S. Chou, “Characteristics of coplanar transmission lines on multilayer substrates: modeling and experiments,” IEEE Trans. Microw. Theory Tech. **45**, 939 (1997) `10.1109/22.588606`.

[84] M. Göppl, A. Fragner, M. Baur, et al., “Coplanar waveguide resonators for circuit quantum electrodynamics,” J. Appl. Phys. **104**, 113904 (2008) `10.1063/1.3010859`.

[85] D. P. Pappas, M. R. Vissers, D. S. Wisbey, J. S. Kline, and J. Gao, “Two Level System Loss in Superconducting Microwave Resonators,” IEEE Trans. Appl. Supercond. **21**, 871 (2011) `10.1109/TASC.2010.2097578`.

[86] J. Gao, M. Daal, J. M. Martinis, et al., “A semiempirical model for two-level system noise in superconducting microresonators,” Appl. Phys. Lett. **92**, 212504 (2008) `10.1063/1.2937855`.

[87] S. Probst, F. B. Song, P. A. Bushev, A. V. Ustinov, and M. Weides, “Efficient and robust analysis of complex scattering data under noise in microwave resonators,” Rev. Sci. Instrum. **86**, 024706 (2015) `10.1063/1.4907935`.

[88] B. D. Josephson, “Possible new effects in superconductive tunnelling,” Physics Letters **1**, 251 (1962) `10.1016/0031-9163(62)91369-0`.

[89] P. W. Anderson and J. M. Rowell, “Probable Observation of the Josephson Superconducting Tunneling Effect,” Phys. Rev. Lett. **10**, 230 (1963) `10.1103/PhysRevLett.10.230`.

[90] M. Hermele, G. Refael, M. P. A. Fisher, and P. M. Goldbart, “Fate of the Josephson effect in thin-film superconductors,” Nat. Phys. **1**, 117 (2005) `10.1038/nphys154`.

[91] M. Tinkham, *Introduction to Superconductivity* (Dover Publications, Inc., Mineola, New York, 2004).

[92] R. Gross and A. Marx, *Festkörperphysik* (De Gruyter, Oldenbourg, 2018).

[93] R. Kleiner, D. Koelle, F. Ludwig, and J. Clarke, “Superconducting quantum interference devices: State of the art and applications,” Proc. IEEE **92**, 1534 (2004) `10.1109/JPROC.2004.833655`.

[94] P. Rembold, N. Oshnik, M. M. Müller, et al., “Introduction to quantum optimal control for quantum sensing with nitrogen-vacancy centers in diamond,” AVS Quantum Science **2**, 024701 (2020) `10.1116/5.0006785`.

[95] E. M. Levenson-Falk, R. Vijay, N. Antler, and I. Siddiqi, “A dispersive nanoSQUID magnetometer for ultra-low noise, high bandwidth flux detection,” Supercond. Sci. Technol. **26**, 055015 (2013) `10.1088/0953-2048/26/5/055015`.

[96] A. I. Braginski and J. Clarke, in *The SQUID Handbook* (Wiley VCH, Weinheim, 2005), pp. 1–28, `10.1002/3527603646.ch1`.

[97] B. Chesca, R. Kleiner, and D. Koelle, in *The SQUID Handbook* (Wiley VCH, Weinheim, 2005), pp. 29–92, `10.1002/3527603646.ch2`.

[98] J. A. B. Mates, G. C. Hilton, K. D. Irwin, L. R. Vale, and K. W. Lehnert, “Demonstration of a multiplexer of dissipationless superconducting quantum interference devices,” Appl. Phys. Lett. **92**, 023514 (2008) `10.1063/1.2803852`.

[99] M. Hatridge, R. Vijay, D. H. Slichter, J. Clarke, and I. Siddiqi, “Dispersive magnetometry with a quantum limited SQUID parametric amplifier,” Phys. Rev. B **83**, 134501 (2011) `10.1103/PhysRevB.83.134501`.

[100] B. Abdo, F. Schackert, M. Hatridge, C. Rigetti, and M. Devoret, “Josephson amplifier for qubit readout,” Appl. Phys. Lett. **99**, 162506 (2011) `10.1063/1.3653473`.

[101] M. Wallquist, V. S. Shumeiko, and G. Wendin, “Selective coupling of superconducting charge qubits mediated by a tunable stripline cavity,” Phys. Rev. B **74**, 224506 (2006) `10.1103/PhysRevB.74.224506`.

[102] C. Eichler, Y. Salathe, J. Mlynek, S. Schmidt, and A. Wallraff, “Quantum-Limited Amplification and Entanglement in Coupled Nonlinear Resonators,” Phys. Rev. Lett. **113**, 110502 (2014) `10.1103/PhysRevLett.113.110502`.

[103] S. E. Nigg, H. Paik, B. Vlastakis, et al., “Black-Box Superconducting Circuit Quantization,” Phys. Rev. Lett. **108**, 240502 (2012) `10.1103/PhysRevLett.108.240502`.

[104] J. Bourassa, F. Beaudoin, J. M. Gambetta, and A. Blais, “Josephson-junction-embedded transmission-line resonators: From Kerr medium to in-line transmon,” Phys. Rev. A **86**, 013814 (2012) `10.1103/PhysRevA.86.013814`.

[105] S. Pogorzalek, K. G. Fedorov, L. Zhong, et al., “Hysteretic Flux Response and Nondegenerate Gain of Flux-Driven Josephson Parametric Amplifiers,” Phys. Rev. Appl. **8**, 024012 (2017) `10.1103/PhysRevApplied.8.024012`.

[106] P. Bhupathi, P. Groszkowski, M. P. DeFeo, et al., “Transient Dynamics of a Superconducting Nonlinear Oscillator,” Phys. Rev. Appl. **5**, 024002 (2016) `10.1103/PhysRevApplied.5.024002`.

[107] N. Imoto, H. A. Haus, and Y. Yamamoto, “Quantum nondemolition measurement of the photon number via the optical Kerr effect,” Phys. Rev. A **32**, 2287 (1985) `10.1103/PhysRevA.32.2287`.

[108] G. Kirchmair, B. Vlastakis, Z. Leghtas, et al., “Observation of quantum state collapse and revival due to the single-photon Kerr effect,” Nature **495**, 205 (2013) `10.1038/nature11902`.

[109] B. Yurke and E. Buks, “Performance of Cavity-Parametric Amplifiers, Employing Kerr Nonlinearites, in the Presence of Two-Photon Loss,” J. Lightwave Technol., JLT **24**, 5054 (2006).

[110] C. Laflamme and A. A. Clerk, “Quantum-limited amplification with a nonlinear cavity detector,” Phys. Rev. A **83**, 033803 (2011) `10.1103/PhysRevA.83.033803`.

[111] C. W. Gardiner and M. J. Collett, “Input and output in damped quantum systems: Quantum stochastic differential equations and the master equation,” Phys. Rev. A **31**, 3761 (1985) `10.1103/PhysRevA.31.3761`.

[112] D. Zöpfl, “Demonstration of nonlinear enhanced backaction cooling in microwave magnetomechanics,” Ph.D. Thesis (Universität Innsbruck, Innsbruck, 2022).

[113] M. J. Collett and C. W. Gardiner, “Squeezing of intracavity and traveling-wave light fields produced in parametric amplification,” Phys. Rev. A **30**, 1386 (1984) `10.1103/PhysRevA.30.1386`.

[114] D. Rugar and P. Grütter, "Mechanical parametric amplification and thermomechanical noise squeezing," Phys. Rev. Lett. **67**, 699 (1991) `10.1103/PhysRevLett.67.699`.

[115] F. J. Hyde, "Analysis of parametric amplifiers incorporating varactor diodes," Proc. Inst. Electr. Eng. **110**, 1313 (1963) `10.1049/piee.1963.0187`.

[116] A. Roy and M. Devoret, "Introduction to parametric amplification of quantum signals with Josephson circuits," C. R. Phys. **17**, 740 (2016) `10.1016/j.crhy.2016.07.012`.

[117] T. Yamamoto, K. Inomata, M. Watanabe, et al., "Flux-driven Josephson parametric amplifier," Appl. Phys. Lett. **93**, 042510 (2008) `10.1063/1.2964182`.

[118] Y. Yamamoto and K. Semba, *Principles and Methods of Quantum Information Technologies*, 1st ed. 2016 Edition (Springer, Heidelberg, 2015).

[119] B. Yurke, L. R. Corruccini, P. G. Kaminsky, et al., "Observation of parametric amplification and deamplification in a Josephson parametric amplifier," Phys. Rev. A **39**, 2519 (1989) `10.1103/PhysRevA.39.2519`.

[120] F. Lecocq, L. Ranzani, G. Peterson, et al., "Microwave Measurement beyond the Quantum Limit with a Nonreciprocal Amplifier," Phys. Rev. Appl. **13**, 044005 (2020) `10.1103/PhysRevApplied.13.044005`.

[121] R. Vijay, D. H. Slichter, and I. Siddiqi, "Observation of Quantum Jumps in a Superconducting Artificial Atom," Phys. Rev. Lett. **106**, 110502 (2011) `10.1103/PhysRevLett.106.110502`.

[122] D. Ristè, C. C. Bultink, K. W. Lehnert, and L. DiCarlo, "Feedback Control of a Solid-State Qubit Using High-Fidelity Projective Measurement," Phys. Rev. Lett. **109**, 240502 (2012) `10.1103/PhysRevLett.109.240502`.

[123] D. Sarchi, I. Carusotto, M. Wouters, and V. Savona, "Coherent dynamics and parametric instabilities of microcavity polaritons in double-well systems," Phys. Rev. B **77**, 125324 (2008) `10.1103/PhysRevB.77.125324`.

[124] C. Eichler and A. Wallraff, "Controlling the dynamic range of a Josephson parametric amplifier," EPJ Quantum Technol. **1**, 2 (2014) `10.1140/epjqt2`.

[125] P. Winkel, I. Takmakov, D. Rieger, et al., "Nondegenerate Parametric Amplifiers Based on Dispersion-Engineered Josephson-Junction Arrays," Phys. Rev. Appl. **13**, 024015 (2020) `10.1103/PhysRevApplied.13.024015`.

[126] C. K. Law, "Interaction between a moving mirror and radiation pressure: A Hamiltonian formulation," Phys. Rev. A **51**, 2537 (1995) `10.1103/PhysRevA.51.2537`.

[127] M. Pinard, Y. Hadjar, and A. Heidmann, "Effective mass in quantum effects of radiation pressure," Eur. Phys. J. D **7**, 107 (1999) `10.1007/s100530050354`.

[128] F. Diedrich, J. C. Bergquist, W. M. Itano, and D. J. Wineland, "Laser Cooling to the Zero-Point Energy of Motion," Phys. Rev. Lett. **62**, 403 (1989) `10.1103/PhysRevLett.62.403`.

[129] J. D. Teufel, T. Donner, D. Li, et al., "Sideband cooling of micromechanical motion to the quantum ground state," Nature **475**, 359 (2011) `10.1038/nature10261`.

[130] F. Brennecke, S. Ritter, T. Donner, and T. Esslinger, "Cavity Optomechanics with a Bose-Einstein Condensate," Science **322**, 235 (2008) `10.1126/science.1163218`.

[131] P. D. Nation, M. P. Blencowe, and E. Buks, "Quantum analysis of a nonlinear microwave cavity-embedded dc SQUID displacement detector," Phys. Rev. B **78**, 104516 (2008) `10.1103/PhysRevB.78.104516`.

[132] S. Etaki, M. Poot, I. Mahboob, et al., "Motion detection of a micromechanical resonator embedded in a d.c. SQUID," Nat. Phys. **4**, 785 (2008) `10.1038/nphys1057`.

[133] N. Diaz-Naufal, D. Zoepfl, M. L. Juan, et al., "[Manuscript in preparation]," (2024).

[134] L. Rayleigh, "On Waves Propagated along the Plane Surface of an Elastic Solid," Proc. Lond. Math. Soc. **s1-17**, 4 (1885) `10.1112/plms/s1-17.1.4`.

[135] J. H. Collins and P. M. Grant, "The role of surface acoustic wave technology in communication systems," Ultrasonics **10**, 59 (1972) `10.1016/0041-624X(72)90249-1`.

[136] C. C. W. Ruppel, "Acoustic Wave Filter TechnologyA Review," IEEE Trans. Ultrason. Ferroelectr. Freq. Control **64**, 1390 (2017) `10.1109/TUFFC.2017.2690905`.

[137] S. Datta, *Surface Acoustic Wave Devices* (Prentice Hall, Englewood Cliffs, 1986).

[138] G. W. Farnell and E. L. Adler, in *Physical Acoustics*, Vol. 9, edited by W. P. Mason and R. N. Thurston (Academic Press, New York and London, 1972), pp. 35–127, `10.1016/B978-0-12-395670-5.50007-6`.

[139] D. Morgan, *Surface Acoustic Wave Filters, 2nd Edition*, 2nd ed. (Academic Press, Amsterdam, 2010).

[140] S. H. Simon, "Coupling of surface acoustic waves to a two-dimensional electron gas," Phys. Rev. B **54**, 13878 (1996) `10.1103/PhysRevB.54.13878`.

[141] E. Adler, "Matrix methods applied to acoustic waves in multilayers," IEEE Trans. Ultrason. Ferroelectr. Freq. Control **37**, 485 (1990) `10.1109/58.63103`.

[142] *COMSOL Multiphysics v. 5.5.* Stockholm, Sweden: COMSOL AB, 2022.

[143] A. Jung, "Development of Surface Acoustic Wave Resonators Based on Thin-Film Lithium Niobate for Circuit Quantum Acoustics Platforms," Master's thesis (Walther-Meissner-Institut and Technische Universität München, München, 2022).

[144] R. Igreja and C. J. Dias, "Analytical evaluation of the interdigital electrodes capacitance for a multi-layered structure," Sensors and Actuators A: Physical **112**, 291 (2004) `10.1016/j.sna.2004.01.040`.

[145] R. Manenti, "Circuit quantum acoustodynamics with surface acoustic waves," Ph.D. Thesis (University of Oxford, Oxford, 2017).

[146] R. Barends, H. L. Hortensius, T. Zijlstra, et al., "Contribution of dielectrics to frequency and noise of NbTiN superconducting resonators," Appl. Phys. Lett. **92**, 223502 (2008) `10.1063/1.2937837`.

[147] P. Macha, S. H. W. van der Ploeg, G. Oelsner, et al., "Losses in coplanar waveguide resonators at millikelvin temperatures," Appl. Phys. Lett. **96**, 062503 (2010) `10.1063/1.3309754`.

[148] P. W. Anderson, B. I. Halperin, and c. M. Varma, "Anomalous low-temperature thermal properties of glasses and spin glasses," Philos. Mag. J. Theor. Exp. Appl. Phys. **25**, 1 (1972) `10.1080/14786437208229210`.

[149] W. A. Phillips, "Two-level states in glasses," Rep. Prog. Phys. **50**, 1657 (1987) `10.1088/0034-4885/50/12/003`.

[150] C. Müller, J. H. Cole, and J. Lisenfeld, "Towards understanding two-level-systems in amorphous solids: insights from quantum circuits," Rep. Prog. Phys. **82**, 124501 (2019) `10.1088/1361-6633/ab3a7e`.

[151] R. Manenti, M. J. Peterer, A. Nersisyan, et al., "Surface acoustic wave resonators in the quantum regime," Phys. Rev. B **93**, 041411 (2016) `10.1103/PhysRevB.93.041411`.

[152] M. Scigliuzzo, L. E. Bruhat, A. Bengtsson, et al., "Phononic loss in superconducting resonators on piezoelectric substrates," New J. Phys. **22**, 053027 (2020) `10.1088/1367-2630/ab8044`.

[153] S. Hunklinger and W. Arnold, in *Physical Acoustics*, Vol. 12, edited by W. P. Mason and R. N. Thurston (Academic Press, 1976), pp. 155–215, `10.1016/B978-0-12-477912-9.50008-4`.

[154] J. Gao, "The Physics of Superconducting Microwave Resonators," Ph.D. Thesis (California Institute of Technology, Pasadena, 2008).

[155] J. Goetz, F. Deppe, M. Haeberlein, et al., "Loss mechanisms in superconducting thin film microwave resonators," J. Appl. Phys. **119**, 015304 (2016) `10.1063/1.4939299`.

[156] R. Meservey and P. M. Tedrow, "Properties of Very Thin Aluminum Films," J. Appl. Phys. **42**, 51 (1971) `10.1063/1.1659648`.

[157] T. Luschmann, P. Schmidt, F. Deppe, et al., "Mechanical frequency control in inductively coupled electromechanical systems," Sci. Rep. **12**, 1608 (2022) `10.1038/s41598-022-05438-x`.

[158] P. E. Schmidt, "Nanomechanical Quantum Systems," Ph.D. Thesis (Walther-Meissner-Institut and Technische Universität München, München, 2019).

[159] D. F. Walls and G. J. Milburn, *Quantum optics*, 2nd ed (Springer, Berlin, 2008).

[160] A. Bruno, G. de Lange, S. Asaad, et al., "Reducing intrinsic loss in superconducting resonators by surface treatment and deep etching of silicon substrates," Appl. Phys. Lett. **106**, 182601 (2015) `10.1063/1.4919761`.

[161] C. M. Quintana, A. Megrant, Z. Chen, et al., "Characterization and reduction of microfabrication-induced decoherence in superconducting quantum circuits," Appl. Phys. Lett. **105**, 062601 (2014) `10.1063/1.4893297`.

[162] W. Woods, G. Calusine, A. Melville, et al., "Determining Interface Dielectric Losses in Superconducting Coplanar-Waveguide Resonators," Phys. Rev. Appl. **12**, 014012 (2019) `10.1103/PhysRevApplied.12.014012`.

[163] L. Koch, N. Bruckmoser, et al., "[Manuscript in preparation]," (2024).

[164] L. Niekamp, “Frequency control and sensing of mechanical properties in nanostring-based electromechanics,” Master’s thesis (Walther-Meissner-Institut and Technische Universität München, München, 2022).

[165] J. Shin, Y. Ryu, M.-A. Miri, et al., “On-Chip Microwave Frequency Combs in a Superconducting Nanoelectromechanical Device,” Nano Lett. **22**, 5459 (2022) `10.1021/acs.nanolett.2c01503`.

[166] A. Potts, G. J. Parker, J. J. Baumberg, and P. A. J. de Groot, “CMOS compatible fabrication methods for submicron Josephson junction qubits,” IEE Proc. - Sci. Meas. Technol. **148**, 225 (2001) `10.1049/ip-smt:20010395`.

[167] M. V. Costache, G. Bridoux, I. Neumann, and S. O. Valenzuela, “Lateral metallic devices made by a multiangle shadow evaporation technique,” J. Vac. Sci. Technol. B **30**, 04E105 (2012) `10.1116/1.4722982`.

[168] J. Van Damme, Ts. Ivanov, P. Favia, et al., “Argon-Milling-Induced Decoherence Mechanisms in Superconducting Quantum Circuits,” Phys. Rev. Appl. **20**, 014034 (2023) `10.1103/PhysRevApplied.20.014034`.

[169] A. Dunsworth, A. Megrant, C. Quintana, et al., “Characterization and reduction of capacitive loss induced by sub-micron Josephson junction fabrication in superconducting qubits,” Appl. Phys. Lett. **111**, 022601 (2017) `10.1063/1.4993577`.

[170] N. Bruckmoser, L. Koch, et al., “[Manuscript in preparation],” (2024).

[171] C. Song, T. W. Heitmann, M. P. DeFeo, et al., “Microwave response of vortices in superconducting thin films of Re and Al,” Phys. Rev. B **79**, 174512 (2009) `10.1103/PhysRevB.79.174512`.

[172] R. Reuschling and E. Schultheiss, “Ion Sources for Vacuum Thin Film Technology,” Vak. Forsch. Prax. **17**, 267 (2005) `10.1002/vipr.200500265`.

[173] K. D. Crowley, R. A. McLellan, A. Dutta, et al., “Disentangling Losses in Tantalum Superconducting Circuits,” Phys. Rev. X **13**, 041005 (2023) `10.1103/PhysRevX.13.041005`.

[174] T. Luschmann, A. Jung, S. Geprägs, et al., “Surface acoustic wave resonators on thin film piezoelectric substrates in the quantum regime,” Mater. Quantum. Technol. **3**, 021001 (2023) `10.1088/2633-4356/acc9f6`.

[175] M. K. Ekström, T. Aref, J. Runeson, et al., “Surface acoustic wave unidirectional transducers for quantum applications,” Appl. Phys. Lett. **110**, 073105 (2017) `10.1063/1.4975803`.

[176] É. Dumur, K. J. Satzinger, G. A. Peairs, et al., “Unidirectional distributed acoustic reflection transducers for quantum applications,” Appl. Phys. Lett. **114**, 223501 (2019) `10.1063/1.5099095`.

[177] D. J. Collins, A. Neild, and Y. Ai, “Highly focused high-frequency travelling surface acoustic waves (SAW) for rapid single-particle sorting,” Lab Chip **16**, 471 (2016) `10.1039/C5LC01335F`.

[178] L. Shao, S. Maity, L. Zheng, et al., “Phononic Band Structure Engineering for High- Q Gigahertz Surface Acoustic Wave Resonators on Lithium Niobate,” Phys. Rev. Appl. **12**, 014022 (2019) `10.1103/PhysRevApplied.12.014022`.

[179] C. T. Earnest, J. H. Béjanin, T. G. McConkey, et al., “Substrate surface engineering for high-quality silicon/aluminum superconducting resonators,” Supercond. Sci. Technol. **31**, 125013 (2018) `10.1088/1361-6668/aae548`.

[180] W. Kern, “The Evolution of Silicon Wafer Cleaning Technology,” J. Electrochem. Soc. **137**, 1887 (1990) `10.1149/1.2086825`.

[181] D. S. Wisbey, J. Gao, M. R. Vissers, et al., “Effect of metal/substrate interfaces on radio-frequency loss in superconducting coplanar waveguides,” J. Appl. Phys. **108**, 093918 (2010) `10.1063/1.3499608`.

[182] N. Bruckmoser, “Development of a Fabrication Process for High-Coherence Niobium Qubits,” Master’s thesis (Walther-Meissner-Institut and Technische Universität München, München, 2022).

[183] T. Luschmann, “Coupling Strings, String Networks and Magnon-Phonon Interaction,” Master’s thesis (Walther-Meissner-Institut and Technische Universität München, München, 2018).

[184] D. Schwienbacher, “Coupling phenomena in nanomechanical hybrid systems,” Ph.D. Thesis (Walther-Meissner-Institut and Technische Universität München, München, 2021).

[185] M. A. Mohammad, M. Muhammad, S. K. Dew, and M. Stepanova, in *Nanofabrication* (Springer Vienna, Vienna, 2012), pp. 11–41, `10.1007/978-3-7091-0424-8_2`.

[186] G. Owen, “Methods for proximity effect correction in electron lithography,” J. Vac. Sci. Technol. B **8**, 1889 (1990) `10.1116/1.585179`.

[187] U. Madhow, *Fundamentals of Digital Communication* (Cambridge University Press, Cambridge, 2008), `10.1017/CBO9780511807046`.

[188] S. Weichselbaumer, “Spin Dynamics in Strongly Coupled Spin-Photon Hybrids,” Ph.D. Thesis (Walther-Meissner-Institut and Technische Universität München, München, 2020).

[189] M. S. Khalil, M. J. A. Stoutimore, F. C. Wellstood, and K. D. Osborn, “An analysis method for asymmetric resonator transmission applied to superconducting devices,” J. Appl. Phys. **111**, 054510 (2012) `10.1063/1.3692073`.

[190] M. J. Martínez-Pérez and D. Koelle, “NanoSQUIDs: Basics & recent advances,” Phys. Sci. Rev. **2**, `10.1515/psr-2017-5001` (2017) `10.1515/psr-2017-5001`.

[191] S. M. Anton, C. Müller, J. S. Birenbaum, et al., “Pure dephasing in flux qubits due to flux noise with spectral density scaling as 1/f,” Phys. Rev. B **85**, 224505 (2012) `10.1103/PhysRevB.85.224505`.

[192] I. Corveira Rodrigues, “Coupling Harmonic Oscillators to Superconducting Quantum Interference Cavities,” Ph.D. Thesis (Delft University of Technology, Delft, 2021), `10.4233/UUID:90C588B1-EBEF-4AB8-B51F-B3221D8AD6CC`.

[193] B. L. Brandt, R. D. Parks, and R. D. Chaudhari, “Intermediate state of thin superconductors,” J. Low Temp. Phys. **4**, 41 (1971) `10.1007/BF00628436`.

[194] K. G. Fedorov, A. V. Shcherbakova, M. J. Wolf, D. Beckmann, and A. V. Ustinov, “Fluxon Readout of a Superconducting Qubit,” Phys. Rev. Lett. **112**, 160502 (2014) `10.1103/PhysRevLett.112.160502`.

[195] L. Embon, Y. Anahory, A. Suhov, et al., "Probing dynamics and pinning of single vortices in superconductors at nanometer scales," Sci. Rep. **5**, 7598 (2015) `10.1038/srep07598`.

[196] J. D. Teufel, T. Donner, M. A. Castellanos-Beltran, J. W. Harlow, and K. W. Lehnert, "Nanomechanical motion measured with an imprecision below that at the standard quantum limit," Nature Nanotech **4**, 820 (2009) `10.1038/nnano.2009.343`.

[197] C. Macklin, K. OBrien, D. Hover, et al., "A nearquantum-limited Josephson traveling-wave parametric amplifier," Science **350**, 307 (2015) `10.1126/science.aaa8525`.

[198] C. M. Caves, "Quantum limits on noise in linear amplifiers," Phys. Rev. D **26**, 1817 (1982) `10.1103/PhysRevD.26.1817`.

[199] D. G. Atanasova, "Fabrication and Characterization of a Dimer Josephson Junction Array Amplier," Master's thesis (Universität Innsbruck, Innsbruck, 2020).

[200] A. Roy and M. Devoret, "Quantum-limited parametric amplification with Josephson circuits in the regime of pump depletion," Phys. Rev. B **98**, 045405 (2018) `10.1103/PhysRevB.98.045405`.

[201] B. Abdo, A. Kamal, and M. Devoret, "Nondegenerate three-wave mixing with the Josephson ring modulator," Phys. Rev. B **87**, 014508 (2013) `10.1103/PhysRevB.87.014508`.

[202] H. H. Meinke and F. W. Gundlach, *Taschenbuch der Hochfrequenztechnik: Band 3: Systeme* (Springer, Berlin, 1985).

[203] P. Winkel, "Superconducting quantum circuits for hybrid architectures," Ph.D. Thesis (Karlsruher Institut für Technologie, Karlsruhe, 2020).

[204] M. U. Renger, "Inter-lab Quantum Microwave Teleportation," Ph.D. Thesis (Walther-Meissner-Institut and Technische Universität München, München, 2023).

[205] L. Planat, R. Dassonneville, J. P. Martínez, et al., "Understanding the Saturation Power of Josephson Parametric Amplifiers Made from SQUID Arrays," Phys. Rev. Appl. **11**, 034014 (2019) `10.1103/PhysRevApplied.11.034014`.

[206] M. Hatridge, S. Shankar, M. Mirrahimi, et al., "Quantum Back-Action of an Individual Variable-Strength Measurement," Science **339**, 178 (2013) `10.1126/science.1226897`.

[207] P. Schmidt, D. Schwienbacher, M. Pernpeintner, et al., "Ultrawide-range photon number calibration using a hybrid system combining nano-electromechanics and superconducting circuit quantum electrodynamics," Appl. Phys. Lett. **113**, 152601 (2018) `10.1063/1.5052414`.

[208] L. Spietz, K. W. Lehnert, I. Siddiqi, and R. J. Schoelkopf, "Primary Electronic Thermometry Using the Shot Noise of a Tunnel Junction," Science **300**, 1929 (2003) `10.1126/science.1084647`.

[209] M. Mariantoni, E. P. Menzel, F. Deppe, et al., "Planck Spectroscopy and Quantum Noise of Microwave Beam Splitters," Phys. Rev. Lett. **105**, 133601 (2010) `10.1103/PhysRevLett.105.133601`.

[210] M. Abramowitz and I. A. Stegun, (Eds.), *Handbook of Mathematical Functions: With Formulas, Graphs, and Mathematical Tables* (Dover Publications Inc., New York, 1965).

[211] I. Besedin and A. P. Menushenkov, “Quality factor of a transmission line coupled coplanar waveguide resonator,” EPJ Quantum Technol. **5**, 1 (2018) `10.1140/epjqt/s40507-018-0066-3`.

[212] F. Behroozi, M. P. Garfunkel, F. H. Rogan, and G. A. Wilkinson, “Temperature and magnetic field dependence of the superconducting penetration depth in pure and impure aluminum single crystals,” Phys. Rev. B **10**, 2756 (1974) `10.1103/PhysRevB.10.2756`.

[213] N. Samkharadze, A. Bruno, P. Scarlino, et al., “High-Kinetic-Inductance Superconducting Nanowire Resonators for Circuit QED in a Magnetic Field,” Phys. Rev. Appl. **5**, 044004 (2016) `10.1103/PhysRevApplied.5.044004`.

[214] J. E. Healey, T. Lindström, M. S. Colclough, C. M. Muirhead, and A. Ya. Tzalenchuk, “Magnetic field tuning of coplanar waveguide resonators,” Appl. Phys. Lett. **93**, 043513 (2008) `10.1063/1.2959824`.

[215] B. Ho Eom, P. K. Day, H. G. LeDuc, and J. Zmuidzinas, “A wideband, low-noise superconducting amplifier with high dynamic range,” Nat. Phys. **8**, 623 (2012) `10.1038/nphys2356`.

[216] T. Yamaji, S. Kagami, A. Yamaguchi, et al., “Spectroscopic observation of the crossover from a classical Duffing oscillator to a Kerr parametric oscillator,” Phys. Rev. A **105**, 023519 (2022) `10.1103/PhysRevA.105.023519`.

[217] L. F. Deeg et al., “[Manuscript in preparation],” (2024).

[218] F. Hoehne, Yu. A. Pashkin, O. Astafiev, et al., “Damping in high-frequency metallic nanomechanical resonators,” Phys. Rev. B **81**, 184112 (2010) `10.1103/PhysRevB.81.184112`.

[219] M. Poot, S. Etaki, I. Mahboob, et al., “Tunable Backaction of a DC SQUID on an Integrated Micromechanical Resonator,” Phys. Rev. Lett. **105**, 207203 (2010) `10.1103/PhysRevLett.105.207203`.

[220] M. Fleischhauer, A. Imamoglu, and J. P. Marangos, “Electromagnetically induced transparency: Optics in coherent media,” Rev. Mod. Phys. **77**, 633 (2005) `10.1103/RevModPhys.77.633`.

[221] J. M. Dobrindt, I. Wilson-Rae, and T. J. Kippenberg, “Parametric Normal-Mode Splitting in Cavity Optomechanics,” Phys. Rev. Lett. **101**, 263602 (2008) `10.1103/PhysRevLett.101.263602`.

[222] A. Schliesser, O. Arcizet, R. Rivière, G. Anetsberger, and T. J. Kippenberg, “Resolved-sideband cooling and position measurement of a micromechanical oscillator close to the Heisenberg uncertainty limit,” Nat. Phys. **5**, 509 (2009) `10.1038/nphys1304`.

[223] H. J. Mamin and D. Rugar, “Sub-attonewton force detection at millikelvin temperatures,” Appl. Phys. Lett. **79**, 3358 (2001) `10.1063/1.1418256`.

[224] J. D. Thompson, B. M. Zwickl, A. M. Jayich, et al., “Strong dispersive coupling of a high-finesse cavity to a micromechanical membrane,” Nature **452**, 72 (2008) `10.1038/nature06715`.

[225] B. Lassagne, Y. Tarakanov, J. Kinaret, D. Garcia-Sanchez, and A. Bachtold, "Coupling Mechanics to Charge Transport in Carbon Nanotube Mechanical Resonators," Science **325**, 1107 (2009) `10.1126/science.1174290`.

[226] H. R. Ott, "The volume change at the superconducting transition of lead and aluminum," J. Low Temp. Phys. **9**, 331 (1972) `10.1007/BF00654850`.

[227] J.-Q. Liao and F. Nori, "Single-photon quadratic optomechanics," Sci. Rep. **4**, 6302 (2015) `10.1038/srep06302`.

[228] A. Kamra, S. von Hoesslin, N. Roschewsky, et al., "An all-electrical torque differential magnetometer operating under ambient conditions," Eur. Phys. J. B **88**, 224 (2015) `10.1140/epjb/e2015-60380-2`.

[229] A. Kamra, M. Schreier, H. Huebl, and S. T. B. Goennenwein, "Theoretical model for torque differential magnetometry of single-domain magnets," Phys. Rev. B **89**, 184406 (2014) `10.1103/PhysRevB.89.184406`.

[230] I. Petkovic, A. Lollo, and J. G. E. Harris, "Phase-Slip Statistics of a Single Isolated Flux-Biased Superconducting Ring," Phys. Rev. Lett. **125**, 067002 (2020) `10.1103/PhysRevLett.125.067002`.

[231] M. Misakian, "Equations for the magnetic field produced by one or more rectangular loops of wire in the same plane," J. Res. Natl. Inst. Stand. Technol. **105**, 557 (2000) `10.6028/jres.105.045`.

[232] E. H. Brandt, P. Esquinazi, and H. Neckel, "A superconducting vibrating reed applied to flux-line pinning. I. Theory," J. Low Temp. Phys. **63**, 187 (1986).

[233] P. Esquinazi, "Vibrating superconductors," J. Low Temp. Phys. **85**, 139 (1991) `10.1007/BF00681969`.

[234] A. A. Abrikosov, "The magnetic properties of superconducting alloys," J. Phys. Chem. Solids **2**, 199 (1957) `10.1016/0022-3697(57)90083-5`.

[235] J. Kober, A. Gupta, P. Esquinazi, H. F. Braun, and E. H. Brandt, "Vibrating-reed experiments on superconducting suspensions," Phys. Rev. Lett. **66**, 2507 (1991) `10.1103/PhysRevLett.66.2507`.

[236] I. Khukhareva, "The Superconducting Properties of Thin Aluminum Films," Sov. Phys. JETP **16**, 828 (1963).

[237] A. Gupta, P. Esquinazi, H. F. Braun, et al., "Vibrating reed studies on high-Tc superconductors," Bull. Mater. Sci. **14**, 877 (1991) `10.1007/BF02744742`.

[238] K. Länge, B. E. Rapp, and M. Rapp, "Surface acoustic wave biosensors: a review," Anal. Bioanal. Chem. **391**, 1509 (2008) `10.1007/s00216-008-1911-5`.

[239] T. Franke, S. Braunmüller, L. Schmid, A. Wixforth, and D. A. Weitz, "Surface acoustic wave actuated cell sorting (SAWACS)," Lab Chip **10**, 789 (2010) `10.1039/b915522h`.

[240] Y. Chu, P. Kharel, T. Yoon, et al., "Creation and control of multi-phonon Fock states in a bulk acoustic-wave resonator," Nature **563**, 666 (2018) `10.1038/s41586-018-0717-7`.

[241] S. A. Tadesse and M. Li, "Sub-optical wavelength acoustic wave modulation of integrated photonic resonators at microwave frequencies," Nat. Commun. **5**, 5402 (2014) `10.1038/ncomms6402`.

[242] K. C. Balram, M. I. Davanço, J. D. Song, and K. Srinivasan, “Coherent coupling between radiofrequency, optical and acoustic waves in piezo-optomechanical circuits,” Nat. Photonics **10**, 346 (2016) 10.1038/nphoton.2016.46.

[243] M. Shen, J. Xie, C.-L. Zou, et al., “High frequency lithium niobate film-thickness-mode optomechanical resonator,” Appl. Phys. Lett. **117**, 131104 (2020) 10.1063/5.0020019.

[244] Y. Xu, A. A. Sayem, L. Fan, et al., “Bidirectional interconversion of microwave and light with thin-film lithium niobate,” Nat. Commun. **12**, 4453 (2021) 10.1038/s41467-021-24809-y.

[245] B. A. Moores, L. R. Sletten, J. J. Viennot, and K. W. Lehnert, “Cavity Quantum Acoustic Device in the Multimode Strong Coupling Regime,” Phys. Rev. Lett. **120**, 227701 (2018) 10.1103/PhysRevLett.120.227701.

[246] G. Poberaj, H. Hu, W. Sohler, and P. Günter, “Lithium niobate on insulator (LNOI) for micro-photonic devices,” Laser & Photon. Rev. **6**, 488 (2012) 10.1002/lpor.201100035.

[247] A. Boes, B. Corcoran, L. Chang, J. Bowers, and A. Mitchell, “Status and Potential of Lithium Niobate on Insulator (LNOI) for Photonic Integrated Circuits,” Laser & Photon. Rev. **12**, 1700256 (2018) 10.1002/lpor.201700256.

[248] C. Wang, M. Zhang, B. Stern, M. Lipson, and M. Lonar, “Nanophotonic lithium niobate electro-optic modulators,” Opt. Express, OE **26**, 1547 (2018) 10.1364/OE.26.001547.

[249] L. Cai, S. Zhang, and H. Hu, “A compact photonic crystal micro-cavity on a single-mode lithium niobate photonic wire,” J. Opt. **18**, 035801 (2016) 10.1088/2040-8978/18/3/035801.

[250] A. Guarino, G. Poberaj, D. Rezzonico, R. Degl’Innocenti, and P. Günter, “Electrooptically tunable microring resonators in lithium niobate,” Nat. Photonics **1**, 407 (2007) 10.1038/nphoton.2007.93.

[251] W. Jiang, R. N. Patel, F. M. Mayor, et al., “Lithium niobate piezo-optomechanical crystals,” Optica **6**, 845 (2019) 10.1364/OPTICA.6.000845.

[252] F. V. Pop, A. S. Kochhar, G. Vidal-Alvarez, and G. Piazza, “Laterally vibrating lithium niobate MEMS resonators with 30% electromechanical coupling coefficient,” in 2017 IEEE 30th Int. Conf. Micro Electro Mech. Syst. MEMS (2017), pp. 966–969, 10.1109/MEMSYS.2017.7863571.

[253] C. J. Sarabalis, Y. D. Dahmani, A. Y. Cleland, and A. H. Safavi-Naeini, “S-band delay lines in suspended lithium niobate,” J. Appl. Phys. **127**, 054501 (2020) 10.1063/1.5126428.

[254] W. Jiang, C. J. Sarabalis, Y. D. Dahmani, et al., “Efficient bidirectional piezo-optomechanical transduction between microwave and optical frequency,” Nat. Commun. **11**, 1166 (2020) 10.1038/s41467-020-14863-3.

[255] P. Arrangoiz-Arriola, E. A. Wollack, Z. Wang, et al., “Resolving the energy levels of a nanomechanical oscillator,” Nature **571**, 537 (2019) 10.1038/s41586-019-1386-x.

[256] M. Kadota and T. Ogami, “5.4 GHz Lamb Wave Resonator on LiNbO $_3$ Thin Crystal Plate and Its Application,” Jpn. J. Appl. Phys. **50**, 07HD11 (2011) `10.1143/JJAP.50.07HD11`.

[257] J. Hayashi, M. Gomi, M. Suzuki, et al., “High-coupling leaky SAWs on LiTaO3 thin plate bonded to quartz substrate,” in 2017 IEEE Int. Ultrason. Symp. IUS (2017), pp. 1–4, `10.1109/ULTSYM.2017.8091566`.

[258] T. Kimura, M. Omura, Y. Kishimoto, and K. Hashimoto, “Comparative Study of Acoustic Wave Devices Using Thin Piezoelectric Plates in the 35-GHz Range,” IEEE Trans. Microw. Theory Tech. **67**, 915 (2019) `10.1109/TMTT.2018.2890661`.

[259] H. Wang, S. Singh, C. R. H. McRae, et al., “Cryogenic single-port calibration for superconducting microwave resonator measurements,” Quantum Sci. Technol. **6**, 035015 (2021) `10.1088/2058-9565/ac070e`.

[260] M. A. Krivoglaz, *X-Ray and Neutron Diffraction in Nonideal Crystals* (Springer Science & Business Media, Berlin, 2012).

[261] U. Pietsch, V. Holy, and T. Baumbach, *High-Resolution X-Ray Scattering: From Thin Films to Lateral Nanostructures* (Springer Science & Business Media, 2004).

[262] A. Ulyanenkov, “LEPTOS: a universal software for x-ray reflectivity and diffraction,” in Adv. Comput. Methods X-Ray Neutron Opt. Vol. 5536 (2004), pp. 1–15, `10.1117/12.563302`.

[263] A. J. Annunziata, D. F. Santavicca, L. Frunzio, et al., “Tunable superconducting nanoinductors,” Nanotechnology **21**, 445202 (2010) `10.1088/0957-4484/21/44/445202`.

[264] M. J. Schwarz, “Gradiometric tunable-gap flux qubits in a circuit QED architecture,” Ph.D. Thesis (Walther-Meissner-Institut and Technische Universität München, München, 2014).

[265] F. E. Terman, *Radio Engineers’ Handbook*, 1. (McGraw-Hill Book Company, New York and London, 1943).

List of publications

[1] D. Schwienbacher, T. Luschmann, R. Gross, and H. Huebl, *Dia- and adiabatic dynamics in a phononic network*, (2020) `http://arxiv.org/abs/2011.08080` (visited on 03/12/2024), preprint.

[2] T. Luschmann, P. Schmidt, F. Deppe, et al., “Mechanical frequency control in inductively coupled electromechanical systems,” Sci. Rep. **12**, 1608 (2022) `10.1038/s41598-022-05438-x`.

[3] M. Müller, T. Luschmann, A. Faltermeier, et al., “Magnetic field robust high quality factor NbTiN superconducting microwave resonators,” Mater. Quantum. Technol. **2**, 015002 (2022) `10.1088/2633-4356/ac50f8`.

[4] T. Luschmann, A. Jung, S. Geprägs, et al., “Surface acoustic wave resonators on thin film piezoelectric substrates in the quantum regime,” Mater. Quantum. Technol. **3**, 021001 (2023) `10.1088/2633-4356/acc9f6`.

[5] M. Müller, J. Weber, F. Engelhardt, et al., “Chiral phonons and phononic birefringence in ferromagnetic metalbulk acoustic resonator hybrids,” Phys. Rev. B **109**, 024430 (2024) `10.1103/PhysRevB.109.024430`.

Acknowledgements

Dr. Hans Huebl, my doctoral advisor, for hiring me as a PhD student and supervising my research over the course of the last five years. From day one you put your trust in me and gave me the freedom to pursue my project in the way that I saw fit. At the same time, you were always available when I needed support and advice – or a random spare part out of the depths of your office. Thank you for encouraging me to visit a variety of conferences and always finding the funds to make it possible. I could not have wished for a better supervisor.

Prof. Rudolf Gross, for supporting my research both with the resources of the institute and as a mentor and scientific advisor. Your vast knowledge on superconductivity and fundamental physics proved invaluable for my project on more than one occasion. During our talks, it showed that teaching the next generation of scientists and ensuring the success of the WMI's students remains a top priority for you – and I have the utmost respect for that.

Prof. Gerhard Kirchmair and his group at the University of Innsbruck, including *David Zoepfl* and *Lukas Deeg*, for providing us with the DJJAA parametric amplifier and for many valuable discussions about magnetomechanics. In particular, I want to thank *Lukas Deeg* for our helpful discussions about the Kerr non-linearity and for sharing his code to perform the non-linear circlefit.

Prof. Anja Metelmann, *Nicolás Díaz-Naufal* and *Shivangi Dhiman*, for their theoretical support regarding a variety of our experiments, in particular the model for optomechanical cooling with non-linear microwave resonators.

Matthias Althammer, for valuable advice and discussions in the AC-meetings and maintaining the deposition tools and the bonder.

Philip Schmidt, my predecessor, who built the foundation for the inductively coupled electromechanics experiments and taught me a lot about microwave measurements in the first few months of my PhD. You gave me plenty of useful advice about the life of a PhD in general and at the WMI in particular, thank you.

Korbinian Rubenbauer, for his work on the multi-step fabrication process and allowing me to present his promising measurement data in the outlook. I am happy that you will carry on the electromechanics research at the WMI. I wish you the best of luck and am excited to see what you will accomplish!

My office mates and/or colleagues *Leon Koch, Kedar Honasoge,* and *Daniil Bazulin*, for the always helpful discussions about fabrication recipes, fitting procedures and experiments. Also for the countless lunches, coffee breaks, friday beers and chats about non-scientific topics. But mainly, for becoming my close friends, hopefully for a long time to come.

Niklas Bruckmoser, *Johannes Schirk* and *Ivan Tsitsilin*, for being very generous with their time and knowledge about fabrication, (package) design, and microwave wiring. I appreciate it.

Christopher Waas, *Lukas Niekamp* and *Alexander Jung*, the master students I had the pleasure of supervising, and whose projects have contributed greatly to this thesis. All three of you have proven to be formidable scientists and I greatly enjoyed working with every single one of you. I am proud to see each of you pursuing his own PhD and am curious to see where your respective journeys will take you.

Achim Marx, *Thomas Brenninger*, *Andreas Russo*, and *Sebastian Kammerer*, for taking care of the infrastructure and the ever growing number of machines.

Sybilla Plöderl and *Maria Botta*, for making sure the institute remains clean and presentable, and for many enjoyable chats in between.

Emel Dönertas, for always finding a timely solution to the problems caused by german bureaucracy and shielding us scientists from the worst of it.

My former colleagues *Daniel Schwienbacher* and *Lukas Liensberger* for the regular coffee-talks, which remain welcome breaks, even across timezones and continents.

All current and former members of the WMI, including *Fabian Kronowetter*, *David Bunch*, *Max Werninghaus*, *Monika Scheufele*, *Florian Wallner*, *Matthias Grammer*, *Lucia Valor*, and many many more, for building and maintaining the unique working atmosphere that makes the institute such an amazing place to work.

Finally, I want to thank my friends and family.
My parents, *Anna* und *Karl*, and my sister, *Edith*, for always supporting me in finding my own path.
Lorenz and *Max*, for being a dependable constant in my life for more than 18 years now. I couldn't imagine it any other way. Thanks for sticking around.
Saskia and *Philip*, for coming into my life, and changing it for the better. Without you, I would not be where I am today and this thesis might not exist. Thank you with all my heart.
And last but not least, *Maria*, for being immensely supportive even when this thesis consumed a large part of my private life. I'm glad to have you in my life!